The First Second of a Strombolian Volcanic Eruption

Dissertation

Zur Erlangung des Doktorgrades der Naturwissenschaften im Department Geowissenschaften der Universität Hamburg

vorgelegt von

Alexander Gerst

aus Künzelsau

Hamburg, 2010

Als Dissertation angenommen vom Department Geowissenschaften der Universität Hamburg auf Grund der Gutachten von
Prof. Dr. Matthias Hort, Prof. Dr. Richard C. Aster und Dr. Bernard Chouet.

Accepted as dissertation by the Department of Geosciences of the University of Hamburg, based on the reviews of
Prof. Dr. Matthias Hort, Prof. Dr. Richard C. Aster and Dr. Bernard Chouet.

Hamburg, 12. Mai 2010

Prof. Dr. Jürgen Oßenbrügge

Leiter des Department Geowissenschaften
Head of the Department of Geosciences

To strive, to seek, to find,
and not to yield.

Tennyson

ABSTRACT

The exact mechanism behind Strombolian volcanic eruptions is unknown to the present day. Therefore, despite numerous studies using increasingly sophisticated measuring techniques, it is still a frequent subject of debate. Little information has so far been gained on pressures and energies involved during an explosion, mainly due to the lack of precise in-situ measurement techniques of the physical conditions at the source and during the very first moments of a Strombolian explosion. These techniques are now available, and can therefore provide the key to resolving this debate.

In 2005/06 the author of this study deployed three newly-developed, continuous wave Doppler radar instruments at the crater rim of Mount Erebus volcano in Antarctica. Erebus is one of the few volcanic open vent systems that allows the unobstructed observation of source processes from the crater rim. Therefore, the volcano represents an ideal outdoor laboratory and a model for Strombolian-style volcanoes in general. Strombolian explosions at Erebus are most likely generated by the adiabatic expansion of pressurised gas slugs rising in the conduit. Erebus' crater features a 1000°C hot, active phonolite lava lake, which at the time of the experiment was about 40 m wide and produced 2–6 large explosions per day. Part of this study was the development of a wireless data recording system suitable to withstand extreme environmental conditions, such as the ones that can be found in Antarctica and on many volcanoes worldwide. The deployed radar instruments measured the in-situ lava surface velocities of 55 explosions at Erebus, at a sampling rate of 1-15 Hz. Additional instrumentation consisted of a combined infrared/visual video camera and a network of infrasound microphones operated by the Mount Erebus Volcano Observatory. This multi-parameter experiment provides detailed new insights into the still largely unknown mechanism of Strombolian eruptions, and helps to improve existing eruption models.

The main goal of this study is to provide a tool to determine concrete physical eruption parameters as a function of time. The technique developed here will allow the calculation of energy freed during the first second of a Strombolian volcanic eruption as a detailed function of time, including its partitioning into all relevant energy types. In a similar way, the history of gas pressure and volume during an explosion will be derived as a function of time, thus allowing for a detailed analysis of the physical state of the vent system at any given time during the first moments of an explosion.

The study also provides a comprehensive source model for acoustic signals associated with explosions. Furthermore, it supplies a simple way to determine the explosion's vertical ground forces that are expected to generate seismic waves. The above was achieved by developing and applying a simple geometrical explosion model to the data. As an additional output, explosion direction vectors were calculated in 3D as a function of time, allowing for conclusions on the symmetry of the vent system.

A major general conclusion of this study is that energies and pressures of Strombolian explosions cannot be determined by distant acoustic pressure recordings alone. Any attempt to do so will cause misleading results. The outcome of this study suggests, however, a very simple tool for determining gas slug lengths from acoustic signals, which are very similar amongst Strombolian-type volcanoes. While acoustic signals **before** the burst of bubbles are generated by a short monotonic volumetric expansion of the bulging lava lake, signals generated **after** the burst of the bubble are most likely the result of a "$\lambda/4$-type" resonance of the cavity formed by the gas slug in the uppermost conduit. These post-burst signals are higher in amplitude and longer in duration than the pre-burst part, therefore strongly dominating the acoustic signal of explosions. By measuring the frequency and decay rate of the resonance signal, the inferred slug length and possibly the width of the conduit can be determined in a very simple way.

During explosions, the absolute gas pressure inside expanding bubbles rapidly drops from $\sim$3–7 atm to $\sim$2 atm just before the burst. The overall energy budget of explosions is dominated by the quasi-static output of thermal energy through the ejection of hot lava, amounting to more than 10^{12} J per explosion. The dynamics of explosions are controlled by kinetic and potential energy of the expanding bubble shell, whereas other forms of energy play only a minor role. The dynamic energy release (i.e. not counting thermal energy) is typically around 10^9 J for large explosions, with a peak discharge rate frequently exceeding 5×10^9 W, which for a short time equals the power output of several nuclear power plants.

Remarkably, about half of the explosions at Erebus show two distinct surface acceleration peaks separated by $\sim$0.3 seconds. This suggests that rising gas bubbles fragment into two or more parts shortly before reaching the lava lake surface, most likely caused by a change in conduit diameter at the bottom of the lava lake. Results suggest a total gas volume of $>$20,000 m^3 for large explosions, of which typically less than 10% are contained in the respective first approaching bubble fragment of each explosion. Ground forces, caused by the inertia of the accelerated material, lie in the order of 10^8 N and have a dominating frequency of 3 Hz, therefore providing possible source parameters of the expected seismic signal.

The technique developed in this study can be applied to other volcanoes with similar observation conditions. Additionally, the results derived from Erebus provide valuable information on Strombolian explosions in general. For example, the physical parameters determined in this study provide the necessary boundary conditions for sophisticated conduit modelling, not only at Erebus but at many other Strombolian volcanoes. Furthermore, existing eruption models can now be constrained and improved.

CONTENTS

List of Figures

List of Tables

Part I

MOTIVATION & BACKGROUND

CHAPTER 1

INTRODUCTION

Volcanoes are a phenomenon that has always fascinated humans. On average, the population density around active volcanoes is 2 - 5 times as large as the global median (*Small and Naumann*, 2001), paying tribute to their fertile soil. Yet while they are fascinating and fertile, they can also be deadly, with eruptions occurring with little or effectively no detected warning signs (*Larsen et al.*, 2009; *Carn et al.*, 2009). Considering that more than 600 million people live in the vicinity (<100 km) of an active volcano (*Small and Naumann*, 2001), this fact highlights the need for a thorough understanding of volcanic systems in general.

Strombolian volcanoes are an abundant subtype of volcanoes whose incandescent and often picturesque eruptions usually pose no life-threatening danger to the wider population around them. Nevertheless, they can induce secondary catastrophic events such as land slides and tsunamis, and they pose an immediate hazard to individuals and property located on the volcanic edifice. It is therefore important to understand their eruption dynamics, including their general mechanism as well as their detailed physical parameters.

1.1 Motivation for this study

MacDonald (1972) correctly interpreted explosions on lava lakes as bursting gas bubbles. This idea evolved in the following years, and *Blackburn et al.* (1976) suggested the bursting of large gas bubbles as a mechanism for Strombolian explosions[1] in general (Fig. 1.1). They used cine film recordings of explosions at various volcanoes to determine the velocity of explosion ejecta and to estimate gas overpressures. For example, they suggested an overpressure of 600 Pa (0.006 atmospheres) for bubble explosions at Stromboli, and 25 kPa (0.25 atmospheres) for Heimaey. Even though these numbers are much too low in the light of results delivered by newer technologies, they highlight the importance of knowing physical parameters of explosions for the generation of an acceptable eruption model.

Most of the existing studies at Strombolian volcanoes were targeted at determining the source processes of eruptions, and, as will be reviewed later in this chapter, a wealth of

[1] In the following I will use the term *explosion* to describe a single explosive event at a volcano, whereas the term *eruption* refers to the time span of increased activity at a volcano, i.e. an eruption can include several or many explosions.

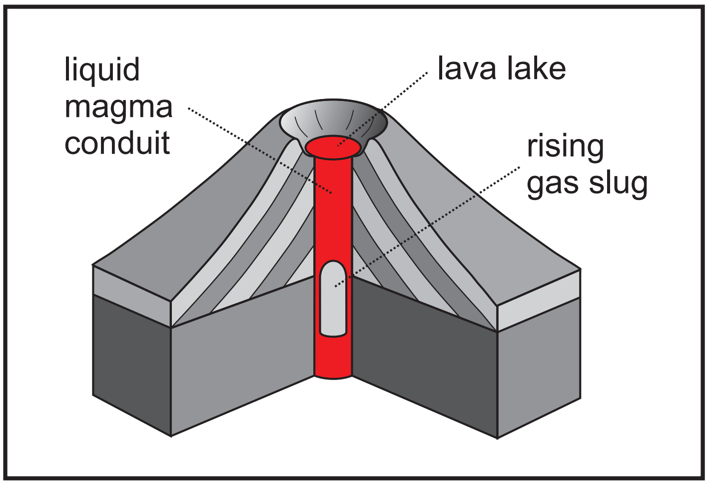

***Figure 1.1:* Sketch of a gas slug rising in a volcanic conduit**

information was derived from numerous field experiments. Nevertheless, a variety of fundamental questions are still open, whose answers play an important role in the way we regard Strombolian volcanic eruptions. The most relevant of these are:

1. *What happens during a Strombolian explosion, and how do bubbles burst?*
2. *What are the energies involved, and what is their partitioning?*
3. *What are the gas overpressures of a rising gas bubble just before its explosion?*
4. *How large are the gas volumes of exploding bubbles?*
5. *What causes the acoustic signal that is typically observed during Strombolian explosions, and what can we learn from it?*
6. *What are the associated ground forces, and can they explain the seismic signals that usually accompany Strombolian explosions?*

In this study, I will attempt to find an answer for each of these questions. I will use the following sections to introduce the necessary background on Strombolian eruptions and the measurement techniques that are of relevance to this study. Finally, at the end of this chapter, in Section 1.7, I will outline the strategy for answering the above questions.

So why is the first second of a volcanic eruption so important? One of the most important parameters that is needed to improve our understanding of the dynamics involved in a Strombolian eruption is the expansion velocity of the gas bubble that is driving it, as well as the velocity of ejected particles during the bubble's burst. Understanding the history of these velocities is the key to calculating the fundamental parameters of an explosion, such as energies, gas pressures and gas volumes, and to explain secondary effects such as resulting acoustic airwaves or seismic ground waves. Additionally, these parameters deliver the necessary boundary conditions for conduit modelling, therefore providing a reference

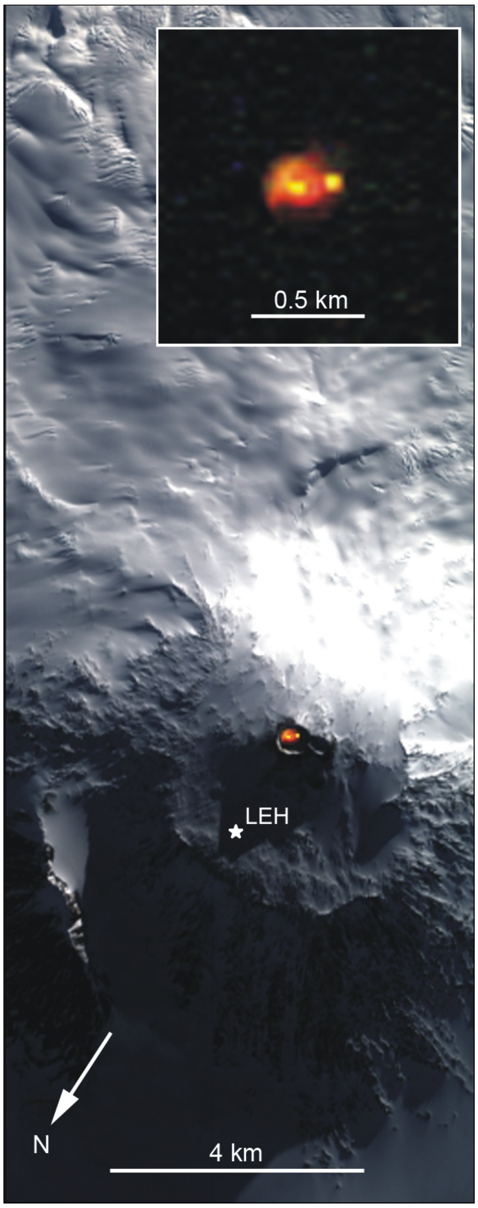

Figure 1.2: Combined thermal and daylight image of Mt. Erebus, *taken by the Hyperion hyperspectral imager aboard the NASA Earth Observing-1 (EO-1) spacecraft. The inlay shows so-called Hyperion L1 data pixels (30x30m in size) of the lava lake, classifying it as "hot" (adapted from Davies et al., 2006, with friendly permission). The field camp at* Lower Erebus Hut *is marked as a star.*

frame for future studies. Processes that occur after the important first moments are a causal result of the explosion process, but they have no great significance for our understanding of the explosion mechanism itself.

1.2 A bubble bursts

As will be shown in the sections ahead, a wealth of literature exists concerning the mechanisms that are responsible for the birth of a Strombolian volcanic eruption. It is understood that before Strombolian explosions, large bubbles of gas rise in a volcanic conduit (so-called *"slug flow"*, see Fig. 1.1). These bubbles typically burst upon reaching the top of the conduit, resulting in a powerful explosion and the ejection of lava fragments several hundred metres high into the atmosphere (Figs. 1.3 and 1.4). The style of explosion is largely deter-

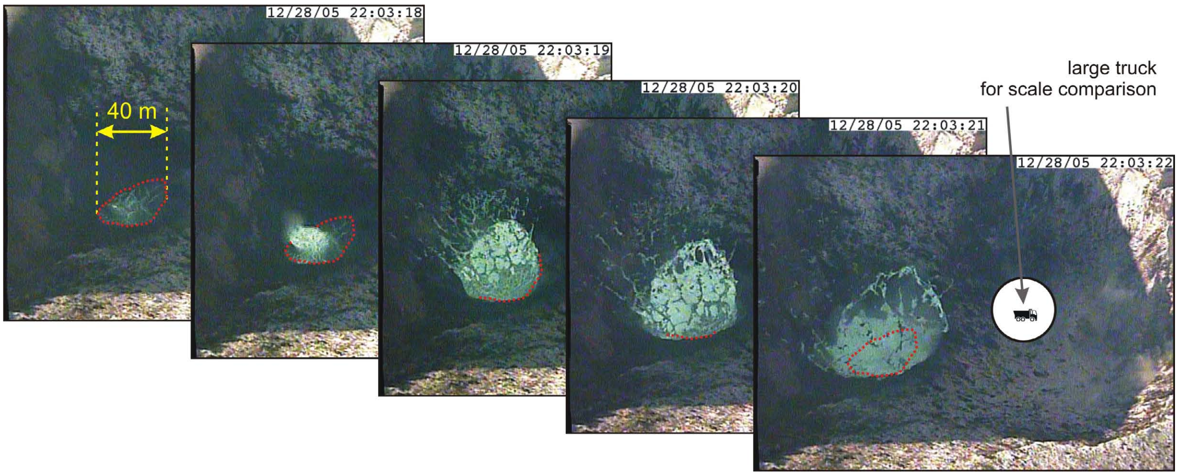

Figure 1.3: ***Image sequence of a 40 m wide bursting gas bubble at Erebus volcano, 2005*** *(infrared false colour, provided by the mount Erebus Volcano Observatory (MEVO).)*

mined by the geometry of the uppermost conduit system. At large lava lakes such as Erta 'Ale, bubbles have enough lateral space to freely expand in all directions before bursting. In contrast, at volcanoes like Stromboli, bubbles burst several tens of metres deep inside the conduit (*Harris and Ripepe*, 2007), and are therefore unable to expand laterally. Erebus is right between those two endmembers, allowing for a burst on the surface but with a lateral constraint through the size of its lava lake.

While it is generally accepted that the rise and burst of a bubble is accompanied by a ground force generating a seismic signal, and by a disturbance of the atmosphere generating an acoustic signal, the underlying mechanisms are still unclear and under discussion (e.g. *Parfitt*, 2004; *Allard et al.*, 2005; *Burton et al.*, 2007; *Aster et al.*, 2008). This is partially due to the lack of in-situ data, which naturally are hard to obtain on active volcanoes.

Until recently, most of what has been learned about Strombolian eruption dynamics has been derived from seismic and/or acoustic data (e.g. *Neuberg et al.*, 1994; *Vergniolle and Brandeis*, 1994; *Ripepe et al.*, 1996; *Rowe et al.*, 1998, 2000; *Johnson and Lees*, 2000; *Johnson*, 2003; *Garcés et al.*, 2000; *Ripepe et al.*, 2004a; *Chouet et al.*, 1997, 2003; *Aster et al.*, 2003, 2008) [2], direct observations (e.g. *Chouet et al.*, 1974; *Blackburn et al.*, 1976, and many more) and laboratory experiments (*Seyfried and Freundt*, 2000; *James et al.*, 2006, 2008). Only in recent years, interdisciplinary observation campaigns have become more and more common (e.g. *Ripepe et al.*, 2002, 2004b; *Aster et al.*, 2004; *Harris and Ripepe*, 2007) in order to record additional observable parameters that allow to better constrain new models. Additional instrumentation typically consisted of passive sensors, such as continuous gas measurements (COSPEC, FTIR, DOAS, e.g. *Burton et al.*, 2003), temperature measurements (e.g. *Ripepe et al.*, 2002), and video surveillance (both visual and thermal, e.g. *Chouet et al.*, 1974; *Ripepe et al.*, 1993; *Calvari et al.*, 2005; *Patrick et al.*, 2007; *Calkins et al.*, 2008).

[2] while these studies cover only a small fraction of the available literature, a more comprehensive overview of existing studies is provided by *Harris and Ripepe* (2007).

Active sensors providing in-situ measurements have been used more rarely, and mainly consisted of Doppler sounding techniques such as acoustic sounders and Doppler radar (e.g. *Weill et al.*, 1992; *Hort and Seyfried*, 1998; *Dubosclard et al.*, 1999; *Seyfried and Hort*, 1999; *Urbanski et al.*, 2002; *Vöge et al.*, 2005; *Donnadieu et al.*, 2005). In addition to field studies, several interesting models were developed (analogue, digital, and theoretical e.g. *Jaupart and Vergniolle*, 1988; *Seyfried and Freundt*, 2000; *James et al.*, 2004, 2008) and underwater explosion experiments were conducted (*Ichihara et al.*, 2005, 2009) that gave clues about the underlying physical principles (as will be discussed in Sec. 2.2).

Bubble bursts have extensively been studied at Stromboli volcano, Italy (see above), which has the advantage of relatively small logistical challenges to a field experiment at the cost of a lack of sufficient visibility onto the surface of the magma column. The same is true for Hawaiian volcanoes, Mt. Etna, and Arenal volcano (e.g. as summarised by *Schmincke*, 2004). Recently, Strombolian eruptions have even been observed underwater at a depth of 550 m by *Chadwick et al.* (2008). In contrast to these examples, much better observation conditions are offered by volcanoes that display an active lava lake. Lava lakes are typically sustained by convective heat and mass transport from a magma reservoir at depth to the top of the conduit (i.e. the lava lake surface; *Witham and Llewellin*, 2006; *Calkins et al.*, 2008).

Unfortunately, amongst the numerous Strombolian volcanoes on our planet, only a very small number sustain a long-lived active lava lake inside the vent that can be observed directly from the crater rim without much risk. These rare model volcanoes provide a unique opportunity for investigating eruption and conduit processes, since they represent an open window into the interior of a volcano. At the present time they are limited to only a few cases worldwide, e.g. Erta Ale volcano in Ethiopia (*Le Guern et al.*, 1979; *Oppenheimer and Francis*, 1998; *Harris et al.*, 2005), Nyiragongo in the Democratic Republic of the Congo (*Tazieff*, 1984; *Demant et al.*, 1994), Ambrym volcano in Vanuatu (*McCall et al.*, 1971; *Carniel et al.*, 2003), and Erebus volcano in Antarctica (*Giggenbach et al.*, 1973). Unfortunately, the good observation conditions at these volcanoes come at the cost of very challenging logistical conditions.

Of the above volcanoes, Erebus is the only one that provides reliable observation conditions[3] at close range (i.e. from the crater rim, within several 100 m), and additionally it is the only one covered with a highly developed existing geophysical network (*Aster et al.*, 2004). It therefore represents an ideal "outdoor laboratory" for the investigation of Strombolian eruption processes.

Yet, as outlined in Section 1.1, despite these numerous studies on Strombolian volcanoes, several important questions are still open. For example, the strength of ground forces generated by explosions is not entirely clear, and there is debate about the source and interpretation of the associated acoustic signal (*Vergniolle and Brandeis*, 1994, 1996; *Seyfried*, 1997; *Seyfried and Freundt*, 2000; *Garcés et al.*, 2000; *Hagerty et al.*, 2000; *Rowe et al.*, 2000; *Johnson and Lees*, 2000; *Johnson*, 2003; *Johnson et al.*, 2003; *Vergniolle et al.*, 2004; *James et al.*, 2004, 2008). Fur-

[3]e.g. Erta Ale's lava lake was found solidified in January 2005 by the author, and numerous reports exist on the variability of conditions at Nyiragongo and Ambrym.

Figure 1.4: *Bursting gas bubbles (centimetre-sized) in a thermal mud pool. Wai-O-Tapu, New Zealand, 2008.*

thermore, basic physical parameters of the gas bubbles are unconstrained, such as their gas pressure and volume at burst (reflected in widely varying estimates, e.g. *Chouet et al.*, 1974; *Blackburn et al.*, 1976; *Wilson*, 1980; *Vergniolle*, 1998; *Vergniolle et al.*, 2004), and their energy balance (e.g. *McGetchin and Chouet*, 1979).

Vergniolle and Brandeis (1994, 1996), based on non-visual data, propose that pressurised gas bubbles, instead of immediately bursting upon reaching the surface of the magma column, rest there for several seconds and vibrate around their equilibrium pressure before they finally burst. They believe that bubbles burst close to the minimum of their suggested oscillation cycle, i.e. when they have reached their smallest dimension of the contraction phase that follows their initial expansion. They include bubbles at Stromboli as an example, where, in order to fit their model to acoustic data, they suggest that bubbles grow from a diameter of two metres to a diameter of more than five metres with a wall thickness of 1 cm, before the bubbles deflate and contract again to a size of 2 m, at which point they burst. Furthermore, *Vergniolle et al.* (2004) propose, again based solely on acoustic data, that bubbles during Strombolian explosions of Shishaldin volcano, Alaska, oscillate in the same fashion before they violently burst. They claim that bubbles inflate from a diameter of 10 m to a diameter of 30 m, while at the same time thinning out to a shell thickness of around 1 cm without bursting, before they shrink again to their minimum size of $\sim$10 m, after which they finally burst.

To the knowledge of the author, bubble oscillations similar to the ones described above (i.e. with a contracting phase) have never been visually observed during Strombolian explosions. Therefore, an independent quantitative or qualitative confirmation does not exist.

Additionally, it appears counterintuitive that a highly viscous magma bubble can grow from a diameter of 10 m to 30 m, at a wall thickness of ∼1 cm, without rupturing or bursting early in the process (as generally discussed by, e.g. *James et al.*, 2009). It appears even more counterintuitive that this bubble should be able to develop an underpressure and subsequently shrink again to a third of its size before it eventually bursts at its minimum size. This study will therefore challenge these assumptions, based on multi-parameter data acquired at Erebus volcano, and propose a much simpler scenario that can explain the available data.

1.3 Volcanic sound

Volcanoes generate sound. While this is obvious for audible frequencies (i.e. >20 Hz) during large eruptions, most of this sound is actually inaudible, located in the *near-infrasound* range below 20 Hz. Such infrasonic signals are usually generated even during minor activity of volcanoes.

It is typically observed at volcanoes that spectral energies of infrasonic signals are several orders of magnitude higher than those of audible signals (e.g. *Vergniolle et al.*, 1996; *Johnson*, 2003; *Johnson et al.*, 2004), usually dominating in the 0.5–10 Hz range (*Garcés and McNutt*, 1997; *Hagerty et al.*, 2000; *Rowe et al.*, 2000; *Johnson and Lees*, 2000). This behaviour is caused by the typical dimensions of volcanic sound sources (i.e. gas-filled resonating chambers, degassing surfaces, vents, lava lakes), which favour generating acoustic wavelengths in the same size dimensions (e.g. in a standard atmosphere, a 4 Hz wave has a wavelength of ∼85 m). Scientists have long made use of these properties, exploiting the fact that acoustic transport mechanisms over short distances in the atmosphere are much simpler than that of seismic waves. A Green's function in the "fluid" atmosphere is much simpler than that in the complex subsurface structure of a volcanic edifice, therefore minimising propagation effects (*Johnson*, 2003). Additionally, the local sound speed is mainly a function of temperature and can therefore be determined relatively easy.

In an early study, *Richards* (1963) measured high frequency (mainly audible) volcanic sound at several types of volcanoes, and concluded that there must be large differences in the sound generation mechanisms of different types of volcanic activity. At almost the same time, *Machado et al.* (1962) tape-recorded eruption sounds from the 1957 eruption of Fayal volcano on the Azores and attributed different types of (mainly audible) acoustic signals to different eruption features. They also found first hints that volcanoes produce signals in the infrasound frequency range by noticing strong movements of the recorder needle when no audible eruption sound was present.

Several studies targeted the sound that is produced by large volcanic eruptions, and found that these eruptions are capable of producing very long period infrasonic signals that circumnavigate our planet (e.g. *Gorshkov*, 1960; *Gorshkov and Dubik*, 1970; *Simkin and Howard*, 1970; *Donn and Balachandran*, 1981; *Mikumo and Bolt*, 1985; *Kanamori and Mori*, 1992; *Morrissey and Chouet*, 1997). *Donn and Balachandran* (1981) used seismic and acoustic waves generated by the 1981 Mt. St. Helens eruption to calculate the explosive yield of the eruption, which they estimated to be equivalent to around 35 megatons of TNT. Such results highlight the potentially destructive effects of volcanic pressure waves (*Yokoo et al.*, 2006).

While it appears intuitive that infrasonic and seismic waves caused by a volcanic eruption yield important information about the eruption intensity, *Johnson et al.* (2005) showed that this is not always the case, concluding that seismic and acoustic amplitudes do not generally scale well, or in an obvious relationship, with eruption intensities (see also *Yamasato*, 1998; *Hagerty et al.*, 2000; *Johnson and Lees*, 2000). This was supported by a laboratory study by *Vidal et al.* (2006), showing that there is no simple relationship between measured acoustic pressure amplitudes at the receiver and the pressure inside an acoustic source. Nevertheless, acoustic measurements at volcanoes have greatly increased the knowledge of eruption processes. An important asset of acoustic measurements at volcanoes is the simple determination of vent locations, allowing for precise activity mapping (*Yamasato*, 1997; *Ripepe and Marchetti*, 2002; *Johnson et al.*, 2003; *Garcés et al.*, 2003; *Johnson*, 2004; *Matoza et al.*, 2007; *Jones et al.*, 2008).

Several studies investigated the propagation of volcano-induced acoustic waves in the atmosphere (e.g. *Buckingham and Garcés*, 1996; *Garcés and McNutt*, 1997; *Garcés et al.*, 1998; *Matoza et al.*, 2007, 2009; *Fee and Garcés*, 2007), an important aspect of volcano acoustics when measuring sound at medium to large distances from the source. *Johnson et al.* (2008), in accordance with earlier studies (e.g. *Vergniolle et al.*, 1996; *Pierce*, 1981; *Dowling and Williams*, 1983; *Johnson*, 2003) argue that acoustic path effects such as multipathing, diffraction, and non-linearities are often negligible when certain conditions are given, such as measuring infrasonic frequencies with a moderate amplitude within a few kilometres of the crater rim of a volcano, and when considering only the first moments of an explosion signal.

The sound of a Strombolian explosion is an especially promising information source for determining the underlying processes. Accordingly, many volcano-acoustic studies targeted Strombolian volcanoes.

Woulff and McGetchin (1976) studied volcanic noise caused by explosions at Stromboli and calculate gas velocities from acoustic power. They conclude that the acoustic source geometry mainly resembles that of a dipole, which was later, however, shown to be only partially true (*Vergniolle and Brandeis*, 1994) and can be attributed to the lack of low frequency data at the time. *Neuberg et al.* (1994) showed that seismic broadband recordings at Stromboli contain a large frequency content below 1 Hz, highlighting the importance of broadband recordings not only when recording seismic signals but also when recording acoustic signals.

Erebus volcano, which has exhibited periods of Strombolian explosions ever since it was first visited, was the target for several seismo-acoustic studies by *Dibble et al.* (1984); *Dibble* (1989) and later by *Rowe et al.* (2000); *Johnson et al.* (2003, 2004); *Johnson and Aster* (2005); *Johnson et al.* (2008); *Jones et al.* (2008). These studies revealed a wealth of information and showing that seismo-acoustic explosion signals are generated by the burst of large bubbles on the surface of Erebus' lava lake.

On the theoretical side, *Lu et al.* (1989) described oscillations of a small floating gas bubble at the surface of a liquid, and concluded that gas bubbles can be an effective monopole source of sound. These and similar observations of possible sound sources led to a variety of proposed source mechanisms for Strombolian explosions.

Several studies discuss the effects of a Strombolian explosion on the surrounding atmosphere, ranging from models suggesting a gas-filled conduit that resonates like an open organ pipe (*Chouet et al.*, 1974), a bursting bubble (e.g. *Ripepe and Gordeev*, 1999; *Rowe et al.*, 2000; *Johnson et al.*, 2003), a vibrating bubble (*Vergniolle and Brandeis*, 1994, 1996), a Helmholtz resonator (*Vergniolle and Caplan-Auerbach*, 2004; *Cannata et al.*, 2009), an explosion source deep within the magma conduit (*Buckingham and Garcés*, 1996; *Garcés and McNutt*, 1997; *Hagerty et al.*, 2000), or a bursting balloon (as discussed by *Vergniolle and Brandeis*, 1994; *Kulkarny*, 1978; *Blackstock*, 2000).

Recent studies increasingly acknowledge that volcanic sound sources are often volume sources, meaning that sound is produced by introducing additional volume into the atmosphere, which during Strombolian explosions is mostly volcanic gas (e.g. *Vergniolle and Brandeis*, 1994; *Firstov and Kravchenko*, 1996; *Ripepe and Gordeev*, 1999; *Rowe et al.*, 2000; *Johnson*, 2003; *Johnson et al.*, 2004; *Ichihara et al.*, 2009). Most of the studies assumed these volume sources to be representable both by a monopole and by a compact source (*Lighthill*, 1978; *Dowling*, 1998). While the former assumption was shown to be wrong in some cases by *Johnson et al.* (2008), results from *this* study will show that Strombolian sources cannot always be modelled as a compact, or point source, either. Only recently bubble explosions are modelled with more complexity, including dipole signatures, which unfortunately requires a much better azimuthal instrument coverage of the source, and which therefore demands a greater effort in the field (*Johnson et al.*, 2008).

As for the mechanics behind Strombolian explosions, the wealth of existing literature and proposed models demonstrates that the issue is far from being resolved. This question is therefore one of the major issues in volcano acoustics, and will be extensively discussed in this study. Fortunately, the excellent observation conditions at Erebus volcano combined with new in situ measuring devices such as Doppler radar offer a unique possibility to shed more light on the answer.

1.4 Measuring the energy of a volcanic eruption

The total energy output of a volcanic eruption varies greatly with the style of eruption, the individual volcano, and even with the individual explosions within a single eruption. For this reason, the absolute energy output of an explosion or an eruption can be regarded as an individual property of the volcano in question. Comparing absolute energy values therefore

***Figure 1.5:* Mt. Erebus volcano**, *towering almost 4,000 m above the Ross Sea, seen from the McMurdo dry valleys (A. Gerst, 2002).*

only makes sense when characterising different volcanoes. However, the individual partitioning of involved energy types shares some interesting common properties between different styles of volcanic eruptions. Therefore, studying the energy partitioning of volcanic eruptions and explosions can give us important clues about the underlying mechanisms. Furthermore, like an individual fingerprint, the energy partitioning of a certain volcano might be characteristic, and stable over a longer period of time, yielding information on the individual explosion mechanism of the volcano in question.

In an early study, *Minakami* (1942) determined the speed and kinetic energy of bombs at the Vulcanian-style Asama volcano from geometrical calculations, concluding that the ejection velocity of bombs often exceeds 150 m/s. While the technique at the time possibly produced adequate results regarding the exit velocity of ejecta, the derived pressure values exceeding 500 atmospheres seem crudely overestimated. *Yokoyama* (1956, 1957), in a more comprehensive study, estimates several different energy output forms of the Strombolian-style Mihara volcano, Japan, as well as the total energy output of a variety of volcanoes on Earth. *Hédervári* (1963) further refined this work, explicitly naming thermal, kinetic and potential energy of ejecta, as well as seismic and acoustic waves as participating energy forms. While technical capabilities prevented a quantification of these partitions, the study provided an important base for further work that eventually led to the definition of the *"Volcanic Explosivity Index"* (*VEI*, *Newhall and Self*, 1982).

Shimozuru (1968) made an approach to partially quantify the energy partitioning at several volcanoes and compare it to chemical explosions. While his theoretical considerations are very interesting, again, the lack of solid physical data prevented him from reaching a comprehensive conclusion. Yet he was able to conclude that the ratio of seismic energy output to total eruption energy can be similar to chemical explosions.

McGetchin and Chouet (1979) analysed field observations and data from *Chouet et al.* (1974) and *Woulff and McGetchin* (1976), and presented a partial energy budget of Stromboli volcano. Although their energy budget was not broken up into single explosions, they found that by far the most energy is released as heat, followed by the kinetic energy of ejected gas and particles and acoustic energy.

Existing studies about the general energy partitioning of volcanic eruptions unanimously highlight the importance of thermal energy, followed by kinetic and potential energies, which often are several orders of magnitude smaller than thermal energy (e.g. *Yokoyama et al.*, 1992). The observation that Strombolian volcanoes typically emit large amounts of thermal energy without a large output of lava led *Francis et al.* (1993) to suggest that such volcanoes might grow endogenously, i.e. by the storage and cooling of magma underneath the volcano.

While in the last decades, the calculation of a simple form of energy budget has been attempted for several types of volcanic activity, such as silicic explosive volcanism (e.g. *Gorshkov*, 1960; *Gorshkov and Dubik*, 1970; *Wilson et al.*, 1978; *Pyle*, 1995; *Yokoyama et al.*, 1992; *Woods*, 1995; *Heki*, 2006; *Zobin et al.*, 2009), crater lakes containing meteoric water (*Brown et al.*, 1989, 1991; *Hurst et al.*, 1991), or phreatomagmatic explosions (*Raue*, 2004), little is known about the detailed energy partitioning in Strombolian explosions.

Up to now, the general problem for experimenters was that physical data was either impossible to obtain in the necessary detail, or it lacked the diversity of a multi-parameter dataset. At many volcanoes, safety conditions at or near the vent prevent the collection of data during the eruption itself, so that much information must be reproduced from post-eruptive clues. Unfortunately, calculating an energy budget from distant or post-eruptive observations alone requires a large number of assumptions, which makes the interpretation of the results difficult. Additionally, in such a situation, conclusions can only be drawn on the overall eruption, so that different mechanisms acting at different times of the eruptions, or during single explosions, remain unclear.

A solution to the above problem is a multi-parameter experiment at a location that allows the observation of single Strombolian explosions from a safe but prominent position with a variety of sensors. Ideally, this multi-parameter dataset includes in-situ sensors to obtain data in the most direct way possible. Doppler radar devices allow for such in-situ measure-

Figure 1.6: **An FMCW Doppler Radar device,** *with a sketch of the radar beam.*

ments, providing detailed information about the velocity and relative number of particles that are participating in the explosion process.

1.5 Using Doppler radar at volcanoes

The ***r****adio* ***d****etection* ***a****nd* ***r****anging* technology was developed during the first half of the 20th century, mainly motivated by its potential military use. Yet, soon after the technology was made available, scientists were intrigued by the prospect of using its capabilities to obtain information on volcanic eruptions. A first volcanological use of radar included a volcanic crisis at Montserrat in the 1950s (*Robson, pers. comm., 1997*). *Kienle and Shaw* (1979) used radar data recorded by Alaskan military stations during volcanic eruptions to determine the width and height of eruption columns. These first uses of radar in volcanology highlighted one of the main advantages of radar: it allows the obtainment of in-situ data where other techniques fail due to inclement weather and poor visibility conditions, as are often the case during large volcanic eruptions.

There are several Doppler techniques available that can be used on a volcano to obtain information of eruption velocities. This includes, apart from the microwaves used in Doppler radar, techniques based on sound (e.g. *Weill et al.*, 1992) and on laser. While both these techniques have the capability of obtaining in-situ data of velocities and the dimensions of a volcanic target, they also have their limitations. For example, sonic Doppler measurements require the precise knowledge of the sound speed around the target, which is strongly altered by the presence of hot volcanic gases. Laser devices typically require a very stable mounting, have a considerable power consumption, a requirement for frequent maintenance, and they typically do not provide a sufficiently wide observational field of view. Additionally, they often fail during poor visibility conditions.

The use of radar in volcanology was strongly promoted by the 1981 eruption of Mt. St. Helens, where its capabilities were demonstrated by *Harris et al.* (1981) and the U.S. National Weather Survey. A 5 cm weather radar was used to precisely track the eruption cloud, enabling them to calculate the mass flux of the eruption and the cloud density during various phases of the eruption, thus providing important information to civil authorities. A weather radar was also used to track the following eruption of Mt. St. Helens in 1982 (*Harris and Rose*, 1983).

After this impressive display of the capabilities of radar, the U.S. National Weather Survey installed a C-band radar to monitor the activity of Alaskan volcanoes in the Cook Inlet, providing vital information for the city of Anchorage and international aviation routes, which are both endangered by ash fall and eruption clouds from volcanoes in the area. Its superb functionality was demonstrated in 1992 during an eruption of Mt. Spurr volcano (*Schneider et al.*, 1995).

Unfortunately, the radar systems discussed above are largely immobile devices that need to be transported by truck; others cannot be transported at all. They also are pulsed radars, which means that they send out strong microwave pulses in the megawatt range, requiring a large amount of power. Therefore, these devices are not suitable for the use on smaller-scale eruption processes, such as Strombolian explosions or lava domes, which require the installation of devices in the close proximity of volcanic vents or domes, an area that on most volcanoes can only be accessed on foot. This lack of versatility triggered the development of much smaller and lighter devices.

In 1996, *Hort and Seyfried*, inspired by the existence of lightweight *frequency modulated continuous wave (FMCW)* Doppler radars that are used in meteorology to detect rainfall (*Strauch*, 1976; *Peters*, 1995), modified such a device to be used on volcanoes. FMCW radars offer several important advantages over pulsed radars, including their low power consumption, their small size and their light weight. The device used by *Hort and Seyfried* (1998), which was later called *MVR (Mobile Volcano Radar)*, operates with 24 GHz K-Band microwaves, has a range of a several kilometres, and its initial version ("*MVR3*") had a maximum sampling rate of about 1 Hz. Its most important feature for volcanological measurements is that at the used frequency, measurements are largely undisturbed by clouds, rain, snow, wind and darkness, allowing for continuous observations independent of meteorological or visibility conditions.

In 1998, two years after the MVR was introduced, a small pulsed Doppler radar instrument (*VOLDORAD, Volcano Doppler Radar*) was developed by a group of scientists in

Clermont-Ferrand, and was first used at Mt. Etna (*Dubosclard et al.*, 1999, 2004). While the pulsed Doppler radar offers a wider swath (or field of view) and a much better temporal resolution than the early MVR system (*Hort and Seyfried*, 1998), it has the important disadvantage of a high power consumption and weight, prohibiting its transport by foot or an operation without a power generator attached. A more comprehensive comparison of the two instruments can be found in *Vöge et al.* (2005), while technical and operational details of the MVR system are discussed by *Hort et al.* (2003) and *Vöge and Hort* (2009).

Following these first steps of designing a light and portable volcano Doppler radar, the MVR system has been extended and used at a variety of volcanoes displaying several different eruption styles. *Vöge et al.* (2005) used the MVR system to measure instabilities of Merapi volcano's notoriously dangerous lava dome (see also *Hort et al.*, 2006; *Vöge and Hort*, 2008; *Vöge et al.*, 2008; *Vöge and Hort*, 2009). Further examples of its successful use included measurements of explosion velocities at Stromboli volcano (*Urbanski et al.*, 2002; *Hort et al.*, 2003; *Scharff et al.*, 2008), monitoring of explosions from Santiaguito's lava dome (*Scharff et al.*, 2007), the investigation of particle size distributions within eruption clouds from Colima (*Scharff et al.*, 2009), and the testing for eruption models at Yasur volcano on the island archipelago of Vanuatu (*Meier et al.*, 2009).

In a similar manner to the MVR system, the pulsed and somewhat heavier VOLDORAD system provided valuable insights into ash cloud dynamics of Arenal volcano (*Donnadieu et al.*, 2005), as well as mass estimations for explosions at Stromboli (*Gouhier and Donnadieu*, 2008). During average measurements of entire eruption clouds, VOLDORAD's wider beam width of 9° compared to MVR's 1–3° (Sec. A.1) provides an advantage, while the smaller beam width of the MVR system enables it to spotlight certain areas of the cloud. The two systems therefore complement each other in their capabilities.

A third radar system intended to be used on volcanoes was developed by a group of scientists from the University of Reading, and was named *AVTIS* (*All-weather Volcano Topography Imaging Sensor*; *Wadge et al.*, 2005). Even though AVTIS is also a portable FMCW type radar (working at 94 GHz), it is somewhat different in style than the two systems discussed above, because it does not measure velocities by making use of the Doppler effect. Instead, AVTIS has its strengths in producing a 3D image of a target up to 7 km away by producing a raster grid of distance measurements. Additionally, it operates as a passive radiometer. When comparing successive AVTIS raster images, moderate deformations in the range of a few metres can be resolved (*Wadge et al.*, 2005). Accordingly, it was successfully used for imaging the growing lava dome of Montserrat volcano (*Wadge et al.*, 2006), and to track an advancing lava flow at Arenal Volcano, Costa Rica (*Macfarlane et al.*, 2006).

Hort et al. (2001, 2003) extended the volcanic radar toolbox by introducing the technique of measuring an explosion simultaneously with three radars in order to reproduce a 3D velocity vector (this technique will be used and further refined here), while *Vöge et al.* (2008) introduced an automatic classification algorithm for large amounts of radar data, based on neural networks. Newest developments of the MVR system include the use of a much faster

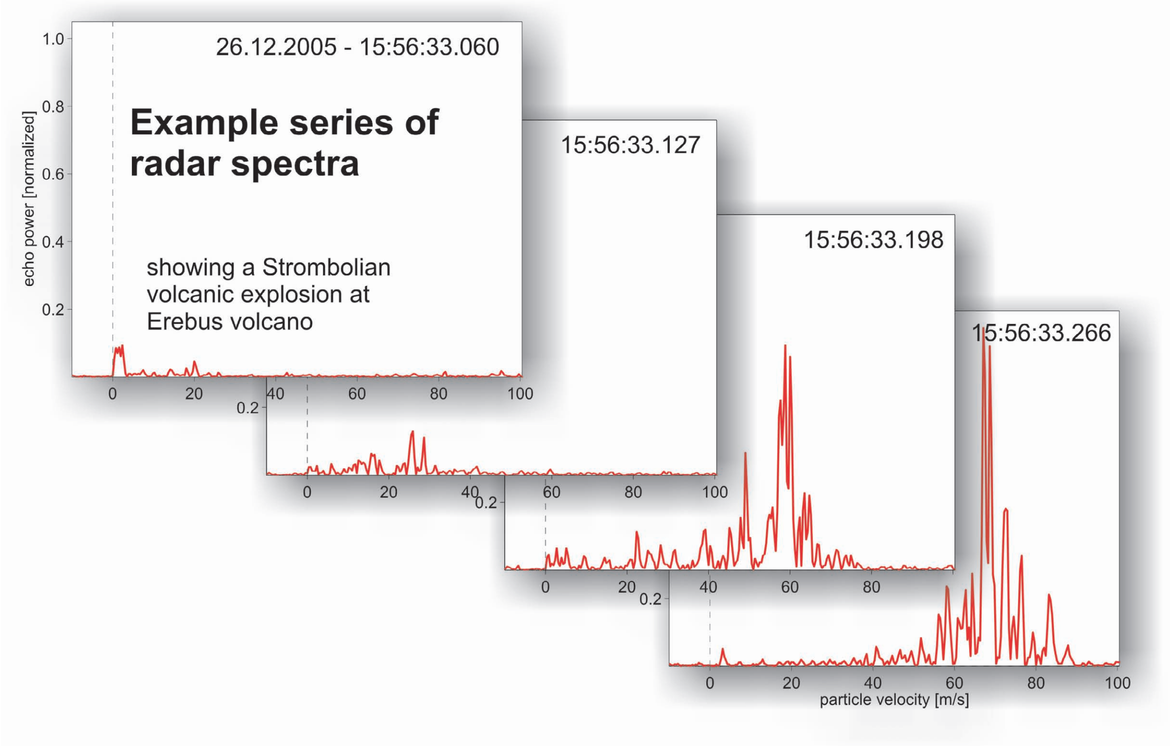

Figure 1.7: Series of Doppler radar velocity spectra. *The horizontal axis of each spectrum denotes the particle's radar velocity, the vertical axis denotes echo power in arbitrary units. The red line therefore shows how much material moves at which speed towards the radar. This example sequence covers an explosion from the active lava lake of Mt. Erebus volcano, Antarctica (similar to that shown in Fig. 1.3). At the start of the explosion, only a few fragments move at a low speed, which then increase in amount and velocity towards the climax of the explosion. Note that the whole sequence shown here covers only the very start of an explosion, equivalent to the first two frames shown in Fig. 1.3.*

and more precise MVR device (”*MVR4*”), which I will present in this study, and the use of the device in interferometric mode, allowing it to detect millimetre scale deformations at distances of up to several kilometres (*Scharff et al.*, 2007).

A radar spectrum. In order to interpret data measured with an FMCW radar, it is necessary to understand the underlying measurement principle, as well as the nature and shape of radar data. Radar illuminates its target with electromagnetic waves and subsequently records their echo. According to the Doppler effect, the reflected signal will have a frequency shift that is proportional to the target's velocity component pointing towards the radar. This property allows the device to determine this component of the target's velocity (subsequently called ”*radar velocity*”), as well as its distance (*Hort et al.*, 2003; *Vöge and Hort*, 2009).

At volcanoes, a radar device typically does not illuminate only one target, but many objects that are located in its beam, or field of view. Therefore, the device receives many echoes from objects with different speeds. For this reason, every sample from the MVR radar system combines information about the velocity, distance and relative abundance of all objects illuminated by the radar beam. A natural way to visualise this multitude of information is a so-called *"radar spectrum"*.

Figure 1.7 shows an example sequence of four radar spectra, recorded during a Strombolian explosion at Erebus volcano. A spectrum is a relative measure of the amount of material in the radar beam, sorted by the material's radar velocity. Even though the radar has its strengths in the precise measurement of the particles' velocity, the echo power does not easily translate into the exact amount of material, and strongly depends on the material's grain size (e.g. *Ziemen*, 2008; *Seyfried and Hort*, 1999; *Marzano et al.*, 2006a,b). As long as the grain size distribution is not known, echo power can only be regarded as a **relative** measure of the amount of material in the radar beam. Since in this study, knowing the exact amount of material in the radar beam is of no great significance, I will not go into further details of this property.

Figure 1.8 shows a simulation of a radar spectrum, generated by a hypothetical bubble explosion from a lava lake. Since the correctness of such an explosion model will be a main focus point of this study, I leave it undiscussed for now, but use the spectrum generated by this model as a demonstration and aid for interpreting radar spectra in general. The explosion model assumes that the initially flat surface of the lava lake bulges up towards a hemispherical shape, pushed by pressurised gas underneath (similar to an inflating balloon). A large number of radar reflectors are assumed to be randomly distributed over the whole surface of the lake, each one contributing to the spectrum on the right. Accordingly, the spectrum was simulated by adding up the contribution of each reflector, depending on its surface angle, velocity, as well as distance from the beam axis, assuming that the radar device was located at 300 m distance on a fictional crater rim.

The shape of the resulting spectrum (Fig. 1.8, right) has a characteristic peak, ending abruptly at exactly the velocity signal that is, in this case, caused by a point near the centre area of the bulging lake surface. No particle is moving faster than that, therefore no echo power exists above that velocity. Below the peak, the signal slowly fades out, representing the speeds of particles on the side of the lake, which move slower and also generate a smaller echo due to the radially decreasing intensity of the radar beam towards the edges of the lake (see Fig. A.1 in the appendix).

While the characteristic features of a radar spectrum will be of importance later in this study (e.g. it will be discussed in more detail in Secs. 4.1.2 and 6.2), the example shown here is simply meant to serve as a demonstration of the connection between radar target and the resulting data.

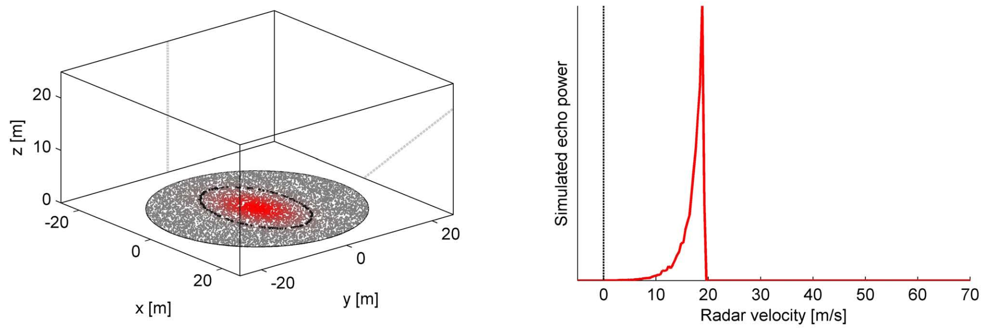

Figure 1.8:* Simulated radar spectrum. *Left: *simulated surface of a lava lake (gray dots), starting to bulge towards a hemispherical shape with a vertical centre velocity of 30 m/s. The red area is illuminated by the radar beam, fading away from the beam centre according to the antenna gain pattern (Appendix Fig. A.1). The black line marks where the radar's sensitivity reaches -10 dB, i.e. where the receivable echo power has fallen to 1/10 of that in the beam centre. Projections of the beam's centre axis, at an elevation angle of 39°, are indicated as dotted lines on the box walls.* ***Right:*** *Expected radar spectrum. The strong peak results from reflectors near the lake centre in this case, and is located at their velocity projected in beam direction, i.e. at* $\sin 39° \times 30$ *m/s* $= 18.9$ *m/s.*

1.6 Mount Erebus volcano

Mount Erebus volcano was discovered in 1841 by the polar explorer Sir James Clark Ross, who named it together with the neighbouring Mount Terror after his two ships, Erebus and Terror. Appropriately, Erebus was a Greek god of darkness. At 78° South, Erebus is the southernmost active volcano on Earth (Figs. 1.2, 1.5, & 1.9), a large alkaline intraplate stratovolcano towering 3794 m above the Antarctic Ross sea (Fig. 1.5) with a subaerial volume of ~2000 km^3 (*Esser et al.*, 2004). Its most important features are its frequent episodes of Strombolian activity (Volcano Explosivity Index 0-1) ever since it was first visited and documented by scientists in the seventies, and its long-lived active lava lake (Fig. 1.10). The lava lake is directly connected to a magma reservoir at depth, therefore the lake represents the topmost part of this magma reservoir and the overlying conduit system.

Erebus is part of the Terror Rift at the western boundary of the West Antarctic rift system (*Kyle*, 1990; *Behrendt*, 1999), and overlies only very thin continental crust (~20 km; *Bannister et al.*, 2000). Together with its subsidiary volcanoes Terror and Bird it forms Ross island. Petrologic evidence (*Kyle et al.*, 1992) suggests a hot spot or a mantle plume beneath Erebus, which is consistent with seismic evidence suggesting a major thermal anomaly under Ross Island (*Watson et al.*, 2006).

The distinctive shape of Erebus (Fig. 1.5) is caused by a summit plateau composed of interbedded phonolitic pyroclastic bomb deposits and lava flows, starting at an elevation of ~3500 m (*Kelly et al.*, 2008a). A summit cone is located in the centre of the summit plateau,

Figure 1.9: Crater region and summit plateau of Erebus volcano. *The mountain in the background is the extinct volcano Mt. Terror (photograph kindly provided by George Steinmetz © 2005).*

hosting a 500 m wide and 200 m deep crater (Fig. 1.9) with a smaller *Inner Crater* embedded (Fig. 5.10 below). Erebus' long-lived *Ray Lava Lake* is located inside the Inner Crater (Fig. 1.10). The main crater hosts two further vents, which is the sporadically appearing *Werner Lava Lake* and an active ash vent that frequently displays ash and gas explosions.

After first being climbed in 1908 by Douglas Mawson and other members of Sir Ernest Shackleton's "Nimrod" British Antarctic Expedition (*Oppenheimer and Kyle*, 2008a), Erebus largely remained outside the focus of scientific interest until it was revisited by *Giggenbach et al.* in 1972. Early scientific studies, carried out by *Giggenbach et al.* (1973); *Kyle* (1977), and *Kyle et al.* (1982), produced first outlines of Erebus' eruptive activity as well as its geochemical and stratigraphic history.

Erebus' magma, and therefore Ray Lava Lake (Fig. 1.10), consists of phonolite, which is a high-temperature, highly alkalic magma with basic-to-intermediate silica content (*Kyle*, 1977; *Kyle et al.*, 1992; *Kelly et al.*, 2008b). It is relatively rare compared to basaltic magmas (*Dibble et al.*, 1984). The lava lake contains 25 – 40% anorthoclase feldspar phenocrysts (*Kyle*, 1977; *Dunbar et al.*, 1994; *Sweeney et al.*, 2008), and its chemical and isotopic composition has remained stable during the last decades (*Kelly et al.*, 2008b; *Sims et al.*, 2008). Geochemical modelling by *Dunbar et al.* (1994) revealed that the phenocrysts in Ray Lava Lake require centuries of convective circulation between the surface and a depth of ~400 m for their formation, suggesting a stable conduit system with a lifetime of at least several centuries.

Magma viscosities of Erebus' phonolite, as derived from geochemical modelling, are likely to be in the $5 \times 10^3 - 10^4$ Pa s range (*Carmichael et al.*, 1974; *Sweeney et al.*, 2008; *Oppenheimer et al.*, 2009), and are therefore somewhat greater than that of other know lava lakes (*Oppenheimer et al.*, 2009). The width of Ray Lava Lake varied from 10 – 40 m during the last decades (e.g. *Kyle*, 1977; *Kyle et al.*, 1990; *Aster et al.*, 2003; *Dibble et al.*, 2008), and was ~40 m in 2005/06.

The temperature of Erebus magma, and therefore that of fresh magma entering Ray Lava Lake, lies around 1000° C, which was determined by several independent empirical and experimental approaches, e.g. by optical pyrometer and mineral thermometer (*Kyle*, 1977), olivine-cpx thermometry (*Caldwell and Kyle*, 1994), melt inclusion homogenisation (*Dunbar et al.*, 1994), and with a Forward Looking Infrared (FLIR) camera (*Calkins et al.*, 2008). The temperature at the uppermost surface layer of the lake is controlled by radiative and convective cooling, and is therefore up to a few hundred degrees cooler than the magma temperature (*Calkins et al.*, 2008). However, due to the strong convection of hot magma inside the lake, this cooled surface layer is constantly reworked, so that its thickness is likely to be only a few centimetres. Its influence on the explosion mechanics is therefore assumed to be negligible in this study.

The predominant eruption style of Erebus is Strombolian, and includes sporadic explosions that originate from the surface of Ray Lava Lake, caused by the expansion of overpressured bubbles of magmatic gas (e.g. *Giggenbach et al.*, 1973; *Dibble et al.*, 1984; *Kaminuma*, 1994; *Rowe et al.*, 2000; *Aster et al.*, 2003, 2004, 2008; *Dibble et al.*, 2008). During these explosions, which show a degree of high self-similarity (*Dibble*, 1994; *Aster et al.*, 2003; *Henderson*, 2007), magma bombs are frequently thrown several hundred metres beyond the crater rim. This Strombolian activity ebbs and increases over long cycles (months to years), including periods without any explosions (*Jones et al.*, 2008). In 2005/06, around 2 – 6 explosions per day occurred at Erebus.

Since Erebus is an open magmatic system, its overall style of activity was frequently recurring but episodical during the last 30 years and did not include major eruptions or paroxysms (*Dibble et al.*, 2008). During several occasions, however, the lake was buried by landslides of eruptive debris for a short while, therefore temporarily altering the volcano's eruption style (*Kienle et al.*, 1985; *Caldwell and Kyle*, 1994; *Kaminuma*, 1994; *Dibble et al.*, 2008). Yet, such departures from Erebus' typical Strombolian activity were rare in the last decades. Explosion sounds similar to today's were already observed by J. C. Ross in 1841 (*Kyle et al.*, 1982; *Kyle*, 1994), suggesting a similar style of activity at that time.

Consistent with its open magmatic system that does not accumulate large pressures or deviatoric stresses, Erebus displays a lack of internal earthquakes and volcanotectonic events (*Rowe et al.*, 2000; *Aster et al.*, 2008). Seismic signals are typically associated with explosions, and are found in a wide frequency range (e.g. *Dibble et al.*, 1984, 2008; *Rowe et al.*, 1998, 2000; *Aster et al.*, 2003, 2008; *De Lauro et al.*, 2009). Additionally, explosions excite strong acous-

Figure 1.10: ***Left:*** *Erebus crater on a day with good visibility. Still, the red glowing liquid lava lake at its bottom is not bright enough to show on this picture.* ***Right:*** *Closeup view of Ray Lava lake (A. Gerst, 2005).*

tic signals in the audible and infrasonic frequency range (e.g. *Dibble*, 1989; *Rowe et al.*, 2000; *Johnson and Aster*, 2005; *Johnson et al.*, 2008; *Jones et al.*, 2008).

Oppenheimer and Kyle (2008b) measured the gas composition from Erebus' plume in 2004, showing that it mainly consists of water vapour (H_2O) and carbon dioxide (CO_2), accounting for 58 and 36 mol percent, respectively (equivalent to 37 and 56 wt. %). These are followed by CO (2.3 mol %), SO_2 ($\sim$1.4 mol %), HF ($\sim$1.3 mol %), and HCl ($\sim$0.7 mol %). The resulting total gas flux inferred for Erebus' crater is 2,360 tons per day in 2004 (*Oppenheimer and Kyle*, 2008b), of which 74 tons per day consist of SO_2. *Harris et al.* (1999), using satellite measurements, estimated the SO_2 flux from Erebus volcano in 1984/85 at a few hundred tons per day.

Presently existing long term instrumentation at Erebus includes a seismic broadband monitoring network as well as an acoustic network, an infrared camera on the crater rim, GPS receivers, tiltmeters and meteorological instruments (*Aster et al.*, 2004, 2008; *Jones et al.*, 2008), run by the *Mount Erebus Volcano Observatory (MEVO)*. The instruments are operating continuously as long as the power systems work, which is usually the case during the austral summer, where solar power is abundantly available, and often they even run throughout the winter. During summer seasons, the instrumentation network at Erebus is regularly supplemented by temporary surveys, such as gas composition and flux measurements (*Sweeney et al.*, 2008; *Wardell et al.*, 2008; *Oppenheimer and Kyle*, 2008b), observations with thermal cameras (*Calkins et al.*, 2008; *Davies et al.*, 2008), laser topography scanning (*Csatho et al.*, 2005, 2008), geological investigations (e.g. *Dunbar et al.*, 1994; *Caldwell and Kyle*, 1994; *Sims et al.*, 2008; *Kelly et al.*, 2008a), or, in this case, Doppler Radar measurements.

1.7 Strategy

This study aims to provide an answer to the questions listed in Section 1.1 by looking at them from a new perspective, combined with various established observation techniques. To achieve this goal I have attempted to overcome the problems faced by previous studies by ***A)*** choosing a more suitable observation target, ***B)*** utilising a type of in-situ sensor that is relatively new to volcanology, and ***C)*** using an integrated approach of three different but complementary instrument types to form a unique multi-parameter dataset.

A prime objective of this study is to shed more light on Strombolian explosions by investigating explosions at a relatively simple model volcano. As shown in Section 1.6, the chosen observation target, Erebus volcano, offers ideal observation conditions and reliable activity at the convenience of relatively simple logistics in the Antarctic summer season. Strombolian bubble explosions at Erebus occur several times per day from an active lava lake, and can be fully observed from several positions on the crater rim. They show a high degree of self-similarity, allowing relatively constant experiment conditions over the course of a field season. This condition allows for the development of a geometrical explosion model, which will be the basis for several important results of this study.

To fulfill the above set objectives, in this study I will present a unique multidisciplinary dataset. It is obtained through the synchronous observation of the birth of a Strombolian explosion with acoustic microphones, a thermal camera, and Doppler radar instruments (Sec. 1.5). These three types of instruments have the advantage of providing a very direct kind of observation through a simple atmospheric transport function from source to instrument, and additionally provide a precise in-situ measurement of explosion velocities. As will be shown in the following chapters, the synergy of their strengths allows the constraint of important and previously unknown parameters of Strombolian volcanic eruptions, therefore taking a substantial step towards answering the open questions listed in Section 1.1. The results will serve as a guideline, and in some cases as a constraint, for the interpretation of data from other, less accessible or more complex volcanoes.

In the following Chapters I will introduce the necessary background to understand the roots and causes of a Strombolian volcanic eruption (Ch. 2), followed by the development of the theoretical tools that are necessary to calculate the expected acoustic signal generated by a bubble burst from a lava lake (Ch. 3). The theoretical core of this study will be the development of a model that describes the geometry of an exploding (i.e. expanding) gas bubble on the surface of a lava lake (Ch. 4), designed to allow for the use of field data for identifying and constraining important physical parameters of the explosion process.

The practical part of this study describes the design and implementation of a field experiment at Mt. Erebus volcano, Antarctica (Ch. 5), which delivered the necessary field data to validate and to make use of the model. These data will be shown in detail (Ch. 6), after which they enter the bubble expansion model to derive physical properties of explosions at Erebus (Ch. 7). An additional and somewhat separate Chapter (Ch. 8) will introduce a special mode of measuring an explosion with three radars at the same time, allowing for the determination of the three-dimensional expansion direction of bubbles. All obtained results will be discussed in Chapter 9 in the context of existing literature, and the final Chapter 10 will highlight the achieved knowledge and remaining controversies.

The strategy of using a geometrical model that is applied to radar data to constrain explosion parameters is somewhat different to the approach followed by previous studies. Instead of building a model that attempts to completely simulate the mechanics behind a bubble explosion, and subsequently comparing the outcome of this model with real world observations, this study uses the reverse approach. The model will first be developed on the basis of visual observations to represent a simple geometrical description of the natural process, leaving only one free parameter. This parameter will later be constrained by radar data, so that the adjustment of free parameters to make the model fit to the data will not be necessary. This strategy provides an unambiguous source of information on the dynamics of the model explosion. After discussing the validity of the model's assumptions in each case, several of the gained explosion parameters can be assumed to reflect parameters of the natural system. The model will provide information on the explosion energies, gas pressures and volumes that are needed to cause the observed surface movements. Additionally, the model allows the prediction of expected acoustic and seismic signals, therefore facilitating their interpretation not only at Erebus volcano but also at other Strombolian-type volcanoes worldwide.

CHAPTER 2

A REVIEW: THE ROOTS OF A STROMBOLIAN ERUPTION

It is generally accepted that Strombolian explosions are caused by the generation and subsequent rise of large gas bubbles in a liquid magma conduit, often resulting in a powerful explosion when reaching the surface. Nevertheless, many underlying mechanisms are still unclear and subject to debate. This Chapter will discuss the physics and possible mechanisms behind rising slugs and Strombolian explosions, including a simulation of conduit rise processes expected at Erebus volcano.

2.1 The formation of large gas bubbles

Currently there are two main models attempting to explain the formation of gas bubbles at depth (see review by *Slezin*, 2003; *Parfitt*, 2004). While it is commonly accepted that large gas bubbles form through coalescence of small bubbles with magmatic gas originating from a magma reservoir, the two models differ in the exact way these large bubbles form. The first of the models attributes the generation of large gas bubbles to the collapse of an accumulation of small bubbles, or foam that has previously collected at the top of a magma reservoir or beneath a structural barrier like a dike-to-conduit transition (*Jaupart and Vergniolle*, 1988; *Vergniolle and Jaupart*, 1990; *Chouet et al.*, 1997; *Ripepe and Gordeev*, 1999; *Ripepe et al.*, 2001). The model assumes that upon collapse, the generated bubble starts to move and subsequently travels up the liquid magma conduit.

The model predicts a pressure change associated with the sudden collapse of the foam layer, a process which could be responsible for some of the *very long period (VLP)* seismic signals observed at volcanoes (e.g. at Stromboli volcano, *Neuberg et al.*, 1994; *Chouet et al.*, 2003). While *Ripepe and Gordeev* (1999) concluded that this effect would only generate small pressure changes in basaltic systems (around 80–800 Pa), *Chouet et al.* (2003) show that in some cases much larger pressure changes (as high as 10^6 Pa) can be expected when liquid inertia and dynamic bubble growth effects are also included. Such pressures could excite a resonance of the whole liquid conduit above, acting as an efficient source for seismic waves.

The second model attributes the generation of large gas bubbles to the coalescence of smaller bubbles that are rising in the magma column with different speeds relative to the magma, depending on their size (*Wilson*, 1980; *Parfitt and Wilson*, 1995). Additionally to the rise of bubbles within the magma, depending on the magmatic system, the magma itself can also rise in the conduit. According to the model, as a result of the rise speed of the magma, two situations can evolve. In slowly rising magma the bubbles have enough time to coalesce into large bubbles and generate Strombolian eruptions. In fast rising magma, they do not have time to coalesce before being erupted, and therefore remain relatively small and dispersed in the liquid upon reaching the surface (resulting in fire fountains, so-called *Hawaiian-style* eruptions).

In reality, it is possible that these two principal mechanisms (foam collapse vs. coalescence during rise) are simply endmember scenarios of a variety of effects, meaning that the true mechanism might be a mixture of both. Small and large bubbles might be continuously be collecting at magma chamber roofs and beneath structural barriers, possibly leading to discrete foam collapse events, while at the same time the bubbles further coalesce on their way up (especially in inclined conduits), that way explaining a broad spectrum of bubble sizes (as will be shown here to exist at Erebus).

Even though the two models have a large significance in explaining the deep mechanisms that distinguish Strombolian from Hawaiian-style eruptions, their difference does not have much significance once a large gas bubble has formed one way or the other. Seismic evidence suggests that a volumetric expansion of gas bubbles occurs at a depth of several hundred metres below the surface of the magma column (e.g. *Neuberg et al.*, 1994; *Wassermann*, 1997; *Kirchdörfer*, 1999; *Chouet et al.*, 1999; *Rowe et al.*, 2000; *Chouet et al.*, 2003; *Marchetti and Ripepe*, 2005). Other studies based on chemical techniques find evidence that large bubbles coalesce at much deeper parts of the magmatic systems. *Allard et al.* (2005) found evidence from chemical gas measurements suggesting that during the fire fountaining episode of the 2000 Etna eruption, large gas bubbles formed at a depth of around 1.5 km below the vent. At Stromboli, gas chemistry data suggests that large gas bubbles form at depths of 0.8 – 2.7 km (*Burton et al.*, 2007). Consistent with these results, several authors suggested that the more shallow seismic sources at Stromboli (and at comparable volcanoes) are dynamic effects associated with the bubble's rise, such as the flow around structural barriers (e.g. *Chouet et al.*, 2008), or conduit response effects associated with bubble bursts.

2.2 A rising gas slug in a volcanic conduit

When gas bubbles rise in a confined tube of liquid, four different characteristic flow regimes tend to form, mainly depending on the amount of gas supplied from below (e.g. *Seyfried and Freundt*, 2000; *Krüssenberg et al.*, 2000). **Bubbly flow** describes the rise of well-dispersed, relatively small bubbles (compared to the conduit diameter), whose size distribution tends to be highly uniform (*James et al.*, 2004). **Transitional flow** describes a regime in which bubbles

Figure 2.1: Strombolian explosion at Etna volcano, *taken during an eruption in 2001.* © *A. Gerst.*

start to form clusters and coalesce to larger bubbles. The bubble size distribution is therefore wider, or even bimodal (*Krüssenberg et al.*, 2000). The **slug flow** regime is characterised by large bubbles that usually fill the entire diameter of the confining tube (apart from a thin film of liquid on the side), resembling a long vertical gas cylinder more like a spherical bubble. When the gas supply from below increases beyond a critical threshold, slug flow develops into **annular flow**, where the gas phase forms a continuous cylinder from the bottom to the top of the conduit, surrounded by a "pipe" of liquid.

Each of the above flow regimes are assumed to develop in volcanic conduits under the right circumstances, thereby successfully explaining a variety of different observed eruption styles (e.g. *Seyfried and Freundt*, 2000; *Parfitt*, 2004). Bubbles of the conduit filling type (i.e, in a *slug flow*) are in the volcanological literature typically called *gas slugs* (*Jaupart and Vergniolle*, 1989; *Seyfried and Freundt*, 2000; *Ripepe et al.*, 2001; *James et al.*, 2004)[1], and their dynamic behaviour is largely controlled by the conduit geometry (i.e. shape and diameter) as well as the magma rheology (viscosity, density). Bubbles of this type are commonly assumed to be responsible (*Blackburn et al.*, 1976) for Strombolian eruptions (or, rather, explosions) by rising in a volcanic conduit and subsequently exploding at the top (Sec. 1.2 and Figs. 1.3 & 2.1).

Since this study concentrates on Strombolian eruptions, and thus on slug type bubbles, I

[1] in the engineering literature, somewhat confusingly, the gas phase is typically called "Taylor bubble", and the liquid phase is called the "liquid slug" (*James et al.*, 2004).

will use the terms *slug* and *bubble* interchangeably from now on, referring to a large conduit-filling gas bubble that rises in a conduit and eventually explodes on the top.

James et al. (2004) show that the formation of slug flow is strongly promoted when the confining tube is even only slightly inclined, due to increased bubble coalescence. Since any volcanic conduit is very likely to include segments that are not completely vertical, they argue that slug flow should be a common phenomenon in volcanic conduits, independent of the process that generates the gas bubbles at depth (e.g. foam collapse vs. rise speed dependent models).

Mathematical models for the rise of slugs in vertical pipes have been developed, along with considerable research (e.g. *Davies and Taylor*, 1950; *White and Beardmore*, 1962; *Brown*, 1965; *Wallis*, 1969; *Polonsky et al.*, 1999a; *Taha and Cui*, 2006). Unfortunately, few of these placed any emphasis on the slug expansion due to pressure gradients, an effect that is of strong importance for the rise of slugs in volcanic conduits (*Polonsky et al.*, 1999b; *Seyfried and Freundt*, 2000). Nevertheless, a few models specialising in this effect have been proposed (*Blackburn et al.*, 1976; *Vergniolle*, 1998; *Seyfried and Freundt*, 2000; *James et al.*, 2004), discussing the slug rise in volcanic conduits. These models become more and more successful in describing the behaviour of gas slugs in laboratory experiments (*James et al.*, 2004; *Lane et al.*, 2005; *James et al.*, 2006) as well as during Strombolian-style eruptions on active volcanoes (e.g. *Neuberg et al.*, 1994; *Ohminato et al.*, 1998; *Rowe et al.*, 1998, 2000; *Ripepe and Gordeev*, 1999; *Kirchdörfer*, 1999; *Aster et al.*, 2003; *Chouet et al.*, 2003; *Gerst et al.*, 2006, 2008).

The work by *James et al.* (2008), which was largely validated by analogue laboratory experiments, makes interesting predictions about the last moments of a bubble's rise in a conduit, just before its burst. Since the behaviour of gas slugs in this upper region of the conduit is directly connected with their behaviour during the final explosion, available information about the upper conduit slug dynamics will be used to improve the model used in this study.

Typically, studies investigating volcanological fluid flow problems assume that basaltic high temperature magma behaves like a Newtonian fluid[2]. Yet, *Shaw* (1969) shows that at temperatures below 1130°C, the rheology of basalt becomes increasingly non-Newtonian. However, *James et al.* (2008) point out that due to the large flow velocities involved with the rise of a gas slug, these deviations from the Newtonian model are small compared to effects from other poorly constrained parameters, such as viscosity. This is in accordance with assumptions made by other authors, such as *Vergniolle and Brandeis* (1996), arguing that the relaxation times (*Dingwell et al.*, 1993) for typical magmas at Strombolian volcanoes are much smaller than the time scales considered here (*Webb and Dingwell*, 1990). Nevertheless, departure from Newtonian rheology is still possible through a very high crystal content (*Lejeune and Richet*, 1995). At Erebus, this crystal content is in the order of 25 – 40% (*Kyle*, 1977; *Dunbar et al.*, 1994; *Sweeney et al.*, 2008), which is considerable but still inside the range that can be approximated as Newtonian (*Lejeune and Richet*, 1995).

[2]A fluid is called **Newtonian** when its stress vs. strain-rate curve is linear and passes through the origin. The slope of this curve is determined by the fluid's viscosity. The flow properties of a **Non-Newtonian** fluid cannot be described by a single constant viscosity value.

James et al. (2008) use a straight-forward 1D model to provide first-order predictions about the dynamics of rising slugs, refine these results by using a 3D computational fluid dynamics (CFD) model, and finally verify some of their results with an analogue model. Their model suggests that slugs rise with a constant speed of their tail, while the slug nose accelerates due to volume expansion caused by the decreasing hydrostatic pressure on the slug (*Polonsky et al.*, 1999b; *Seyfried and Freundt*, 2000). Since the thickness of the wall film (as sketched in Fig 1.1) is found to be relatively constant, the acceleration of the slug nose leads to an ever increasing amount of liquid draining past the slug nose, i.e. the slug nose not only accelerates relative to the inertial system, but also accelerates relative to the speed of liquid pushed upward by the slug nose. A consequence of this is that the height of the remaining liquid column above the slug does not decrease in a linear way, as previously assumed (e.g. *Vergniolle*, 1998), but with an accelerated speed.

There are several factors governing the rise of a slug in a conduit or tube. They can be described by several dimensionless numbers, which are all hydrodynamic properties of the system. The first one is the *Morton number*, which describes the importance of viscous effects in relation to surface tension effects (*White and Beardmore*, 1962):

$$Mo = \frac{g\mu^4}{\rho\sigma^3} \tag{2.1}$$

where g is the gravitational acceleration, μ, ρ, and σ are the viscosity, density and surface tension of the liquid, respectively. In a highly viscous system such as a Strombolian volcanic conduit, the Morton number is expected to be rather large.

The second important parameter is the *Eötvös number*, which describes the buoyancy forces in relation to surface tension forces:

$$Eo = \frac{\rho g D^2}{\sigma} \tag{2.2}$$

where D is the conduit diameter. Again, this number is expected to be rather large in the case of a slug in a volcanic conduit. At Erebus, with an assumed magma viscosity in the order of $\mu_m = 5 \times 10^3$ Pa s (*Sweeney et al.*, 2008), a magma density of around 2600 kg/m^3 below a depth of 50 m (*Dibble*, 1994), and a surface tension around 0.4 $\frac{N}{m}$ (e.g. *Walker and Mullins Jr.*, 1981; *Koopmann*, 2004), the Morton number is in the 10^{13} range. Assuming a conduit diameter around 10 m (*Dibble et al.*, 2008), the Eötvös number lies in the 10^6 range. These two numbers show that slugs in Strombolian volcanic conduits are mainly driven by buoyancy and viscosity, whereas surface tension effects can be neglected (*Wallis*, 1969).

The third characteristic number is the *Froude number*, which describes the ratio of inertial to buoyancy forces, or, in other words, the ratio of kinetic to potential energy. It can be determined in a system that is controlled by mixed viscous and inertial effects through (*James et al.*, 2008)

$$Fr = 0.345(1 - e^{-N_f/34.5}) \tag{2.3}$$

where N_f is the *inverse viscosity*. It describes the importance of viscous effects and can be determined from the above numbers through (*Fabre and Liné*, 1992)

$$N_f = \left(\frac{Eo^3}{Mo}\right)^{1/4} \tag{2.4}$$

For the above values assumed at Erebus, N_f calculates to ~50. This value characterises a flow regime in the intermediate zone ($2 < N_f < 300$, *Fabre and Liné*, 1992; *James et al.*, 2008), where viscous and inertial forces both play an important role during slug rise. Finally, the Erebus Froude number calculates to 0.267 for the above assumptions, allowing for the calculation of a slug's rise speed (see next section).

Another interesting parameter of a flow regime is the *Reynolds number*, which, similar to N_f, describes the ratio of viscous to inertial forces, and provides an important indicator for the likelihood of turbulence in a system. It is defined through $Re = \rho U_s D/\mu$ (e.g. *Seyfried and Freundt*, 2000), where U_s is the rise speed of the slug. Typically, during flow in a pipe, the transition from laminar to turbulent flow starts at a Reynolds number in the range of $10^3 - 10^4$. At Erebus, this number is in the $10^1 - 10^2$ range, therefore slug flow is far from turbulent. The same can be said for other Strombolian volcanoes.

The numbers determined above allow the estimation of several important parameters of interest for slug flow. For example, with a formula supplied by *Brown* (1965), the equilibrium thickness δ_∞ of the liquid film on the side of the slug can be estimated (*James et al.*, 2004, 2008):

$$\delta_\infty = \frac{\sqrt{1+ND}-1}{N}\ , \quad \text{where} \quad N = \sqrt[3]{14.5\frac{\rho^2 g}{\mu^2}}\ . \tag{2.5}$$

For Erebus, assuming a conduit diameter of 10 m, this yields a liquid film thickness in the order of 1.5 m, i.e. ~30% of the conduit radius. The formula provides an interesting way of estimating the conduit diameter if the downward drag force caused by this liquid film around the rising slug can be determined by other means (e.g. through seismic source modelling, *Chouet et al.*, 2003).

Figure 2.2 shows an implementation of the 1D fluid dynamic model by *James et al.* (2008), displaying the slug rise of three differently sized slugs at Erebus. The values used for the conduit width and the magma properties are adapted to the above made assumptions. From these plots, slug lengths at depth can be estimated, as well as the slug rise speed (2.6 m/s), which is independent from the slug's mass or volume.

2.2.1 Expected slug overpressure and rise speed

A rising gas bubble always attempts to equalise its pressure with the surrounding hydrostatic pressure. Because the hydrostatic pressure decreases on the bubble's way up, the bubble continuously expands, therefore adjusting its pressure. If the bubble were always

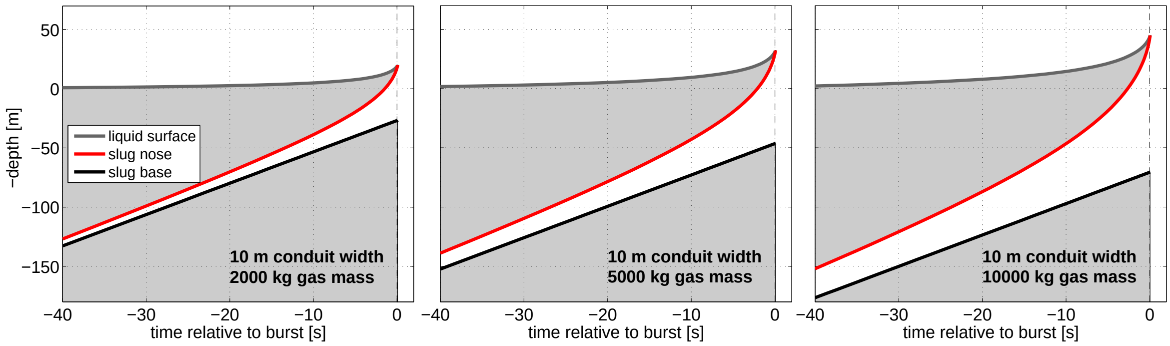

***Figure 2.2:* Simulation of rising gas slugs in a volcanic conduit** *with parameters adapted to Erebus conduit conditions, using the 1D model developed by James et al. (2008) and an implementation by M. Hort, (pers. comm.). Lines show the positions of the slug nose (red), the slug base (black), and the liquid surface (grey) as a function of time relative to the burst time. The only difference between the plots is the gas slug mass (as annotated). Surface displacement is plotted for a 10 m wide conduit, not considering that in reality the conduit feeds into a lava lake with a much wider cross sectional area, therefore the surface lift will not be as strong in a real lava lake.*

successful in doing so, it would arrive at the top of the liquid with no significant overpressure, and it could not burst. An example for such a situation is bubbles in water. On the other hand, bubbles in Strombolian volcanic eruptions must have a significant overpressure upon arrival at the surface, as can be seen in their powerful explosions (Fig. 2.1). Therefore, a mechanism must exist that leads to such an overpressure despite the bubble's attempt to equalise it through expansion.

The overpressure inside a rising slug before its burst, i.e. the pressure in excess of the hydrostatic pressure at the current position of the slug nose, can only be generated by two main mechanisms (*Blackburn et al.*, 1976; *Sparks*, 1978). The first one is negligible in the case of magma conduits – it is the surface tension of the bubble (which is small for large bubbles in magma). The second and much more important source of overpressure is the restriction that the expanding gas slug experiences by the viscosity and inertia of the surrounding liquid. It is small as long as the bubble does not grow much, but it can increase significantly when the slug expansion rate is large, as it typically is shortly before a slug approaches the surface.

Figure 2.3 shows the history of gas pressure in a rising slug at Erebus. The gas slug mass (2,000 kg) was arbitrarily chosen and matches that of the left plot in Figure 2.2. The figure also shows the gas slug volume, which strongly increases with time, eventually even tripling in the last 10 seconds before the slug arrives at the surface. The plot stops at a slug volume of ∼1,600 m^3, at which the overpressure of the slug is around 400 kPa, and the remaining liquid head above the slug is 1.4 m thick. From this point on, the final expansion and burst of the slug starts, which cannot be modelled with the 1D model (*James et al.*, 2009). It is these final processes that will be one of the main focus points of this study.

Figure 2.3 demonstrates that the overpressure of a bubble at burst is generated to a large part through dynamic processes in the last tens of metres of its ascent. These are mainly con-

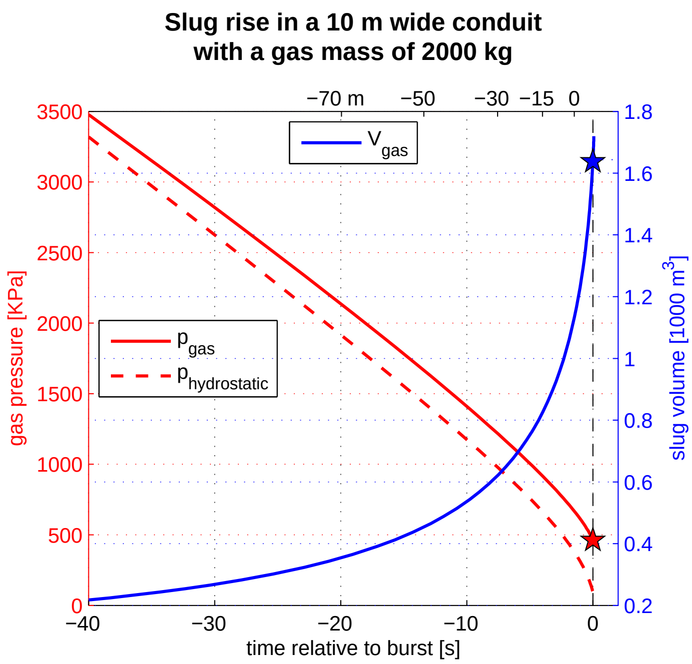

***Figure 2.3:* Simulation of pressure and volume of a rising slug.** *Parameters are similar to Fig. 2.2 (left). Slug overpressure (above hydrostatic pressure) can be estimated from the vertical distance between the gas pressure (red line) and the hydrostatic pressure at the slug nose (dashed red line). The blue line shows the slug volume at the respective time before burst (marked as star). The upper horizontal axis denotes the slug nose depth at the respective time.*

trolled by the hydrostatic pressure gradient, the viscosity and the inertia of the liquid. The relative hydrostatic pressure gradient, which is responsible for the slug expansion, strongly increases towards the top of the conduit, therefore the slug overpressure increases shortly before reaching the surface. Nevertheless, Figure 2.3 shows that even at depth, when its expansion rate is still slow, the slug has a significant overpressure. The reason for this is that the slow expansion rate at that time is counterbalanced by the still very high inertia of the large liquid column above the slug, which has to be accelerated in order for the slug to expand. This way even a small expansion rate can lead to a significant overpressure at depth.

Viscous overpressures caused by the ascent of slugs in volcanic conduits can reach significantly higher values in magmas with intermediate viscosity (e.g. intermediate magmas, such as andesites, dacites, or phonolites) than in low viscosity magmas (e.g. ultramafic or mafic magmas, such as basalt).

In contrast to the importance of dynamic and near surface effects for slug overpressure, initial overpressures that are acquired at depth (e.g. during formation of the slug or during passage of constrained conduit areas) are rapidly equalised during the following ascent phase and are therefore irrelevant for the burst process.

James et al. (2004) show that inclined tubes or conduits promote the formation of slugs with an increased size and an increased speed of up to 50%. Additionally they find that liquid mixing is strongly enhanced in that case, often generating a complete circulatory system filling the tube. At Stromboli volcano, Italy, the conduit is assumed to be inclined by about 30° from the vertical, with an assumed depth of about 200 m below the surface (*Chouet et al.*, 2003). New evidence suggests that the same might be true for Erebus volcano (*Aster et al.*, 2008).

As demonstrated by *Wallis* (1969) and *James et al.* (2004, 2008), a slug in a tube rises with a largely constant base velocity, while its nose accelerates as a reaction to hydrostatic decompression during the rise. The base velocity is controlled by the flow regime, i.e. depending on the relative importance of viscous and inertial forces. It can be estimated from the above calculated dimensionless parameters of the system:

$$U_s = Fr\sqrt{gD} \tag{2.6}$$

For Erebus, this implies a slug base rise speed of $U_s \approx 2.6$ m/s, and is reflected in the 1D conduit rise model shown in Figure 2.2.

2.2.2 Resulting conduit pressures and net forces on the system

The rising gas slug exerts force on the surrounding medium mainly through two different processes: i) changing the liquid's pressure, which is acting on the conduit wall and bottom, and ii) causing friction forces between moving liquid and the wall. Both these processes add up to the final net force that is applied to the system.

James et al. (2004) demonstrate that the pressure acting on the conduit walls changes during the entire rise-time of the slug (not just during the passage of the slug). These pressure changes consist of several different phases, dependent on the actual position of the slug relative to the point where the pressure is measured (see Fig. 2.4). The gas volume increase during the rise of a slug leads to an upward acceleration of the entire liquid column above, and therefore to a downward force. Additionally, by lengthening the slug, the area of the liquid film surrounding the slug increases, creating more downward drag at the conduit walls (where the thickness of the film was observed to remain almost constant, see *James et al.*, 2008). Both these effects influence the pressure in the entire conduit (Fig. 2.4).

While the slug rises and expands, the pressure at an arbitrarily chosen reference point at the conduit wall **above** the slug head will slowly increase due to the increasing static overhead of liquid (Fig. 2.4, phase I). When the slug passes that point, the pressure rapidly drops (phase II) because some of the space above the point, which was formerly occupied by liquid, now gets replaced by the light gas (which has a lower density than the liquid). This rapid pressure drop associated with the loss of static overhead as the bubble passes is largely persistent (*James et al.*, 2004) even after the bubble has burst on the surface (i.e. the magma surface level has dropped), and can only be reversed by a subsequent resupply of magma from below.

However, even after the bubble has passed the reference point, the pressure at this point keeps on changing (Fig. 2.4). This pressure change is caused by the expanding slug (now **above** the reference point) increasing the area of the liquid film running down its sides, creating more and more downward drag at the conduit walls as the slug gets longer. The material within the film of liquid is running down the side of the slug, which means it is either accelerating in free fall, or it has reached its terminal velocity and is suspended by

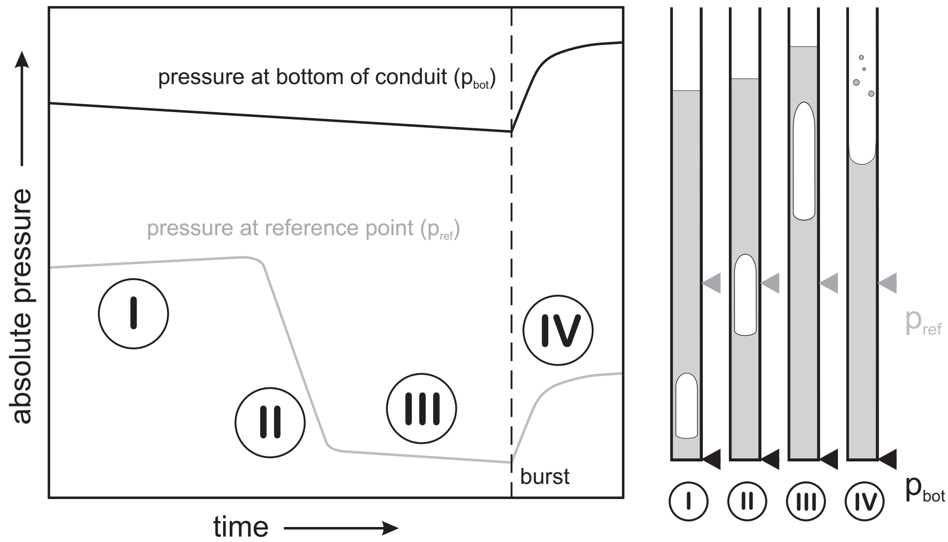

Figure 2.4: ***Sketch of conduit pressure caused by a rising gas slug****, schematically summarising results by James et al. (2004). The slug is released before the start of the time axis, i.e. off the left side, and its burst time is marked by a dashed line. The black curve shows the pressure measured at the bottom of the conduit, whereas the grey curve shows the pressure at an arbitrarily chosen reference point on the conduit wall (grey triangle on right). The four different phases marked in the pressure plot are shown as little sketches on the right. Note that in the case of a conduit that is connected to a large pressure-stable reservoir at the bottom, the reservoir would react by injecting liquid into the bottom of the conduit immediately after the slug has entered the conduit, equalising this loss of static overhead (see concluding note on page 35).*

wall friction. In either case it is not supported by the liquid column any more, so the mass contained in it is not contributing to the hydrostatic pressure underneath (*James et al.*, 2004). Thus, because this mass is ever increasing with the size of the slug, the hydrostatic pressure underneath the slug (i.e. at our reference point) constantly decreases while the slug rises[3] (Fig. 2.4, phase III). When the slug bursts, the film collapses into the column and suddenly contributes to the hydrostatic pressure underneath, causing one last positive pressure leap at our reference point (phase IV).

Since the described pressure changes not only affect the conduit walls but also act on the bottom of the conduit or whatever is underneath (e.g. like a magma chamber), they induce a net force acting on the whole system. Yet, the force resulting from pressure loss caused by wall friction (Fig. 2.4) is exactly counterbalanced by the resulting downward force **on** the wall (*James et al.*, 2008). Only the counter force in reaction to the upward acceleration of the column above the slug remains (*Takei and Kumazawa*, 1994). This force is relatively weak, especially when the slug is still deep, i.e. where it is not expanding much due to a small pressure gradient. Therefore, no strong net forces on the system are expected during this phase of the bubble rise[4].

[3]this effect is only somewhat diminished by the liquid nose accelerated upward ahead of the slug, creating an upward drag force on the wall.

[4]unless the bubble passes through a region of a sudden diameter change of the conduit, as will be discussed below (Sec. 9.8.1).

Burst effects. Further up in the conduit, when approaching the surface, the slug expands significantly faster than before, but still the momentum force caused by the acceleration of fluid above the slug is largely counterbalanced by the now increasing amount of fluid that is accelerated downward alongside the bubble during its rise (*James et al.*, 2008). Only when the slug approaches the surface, just before its burst, this delicate force balance is disturbed by the dynamic processes that are associated with the final rapid expansion of the slug and the associated acceleration of mass.

These final burst effects are highly dependent on the conduit geometry and on the circumstances of the burst itself. Nevertheless, the above shows that ground forces associated with the bubble's burst are not merely a small contribution to forces that are generated during the whole process of slug rise. Instead, they are a very important part of the process because they are one of the few occasions where the slug can actually generate a net force on the ground (along with the generation process of the slug at depth, and when passing through a conduit constriction). The burst process is thus expected to play a considerable role in the generation of seismic waves that can be observed during Strombolian eruptions. To investigate this, one objective of this study will be to use radar data to calculate the ground forces generated by an expanding gas slug near the surface of a magma conduit.

A concluding note. The above mentioned laboratory experiments by *James et al.* (2004) operate with a fixed liquid volume and do not have a large fluid reservoir underneath that could act as a pressure equaliser (as described by, e.g., *Seyfried and Freundt*, 2000). Therefore, the pressure at the bottom of the laboratory conduit is allowed to vary while the liquid flux is zero at this point. In a situation where a magma chamber is located at the bottom of the conduit, such a pressure equaliser exists, i.e. the pressure at the base of the conduit can be assumed to be constant (the pressure inside a large magma chamber can be considered unaltered by the relatively small volume loss caused by the rise of one slug). This slightly changes the reaction of the system. As soon as a bubble has entered the conduit from below, the system reacts to the loss of static overhead (and to the pressure loss through wall friction) by a restoring force pressing magma into the column from below (*Witham and Llewellin*, 2006). This means that as soon as the bubble has entered the column from below, the magma level at the surface of the column not just rises due to the volume expansion of the slug, but also due to the influx of magma into the conduit resulting from the loss of hydrostatic pressure. Theoretical considerations by *Witham and Llewellin* (2006) show that this behaviour leads to tight geometry constraints for stable conduit-lake systems. If these are not met, the lake system will be unstable and eventually drain.

In summary, the most important point of this Chapter was to show that even though pressure changes occur during the slug generation and rise process, the burst overpressure and the net forces are still dominated by the dynamic overpressure generated in the last moments of the slug rise. Any initial overpressure of the bubble at depth is rapidly equalised and is therefore insignificant for the burst process. Furthermore, conduit forces acting on the whole system are mainly expected during the generation of the slug, when passing a sudden change in conduit diameter, and finally, during burst. From a fluid dynamics point of view, impulsive seismic signals from Strombolian eruptions are therefore expected to mainly originate from either one of these three processes, and will mostly couple to the surrounding rock at locations of conduit discontinuities.

Part II

THE FIRST SECOND OF A STROMBOLIAN ERUPTION

CHAPTER 3

THE THEORY OF SOUND FIELDS AND THEIR SOURCES

An important part of this study is to make useful predictions about the acoustic signal generated by a Strombolian volcanic eruption. However, the requirements for mathematical tools to study the sound field and the sound energy generated by an exploding magma bubble often exceed the capabilities of the standard equations used in textbooks. This can mostly be attributed to the fact that in the case of volcanoes, the usual assumptions of a compact source and an observer in the far-field often do not hold, or at least they must be examined very carefully.

Some of the standard acoustic equations are occasionally used in a somewhat imprecise manner in the literature, i.e. without the necessary testing for their valid range. In the following section, to cast more light on these formulae, I will distill some of the necessary tools in detail from the multitude of available literature on the topic. I will place the main emphasis on highlighting the assumptions and simplifications that were emplaced, and pointing out their valid range of use. My approach will follow, to a certain point, the approach by *Lighthill* (1978), but includes argumentations and various other elements from further literature (e.g. *Dowling and Williams*, 1983; *Dowling*, 1998; *Stepanishen*, 1998; *Temkin*, 1981; *Ehrenfried*, 2003).

The sound fields that we deal with in daily life as well as on volcanoes are pressure disturbances in the atmosphere travelling away from their source, which are in the simplest analogy somewhat similar to ripples on a pond after tossing a rock. The difference is, however, that sound waves travel in a three dimensional space and are driven by pressure differences rather than gravity. The following sections will describe how to deal with these disturbances mathematically, and how to develop useful tools to better predict their behaviour.

3.1 Wave equation and sound potential

To a sound wave, physically speaking, the atmosphere is not much more than a compressible fluid, i.e. its density fluctuates as a function of pressure. In such a fluid, the properties of sound propagation can be best described with a ”velocity potential”, or ”sound potential” Φ_A. This potential is the non-rotational part (i.e. it does not contain any vortices) of the general "velocity field" of the fluid. Only this non-rotational part can contribute to the propagation of sound in the medium (*Lighthill*, 1978, p. 3). Since the fluid is compressible[1], Laplace's equation ($\Delta\Phi_A = \vec{\nabla}^2\Phi_A = 0$) is not fulfilled and must be replaced by the homogeneous wave equation for Φ_A:

$$\left(\frac{1}{c^2}\frac{\partial}{\partial t^2} - \Delta\right)\Phi_A = 0, \tag{3.1}$$

which is valid at all places outside the source region of the sound field. c is the medium's speed of sound. This wave equation can directly be derived from the core of the Navier-Stokes equations, i.e. basically from the differential form of Newton's second law describing the movement of a *potential flow*.

Assuming spherical geometry, i.e. parameters only vary with their distance r from the origin, $\Delta\Phi_A$ can be rewritten as

$$\Delta\Phi_A = \frac{1}{r}\frac{\partial}{\partial r^2}(r\Phi_A), \tag{3.2}$$

leading to a homogeneous wave equation in spherical coordinates:

$$\left(\frac{1}{c^2}\frac{\partial}{\partial t^2} - \frac{\partial}{\partial r^2}\right)(r\Phi_A) = 0, \tag{3.3}$$

which has the general solution (*Lighthill*, 1978, p. 18)

$$r\Phi_A = f(r - ct) + g(r + ct). \tag{3.4}$$

This solution describes spherical waves travelling in increasing directions of r (function f), as well as in the opposite direction (function g). Since the latter case represents incoming waves, which are of no interest for this study, we will from now on only concentrate on solutions for outgoing waves (f), caused by "our" source.

From the velocity potential Φ_A, the physical properties of the sound field, such as velocity $u(r,t)$, pressure $p(r,t)$ or the transport of energy can be derived (e.g. *Lighthill*, 1978; *Temkin*, 1981):

$$\vec{u}(r,t) = \vec{\nabla}\Phi_A \tag{3.5}$$

$$p(r,t) = -\rho_a\frac{\partial\Phi_A}{\partial t}, \tag{3.6}$$

[1] in fluid dynamics, an *incompressible* ***fluid*** is a material that does not change its density with pressure (i.e. it does not compress), assuming a constant temperature. Its density can, however, change with temperature. An *incompressible* ***flow*** is a solid or fluid (including gas) flow in which the divergence of velocity is zero. While incompressible materials always undergo incompressible flow, under certain circumstances even compressible materials can undergo (nearly) incompressible flow, e.g. when the fluid's speed is much less than the sound speed. Assuming incompressible flow greatly simplifies the governing equations.

where $p(r,t)$ is the excess pressure above the surrounding fluid or atmospheric pressure p_{atm}, i.e. the total pressure will be $\hat{p} = p + p_{\text{atm}}$. However, for the transport of energy, p_{atm} will not be important (*Lighthill*, 1978, p. 13). ρ_a is the density of the surrounding atmosphere.

The origin of the above relations (Eq. 3.5 and 3.6) becomes obvious when combining the homogeneous wave equation (Eq. 3.1) with the continuity equation of fluid dynamics. The latter is

$$\frac{1}{\rho_a}\frac{\partial\rho}{\partial p}\frac{\partial p}{\partial t} + \vec{\nabla}\cdot\vec{u} = 0 \tag{3.7}$$

where ρ is the density of the atmosphere slightly fluctuating around its undisturbed value ρ_a ($\vec{\nabla}\rho \approx 0$). The assumption of small variations in ρ can be made because, as will be shown later in this section, almost all sound waves we are confronted with are only minor perturbations of the atmospheric pressure, leading to only minor changes in density (*Dowling and Williams*, 1983, p. 13). With the speed of sound $c = \sqrt{\frac{\partial p}{\partial \rho}}$ the continuity equation can be rewritten as

$$\frac{1}{\rho_a c^2}\frac{\partial p}{\partial t} + \vec{\nabla}\cdot\vec{u} = 0 \tag{3.8}$$

Inserting relations 3.5 and 3.6 into this equation immediately leads to the homogeneous wave equation (Eq. 3.1), showing that Equations 3.5 and 3.6 are the necessary link between wave equation and continuity equation.

From equations 3.5 and 3.6, a true rate of energy[2] transport I across a small plane element of unit area can be defined, also called **acoustic intensity** (*Lighthill*, 1978, p. 13):

$$\vec{I} = p\vec{u} = -\rho_a(\frac{\partial\Phi_A}{\partial t})\vec{\nabla}\Phi_A\ , \tag{3.9}$$

which, when multiplied by the respective area of energy flux, has a similar form than the most basic equation relating power to force and velocity (i.e. $P = \vec{F}\vec{v}$). I is measured in W/m^2 and due to its wide range is often expressed in a decibel (dB) scale, resembling the **sound intensity level (SIL)** of a sound wave (*Lighthill*, 1978, p. 17):

$$\text{SIL}\ \ [\text{in dB}] = 10\log_{10}\left(\frac{I_{\text{mean}}}{I_{\text{ref}}}\right) = 120 + 10\log_{10}(\left(\frac{I_{\text{mean}}}{W/m^2}\right)\ , \tag{3.10}$$

where I_{mean} is the mean acoustic intensity and I_{ref} is a reference value, usually chosen so that the threshold of hearing marks 0 dB. A typical minimum intensity level for audibility of sounds (i.e. the hearing threshold) at ”higher” frequencies (500 to 8000 Hz) within the audible spectrum (around 20 to 20,000 Hz) is around $I = 10^{-12}\,W/m^2$, thus this is a widely accepted value for I_{ref} (*Lighthill*, 1978, p. 17). It approximately resembles the sound intensity caused by a flying mosquito at a distance of 3 m. The audibility threshold rapidly increases

[2]both potential and kinetic

for frequencies above and below that range. At 100 Hz, the level of audibility is around 40 dB ($10^{-8} W/m^2$). Below about 20 Hz, audibility disappears completely (*Lighthill*, 1978). The typical pain threshold for most audible frequencies lies around 120 - 140 dB ($1 - 100\, W/m^2$).

By integrating the sound intensity over a given surface, the total energy transport rate through that surface can be calculated. The total sound power output W_{sound} of a sound source is obtained by integrating over a closed surface enclosing the sound source. This total power output is also often described in a decibel scale, resembling the **sound power level (SWL)** (*Dowling and Williams*, 1983, p. 12):

$$\text{SWL} \;\; [\text{in dB}] = 10 \log_{10} \left(\frac{W_{\text{sound}}}{W_{\text{ref}}} \right) = 120 + 10 \log_{10} \left(\frac{W_{\text{sound}}}{\text{Watt}} \right) , \tag{3.11}$$

where W_{ref} is the standard reference sound power and equals 10^{-12} W. For comparison it is interesting to note that the typical total power output of a human shout is only about 10^{-5} W (e.g. *Dowling and Williams*, 1983, p. 12)[3], whereas a large jet aircraft at take-off generates more than 10^5 W of sound waves. A rocket or a spacecraft at take-off can produce sound as powerful as 10^5 to 10^7 W (*Lighthill* (1978), p. 17, or *Dowling and Williams* (1983), p. 12). The relatively small amount of power generated by the human voice leads to astonishing results when compared to other energy sources. For example, *Dowling and Williams* (1983, p. 12) point out that the total sound energy created by the combined shouts of a stadium crowd during an exciting sports game roughly equals the energy required to fry one egg. Even more astounding, the above numbers show that a large aircraft at take-off generates about as much sound power as the whole Earth's population shouting at once.

The above **sound power level (SWL)** should not be confused with the **sound pressure level (SPL)**, which is somewhat confusingly measured in decibel, too. While the former describes the power output of a sound source (i.e. it is a property of the **source**), the latter is a measure of the mean amplitude of the pressure disturbance p_{rms} in the atmosphere at a certain distance from the source (i.e. it is a property of the sound **field**, see *Dowling and Williams*, 1983, p. 13):

$$\text{SPL} \;\; [\text{in dB}] = 10 \log_{10} \left(\frac{p_{\text{rms}}^2}{p_{\text{ref}}^2} \right) = 20 \log_{10} \left(\frac{p_{\text{rms}}}{2 \times 10^{-5}\, N/m^2} \right) , \tag{3.12}$$

where p_{ref}, like on the other intensity scales, marks the threshold of human audibility, which accordingly is equal to 0 dB on this scale. p_{rms} is the root mean squared overpressure of the sound wave. The most commonly used value for p_{ref} is 2×10^{-5} Pa, which represents a pressure fluctuation of only about 10^{-10} atmospheres. This means the particle vibration amplitude at the threshold of human hearing is only around 10^{-11} metres (*Dowling and Williams*, 1983, p. 13), i.e the human ear can detect (coherent) particle movements as small as 1/10 of the size of a Helium atom. Again, the threshold of pain at audible frequencies is around 120 to 140 dB SPL (20 to 200 Pa), which is still only a pressure variation of about 1/1000

[3]Some sources state slightly higher values for a human shout, up to 10^{-4} – 10^{-3} W (e.g. *Lighthill*, 1978, p.16)

of the atmosphere. This shows that most sound waves we are confronted with can be regarded as only minor pressure perturbations of the atmosphere, which means that products of perturbed quantities are negligible, resulting in a linear acoustic field. Theoretically, a fluctuation with an amplitude of 1 bar (i.e. one *atmosphere*) at sea level would correspond to 194 dB SPL.

Interestingly, the sound intensity level of a **plane** wave travelling in a **standard atmosphere** is equal to its sound pressure level: SIL $=$ SPL, because the acoustic intensity of a plane sound wave increases proportionally to the squared pressure (Eq. 3.9 reduces to $I = \frac{p^2}{\rho_a c}$, because $u = \frac{p}{\rho_a c}$ for plane waves, see e.g. *Lighthill*, 1978, p. 4). However, this is not true under conditions where the air density ρ_a or the speed of sound c vary significantly from the conditions ρ_0, c_0 under which the reference values I_{ref} and p_{ref} were obtained (i.e. where $I_{\text{ref}} = \frac{p_{\text{ref}}^2}{\rho_0 c_0}$).

3.2 The speed of sound, air pressure & density

Several formulae for the propagation of sound were derived in the last section, most of which depend on physical parameters of the surrounding atmosphere, such as air density and the speed of sound. These parameters can be calculated using the ideal gas law

$$\hat{p}V = nR_mT = \frac{m}{M_A}R_mT \tag{3.13}$$

where V is the volume occupied by an ideal gas of mass m, absolute pressure $\hat{p}$ and temperature T [K]. M_A is the molar mass of dry air ($\approx$ 0.0289645 kg/mol, see list of symbols on p. 239), R_m is the molar (universal) gas constant, and n is the number of moles of gas. Consequently, air density ρ is a direct function of pressure and temperature

$$\rho(\hat{p}, T) = \frac{m}{V} = \frac{nM_A}{V} = \hat{p}\frac{M_A}{R_mT} \,. \tag{3.14}$$

For example, at Lower Erebus Hut (station LEH) on Mt. Erebus volcano the air pressure at an altitude of 3400 m above sea level varies between 61 kPa and 64 kPa, with an annual mean at around 62.5 kPa (Mount Erebus Volcano Observatory webpage *MEVO*, 2008). A good estimation for the mean air pressure at the crater rim at an altitude of approximately 3770 m is therefore 60 kPa. With an average summer temperature of -30°C this gives an air density of around 0.86 kg/m^3.

In classical mechanics the speed of sound in a gas is found to be the square root of the quotient between the gas' bulk modulus and its density ($c = \sqrt{\kappa/\rho}$), where $\kappa = \gamma\,\hat{p}$ is the bulk modulus of the gas, an equivalent to the *stiffness* of solid media. γ is the *ratio of specific heats* (also called the *adiabatic index*, *isentropic exponent*, or *isentropic expansion factor*)

$$\gamma = \frac{C_p}{C_V} \tag{3.15}$$

temp [°C]	c_a[m/s]
-40	306.0
-30	312.5
-20	318.9
-10	325.1
0	331.2
10	337.2
20	343.1
30	349.0
40	354.7

Table 3.1: Sound speed in dry air at different temperatures. *Note that these values are practically independent of air pressure (and therefore independent of altitude).*

γ is equal to 1.4 for air at standard conditions, and 1.1 for hot gases (*Lighthill*, 1978).

Since the gases that are of interest in this study (i.e. air and hot magmatic gases such as water vapour or CO_2) are behaving much like an ideal gas, we can rephrase the formula for the speed of sound using the ideal gas law (*White*, 1961; *Ford*, 1970):

$$c_a = \sqrt{\gamma \frac{\hat{p}}{\rho}} = \sqrt{\gamma \frac{R_m T}{M_A}} \underbrace{\approx 20.047\sqrt{T}}_{\text{for air}} \tag{3.16}$$

It is somewhat counterintuitive that air pressure, and therefore also altitude, does not influence the speed of sound in dry air (Eq. 3.16). Even in moist air its influence is almost negligible. The controlling term is the ratio of air pressure to density, which in an ideal gas is independent of pressure. Table 3.1 shows the calculated sound speeds for a variety of air temperatures (for example, at the crater rim of Mt. Erebus volcano, at a mean summer temperature of $-30°C$ the speed of sound is $\approx 312.5\ \frac{m}{s}$).

3.3 The sound potential of a simple monopole source

One of the most basic but also most important sources of sound is the so-called "*simple source*". It describes a homogeneous sound field that only has one infinitely small source region, i.e. a point source. Equation 3.1 is only valid outside this source region. The infinitely small source of sound, which is yet to be specified, can be included in the wave equation through the parameter ξ, acting only in its infinitely small source volume at position $\vec{x}_0$:

$$\left(\frac{1}{c^2}\frac{\partial}{\partial t^2} - \Delta\right)\Phi_A = \xi(t)\delta(\vec{x}_0), \tag{3.17}$$

where $\delta(\vec{x}_0)$ is the Dirac delta function. To learn more about the nature of this source term, Equation 3.17 will be integrated over the volume V_S of a sphere of radius r, whose centre is located at $\vec{x}_0$. Additionally, the resulting equation will be analysed for a diminishing radius r of the integration sphere, leading to

$$\underbrace{\lim_{r\to 0}\int_{V_S}\frac{1}{c^2}\frac{\partial}{\partial t^2}\Phi_A\,dV_S}_{I}-\underbrace{\lim_{r\to 0}\int_{V_S}\Delta\Phi_A\,dV_S}_{II}=\underbrace{\lim_{r\to 0}\int_{V_S}\xi(t)\delta(\vec{x}_0)\,dV_S}_{III} \tag{3.18}$$

Since the integral in term III only includes contributions from the source itself, term III can be replaced with $\xi(t)$. By expanding Φ_A into a series of harmonic oscillations it can be shown (*Ehrenfried*, 2003, p. 149) that even though the integrand in term I possesses a singularity at $\vec{x}_0$, the value of the integral is zero in this case. Therefore, the only term remaining on the left side of Equation 3.18 is term II, which can be transformed to a surface integral using the divergence theorem (also known as Gauss's theorem), together with Equation 3.5 (*Ehrenfried*, 2003, p. 149):

$$-\lim_{r\to 0}\int_{V_S}\Delta\Phi_A\,dV_S=-\lim_{r\to 0}\int_{A_S}\hat{\vec{n}}\,\vec{\nabla}\Phi_A\,dA_S=-\lim_{r\to 0}\int_{A_S}u_R\,dA_S=-\lim_{r\to 0}4\pi r^2\dot{r}=-\dot{V}_{\text{source}}, \tag{3.19}$$

where $\hat{\vec{n}}$ is the surface unit vector of the integration sphere, A_S is its surface, and u_R is the surface velocity of the sphere, radially pointing away from the centre. Equation 3.18 therefore reduces to

$$\xi(t)=-\dot{V}_{\text{source}}(t). \tag{3.20}$$

This means that the source term in Equation 3.17 can simply be interpreted as the volume flux of the source, i.e. the rate at which volume V_{source} is produced in the source. In this case, a solution for the inhomogeneous wave equation (3.17) in spherical coordinates can be found (e.g. *Lighthill*, 1978; *Temkin*, 1981), yielding a sound potential of

$$\Phi_A(r,t)=-\frac{\dot{V}_{\text{source}}(t)}{4\pi r}, \tag{3.21}$$

where the source is located at $r=0$. This solution does not yet include the transport of energy away from the source with a finite wave speed, a feature that can easily be corrected for by incorporating a time-lag r/c_a, effectively describing the transport of energy away from the source with the average speed of sound c_a (*Lighthill*, 1978, p. 18). The general solution for Φ_A is then

$$\Phi_A(r,t)=-\frac{\dot{V}_{\text{source}}(t-r/c_a)}{4\pi r}\;. \tag{3.22}$$

This type of source is widely known as **acoustic monopole, simple source, or Lighthill's monopole**. It describes the sound field generated by an infinitesimal monopole source of sound of the so-called **strength** $\dot{V}_{\text{source}}$. As an example, such a source can be approximated by a popping firecracker. Using Equations 3.5 and 3.6, the physical properties of the resulting wave field can be calculated from (3.22). The pressure at any given point outside the source region is

$$p(r,t) = -\rho_a \frac{\partial \Phi_A}{\partial t} = \frac{\rho_a \ddot{V}_{\text{source}}(t - r/c_a)}{4\pi r} \, . \tag{3.23}$$

This relation shows that the pressure at a given distance from the source will only depend on the rate of change of volume outflow, i.e. the **volume acceleration** of material being emitted from the source. The particle velocity $\vec{u}$ of a given point in the atmosphere is only slightly more complicated:

$$|\vec{u}(r,t)| = u_r(r,t) = \frac{\partial \Phi_A}{\partial r} = \frac{\dot{V}_{\text{source}}(t - r/c_a) + \frac{r}{c_a} \ddot{V}_{\text{source}}(t - r/c_a)}{4\pi r^2} \, . \tag{3.24}$$

Integrating the particle velocity over the surface of a closed volume surrounding the source yields the volume flow out of this surface. Interestingly, the volume flow $4\pi r^2 u_r$ from a monopole source through the surface of a sphere at distance r from the centre is not equal to $\dot{V}_{\text{source}}(t)$ (as might seem logical when only keeping the continuity equation in mind), but is

$$4\pi r^2 u_r = \dot{V}_{\text{source}}(t - r/c_a) + \frac{r}{c_a} \ddot{V}_{\text{source}}(t - r/c_a). \tag{3.25}$$

The second term in this equation has its origin in the dynamic, wave-like behaviour of the volume flow (introduced by the time-lag r/c), which increases with increasing distance from the source. Consequently, at large distances from the source the movement of the atmosphere is not controlled by the volume outflow (or flux) from the source but by the volume acceleration of the source. This important observation will later lead to the definition of the so-called **near and far fields**. For simplicity reasons, $t - r/c_a$ is from now on replaced by t', which is called the "retarded time".

Another important physical parameter is the total power flux away from the source through the surface of a sphere of radius r. It can be calculated using Equation 3.9, multiplied by the surface area $4\pi r^2$:

$$\dot{E}_{\text{sound,mono}}(t', r) = 4\pi r^2 I = 4\pi r^2 p u_r \tag{3.26}$$

$$= \frac{\rho_a}{4\pi c_a} \ddot{V}^2_{\text{source}}(t') + \frac{\rho_a}{4\pi} \frac{\dot{V}_{\text{source}}(t') \ddot{V}_{\text{source}}(t')}{r} \, . \tag{3.27}$$

Considering the law of conservation of energy it may seem irritating that the total power output through the surface of the sphere is a function of r, since this basically means that the total energy flux through the surface of the closed integration sphere depends on its radius, which seems counterintuitive when keeping in mind that energy must be conserved.

Rephrasing the term in question (Eq. 3.27) sheds some light on its nature:

$$\dot{E}_{\text{sound,mono}} = \frac{\rho_a}{4\pi c_a}\ddot{V}^2_{\text{source}} + \frac{\partial}{\partial t}\left(\frac{\rho_a}{8\pi r}\dot{V}^2_{\text{source}}\right) , \tag{3.28}$$

showing that the left term on the right side of (3.28) is always positive, representing the amount of energy that is radiated into the atmosphere by the source. In contrast to this, the right term can change its sign, i.e. becoming negative when the absolute value of the volume flux from the source decreases (see also *Temkin*, 1981, p. 272). This term represents the inertia and kinetic energy of the atmosphere being displaced and accelerated by the volume expansion in the vicinity of the source, transferring energy back and forth from the source to the atmosphere in the case of an oscillating source. Right at the location of a point source this term is infinite, since a source of infinitesimal size would have to move with an infinite velocity to generate a finite volume acceleration. At large distances from the source this term vanishes, simply because the squared velocity of the displaced atmosphere at large distances is too small to play an important role in the energy flux. Also, integrating over a time period longer than a typical cycle period of the system eliminates the effect of this term, resulting from the fact that in a stable system, whatever is accelerated must be decelerated sooner or later, and energy is conserved. Therefore, the effect described by this term does not radiate energy, i.e. it does not generate sound waves. However, when estimating the energy output during the first moments of an explosion (Sec. 4.2.7), this term cannot be neglected, even though the energy stored in it will be given back to the system eventually.

Special case: a half space boundary. Note that both p and $\vec{u}$ are doubled if the source is located right on the interface between a solid half space and the atmosphere. This is because only a negligible amount of pressure and particle velocity can be transferred into the solid half space (see also end of Section 3.6). Since the energy flux from the source is proportional to the product of p and $\vec{u}$ (Eq. 3.9), it will be twice as high in the half space case as if the same source would radiate into a full space atmosphere (i.e. in Eq. 3.26, both p and $\vec{u}$ are multiplied by a factor of two, while the area into which energy is released is divided by two in the half space case. This leaves an overall factor of two in the energy output, compared to a full space case). It means that the energy output of a source will be doubled simply by moving it to a half space boundary – even though its volumetric properties $\dot{V}_{\text{source}}$ and $\ddot{V}_{\text{source}}$ remain unchanged. In other words, twice the energy is required to displace the same amount of atmosphere when only half the space is available.

Also note that rearranging a monopole source into a half space setting does **not** change the source's property of being a monopole, i.e. it does not introduce a dipole component as is the case with a piston moving in and out of a half space (Sec. 3.5). This can be shown through symmetry considerations.

3.4 Compactness, near and far-field

The above paragraph shows that the physical effects caused by a simple sound source vary significantly with the source distance. Additionally, up to this point the established equations only describe a source of infinitesimal size. It is therefore necessary to discuss the area of validity of these equations for source geometries that are closer to real-life applications, i.e. sources of finite sizes. For the judgement of the validity of the above equations there are two critical parameters, namely the **compactness** of the source and the observation distance.

The compactness of a source is a measure for the size of the source compared to a typical wavelength λ of the system, and is given by its *compactness ratio*, or *Helmholtz number*

$$He = \frac{\omega a}{c_a} = \frac{2\pi a}{\lambda} = ka \; , \tag{3.29}$$

where a is the radius of the source area that generates a volume flux, e.g. in the case of a monopole source this might be a breathing or pulsating sphere. k is the wave number, ω is a typical frequency of the system. Since the Helmholtz number is equal to $\frac{2\pi a}{\lambda}$, it represents the ratio of the sphere's circumference $2\pi a$ to the emitted acoustic wavelength λ. This means that *simple sources* as described by Equation 3.23 are always compact, due to their infinitesimal size.

A source is called **non-compact** if $\frac{2\pi a}{\lambda} \gg 1$, and **compact** if $\frac{2\pi a}{\lambda} \ll 1$ (*Dowling and Williams*, 1983, p. 50). From this definition follows that for compact sources the travel time of an acoustic signal travelling from one side of the source to the opposite side is negligible in comparison to the main wave period of the emitted signal. This is not the case for non-compact sources. A sound signal that is emitted from the surface of a **non-compact** source, even if emitted impulsively from all surface points at the same time, will appear smeared (or blurred) over a finite period of time when recorded by a close or distant observer, simply due to the different path lengths between the observer and the various points on the source surface. In this case the assumption of a simple monopole source does not hold, and calculating the physical parameters of the wave field becomes increasingly complicated (Sec. 3.6). An alternative way to judge the compactness of a source is comparing the smallest time scale of interest with the maximum acoustic travel time between any two points on the source (*Stepanishen*, 1998, p. 122). This criterion will later be of interest when judging the compactness of a lava lake as explosion sound source. *Dowling and Williams* (1983, p. 50) show that non-compact sources are far more effective in radiating sound than compact sources – the compactness ratio is therefore also a measure of the sphere's ability to radiate sound by vibration.

Lighthill (1978, p. 23, 31*ff*) and *Stepanishen* (1998, p. 122) show that **compact** sources, even though being of a significant finite size, behave just like simple point sources if the observer is located clearly outside of the source radius, allowing the use of equations derived in Section 3.3. This property follows from the linearity of the sound potential (Eq. 3.22) and from the definition of a compact source, requiring that the sources' size is small compared to the main wave length.

Another consequence of the linearity of the sound potential is that the calculation of the sound field of a group of sources is possible by a simple addition of their individual source functions. If the group itself fulfills the compactness definition, and if the individual sources do not show systematic phase differences, then the resulting sound field at increasing distance from the source will soon evolve into the sound field of a simple source, the strength of which is simply the sum of the strengths of all individual source functions. The effectiveness of this process is controlled by the complexity of the group's geometrical shape. If the shape of the source group is significantly more complex than that of a sphere, then the simple-source character of the sound field only evolves at a large distance from the source, i.e. in the so-called **far-field** (*Lighthill*, 1978, p. 32).

The far-field of a monopole source is defined as the part of the medium that has a distance r to the source that is larger than a typical wave length divided by 2π (*Lighthill*, 1978, p. 22), i.e.

$$\frac{\omega r}{c_a} = \frac{2\pi r}{\lambda} \gg 1 \, . \tag{3.30}$$

This definition also follows from Equations 3.25 and 3.28, showing the volume and energy flux through a closed sphere around a source, both of which fluxes include a term that is dependent on the source distance. The terms that are dominant at large distances are called **far-field** terms, whereas the terms that are dominant at small distances are called **near-field** terms. For example, Equation 3.28 shows that in the near-field of a simple source the output of energy is varying with the **rate of change of the squared volume flow rate** (this change can be positive or negative), whereas in the far-field the energy output depends on the **squared volume acceleration** (which is always positive). Interestingly, the equation for the pressure field (Eq. 3.23) of a simple source (which is always compact) does not show any difference between near and far-field.

For pulsating spheres, *Temkin* (1981, p.274) finds an interesting relationship between the volume of the source and the approximate volume of the near-field V_{nf}:

$$V_{\mathrm{nf}} = V_{\mathrm{source}} \frac{3}{1 + (He)^2} \, . \tag{3.31}$$

This relation shows that for non-compact sources ($He \gg 1$) the near-field volume vanishes in comparison to the source volume, whereas for compact sources the near-field volume is about three times as large as the source volume. This behaviour can be explained by the near-field being defined as the region where the kinetic energy of the disturbed atmosphere plays a significant role, i.e. where energy is transported forth and back between the atmosphere and the source. Non-compact sources, due to their large surface area, will have significantly smaller surface accelerations and velocities compared to compact sources, so the kinetic energy of the atmosphere surrounding a non-compact source is considerably smaller, leading to a smaller near-field volume. *Junger* (1966) shows that the energy radiated away in the far-field is often of comparable size to the energy stored (or "trapped") in the near-field. This temporarily stored energy will eventually be given back to the source or it will be radiated away into the far-field in the final deceleration phase, just before the source comes to rest.

Compact or non-compact lava lake? Since the main object of interest in this study is the active Ray Lava Lake at Mt. Erebus volcano, it is necessary to analyse whether this object can be regarded as a compact source. The lava lake generates sound, mainly in the infrasonic spectrum, by displacing the surrounding atmosphere while bulging up in an explosion. This means that sound is almost exclusively generated on its surface, i.e processes below the surface do not play a significant direct role in sound generation as long as the surface (or bubble shell) is intact, which will be shown is often the case during the early moments of an explosion.

The lake had a radius of roughly 20 metres in 2005/06, and exploding bubbles more or less spanned the whole surface of the lake. The typical duration of the expansion phase of an explosion was around 0.5 s, so a main period of 1 s is a reasonable assumption for its sound output, leading to a typical wavelength of around 313 m (Sec 3.2). The Helmholtz number (Eq. 3.29), or the compactness ratio, calculates to $He \approx 0.4$ in this case, meaning that the source **cannot** be regarded as "non-compact". However, sources with such a compactness ratio (i.e. $He < 1$ but not $He \ll 1$) cannot generally be considered a compact source either, since the ratio, even though being smaller than 1, is still relatively close to unity. Therefore, a closer look is necessary to judge whether the assumption of a compact source is valid in this case.

The maximum travel path length of sound travelling between two arbitrary points on the surface of a bulging exploding bubble can be as high as πR_L, where R_L is the radius of the lava lake. Conservatively assuming that the true speed of sound in the vicinity of the lake is at least as high as the above calculated speed of sound in cold air (Eq. 3.16; Note that in the direct vicinity of the hot lava lake it could even be significantly higher, see Eq. A.2), the sound generated by a point at one side of the bubble travels during a time span smaller or equal to $\pi R_L/c \approx 0.2s$ to a point on the opposite side. This means that an impulsive signal emerging from all points of the bubble surface at the same time will be smeared (blurred) over a time span of up to 0.2 s when being recorded from the side. At Erebus, all infrasonic receivers are located on the crater rim (*Jones et al.*, 2008; *Johnson et al.*, 2008) and beyond, so the sound path is not horizontal but sloping at an elevation angle ϕ_R of around 39° to the horizontal (see Section 4.1.2), leading to a maximum effective time delay of $\Delta t \approx 0.1s$ between signals emerging from the far and the near side of the lake.

This delay amounts to only around 10% of the 1 s wave period in question, thus the lava lake can, when "loosely interpreting" the original definition, still be regarded as a compact source. However, since the sample rate of infrasonic microphones located at and around Erebus crater rim in 2005/06 was around 40 samples per second (*Jones et al.*, 2008), a delay of 0.1 s means that impulsive signals from the lake are, in the worst case, smeared over four samples. Later in this study, Doppler radar signals will be used to compute an expected infrasound trace, which is then compared to real infrasound recordings. For this comparison it is necessary to keep the "smearing effect" in mind. The lava lake can therefore only be regarded as an "almost compact" source in this case. However, for other applications this assumption might not be valid, so care must be taken to repeat these considerations in the case of a modified setup.

Even though the Ray Lava Lake of Mt. Erebus can be assumed to be a compact source of sound under some circumstances, it is still necessary to determine whether near-field terms will have to be considered when calculating the energy output or the velocity field. As shown above, a typical wavelength of the Erebus system is around 313 m, and the closest infrasound receiver microphone is installed at RAY site at a distance of 310 m from the lake centre (*Jones et al.*, 2008). The above ratio (Eq. 3.30) is therefore ≈ 6.2, which is significantly larger than the reference value of 1. The velocity field at the RAY microphone can therefore be considered not a perfect but a fair representation of a velocity far-field. This is in agreement with Equation 3.31, which states that at Erebus the volume of the near-field should be about 2.6 times as large as the volume of the source - the closest microphone is well outside that volume. Yet care must be taken to keep the existence of a near-field in mind.

In Section 4.2.7 an attempt will be made to calculate the sound energy output of an exploding bubble from Ray Lava Lake, i.e. the sound energy emitted from the surface of an expanding bubble through an imaginary control surface close to the bubble. Exploding bubbles at Erebus usually reach radii similar to the lake radius of around 20 m, so the radius of the control surface should be set to a similar value. Equation 3.30 yields a ratio of ≈ 0.4 for this radius, clearly signaling that near-field terms will not be negligible at such distances from the source. Thus, for the calculation of the energy output right at the source, the full Equation 3.28 must be used.

3.5 The lava lake - a simple dipole sound source?

Up to this point only monopole sources have been considered in the study, i.e. sources that vary their volume only isotropically while their their location remains fixed. Yet another important source configuration is an acoustic dipole, which is generated when the source changes its location instead of its net volume, e.g. by an oscillating rigid sphere or by a baffled piston moving in and out of a rigid wall. Dipoles have a characteristic emission pattern that shows a strong directivity, i.e. it mainly radiates sound along its axis of symmetry, the **dipole axis**, while almost no sound is radiated into perpendicular directions. It can be

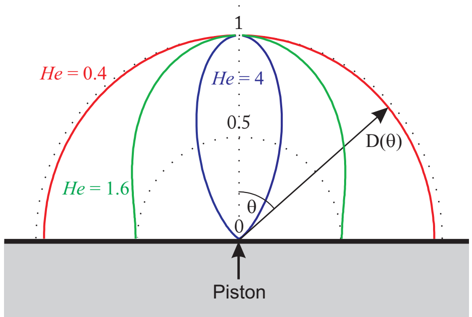

***Figure 3.1:* Sound field directivity $D(\theta)$ of a baffled piston** *with different compactness ratios ($He = 0.4, 1.6, 4.0$). While a piston of compactness 0.4 has an almost isotropic radiation pattern, a piston of compactness 4 shows a strongly directional emission pattern. Note that the active Ray Lava Lake of Mt. Erebus, which resembles a vertically moving piston during the first moments of an explosion, has a compactness ratio of around 0.4 at frequencies of around 1 Hz. Its radiation pattern at these frequencies can therefore be considered as near isotropic, i.e. acting like a monopole. At frequencies of 4 Hz, however, its compactness ratio is around 1.6, leading to a significant directivity. At even higher frequencies the radiation pattern of the lava lake resembles more and more that of a pure dipole.*

argued that the subject of this study, i.e. bubble explosions on lava lakes, are a good manifestation of a volume source and therefore a good representation of a monopole. However, during their first fractions of a second, explosions at Erebus do not resemble a spherical source very well, they rather resemble a piston shooting out of the ground (as will be shown in Section 4.1). It might therefore be argued that a dipole could be the better representation of the source configuration during the first moments of an explosion. And indeed for some compactness ratios (He) of a baffled piston the sound intensity vector can be a strong function of the observation angle. It is therefore necessary to have a closer look at the geometry of interest.

The directional factor of the sound intensity emission pattern of a dipole is the main difference[4] to the sound emission pattern of a monopole (*Stepanishen*, 1998, p. 123). It is given by (*Dowling*, 1998, p. 112):

$$D(\theta) = \left| \frac{2J_1(He\ \sin\theta)}{He\ \sin\theta} \right|^2 \tag{3.32}$$

where $J_1(...)$ denotes a Bessel function (*Abramowitz and Stegun*, 1965), which can be approximated by $J_1(x) \approx 1/4(sin\,x + \sqrt{2}sin(x/\sqrt{2}))$ with an error $< 5\%$ for $x < 4.5$. For example, for a non-compact piston with $He = 4.0$ the ratio between the acoustic intensity radiated in direction of the piston axis ($\theta = 0$) and the intensity radiated perpendicular to it ($\theta = \pi/2$) is indeed very large ($\approx$ 1000; see Fig. 3.1). This means that in this case, a thousand times more energy is emitted along the piston axis than perpendicular to it. However, Figure 3.1 shows

[4]in case of a piston that is placed at the boundary between a solid half space and the atmosphere, the pressure and velocity values have to be doubled, similar to a monopole source placed at such an interface (see end of Sec. 3.3 and *Dowling*, 1998, p. 112)

that at Erebus, with a source compactness of $He \approx 0.4$ at 1 Hz (see Sec. 3.4), the radiation pattern is almost isotropic. In this frequency range the lava lake acts like a monopole source even when it is still flat during the first moments of an explosion. Only at higher frequencies the compactness ratio increases sufficiently ($He \approx 1.6$ at 4 Hz, see Eq. 3.29) to produce a directional radiation pattern (Fig. 3.1). It is therefore justified to regard the lava lake as a monopole source even when the surface is flat during the first moments of an explosion.

3.6 Calculating sound fields of complex bodies via Green's Functions

In Section 3.3 it was shown that a sound source of a simple geometry generates a sound field that can be described analytically in a very simple way. Section 3.4 shows that even in the case of a more complex and continuous source geometry the resulting sound field can be comparatively simple if certain conditions are fulfilled (regarding the compactness of the source, and the observer's distance in comparison to the wavelength). Since these conditions are only partially fulfilled by the objects that are of interest in this study, the question still arises whether there are analytical solutions for complex source geometries when these conditions are not fulfilled. An analytical method to calculate the sound field of a non-compact **pulsating** sphere can be found (*Temkin*, 1981, p. 209), demonstrating the additional properties of such a sound field in comparison to the sound field of a simple source. While this method works for a pulsating sphere, it fails for more complex objects, e.g. like a bulging lava lake. Yet, *Stepanishen* (1998, p. 122) and *Ehrenfried* (2003, p. 156) show that it is still possible in such a case to derive an analytical solution using so-called **Green's functions**, due to the linear nature of sound fields (or, to turn the argument around, the linear nature of the sound field is – as in the above sections – a necessity for this method to work). This method will later be adopted for calculating the sound output of explosions from Erebus' Ray Lava Lake (Sec. 4.5, *non-compact case*)

A Green's function is the system's response to an impulse-like disturbance at a certain point of the medium. In linear systems this principle allows the calculation of the response to continuous and complex source geometries by integrating over the source function multiplied with the Green's function of the medium, just as if the source consists of an infinite number of small point sources at different locations resembling the geometry of the real source. In this case the wave fields generated by every single point source simply add up to form the resulting wave field, consistent with **Huygens's principle** (*Baker and Copson*, 1953).

$$\Phi_A(\vec{x}, t) = \int_V \int_{-\infty}^{+\infty} G(\vec{x}, t, \vec{x'}, \tau)\; s(\vec{x'}, \tau)\; d\tau\; d^3\vec{x'} \tag{3.33}$$

where

$$G(\vec{x}, t, \vec{x'}, \tau) = \frac{\delta(t - |\vec{x} - \vec{x'}|/c - \tau)}{4\pi|\vec{x} - \vec{x'}|} \tag{3.34}$$

is called **Green's function**, containing a Dirac-δ-impulse as a point-like disturbance of the acoustic medium. Similar to Equation 3.22 it includes the retarded time and a geometrical spreading term resembling $\frac{1}{4\pi r}$. $s(\vec{x'}, \tau)$ is the (now continuous) distribution of the source strength (see also Eq. 3.22) in space $\vec{x'}$ and time τ. The integration volume V must, of course, fully enclose the source. The resulting function $\Phi_A(\vec{x}, t)$ is again a solution to the inhomogeneous wave equation, as is G itself:

$$\left(\frac{1}{c^2} \frac{\partial}{\partial t^2} - \Delta \right) \Phi_A = s(\vec{x}, t) \tag{3.35}$$

Since the simple Green's function above does not yet include any information about possible further boundary conditions of the wave field (e.g. foreign bodies in the wave field, or structural boundaries), the result is only valid in an infinite open space (*Ehrenfried*, 2003, p. 156). For example, the Green's function for a planar problem like a baffled piston in a rigid wall (see end of Sec. 3.3, and Sec 3.5) is exactly twice the Green's function for a point source in open space (Eq. 3.34), i.e. it is $2G$ (*Stepanishen*, 1998, p. 123).

This very powerful method is not only used in the field of acoustics, but is widely used in the frame of potential theory in most fields of physics and geophysics, including seismology.

CHAPTER 4

DEVELOPING A THEORETICAL MODEL OF AN EXPLODING MAGMA BUBBLE

From simply looking at raw data, not much can be learnt about the nature of volcanic eruptions. Since there is no instrument that can directly tell us the pressure inside an exploding gas bubble, or the energy of an accelerating piece of magma, we need to find a method of how to combine the data that can be collected from a safe distance, so that it leads to trustworthy conclusions on the parameters in question.

One way to accomplish this is to develop a model of the process that includes all significant physical properties of the system that are contributing to the real process. Knowing that every model of less complexity than the true natural system is only an approximation, it is important to optimise this approximation by choosing the right level of model complexity. Of course, a model that is too simple will not be able to describe the process in the necessary complexity to make useful predictions about the real process. On the other hand, a model that has too many parameters cannot be constrained by the available data, leaving undetermined parameters and therefore ambiguities in the model's predictions.

Assuming that a model with the right amount of complexity exists that is a fair description of the real process occurring in a volcano, it can be constrained with the available data. Ideally, the model thereby allows predictions to be made on the other, not directly observable parameters of interest. Additionally, comparing the model's predictions with complementary observations provides information about the correctness of the model itself, therefore improving the knowledge of the underlying mechanism.

In this chapter I will develop a geometrical model describing the expansion of a pressurised gas bubble under the surface of a liquid lava lake - a process that is commonly believed to occur during Strombolian eruptions at Erebus volcano. The purpose of this model is **not** a complete simulation of the process (such as, e.g., the definition of some starting conditions and the subsequent simulation of the explosion). This is not necessary because the available Doppler radar data gives us ongoing information about the state of the system during the explosion. Therefore, the chosen model only describes the geometry of the process, which can then be constrained by the radar data. This provides us with knowledge – within the exactness of our model – about the current state of the system, such as

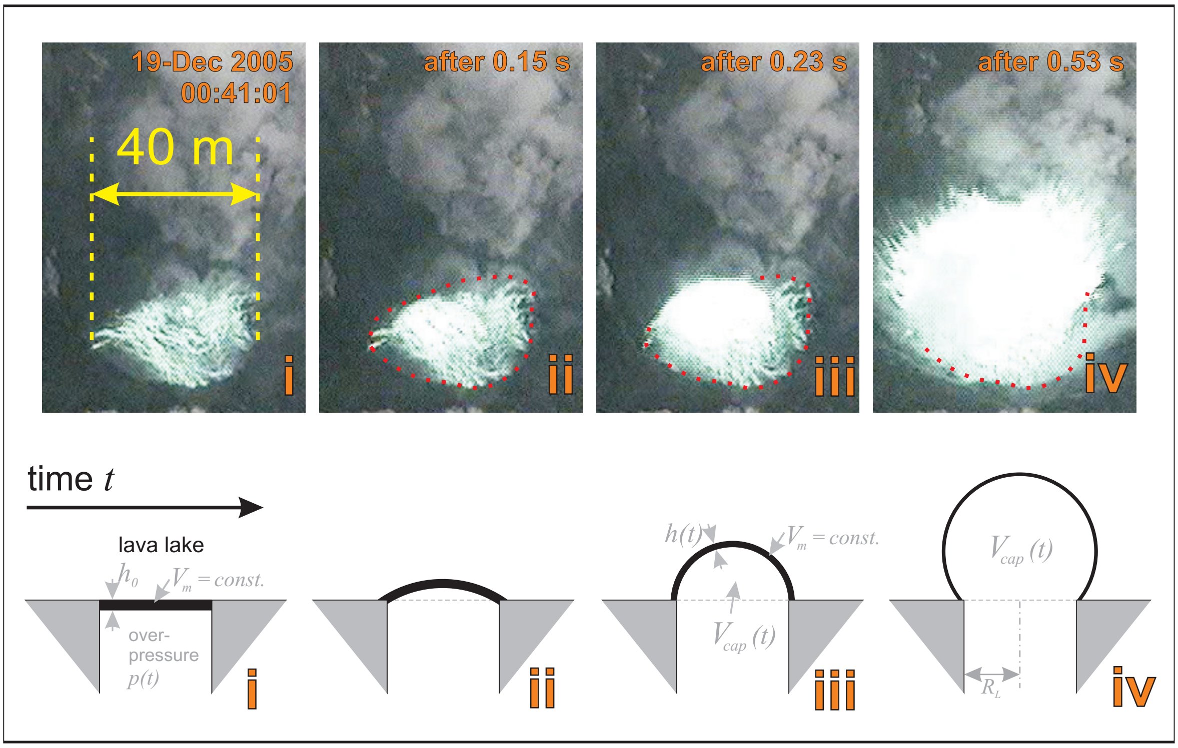

Figure 4.1:* Bubble model.** ***Top: *Thermal video sequence of a typical bubble burst from Ray Lava Lake on Erebus volcano. Shell rupture typically occurs between phase iii and iv.* ***Bottom:*** *Bubble model sketch (side view). The black area is a magma shell of constant volume V_m, spanning up a dome-shaped bubble cap with a total volume $V_{\text{cap}}(t)$. Beneath and inside the cap, hot magmatic gas of overpressure $p(t)$ expands, pushing up and stretching the shell. Due to the expanding area of the shell, its thickness $h(t)$ constantly decreases with time. The shape of the cap is always a section of a sphere, and its edge is tied to the lake edge, a horizontal circle with radius R_L.*

the position or the speed of the magma shell. From these properties I will then calculate the parameters of interest, such as energies, gas pressures, gas volumes, or even the predicted infrasonic signal recorded at distance.

4.1 Geometrical model: an expanding magma shell

For the model of an expanding bubble, several geometries can be assumed, which all must more or less represent the observed shape of a real exploding bubble on the surface of a lava lake. One possible representation of this natural shape is the assumption of an expanding hemispherical shell, which can be considered a fair first-order representation of the true geometry (Sec 1.2). Such a shape has the attractive property of a spherical geometry, and most of its equations can therefore be solved analytically. However, this model has one major flaw: during the start of an explosion (i.e. at the moment when the lava lake surface initially starts to bulge up) the lake's shape is far from hemispherical (e.g. Fig. 1.3). Since the start of an explosion is a very important moment for calculating the parameters of interest, such a model is not suitable for our task.

A suitable model must describe the flat lake surface during the start of an explosion as well as the bulging during later phases of an explosion. Ideally, it does not have any free parameters other than the ones that can either be observed or estimated by the distant observer, i.e. from the crater rim.

4.1.1 Model geometry

The model that I have chosen for this study starts out with a flat sheet of magma forming the surface of the lava lake at the time just before the initial movement of its surface. This sheet represents the material between the approaching hot magmatic gas slug (with a pressure p) and the lake surface. In the model it is approximated by a uniform, relatively thin layer of liquid magma of a thickness h_0 much smaller than the lake radius R_L (Fig. 4.1 i). During an explosion, this shell is pushed up and flexed outward by the expanding gas, just like a round membrane that is attached to the edge of the lake (Fig. 4.1 ii-iv). The shape of this sheet, or shell, is always represented as a section of the surface of a sphere, with the boundary condition that there is no movement at the edges of the lake (i.e. the lake shore is a "hinge"). Figure 4.1 shows that this model is a good representation of the true surface geometry developing during an explosion. In reality, the bubble typically bursts somewhere between phase iii and iv.

The total magma volume V_m contained in the shell is assumed to be constant during the rapid expansion phase of the explosion, because once this phase has started, the loss of material from the shell is negligible due to magma viscosity hindering drainage from the shell. The volume that is encompassed by the doming shell is called V_{cap}, and is assumed to contain hot magmatic gas. During the expansion phase the shell expands its area while thinning out to preserve its total mass and magma volume. The absolute position and shape of the shell at any given time can be described with the single parameter H(t), representing the height of the zenith point of the shell above the initial undisturbed lake level (Fig. 4.2).

I consider this model geometry as a good representation of the true geometry based on video observations of numerous explosions at Erebus (see Figs. 1.3 & 6.2, or videos in the supporting online material, *SOM*). It also fits well to geometries of expanding and bursting bubbles on smaller scales, such as laboratory experiments, e.g. *James et al.* (2004, Fig. 6b), and volcanic mud bubbles (Fig. 1.4). The model is deliberately kept very simple to avoid ambiguities introduced by the guessing and fitting of parameters. The only significant parameters that influence this model are the lake radius and the total mass of the ejected material, both of which can be estimated by an observer on the crater rim.

The position Z of the geometrical centre of the spherical shell section lies beneath the undisturbed lake level surface during the early stages of an explosion, but will eventually move up and cross this plane at some stage. This leads to two geometrical situations that

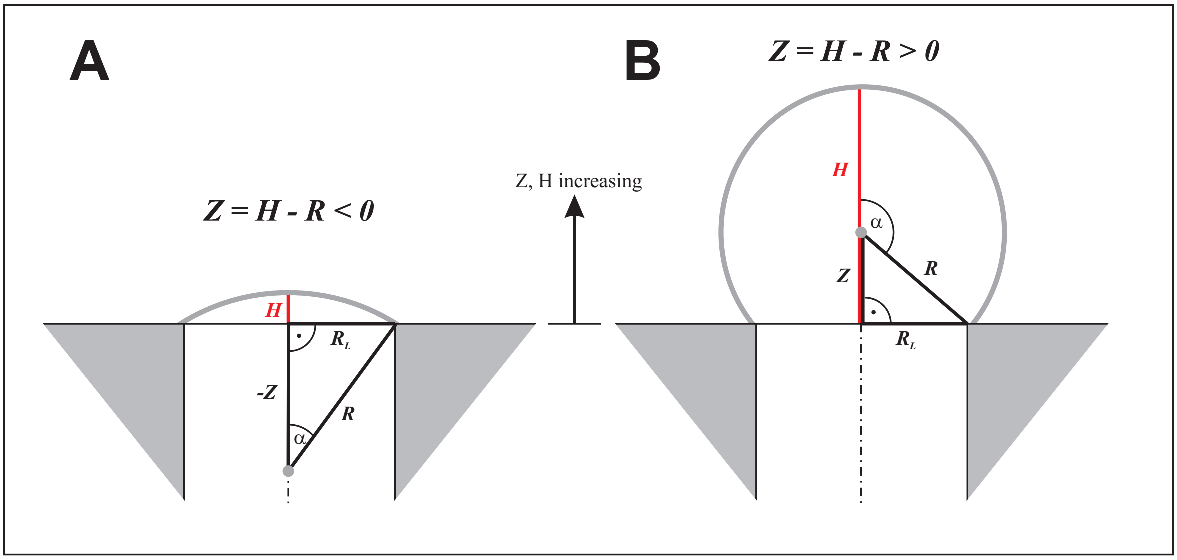

Figure 4.2: ***Model geometry of the expanding gas bubble.***

need to be distinguished (Fig. 4.2 A and B), so care must be taken not to introduce inconsistencies when moving from geometry A ($Z < 0$) to geometry B ($Z > 0$). The following parameter relations are valid for all Z:

$$Z = H - R \tag{4.1}$$

$$R = \frac{H}{2} + \frac{R_L^2}{2H} \tag{4.2}$$

$$\alpha = \arccos\left(\frac{R-H}{R}\right) \tag{4.3}$$

$$H = \begin{cases} R + \sqrt{R^2 - R_L^2} & : \quad Z \geq 0 \\ R - \sqrt{R^2 - R_L^2} & : \quad Z < 0 \end{cases} \tag{4.4}$$

where R is the shell radius and α is the opening angle of the shell cap (Fig. 4.2). It is always equal to, or larger than the lake radius ($R \geq R_L$; $H \geq 0$).

The volume V_{cap} surrounded by the shell and the outside surface area A_{cap} of the spherical cap are

$$V_{\text{cap}} = H^2\pi\left(R - \frac{H}{3}\right) = \frac{\pi}{6}H^3 + \frac{\pi R_L^2}{2}H \tag{4.5}$$

$$A_{\text{cap}} = 2\pi R^2 (1 - \cos\alpha) = 2\pi RH = \pi \left(H^2 + R_L^2\right) \tag{4.6}$$

V_{cap}, which increases during an explosion, should not be confused with V_m (Fig. 4.1), which is the **constant** volume of the magma in the cap shell, i.e.

$$V_m = \frac{m_m}{\rho_m} \approx h\, A_{\text{cap}} \tag{4.7}$$

where m_m is the total mass of the magma in the shell, and ρ_m is its density. The magma volume can be approximated by the product of the shell thickness h and its surface area A_{cap} because the shell thickness is always much smaller than the bubble radius ($h \ll R_L \leq R$).

As the bubble geometry is changing in time, the above parameters (H, R, V_{cap}, h) are functions of time, therefore their time derivatives can be calculated:

$$\dot{R} = \dot{H}\left(\frac{1}{2} - \frac{R_L^2}{2H^2}\right) \tag{4.8}$$

$$\dot{H} = \dot{R}\left(1 + \frac{R(t)}{H - R}\right) \tag{4.9}$$

$$\dot{V}_{\text{cap}} = \frac{\pi}{2}\dot{H}\left(H^2 + R_L^2\right) \tag{4.10}$$

In the following sections, the Zenith height $H(t)$ and its time derivatives $\dot{H}(t)$, $\ddot{H}(t)$ shall be the main parameter describing the bubble geometry and movement, therefore R and Z can be eliminated from all final equations.

Some of the following equations (e.g. for calculating the total kinetic energy of the cap) will require integrations over the whole volume of the magma shell (i.e. the constant volume of magma V_m in the shell[1]). In order to facilitate these integrals by making use of the special symmetry of the geometrical shape, we will introduce a parameter $q \in [0 \ldots 1]$, where $q = 0$ defines the zenith of the cap, and $q = 1$ defines the edge of the cap (Fig. 4.3). As a requirement, q shall be a linear measure of the volume of liquid material enclosed in a shell segment (i.e. V_1 in Fig. 4.3) along the cap surface, starting from the zenith point (enclosing a volume of zero) and increasing towards the edge (enclosing the full cap volume). Therefore, the following assumption must be fulfilled:

$$q = \frac{V_1}{V_m} = \frac{V_1}{V_1 + V_2} = \frac{A_1}{A_1 + A_2} \tag{4.11}$$

where V_1 is the cap volume enclosed by a circle defined by q, V_2 is the remaining volume,

[1] i.e. **not** the total (gas) volume surrounded by the cap V_{cap}.

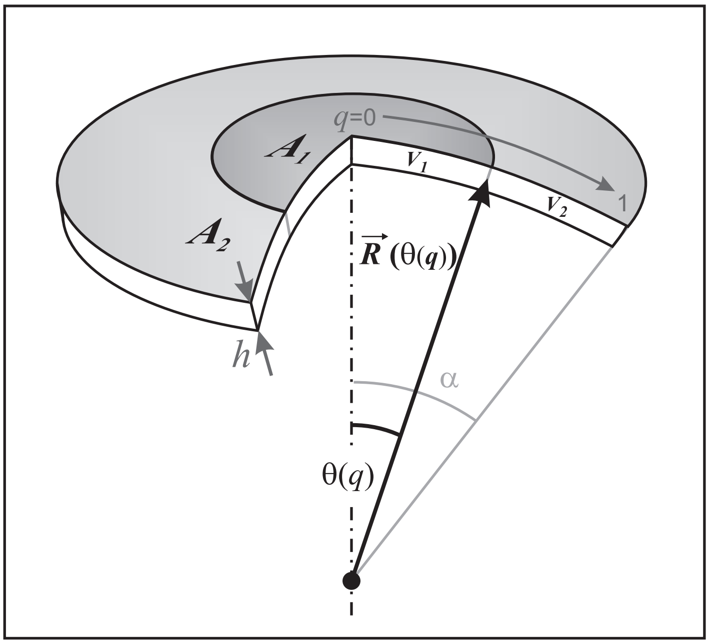

Figure 4.3: Model parametrisation geometry. *The model parameter q increases linearly with the enclosed shell volume V_1.*

and $V_m = V_1 + V_2$ is the total volume of the magma shell (Eq. 4.7). A_1 and A_2 are the upper surface areas of shell sections V_1 and V_2. Since the thickness $h(t)$ is small compared to the lake radius R_L, the volumes can be approximated as $V_i \approx h\ A_i$ (see Eq. 4.7). The surface areas are given by

$$A_1(q) = \int_{A_1} dA = \int_0^{2\pi} \int_0^{\theta(q)} R^2 \sin\theta'\ d\theta' d\Phi = 2\pi R^2(1 - \cos\theta(q)) \tag{4.12}$$

$$A_{\text{cap}} = A_1 + A_2 = 2\pi R^2(1 - \cos\alpha) \tag{4.13}$$

where θ is the angle between $\vec{R}$ and the vertical. Therefore, with Eq. 4.3 and 4.11

$$q(\theta) = \frac{1 - \cos\theta}{1 - \cos\alpha} = \frac{R}{H}(1 - \cos\theta) \tag{4.14}$$

or

$$\theta(q) = \arccos\left(1 - \frac{qH}{R}\right) \tag{4.15}$$

The volume form dV for integrals over a thin shell with thickness $h \ll R$ can be transferred if the function to be integrated is not a function of azimuth Φ. Using Equation 4.11

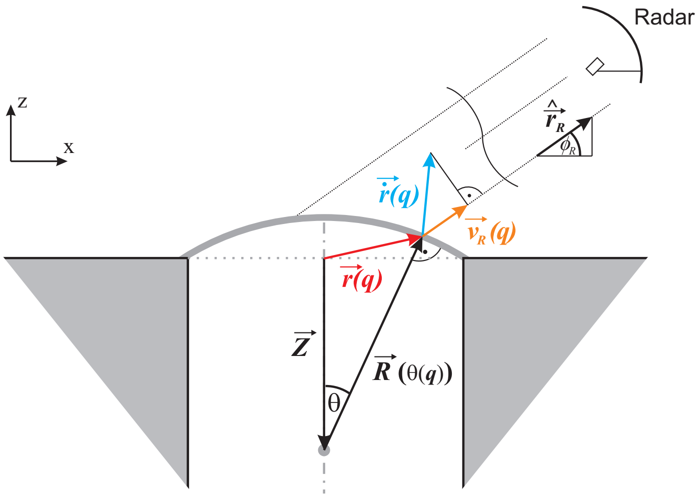

Figure 4.4: *Radar view angle geometry*

(where $V(q) = V_1 = qV_m$), dV can be replaced by

$$dV = V_m \, dq \tag{4.16}$$

This is also evident from the following consideration: in a general spherical geometry the volume form is defined as $dV = r^2 \sin\theta dr \, d\Phi \, d\theta$, which reduces to $dV = 2\pi R^2 h \sin\theta \, d\theta$ for $h \ll R$ and if the function to be integrated is not a function of Φ. h can be replaced by $h = \frac{V_m}{A_{\text{cap}}}$ as given by Equation 4.7, therefore leaving $dV = \frac{RV_m}{H} \sin\theta \, d\theta$. From Eq. 4.14 follows that $dq = \frac{R}{H} \sin\theta \, d\theta$. Combining these two statements, we are left with $dV = V_m \, dq$.

With this parameter q, any given point in the (x,z) plane can now be defined in the form $\vec{r} = \vec{r}(q)$, where $q \in [0 \ldots 1]$ (Fig. 4.3). Due to the cylindrical symmetry we can use two-component vectors of the form $\vec{r} = \binom{r_x}{r_z}$. As shown in Figure 4.4, $\vec{r}(q)$ can be written as

$$\begin{aligned} \vec{r}(q) &= \begin{pmatrix} r_x \\ r_z \end{pmatrix} = \vec{Z} + \vec{R}(\theta(q)) \\ &= \begin{pmatrix} 0 \\ Z \end{pmatrix} + \begin{pmatrix} R\sin\theta(q) \\ R\cos\theta(q) \end{pmatrix} \end{aligned} \tag{4.17}$$

using Equations 4.15 and 4.1 eventually leads to

$$\vec{r}(q) = \begin{pmatrix} \sqrt{qH^2(1-q) + qR_L^2} \\ H(1-q) \end{pmatrix} \tag{4.18}$$

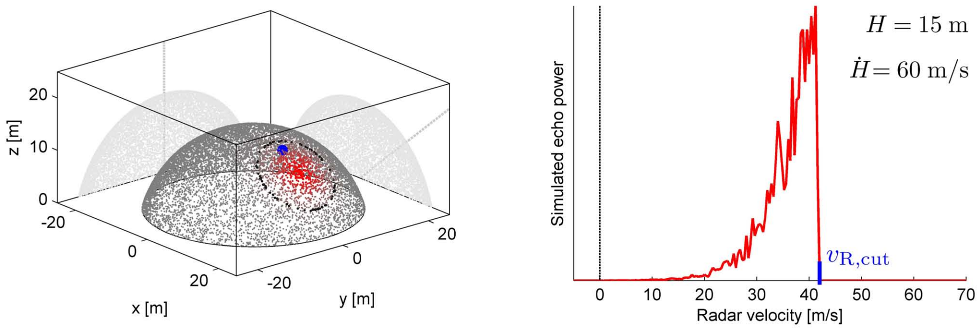

Figure 4.5: Simulated velocity spectrum of an expanding bubble. Left: *surface of a 15 m high bubble, expanding with a zenith velocity of 60 m/s, approximated by randomly located surface reflectors (dots). The red area is illuminated by the radar beam, fading away from the beam centre according to the antenna gain pattern (Appendix Fig. A.1). The black line marks where the radar's sensitivity reaches -10 dB, i.e. where the receivable echo power has fallen to 1/10 of that in the beam centre. The blue dot is the point on the bubble surface moving fastest towards the radar. Projections of the beam's centre axis are indicated as dotted lines on the box walls. The radar's look angle and distance (39° elev., 300 m) were chosen to resemble the geometry at Erebus volcano.* ***Right:*** *Resulting simulated radar spectrum. A typical feature is the distinct cutoff velocity $v_{\mathrm{R,cut}}$ on the right side of the spectrum, caused by the bubble's curved surface. It shows the radar velocity of the blue dot on the left.*

and its time derivative $\dot{\vec{r}}(q)$, giving the surface velocity of the cap at point $\vec{r}(q)$:

$$\dot{\vec{r}}(q) = \begin{pmatrix} \frac{qH\dot{H}(1-q)}{\sqrt{qH^2(1-q)+qR_L^2}} \\ \dot{H}(1-q) \end{pmatrix} \tag{4.19}$$

4.1.2 View from the radar's perspective

For the processing of radar data in this experiment, it is necessary to describe the movement of the cap in its native parameters $H(t)$, $\dot{H}(t)$ and $\ddot{H}(t)$, derived from the measured radar velocities. It is therefore necessary to establish a unique relation between an observable feature in the radar spectrum and the movement of the cap. As shown in Section 1.5, the radar only measures the component of the observed object that is pointing towards the radar, i.e. the beam-parallel velocity component. Moreover, in the used setup the radar will not only measure one single object in the radar beam, but it will observe all surface points on the magma cap that are inside the beam, and sum up all their echoes in one velocity spectrum (Fig. 4.5).

Figure 4.5 (right) shows the simulation of such a spectrum at an arbitrary time during an assumed bubble explosion (similar to Fig. 1.8 shown in the introduction). This was achieved by simulating 10,000 random reflectors on the surface of the bubble (Fig. 4.5 left, grey dots), which is assumed to expand with a zenith velocity $\dot{H}$ of 60 m/s. Every moving reflector has a certain speed component in radar direction, and a weighting, depending on its projected surface area as seen from the radar. Adding up the contribution of every reflector that is located inside the radar beam (red dots) leads to the expected radar velocity spectrum (right).

Figure 4.5 illustrates that a single radar spectrum merges information about a significantly large area of the bubble surface. It is therefore generally difficult to attribute a single observed feature in the radar velocity spectrum (e.g. a peak at a certain velocity) to its respective surface point on the magma cap. One possibility is to determine the mean (or median) velocities of the spectrum and compare them to the expected mean velocities predicted by the model. However, this mean velocity would be strongly dependent on the actual area of the bubble that is observed by the radar[2], and therefore on the distance between radar and bubble, given that the conical radar beam has a fixed opening angle. When comparing data from different radars at different distances, or if the aim of a radar onto the bubble is only slightly misaligned, then using mean or median velocities would introduce a significant systematic error.

Yet there is one prominent feature in the spectrum that can be easily traced, which is practically independent of observation distance, and which additionally is relatively insensitive towards a misalignment of the radar aim. It is the abrupt cutoff of echo power at its maximum velocity (Fig. 4.5), caused by the bubble's round surface moving coherently towards the radar. The peak just before the cutoff represents the radar velocity of the surface region moving fastest towards the radar.

This distinctive *cutoff velocity* ($v_{\mathrm{R,cut}}$) is equal to the *maximum velocity* of the spectrum (i.e. the maximum velocity at which there is significant echo power), as long as the object in the radar beam is an **intact bubble surface**. It can easily be identified in a spectrum, and can also be attributed to a unique point on the cap surface, i.e. the point on the surface that moves fastest towards the radar. Therefore, calculating the velocity of this point in the bubble model will provide the necessary relation between the model ($H(t)$, $\dot{H}(t)$) and the data ($v_{\mathrm{R,cut}}(t)$).

I will now determine this cutoff velocity from model parameters. First it is necessary to calculate the velocity component of a given surface point $\vec{r}(q)$ as seen from the radar. I define a unit vector

$$\hat{\vec{r}}_R = \begin{pmatrix} \hat{r}_{R,x} \\ \hat{r}_{R,z} \end{pmatrix} = \begin{pmatrix} \cos\phi_R \\ \sin\phi_R \end{pmatrix} \tag{4.20}$$

pointing from the source (i.e. the magma cap) towards the radar. Because the beam spread is only $\sim \pm 2°$ and the distance to the radar device (≈ 300 m) is significantly larger than the

[2]If the illuminated area gets larger, more lateral parts of the bubble become illuminated, which move almost perpendicular to the radar beam and therefore have smaller radar velocities. This adds echo power to mainly the lower velocities in the spectrum, therefore dragging the mean velocity down.

target region we consider this unit vector to be constant within the target region. ϕ_R is the elevation angle (inclination) of the radar as seen from the source (Figure 4.4). At Erebus, this angle is $\sim 39°$ for the fast radar located at RAY. The speed of surface point $\vec{r}$ as measured by the radar is simply the projection of $\dot{\vec{r}}$ onto the unit vector pointing in radar direction:

$$v_R(q) = \dot{\vec{r}}(q) \cdot \hat{\vec{r}}_R = \begin{pmatrix} \dot{r}_x(q) \\ \dot{r}_z(q) \end{pmatrix} \cdot \begin{pmatrix} \cos\phi_R \\ \sin\phi_R \end{pmatrix} \tag{4.21}$$

$$= \dot{H} \underbrace{\left(\frac{qH(1-q)\cos\phi_R}{\sqrt{qH^2(1-q)+qR_L^2}} + (1-q)\sin\phi_R \right)}_{Q} \tag{4.22}$$

As argued above, the cutoff velocity in the radar spectrum $v_{\mathrm{R,cut}}$ is the maximum of $v_R(q)$ with respect to q:

$$v_{\mathrm{R,cut}} = \dot{H} \max_{q \in q_0, q_1} \Big(Q(q, H) \Big) \tag{4.23}$$

where $[q_0 \ldots q_1]$ defines the area of the cap that is observed by the radar beam. If the radar beam covers the whole area between zenith and cap edge, then q is allowed to vary over its whole range $[0 \ldots 1]$ (Fig. 4.3). By reversing this equation, the zenith velocity $\dot{H}(t)$ at time t can be determined from $v_{\mathrm{R,cut}}(t)$:

$$\dot{H}(t) = \frac{v_{\mathrm{R,cut}}(t)}{\max\limits_{q \in q_0, q_1} \Big(Q(q, H(t)) \Big)} \tag{4.24}$$

This equation establishes a way to determine the cap velocity directly from radar observations, since the starting value of H is known during every explosion, i.e. it is zero. Using this initial value for H, $\dot{H}$ can be calculated from the cutoff velocity $v_{\mathrm{R,cut}}$. The correct value of H for the next time step can then easily be estimated by integrating $\dot{H}$ over time, and eventually the whole time series of H and $\dot{H}$ can be determined by this iterative process.

4.2 Explosion energies

The aim of this section is to develop an equation for each of the energy types that are involved in an explosion. These separate types of energy can later be added to form the total energy balance of an eruption.

It is the gas internal energy contained in a rising and expanding bubble that drives its final explosion. During the explosion, energy is transferred into various different energy types, all connected to the expanding magma cap. The most significant of these energy types are the cap's kinetic energy, its potential energy in Earth's gravity field, the energy dissipated in the viscous cap, its surface energy, the sound energy emitted into the atmosphere, the seismic energy radiated into the ground, and, somewhat separately, the thermal energy carried by the hot magma.

In the following subsections, I will derive these energy types in detail for the bubble expansion model presented above. I will present each energy type as a function of parameters that can be directly measured by radar (i.e. bubble zenith height H, as derived from radar velocities; Sec. 4.1) and of model parameters that can be estimated (e.g. lake radius R_L and magma shell mass m_m). While some typical features and dependencies of these energy types will be discussed here, they will not be quantified at this point. In Chapter 6 I will provide a detailed and quantified discussion of the data, including all involved energy types and their uncertainties.

4.2.1 Energy balance

When adding up all dynamic types of energy that are involved in an explosion, including the energy in the reservoir that is driving the eruption (i.e. the gas internal energy), the law of the conservation of energy states that this sum must be zero at all times:

$$-W_{\text{gas}} + E_{\text{kin}} + E_{\text{pot}} + E_{\text{diss}} + E_{\text{surf}} + E_{\text{atm}} + E_{\text{seis}} = 0 \tag{4.25}$$

where the indices 'gas', 'kin', 'pot', 'diss', 'surf', 'atm' and 'seis' refer to the energy types of gas internal energy, kinetic energy, potential energy, dissipated energy, surface energy, emitted sound energy, and seismic energy, respectively (Sec. 4.2). An additional but somewhat separate type of energy is the thermal energy contained in the magma cap. This type of energy is not powered by the internal gas energy but is passively carried by the hot ejecta. Since radiative and convective cooling processes are negligible within the time frame of an explosion, thermal energy can be considered as constant during this time, and therefore does not enter the above equation. However, as will be shown later, even though thermal energy does not show up in the dynamic energy balance (Eq. 4.25), it must be included when calculating the total energy output of an explosion, since it is by far the biggest energy transport mechanism.

The following equation shows the amount of energy that is freed from the expanding gas between the start of an explosion and time t, plus the thermal energy. At the end of an explosion, this value can be considered as the **total energy output** of the explosion.

$$E_{\text{total}}(t) = E_{\text{kin}}(t) + E_{\text{pot}}(t) + E_{\text{diss}}(t) + E_{\text{surf}}(t) + E_{\text{atm}}(t) + E_{\text{seis}}(t) + E_{\text{therm}} \tag{4.26}$$

Differentiating this equation with respect to time yields the total power output at any given time t during an explosion (i.e. $P = \frac{d}{dt}E = \dot{E}$):

$$P_{\text{total}}(t) = P_{\text{kin}}(t) + P_{\text{pot}}(t) + P_{\text{diss}}(t) + P_{\text{surf}}(t) + P_{\text{atm}}(t) + P_{\text{seis}}(t) \tag{4.27}$$

4.2.2 Pressure volume work W_{gas}

When gas expands without the addition of external heat, the first law of thermodynamics states that the performed expansion work relates to the gas' internal energy U_{gas} as follows:

$$dW_{\text{gas}} = -dU_{\text{gas}} \tag{4.28}$$

This assumption of an *adiabatic process* is valid in the case of a rapid process such as a bubble burst, since no significant amount of heat will leave the gas in the timescales involved. Chemical thermodynamics finds that the amount of pressure-volume work is given by

$$dW_{\text{gas}} = p_{\text{gas}}\, dV_{\text{gas}} \tag{4.29}$$

which, due to its differential nature, is generally true. Here, p_{gas} is the current gas **overpressure** inside the bubble (i.e. in excess of the surrounding atmospheric pressure), the absolute pressure of the gas is therefore $\hat{p}_{\text{gas}} = p_{\text{gas}} + p_{\text{atm}}$. V_{gas} is the total gas volume in the bubble (i.e. contained inside the cap and the slug tail, see also Fig. 4.6). Please note that when integrating this formula to gain absolute energy values, the type of expansion (i.e. $p_{\text{gas}} = p_{\text{gas}}(V_{\text{gas}})$) has to be considered. As a time derivative, the above formula can be expressed as

$$\dot{W}_{\text{gas}} = p_{\text{gas}}\, \dot{V}_{\text{gas}}, \tag{4.30}$$

Even though V_{gas} is, due to the slug tail inside the conduit, significantly larger than V_{cap} (Fig. 4.1), their time derivatives are equal because the volume of the slug tail is not assumed to change significantly during the time of an explosion. This assumption is reasonable, since a significant rise or drop of the bottom surface of the slug tail would require a rapid acceleration of all magma inside the whole conduit (Fig. 4.6) – a process which would require pressures and forces that are by magnitudes higher than the ones observed, and whose consequences should be easily recognisable if it existed[3]. Therefore, $\dot{V}_{\text{gas}}$ can be replaced by $\dot{V}_{\text{cap}}$ (Eq. 4.10), leaving

$$\dot{W}_{\text{gas}} = p_{\text{gas}}\, \dot{V}_{\text{cap}} = \frac{\pi}{2} p_{\text{gas}} \dot{H} \left(H^2 + R_L^2 \right) \tag{4.31}$$

4.2.3 Kinetic energy E_{kin} of the magma shell

During an explosion, a large amount of energy is transferred into kinetic energy of the material that is accelerated away from the centre of the explosion. This amount of energy is

[3]Note that during the explosion, the bottom of the slug tail might nevertheless continue to (slowly) rise, simply because the magma film on the conduit wall drains to the bottom. However, the net volume increase caused by this effect is zero.

especially high in the case of an exploding magma bubble, simply due to the enormous mass of the magma shell.

The total kinetic energy of material inside the expanding magma shell can be found by integrating over the kinetic energy of all moving material of the shell:

$$E_{\text{kin}} = \int_V \frac{1}{2}\rho_m \, \tilde{v}^2(r)\, dV \tag{4.32}$$

As shown by Equation 4.16, this integral can be replaced by

$$\begin{aligned} E_{\text{kin}} &= \int_0^1 \frac{1}{2}\rho_m V_m \, v^2(q)\, dq && (4.33)\\ &= \frac{m_m}{2}\int_0^1 v^2(q)\, dq, && (4.34) \end{aligned}$$

where ρ_m is the density of the magma in the shell, V_m is the volume of the magma in the shell, and $m_m = \rho_m V_m$ is the total mass of magma (Eq. 4.7). $v^2(q)$ is the square of the velocity of the shell, parameterised with q (Eq. 4.19):

$$v^2(q) = \dot{\vec{r}}(q) \cdot \dot{\vec{r}}(q) = \frac{q^2 H^2 \dot{H}^2 (1-q)^2}{qH^2(1-q) + qR_L^2} + \dot{H}^2(1-q)^2 \tag{4.35}$$

The integral in 4.34 results, after several steps, in the following equation for E_{kin}:

$$E_{\text{kin}} = \frac{m_m \dot{H}^2}{4H^6}\left(H^2 + R_L^2\right)\left(H^4 - 2R_L^2 H^2 + 2R_L^4 \ln\left[1 + \frac{H^2}{R_L^2}\right]\right) \tag{4.36}$$

Even though this equation is considerably more complicated than the well known $E = \frac{1}{2}mv^2$ of a single moving body, it nevertheless bears some resemblance. Accordingly, E_{kin} increases with the magma mass m_m and the square of the zenith velocity $\dot{H}$.

Since the energy balance will be set up as energy **rates**, the time derivative of E_{kin} is needed:

$$\begin{aligned} \dot{E}_{\text{kin}} = \frac{m_m}{2H^7}\Bigg(& \dot{H}^3 R_L^2 \left(H^2\left(H^2 + 6R_L^2\right) - 2R_L^2\left(2H^2 + 3R_L^2\right)\ln\left[1 + \frac{H^2}{R_L^2}\right]\right) + \\ & H\dot{H}\ddot{H}\left(H^2 + R_L^2\right)\left(H^4 - 2H^2R_L^2 + 2R_L^4 \ln\left[1 + \frac{H^2}{R_L^2}\right]\right)\Bigg) \end{aligned} \tag{4.37}$$

During the explosion, kinetic energy is not only stored in the heavy magma shell, but also in the outward accelerating gas inside the bubble itself. Since the overall mass of this accelerated magmatic gas is so low in comparison to the mass of the magma shell (at Erebus typically several 1,000 tons of magma shell mass vs. only a few tons of gas mass), the latter effect is negligible in comparison to the kinetic energy of the shell (e.g. *McGetchin and Chouet*, 1979). An additional part of kinetic energy is stored in atmospheric air that is pushed away by the expanding shell. This so-called *acoustic energy* will be quantified in Section 4.2.7.

4.2.4 Potential energy E_{pot} of the magma shell

During the expansion phase of the bubble, the heavy magma shell is pushed upwards, therefore its overall potential energy in Earth's gravity field increases. We can state that

$$E_{\text{pot}} = g \int_{m_m} z(\vec{r})\, dm = \rho_m\, g \int_{V_m} r_z(\vec{r})\, dV \tag{4.38}$$

where g is acceleration due to gravity; m_m, V_m and ρ_m are the mass, volume and density of the magma shell, respectively, and $z(\vec{r}) = r_z$ is the distance of uplift at point $\vec{r}$. Transforming to an integral over the parameter q (Eq. 4.18 and 4.19) results in

$$E_{\text{pot}} = m_m\, g \int_0^1 r_z(q)\, dq = m_m\, g \int_0^1 H(1-q)\, dq \tag{4.39}$$

and integration gives

$$E_{\text{pot}} = \frac{1}{2} m_m\, gH \tag{4.40}$$

showing that similarly to a weight lifted in Earth's gravity, the potential energy of the magma shell increases linearly with the shell mass, the strength of the gravitational force, and the amount of lift. The difference to the weight analogy is that the magma cap is not lifted as a whole, but its edge is attached to the ground, leading to a factor of $\frac{1}{2}$ in the formula.

The temporal rate of potential energy delivered to the magma shell follows from:

$$\dot{E}_{\text{pot}} = \frac{1}{2} m_m\, g\dot{H} \tag{4.41}$$

4.2.5 Dissipated energy E_{diss} inside shell

During the expansion phase of an explosion the bubble membrane is constantly stretched, leading to the strain of material in the shell and therefore to the dissipation of energy. This dissipated energy will heat up the stretching material, although only by a small amount.

The stretching of the magma shell leads to a differential movement of viscous material in the shell, i.e. material at the inside of the shell moves at a slightly different speed than material at the outside. From this velocity difference I will calculate the largest of the three local principal strain rates $\dot{\varepsilon} = d\tilde{v}/dr$ following *Batchelor* (1967, p. 253ff). $\tilde{v}$ is the radial velocity of magma. Since the shell thickness $h(t)$ is always small against the current radius of the spherical cap section (because $R(t) \geq R_L \gg h(t)$, see Eq. 4.2), the largest principal strain rate inside the shell can be approximated as

$$\dot{\varepsilon} = \frac{d\tilde{v}}{dr} \approx \frac{\dot{h}}{h} \tag{4.42}$$

The shell thickness can be derived from Equation 4.6 through

$$h = \frac{V_m}{A_{\text{cap}}} = \frac{V_m}{\pi(H^2 + R_L^2)} \tag{4.43}$$

Its time derivative is

$$\dot{h} = \frac{-2V_m H\dot{H}}{\pi(H^2 + R_L^2)^2} \tag{4.44}$$

Combining Equations 4.42 to 4.44, we remain with

$$\dot{\varepsilon} \approx -\frac{2H\dot{H}}{H^2 + R_L^2} \tag{4.45}$$

For symmetry reasons, the two other principal strain rates must be $-\frac{1}{2}d\tilde{v}/dr$. This allows the calculation of the local rate of dissipation for each unit volume of the magma, assuming a Newtonian[4] fluid rheology (*Batchelor*, 1967, p. 253ff):

$$3\mu_m\dot{\varepsilon}^2 \tag{4.46}$$

where μ_m is the viscosity of the material.

Integrating Equation 4.46 over the total volume of the shell gives the total rate of dissipation in the magma shell:

$$\begin{aligned} \dot{E}_{\text{diss}} &= \int_V 3\mu_m\dot{\varepsilon}^2 \, dV \qquad (4.47) \\ &= \int_0^1 \frac{12\mu_m H^2\dot{H}^2}{(H^2 + R_L^2)^2} V_m \, dq \end{aligned}$$

Since neither H nor $\dot{H}$ are functions of q, integration is trivial, leading to

$$\dot{E}_{\text{diss}} = \frac{12\mu_m V_m H^2\dot{H}^2}{(H^2 + R_L^2)^2} \tag{4.48}$$

Interestingly, the rate of dissipated energy increases with the square of zenith velocity but roughly decreases with the square of zenith height. If the expansion speed of a bubble would remain constant during the explosion, the most energy would be dissipated when

[4] A fluid is called **Newtonian** when its stress vs. strain-rate curve is linear and passes through the origin. The slope of this curve is determined by the fluid's viscosity. The flow properties of a **Non-Newtonian** fluid cannot be described by a single constant viscosity value.

the bubble is still small.

For the simplicity of the calculation, a Newtonian rheology was assumed for the magma in Equation 4.46. Even though this is not always a valid approximation for real magma (e.g. *Webb and Dingwell*, 1990; *Dingwell et al.*, 1993; *Divoux et al.*, 2008), it is considered a good enough approximation for this task (see also *Vergniolle and Brandeis*, 1996; *James et al.*, 2004), especially since the amount of dissipated energy is small compared to the total amount of energy released during an explosion (Sec. 7.3).

4.2.6 Shell surface expansion energy E_{surf}

During the bubble expansion phase, some energy is consumed by the surface expansion of the shell, similar to the surface tension energy stored in a soap bubble. Even though this effect is very small compared to other energy fractions involved (i.e. a few Kilojoule compared to kinetic energy in the gigajoule range, see Section 7.3), we will quantify this by calculating the surface energy rate. A_{total} is the total inside and outside surface area of the expanding membrane, which can be approximated as twice the cap surface area (Eq. 4.6) of the spherical cap section (because $h(t) << R_L$). The total surface energy is therefore

$$E_{\text{surf}} = \sigma_m \, A_{\text{total}} = 2\pi\sigma_m(H^2 + R_L^2) \; , \tag{4.49}$$

where σ_m is the specific surface energy of the magma in the bubble shell. Note that this value is dependent on magma temperature and water content, but a rough estimate is $\sigma_m = 0.4\frac{N}{m} = 0.4\frac{J}{m^2}$ (e.g. determined by *Walker and Mullins Jr.*, 1981; *Koopmann*, 2004), which is commonly used throughout the literature (e.g. *Vergniolle and Brandeis*, 1996; *Seyfried and Freundt*, 2000). To set this value in context, the total surface energy of a 40 m wide lava lake is 503 J, about as much energy as is needed to heat one litre of water by 0.1°C.

In total, the surface generation energy rate is:

$$\dot{E}_{\text{surf}} = 4\pi\sigma_m H\dot{H} \; . \tag{4.50}$$

After the rupture of the membrane, the surface again increases significantly due to the generation of fragments. However, this contribution is still very small compared to other energy types involved, and shall not be discussed further here.

4.2.7 Energy radiated into the atmosphere E_{atm} (acoustic energy)

A small but important part of the energy released during a Strombolian explosion is used for the displacement and acceleration of the atmosphere surrounding the source of the explosion, leading to a movement away from the centre. This acceleration is often very rapid, thus generating disturbances in the atmosphere that travel away from the source as sound waves (see Chapter 3). It was argued in Sections 3.4 and 3.5 that bubble explosions similar to the ones at Erebus volcano behave close to a simple monopole source in the frequency band of interest. Therefore, some (carefully chosen) aspects of the system can be described by the same formulae as are valid for a point monopole source, allowing the analytical calculation of physical parameters despite the lava lake's complex surface geometry, which would usually prevent any analytical approach.

Equation 3.27 is one of these formulae, describing the energy output of a point source. Therefore, under certain conditions, it is suitable to provide a good estimate of the true sound power output of the exploding bubble considered here. It specifically describes the sound energy flux through the surface of an imaginary sphere surrounding the source, which, due to the conservation of energy, must be representative of the amount of sound energy that is released by the source. Such an imaginary surface is called a **control surface** and is commonly used to calculate the sound field of complex bodies (e.g. *Dowling and Williams*, 1983, p.199).

When only a far-field excitation exists then the use of a control sphere is trivial because any closed integration surface enclosing the source will yield the same result. However, when a near-field exists, as is the case here, using this technique is somewhat more complicated, as the energy flux through the control sphere now depends on its radius (as already discussed in Section 3.3). The nature of this property lies in the fact that the expanding source not only dumps energy into sound waves that radiate away from the source (the far-field, see Sec. 3.4), but also uses energy to accelerate and (temporally) displace the atmosphere around it (the near-field). The latter type of energy will eventually be transferred back to the source when the expansion phase is over, and is therefore only "borrowed" from the system (i.e. the long term **average** energy transfer to the near-field is zero), but right at the start of the explosion the source dumps a significant amount of energy there (Eq. 3.28). Therefore, the near-field energy needs to be included when calculating the sound energy output during the early moments of an explosion. Since velocity contributes as a square to kinetic energy, most of the near-field energy will be stored close to the source, and vanishes in the far-field. Thus care must be taken to choose an appropriate radius for the imaginary control surface (centred on the source), which catches only the energy that is transferred **through** it, but not the energy that is stored **inside** it in the near-field (e.g. if the control surface is placed too far away, it will only "see" the far-field energy, thus being a poor estimate of the true energy output).

To produce a good estimate of the sound output the control surface should be placed as close as possible to the source, preferably into the region where the source reaches its maximum velocity, since in this region the maximum kinetic energy (near-field) is temporally stored in the atmosphere. A control sphere radius similar to the lava lake dimension is most appropriate, so the control sphere effectively describes a hemisphere with roughly the same diameter as the lava lake. This means that Equation 3.27 provides a good estimate of the atmospheric sound power output when r is replaced by the lava lake radius R_L and V_{source} by V_{cap}. As argued at the end of Section 3.3, the sound energy output has to be doubled to account for the source's setting at the interface between a solid half space and the atmosphere:

$$\begin{aligned} \dot{E}_{\text{atm}}(t) &= 2\,\dot{E}_{\text{sound,mono}}(r = R_L, t) \\ &= \frac{\rho_a}{2\pi c_a}\ddot{V}^2_{\text{cap}}(t) + \frac{\rho_a}{2\pi R_L}\dot{V}_{\text{cap}}(t)\ddot{V}_{\text{cap}}(t)\,, \end{aligned} \tag{4.51}$$

where $V_{\text{cap}}(t)$ can be written as a function of parameter $H(t)$ (Eq. 4.5):

$$\begin{aligned} \dot{E}_{\text{atm}} = \; & \frac{\pi\rho_a}{8c_a}\Big(2H\dot{H}^2 + \ddot{H}\big(H^2 + R_L^2\big)\Big)^2 + \\ & \frac{\pi\rho_a}{8R_L}\dot{H}\big(H^2 + R_L^2\big)\Big(2H\dot{H}^2 + \ddot{H}\big(H^2 + R_L^2\big)\Big) \end{aligned} \tag{4.52}$$

The second of the two terms in each of these equations refers to the energy that is temporally stored in the near-field. Both terms contribute in roughly the same orders of magnitude to the sound power output at the given setup (i.e. the geometry of Ray Lava Lake at Erebus volcano). The equations show that the sound power output mainly increases with the second derivative of the volume of the cap.

The above equations are a manifestation of *Lighthill's monopole* (Eq. 3.23), whose sound output is strongly dependent on its volumetric acceleration. Since the cap volume increases with the third power of the cap zenith height (Eq. 4.5), the most effective sound power output is expected late in the explosion, when the bubble has acquired a considerable size.

4.2.8 Seismic energy radiated into the ground E_{seis}

During an explosion, a significant amount of magma mass is accelerated out of the lava lake, leading to a primarily vertical reaction force acting on the ground. Additionally, at the time of the burst, the sharp pressure drop inside the bubble and in the slug tail causes the normal force on the conduit wall to drop, which produces a secondary isotropic deflationary source (*Kanamori et al.*, 1984). These two types of time-varying forces on the ground will excite seismic waves. The seismic amplitudes caused by the isotropic force are typically much smaller (in the order of 10 percent) than those caused by the single force. *Kanamori et al.* (1984) quantify this by arguing that the ratio of the two is approximately equal to the ratio of the gas particle velocity to the seismic wave velocity, and contend that the effect of the isotropic source is secondary. Since the main duration of bubble explosions at Erebus is usually in the second to sub-second range, the resulting seismic signal is expected in the short-period range (0.2–2 s). Note that very long period period (VLP) seismic waves that are excited by the rising bubble in the conduit are not considered here, since the are not directly associated with the bubble's burst.

In order to approximate the amount of energy radiated into the ground we first need to estimate the ground force caused by a bubble burst. Subsequently, through calculating the response of the ground to that variable force, the amount of radiated energy can be estimated.

To approximate the seismic radiation energy we must therefore primarily determine the vertical reaction force caused by a bubble burst. The net vertical force during a bubble burst explosion consists mainly of the reaction force from the upward acceleration of the magma shell, plus a small component resulting from the upward acceleration of the atmosphere. The latter component is, however, smaller than the former one by several orders of magnitude (Sec. 7.3) and can be ignored. Accordingly, the vertical seismic ground force can be calculated from Newton's second law, using Equations 4.16 and 4.19. It is the sum of the vertical acceleration force exerted by each mass element, i.e. the vertical acceleration force integrated over the whole volume of the shell:

$$F_{\text{ground,z}} \approx -m_m \bar{\ddot{r}}_z = -\int_M \ddot{r}_z(\vec{r})\, dm \tag{4.53}$$

$$= -m_m \int_0^1 \ddot{r}_z(q)\, dq = -m_m \int_0^1 \ddot{H}(1-q)\, dq\ , \tag{4.54}$$

where $\bar{\ddot{r}}_z$ is the spatial average of the magma shell's vertical acceleration $\ddot{r}_z$, and m_m is the magma shell mass. Integration yields the vertical seismic force on the ground caused by a bubble burst as a function of time:

$$F_{\text{ground,z}}(t) = -\frac{1}{2} m_m \ddot{H}(t)\ . \tag{4.55}$$

An assumption made here concerns the quantity of accelerated mass. During the last moments of the bubble ascent (just before the rapid acceleration phase sets in) the magma mass above the bubble is constantly decreasing. In those early moments of an explosion, before the rapid acceleration practically fixes the amount of magma in the shell to m_m, the above formula underestimates the true ground force of the explosion. Additionally, bubble surface velocities determined by radar are only valid up to the point of shell rupture. Therefore the ground force can only be reliably estimated up to that point in time. Taking both these limitations into account, the above calculation of the ground force is only valid between the onset of the rapid acceleration phase and the burst time.

The seismic body wave displacement caused by this vertical ground force on the surface of a volcano can be approximated by the displacement $\vec{s}(\vec{r}, t)$ caused by a vertical single force on the surface of an elastic half space. By symmetry, the displacement due to a force applied on the surface of a half space can be estimated as twice the deformation caused in a whole space (e.g. *Aki and Richards*, 1980; *Kanamori et al.*, 1984):

$$\vec{s}(\vec{r},t) = \begin{pmatrix} s_r \\ s_\theta \\ s_\Phi \end{pmatrix} = \frac{2}{4\pi\rho_{\text{rock}} r v_p^2} F_{\text{ground,z}}(t - \frac{r}{v_p}) \begin{pmatrix} -\cos\theta \\ 0 \\ 0 \end{pmatrix} + \frac{2}{4\pi\rho_{\text{rock}} r v_s^2} F_{\text{ground,z}}(t - \frac{r}{v_s}) \begin{pmatrix} 0 \\ \sin\theta \\ 0 \end{pmatrix} \tag{4.56}$$

where v_p, v_s are the p and s wave speeds, and ρ_{rock} is the density of the surrounding medium. θ is the angle to the vertical, and Φ the azimuth. This simple approach neglects the excitation of surface waves and part of the near-field, therefore it represents only an approximation of the far-field radiation that should be suitable for modeling the short-period wave field from Erebus explosions, which are dominated by body waves (e.g. *Rowe et al.*, 2000) and for estimating the radiated seismic energy. A more exact solution can be derived through numerical methods (e.g. *Ohminato and Chouet*, 1997) or from solving so-called *Lamb's problem* (e.g. *Aki and Richards*, 1980). Both of these approaches involve relatively complex calculations that are unnecessary for this task.

Given the displacement field, radiated energy can be calculated by determining the energy flux though a closed surface surrounding the source (*Haskell*, 1964):

$$E_{\text{seis,p}} = \rho_{\text{rock}} v_p \int_0^{2\pi} \int_{\frac{\pi}{2}}^{\pi} \int_{-\infty}^{\infty} \dot{s}_r^2 \, dt \, r^2 \, \sin\theta \, d\theta \, d\Phi \tag{4.57}$$

$$E_{\text{seis,s}} = \rho_{\text{rock}} v_s \int_0^{2\pi} \int_{\frac{\pi}{2}}^{\pi} \int_{-\infty}^{\infty} (\dot{s}_\theta^2 + \dot{s}_\Phi^2) \, dt \, r^2 \, \sin\theta \, d\theta \, d\Phi \tag{4.58}$$

where $E_{\text{seis,p}}$ and $E_{\text{seis,s}}$ are the seismic energies transported by p and s waves, respectively. In our case, using a half space solution (Eq. 4.56) and integrating over a lower hemisphere with its centre located at the force point provides a convenient way of solving these equations. Finally, adding p and s wave energies yields the total radiated seismic energy (*Haskell*, 1964; *Kanamori and Given*, 1982):

$$E_{\text{seis}} = E_{\text{seis,p}} + E_{\text{seis,s}} = \left(\frac{1}{6\pi\rho_{\text{rock}} v_p^3} + \frac{1}{3\pi\rho_{\text{rock}} v_s^3} \right) \int_{-\infty}^{\infty} \dot{F}_{\text{ground,z}}^2 \, dt \tag{4.59}$$

By using Equation 4.55 and assuming the validity of our expansion model, this energy can be directly determined from measured parameters such as the zenith position of the lake surface H:

$$E_{\text{seis}} = \left(\frac{1}{6\pi\rho_{\text{rock}} v_p^3} + \frac{1}{3\pi\rho_{\text{rock}} v_s^3} \right) \frac{m_m^2}{4} \int_{-\infty}^{\infty} \dddot{H}^2 \, dt \tag{4.60}$$

Equation 4.60 shows that the amount of seismic energy radiated by an exploding bubble is very sensitive to dynamic parameters of the system, such as the third temporal derivative of the zenith position H and the square of the accelerated mass. Additionally, since the seismic energy decreases with the third power of the wave speeds, a good knowledge of these speeds significantly improves the quality of the result. As will be shown in later sections, the uncertainty in the accelerated mass and the wave speeds will lead to a relative uncertainty in the seismic energy that is larger than for the other types of energy. Yet, due to the generally small amount of seismic energy radiated by explosions, these uncertainties play a negligible role in the overall energy budget.

4.2.9 Thermal Energy E_{therm}

The thermal energy stored in the hot magma shell is a type of energy that is not powered by the gas internal energy, therefore it does not change during bubble burst. This means that the rate of change of thermal energy $\dot{E}_{\text{therm}}$ can be considered as nearly zero during the time of final expansion and burst. It is thus not important for the energy balance during the time of burst. However, it plays an important role in the overall energy output of an explosion:

$$\Delta E_{\text{therm}} = \eta_m \, m_m \, c_{p,m} \, \Delta T \tag{4.61}$$

where m_m is the mass of the magma shell, while η_m describes the fraction of shell material that does not fall back into the lake after an explosion, and is therefore lost to the lava lake. $c_{p,m}$ is the specific heat of magma, not taking into account any changes in the crystal content during the cooling. An approximate number for it is $c_{p,m} \sim 1000 \frac{J}{kgK}$ (e.g. *Jaeger*, 1964; *Calkins et al.*, 2008).

The importance of this type of energy can be demonstrated by calculating the amount of thermal energy stored in a **single metric ton** of magma at a typical lava lake temperature of $\sim$ 1000°C above the ambient temperature. According to Equation 4.61 it is 10^9 J, or $\sim$280 kWh, i.e. roughly equivalent to the amount of electrical energy that an average one person European household uses up in two months.

In addition to the heat stored in the magma mass, a small amount of thermal energy is stored in the hot magmatic gas that is eventually freed during an explosion, therefore also contributing to the total energy balance. However, in comparison to the energy stored in the heavy magma shell, this amount of energy is negligible (e.g. *McGetchin and Chouet*, 1979) and will not be further considered in this study.

4.3 Deriving gas pressure from the rate of energy output

In the last sections I have developed the necessary formulae to determine the energy output from an exploding bubble constrained by radar measurements. Thermodynamic considerations derived in Section 4.2.2 show that this amount of freed energy is powered by the internal energy contained in the bubble's gas (Eq. 4.28), which is directly dependent on the gas pressure (Eq. 4.29). This means that the higher the underlying gas pressure, the higher the power output of an explosion. By quantifying this simple relation, I will develop a formula to calculate the gas pressure inside a bubble from the observed power output of an explosion.

The necessary link will be Equation 4.25, which can be written as time derivative:

$$\dot{W}_{\text{gas}} = \dot{E}_{\text{kin}} + \dot{E}_{\text{pot}} + \dot{E}_{\text{diss}} + \dot{E}_{\text{surf}} + \dot{E}_{\text{atm}} + \dot{E}_{\text{seis}} \tag{4.62}$$

When combining this with Equation 4.31, the overpressure inside the bubble at time t can be calculated, merely from the rate at which energy is transferred from the gas into the different kinds of energy of the expanding magma cap:

$$p_{\text{gas}}(t) = \frac{\dot{E}_{\text{kin}}(t) + \dot{E}_{\text{pot}}(t) + \dot{E}_{\text{diss}}(t) + \dot{E}_{\text{surf}}(t) + \dot{E}_{\text{atm}}(t) + \dot{E}_{\text{seis}}(t)}{\dot{V}_{\text{cap}}(t)} \tag{4.63}$$

This simple relation shows that indeed, the higher the power output during an explosion, the higher must be the pressure inside the bubble causing this power output. All necessary parameters that enter this equation can directly be observed from the crater rim (mainly the radar cutoff velocity $v_{\text{R,cut}}(t)$, the approximate lake radius and the rough amount of ejected material).

4.4 Determining the volume of rising gas slugs

One of the challenges in volcanology is determining the amount of gas that is released during explosions. Together with gas composition measurements, this knowledge enables the determination of the respective quantities of ejected gas components, and therefore allows an improved judgement about the current status of the magmatic system.

I have developed two different methods to determine the volume of approaching gas slugs, using radar measurements in combination with the above expansion model. Both methods are based on thermodynamic properties of hot magmatic gas, and estimate the initial gas volume $V_{\text{gas},0}$ of the slugs, i.e. their volume at a point in time just before they enter their rapid expansion phase (Fig. 4.6). The first method uses the energy (Sec. 4.2) that is transferred from the gas into various forms of energy during the rapid expansion phase, while the second method evaluates the shape of the pressure drop curve during the rapid expansion phase.

The two methods will be described in detail in the following subsections. Additionally, a third way to estimate the erupted gas volume of an explosion is to estimate from video the size of void, or "missing volume" in the lava lake and conduit underneath. I will later use all three of these methods individually to determine the bubble volumes during explosions at Erebus (Sec. 7.5).

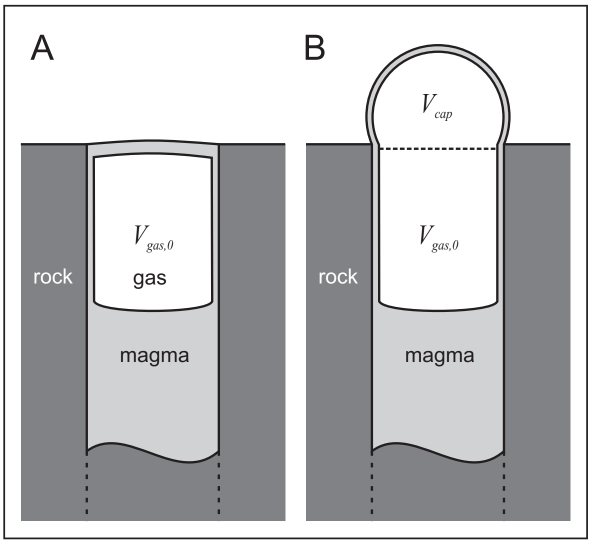

Figure 4.6: ***Sketch of a rising and expanding gas slug in the upper conduit.*** ***A:*** *Just before the last phase of the slug rise process, the "rapid expansion phase", the gas slug volume is called* $V_{\mathrm{gas},0}$. ***B:*** *During the rapid expansion phase, the increasing slug volume can be approximated by* $V_{\mathrm{gas}}(t) \approx V_{\mathrm{gas},0} + V_{\mathrm{cap}}(t)$*, where* $V_{\mathrm{cap}}(t)$ *can be directly calculated from radar measurements. The approximation is valid because the slug base does not move significantly during the short time interval of the expansion phase.*

Once the total volume of the gas bubble and its pressure are known for a single moment in time, then the overall mass m_{gas} of the gas bubble can be calculated, using the ideal gas law (Eq. 3.13):

$$m_{\mathrm{gas}} = \frac{\hat{p}_{\mathrm{gas}}(t)\, V_{\mathrm{gas}}(t)}{T_{\mathrm{gas}}(t)} \frac{M_{\mathrm{gas}}}{R_m} , \tag{4.64}$$

where the temperature $T_{\mathrm{gas}}(t)$ of the gas can be determined through Equation A.1. From these gas mass quantities, an overall gas flux from the volcano during explosions can be calculated, providing a valuable basis for interpreting gas composition measurements (e.g. FTIR, DOAS, see e.g. *Francis et al.*, 2000; *Burton et al.*, 2007), which is otherwise hard to obtain.

4.4.1 Determining gas volume from energy output

To establish a relation between the initial gas volume $V_{\mathrm{gas},0}$ (Fig. 4.6) and the energy that was transferred from the gas into other types of energy during an explosion, I will start out from some basic thermodynamic equations. Since all thermodynamic processes during a Strombolian bubble explosion take place on time scales that do not allow significant heat transfer between the gas and the surrounding conduit walls, all processes can be considered as adiabatic (see also Sec. 4.2.2).

The equation for an ideal fluid that is undergoing an adiabatic process is

$$\hat{p}_{\mathrm{gas}} V_{\mathrm{gas}}^{\gamma} = \mathrm{constant} \tag{4.65}$$

where $\hat{p}_{\mathrm{gas}} = p_{\mathrm{gas}} + p_{\mathrm{atm}}$ is the total pressure (including the ambient atmospheric pressure p_{atm}). γ is the ratio of specific heats ($\gamma = \frac{C_p}{C_V}$, see Eq. 3.15) and is equal to 1.1 for hot gases (*Lighthill*, 1978).

To calculate the work that can be done by an adiabatically expanding volume of gas from

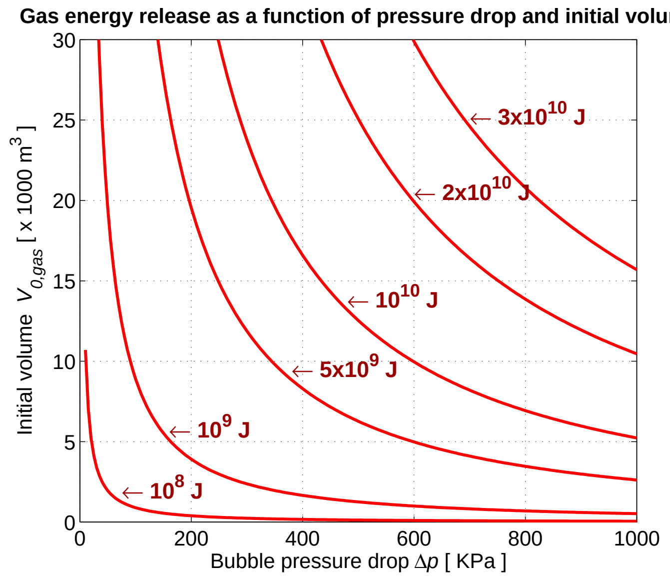

Figure 4.7: Determining initial bubble volume from energy output. *Showing Eq. 4.72 with an assumed end pressure of 160 kPa ($approx$ 100 kPa above ambient at Erebus crater rim), this graph depicts the relation between pressure drop Δp, energy loss through adiabatic work ΔW_{gas}, and the bubble's initial volume $V_{\text{gas},0}$. For example, a gas bubble whose pressure drops by 400 kPa when performing 10^{10} J of expansion work must have had an initial volume of $\sim$ 17,000 m^3.*

state 0 to state 1 (e.g. the start [annotated with index "$_0$"] and the end [index "$_1$"] of the rapid expansion phase), I use (*Kinney and Graham*, 1985):

$$\Delta W_{\text{gas}} = \frac{\hat{p}_{\text{gas},0} V_{\text{gas},0}}{\gamma - 1} \left(1 - \left[\frac{V_{\text{gas},0}}{V_{\text{gas},1}} \right]^{\gamma - 1} \right) \tag{4.66}$$

this can be expressed in terms of pressure by using Eq. 4.65:

$$\Delta W_{\text{gas}} = \frac{\hat{p}_{\text{gas},0} V_{\text{gas},0}}{\gamma - 1} \left(1 - \left[\frac{\hat{p}_{\text{gas},1}}{\hat{p}_{\text{gas},0}} \right]^{\frac{\gamma - 1}{\gamma}} \right) \tag{4.67}$$

$\hat{p}_{\text{gas},0}$, $V_{\text{gas},0}$ are the absolute parameters of the system just before the rapid expansion, $\hat{p}_{\text{gas},1}$, $V_{\text{gas},1}$ are the parameters at its end. ΔW_{gas} is the work that was done by the gas between state 0 and state 1.

Simply rephrasing Equation 4.67 leaves us with an equation for the initial volume:

$$V_{\text{gas},0} = \Delta W_{\text{gas}} \frac{\gamma - 1}{\hat{p}_{\text{gas},0}} \left(1 - \left[\frac{\hat{p}_{\text{gas},1}}{\hat{p}_{\text{gas},0}} \right]^{\frac{\gamma - 1}{\gamma}} \right)^{-1} \tag{4.68}$$

This relation allows the estimation of the initial volume of an expanding gas bubble when 1.) the gas pressure during the start and end of the process is known (i.e. the pressure drop) and 2.) the amount of energy that was withdrawn from the gas during that time is known.

Figure 4.7 shows this relation for a variety of different energy outputs. To simplify the figure, an end pressure $\hat{p}_{\text{gas},1}$ of 100 kPa above the ambient pressure was assumed here, leaving only the pressure drop $\Delta p = \hat{p}_{\text{gas},0} - \hat{p}_{\text{gas},1}$ to be varied. I will show in a later Section that this is not an unrealistic scenario during explosions at Erebus.

4.4.2 Determining gas volume from gas pressure decay

The second method to determine bubble volumes is based on the gas law stating that in an expanding gas volume, the pressure must drop in a certain relation to the amount of volume expansion. This law must be fulfilled at any given time during the expansion phase, and therefore offers a way to test the validity of the model.

The gas law states that, assuming an initial gas volume of $V_{\text{gas},0}$ and an initial gas pressure $p_{\text{gas},0}$, the gas pressure inside the bubble during its expansion is

$$\hat{p}_{\text{gas}}(V) = p_{\text{gas}}(V) + p_{\text{atm}} = p_{\text{gas},0}\left(\frac{V_{\text{gas},0}}{V_{\text{gas}}}\right)^{\gamma} \tag{4.69}$$

or,

$$V_{\text{gas}}(\hat{p}) = V_{\text{gas},0}\left(\frac{\hat{p}_{\text{gas},0}}{\hat{p}_{\text{gas}}}\right)^{\frac{1}{\gamma}} \tag{4.70}$$

Since the volume of the magma cap V_{cap} (Fig. 4.6) can be measured by integrating radar velocities, we introduce it into the equation by eliminating the (unknown) total bubble volume V_{gas}. We achieve this by subtracting $V_{\text{gas},0}$ on both sides, where $\Delta V_{\text{gas}} = V_{\text{gas}} - V_{\text{gas},0} = V_{\text{cap}}$, leaving us with

$$\Delta V_{\text{gas}} = V_{\text{gas},0}\left(\left(\frac{\hat{p}_{\text{gas},0}}{\hat{p}_{\text{gas}}}\right)^{\frac{1}{\gamma}} - 1\right) = V_{\text{cap}} \tag{4.71}$$

Figure 4.8 illustrates this relation for a set of different initial volumes. All graphs start at their initial volume (i.e. zero volume expansion), when their pressure is at 100% of the starting pressure. When the volume increases, the pressure drops and, for example, a bubble with an initial volume of 1000 m^3 will just about halve its pressure[5] when doubling its volume by an expansion of another 1000 m^3. Therefore, by registering how the pressure inside a bubble reacts to a volume increase, the initial volume can be estimated. Rephrasing Equation 4.71 provides us with the necessary formula:

$$V_{\text{gas},0} = V_{\text{cap}}\left(\left(\frac{\hat{p}_{\text{gas},0}}{\hat{p}_{\text{gas}}}\right)^{\frac{1}{\gamma}} - 1\right)^{-1} \tag{4.72}$$

[5] due to the adiabatic process, the pressure will be slightly less than 50% in this case because the gas cools during its expansion.

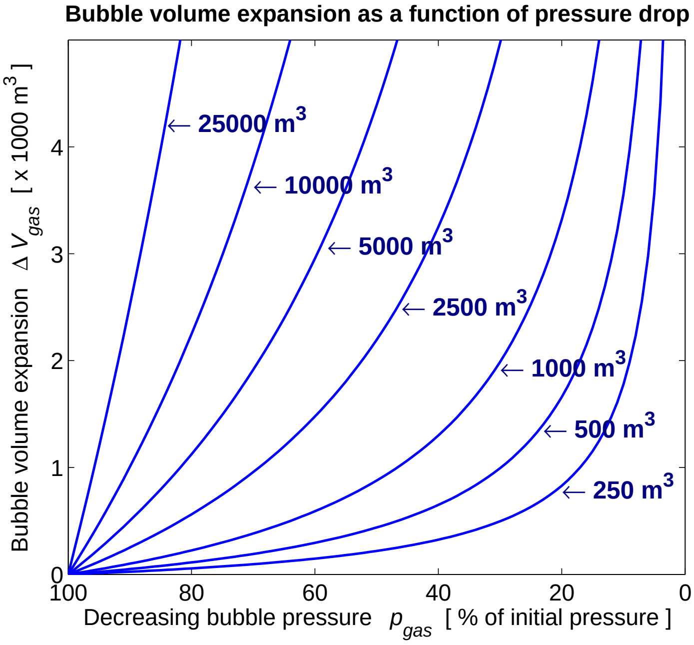

***Figure 4.8:* Determining initial bubble volume from gas pressure decay.** *The figure shows the relation between the volume change of a gas and its pressure change during an adiabatic expansion process (Eq. 4.71). Initial gas volumes* $V_{\mathrm{gas},0}$ *(pressure before the expansion) are annotated. Starting from 100% of their initial pressure (bottom left), the pressure in small bubbles drops quicker than the pressure in large bubbles when the bubble volumes are increased by the same absolute amount. This behaviour can be used to estimate the initial bubble volume.*

All parameters on the right side of this equation can be determined from radar measurements. If the model and the resulting pressure values (Sec 4.3) are correct, then these pressure values are expected to follow one of the curves depicted in Figure 4.8, indicating the bubble's initial volume.

To make sure that this second method to determine bubble volumes is not only a rephrased version of the first method, we will take a closer look at their input parameters. Both equations (Eq. 4.68 and Eq. 4.72, respectively) are dependent on correct pressure values determined from the expansion model (Sec. 4.3). The first method relies on the pressure difference between the start and the end of the rapid expansion phase, not taking into account how the system got from one state to the other (apart from assuming an adiabatic process). The second method offers the possibility to test the model by also taking into account **how** the system got there.

The main difference between the methods, however, is the other important parameter that enters their respective equation: the first (Eq. 4.68) uses the change of internal gas energy between the start and end of the rapid expansion phase. This energy output is measured as the difference in the total energy (Eq. 4.26) between the two points in time. These total energy values are highly dependent on a variety of parameters, such as the membrane's zenith height, velocity, acceleration, and for example the magma shell mass. Each one of these parameters therefore influences the initial bubble volume as determined by the first method. In contrast, the second method (Eq. 4.72) does not rely on this multitude of parameters. In addition to the already mentioned pressure, its only other significant input parameter is the current volume of the magma shell V_{cap}, which can be determined from the radar data in a relatively simple way. In summary, even though both methods rely on correct pressure calculations, they can nevertheless be regarded as largely independent.

4.5 Infrasonic signals caused by expanding bubbles

The theoretical background that is necessary to calculate the pressure signal caused by an expanding bubble was already discussed in Section 3.3. In Section 3.4 I have shown that the lava lake can be considered a **simple source** of sound only under some circumstances. Due to the size of the lava lake, a signal that is coherently emerging from all points of the lake surface will be smeared in time, or blurred, by up to 0.1 s when being recorded by a receiver. Depending on whether this smearing effect is expected to significantly influence the outcome of the calculation, the lake should be regarded either as compact (i.e. without the smearing effect, for simplifying the governing equations) or as non-compact (for greater exactness of the results). Here, I will describe how to calculate the predicted sound field in either of these cases.

Compact case Starting with the more simple case (i.e. regarding the lava lake as a compact source) we can calculate its sound field from Equation 3.23, while the source volume acceleration $\ddot{V}_{\text{source}}$ is simply replaced by the volume acceleration of the bubble cap $\ddot{V}_{\text{cap}}$ (Eq. 4.5):

$$p(r,t) = \frac{\rho_a}{4\pi r} \ddot{V}_{\text{cap}}(t - r/c_a) \, . \tag{4.73}$$

It follows that the amplitude of the sound pressure p decreases with one over the distance between source and receiver.

Since the bubble is gaining in size during its expansion, the distance r between the surface of the bubble (i.e. the source of sound) and the observer on the crater rim decreases constantly. This leads to an acoustic Doppler effect and therefore to a slight increase in frequency. Since the size of the bubble as a function of time is known, this effect will be considered when calculating the expected sound power output via Equation 4.73.

Non-compact case If the lava lake is considered a non-compact source, then the sound generated from two different locations on the lake surface at the same time will arrive at significantly different times at the receiver (Sec. 3.4). I have shown in Section 3.6 that a possible solution for this scenario is the assumption of many small sources of sound that are distributed over the surface of the non-compact source of sound. In this case the source

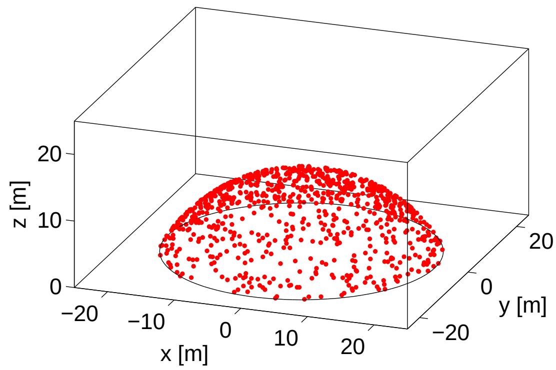

***Figure 4.9:* Approximating a non-compact sound source by multiple compact sources.** *Each of the red dots represents a small compact monopole source. Here, the sources are randomly distributed on the surface of the bulging lava lake, each representing an average surface area of 2 m^2. The strength of each of the sources at a certain time depends on its current acceleration on the expanding surface.*

of sound is the surface of the bulging and expanding lava lake. The analytical solution of this problem involves the integration of individual source strengths over the surface of the lake. Since the special geometry of the problem is too complicated for a simple analytical solution, I have solved the problem numerically.

As shown in Figure 4.9 I have generated a large number of random points on the surface of the lava lake. These points each represent a small compact monopole source of sound, and their combined phase and strength add up to the total generated infrasound signal that can be observed at a defined point in the distance. Their number N_{sources} was chosen in each time step so that the average surface area of each source is 2 m^2 (i.e. more than 1000 points on the surface).

To calculate the strength of each source we first need to know the current surface acceleration at this certain point, defined by the parameters q and Φ. While q was already introduced in Section 4.1.1, Φ is the azimuth of the source point with regard to the centre of the lake. The special properties of q ensure uniform distribution of points on the spherical surface, simply by choosing uniformly distributed values for q $[0..1]$ and Φ $[0..2\pi]$.

The acceleration of a surface point (q, Φ) on the bubble shell at time t follows from Equation 4.19, this time in three dimensions:

$$\ddot{\vec{r}}_n(q,\Phi,t) = \begin{pmatrix} r_x \\ r_y \\ r_z \end{pmatrix} = \begin{pmatrix} \frac{\sqrt{q}(1-q)\left(R_L^2\dot{H}^2+H\ddot{H}\left(R_L^2+H^2(1-q)\right)\right)}{\left(R_L^2+H^2(1-q)\right)^{\frac{3}{2}}}\cos\Phi \\ \frac{\sqrt{q}(1-q)\left(R_L^2\dot{H}^2+H\ddot{H}\left(R_L^2+H^2(1-q)\right)\right)}{\left(R_L^2+H^2(1-q)\right)^{\frac{3}{2}}}\sin\Phi \\ \ddot{H}(1-q) \end{pmatrix} \tag{4.74}$$

where the index n denotes the n-th of N_{sources} surface points. The unit normal at this point is given by

$$\hat{\vec{n}}_n(q, \Phi, t) = \begin{pmatrix} \sin\theta(q,t)\cos\Phi \\ \sin\theta(q,t)\sin\Phi \\ \cos\theta(q,t) \end{pmatrix} \tag{4.75}$$

while $\theta(q)$ is defined by Equation 4.15.

The volume acceleration of each source can be approximated by the projection of the acceleration vector onto the unit vector that is normal to the surface, multiplied by the point's surface area:

$$\ddot{V}_n(q, \Phi, t) = \frac{A_{\text{cap}}}{N_{\text{sources}}} \ddot{\vec{r}}_n(q, \Phi, t) \cdot \hat{\vec{n}}_n(q, \Phi, t) \tag{4.76}$$

where A_{cap} is the surface of the shell cap (Eq. 4.6). The source's individual pressure signal created at the position of an observer or a microphone at distance $r_{\text{mic,n}}$ from the source point is then given by Equation 3.23:

$$p_n(q, \Phi, t, r_{\text{mic,n}}) = \frac{\rho_a}{4\pi r_{\text{mic,n}}} \ddot{V}_n(q, \Phi, t - \tfrac{r_{\text{mic,n}}}{c}) \tag{4.77}$$

$r_{\text{mic,n}}$ is not only a function of the observer's distance and elevation angle, but also a function of q Φ and t, therefore it has to be determined individually for each source point.

Due to the linearity of pressure signals in the atmosphere (Sec. 3.1), the sum of all source signals represents the total pressure signal, expected at a microphone at distance r_{mic} from the lava lake centre at an elevation angle of ϕ_{mic}:

$$p_{\text{mic}}(r_{\text{mic}}, \phi_{\text{mic}}, t) = \sum_n p_n\big(q, \Phi, t, r_{\text{mic,n}}\big) \tag{4.78}$$

In Section 7.6 this equation will be used to calculate expected acoustic signals from lava lake explosions at Erebus volcano, which are then compared to real acoustic signals. Conveniently, this approach not only takes care of the compactness problem, it automatically also includes the directivity of a sound source. Thus, if the geometry of the source results in an emission pattern containing poles of higher order, such as dipoles (e.g. Sec. 3.5) or quadrupoles, this approach will nevertheless calculate the correct sound pressure amplitude at the receiver site.

This property can even be exploited further, because the method allows the systematic investigation of the emission pattern of a sound source with a complex geometry as a function of frequency. Unfortunately, even though promising interesting results, such an investigation is beyond the scope of this study and should be subject to future research.

CHAPTER 5

INSTRUMENT DEVELOPMENT & DATA ACQUISITION

At the time when this study commenced, no reliable radar field recording system existed that could endure the conditions met on the crater rim of an active volcano in Antarctica. Even in the summer months, conditions on the 3794 m high Erebus volcano can deteriorate within minutes into a full blown blizzard, with winds exceeding 150 km/h, temperatures below -45°C, and visibility below a few metres. Instruments on the crater rim are constantly exposed to highly corrosive acidic gases from the volcano's interior, to a wind of abrasive ice particles, to strong UV light, to the accumulation of heavy rime ice, and sometimes to ballistic impacts from the volcano's ejecta.

To allow for a reliable operation under such conditions, a rugged field recording system for radar data needed to be developed, along with necessary improvements to the actual radar devices. The first section in this chapter describes the criteria that I included in the system's design, how I met these criteria, and how the system was eventually tested at a quarry blast site.

The second section in this chapter describes the field experiment conducted by the author of this study at Erebus volcano in 2005/2006, leading to the collection of a unique multidisciplinary dataset that serves as the basis of this study.

5.1 Developing a data collection system for extreme environments

One of the most important criteria in the instrument development was data security, especially given that an effective protection against volcanic bombs, which frequently impact on the crater rim, would require an impractical amount of effort. Accordingly, the system was designed so that all data generated by the radar devices is immediately stored in two independent locations. This includes an on-site location, i.e. on the crater rim, and an off-site location that can freely be chosen. While data transfer from the radar device to the on-site data logger is conducted through a cable, off-site data are transferred through a wireless network. This approach combines the advantages of both methods, namely the safety of

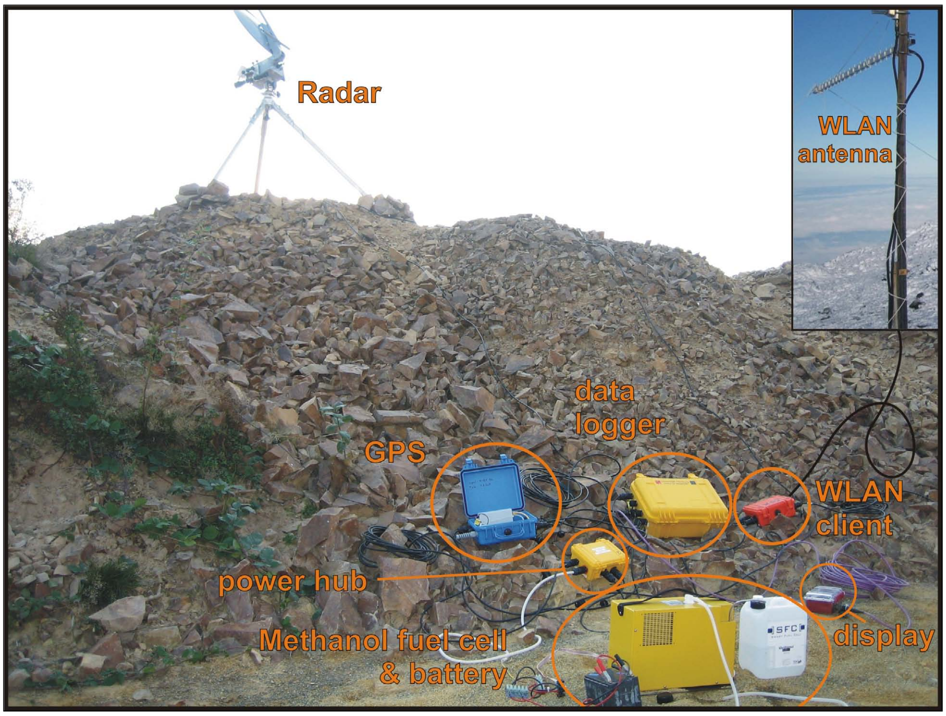

Figure 5.1: ***A modular field data recording system (here shown in a quarry setup).***

off-site data from destruction through volcanic hazards, and the reliability of on-site data, including its independence from network outages.

In the next sections I will describe the various elements of the data logging system (Fig. 5.1), starting with the newly-developed radar device, the data logger, wireless telemetry and timing devices, possible solutions for the power supply, and ending with a system demonstration by monitoring a controlled man-made explosion.

5.1.1 MVR4 - a new and fast FMCW Doppler Radar

The original design idea for the instrument originated from Matthias Hort and Malte Vöge in cooperation with *METEK*® company, as an improved version of the pre-existing MVR3 instrument (Sec. 1.5 and *Hort and Seyfried*, 1998; *Hort et al.*, 2003). Their first prototype of the MVR4 was constructed just when this study commenced, but was not yet adapted to field operation.

Therefore, an integral part of this study was its adaptation to extreme field conditions, which included the

- construction of a sturdy but lightweight portable aluminium tripod (Fig. 5.2);
- hardening against high winds and gusts;
- securing the radar's operation over a broad temperature range (-50°C . . . +40°C);

- improvement of the calibration and aiming mechanism, which needed to be operated with thick gloves at cold temperatures (Fig. 5.2);
- implementation of several soft- and hardware updates.

Major hardware construction and updates were accomplished in cooperation with the mechanical workshop of the *Centre for Marine and Climate Research* of the University of Hamburg. Hardware was optimised for field operationability, which in practice meant a size and weight minimisation to facilitate transport via air freight and on foot, as well as an easy assembly under inclement weather conditions. Accordingly, metal parts were mainly constructed from lightweight aluminium (Fig. 5.2), which additionally proved to be adequately corrosion resistant when exposed to acidic volcanic gases.

Figure 5.2: ***Newly-developed fast radar (MVR4), adapted to extreme environments.***

The radar's antenna was hardened against high winds and gusts by structurally combining two off-the-shelf 60 cm parabolic offset antennae (typically used for satellite receivers), i.e. gluing them on top of each other using a 2 cm layer of construction foam. While the inner one of the two dishes continues to act as the parabolic reflector for radar waves, the outer one merely serves as structural reinforcement. A sturdy gear head (Fig. 5.2) was designed and constructed to allow a precise adjustment of the radar's alignment around three axes while ensuring its stability in high winds. Special care was taken to allow for an easy operation under cold conditions (e.g. by using special silicone grease) and while wearing thick gloves.

The operation of the radar's electronic components under low temperatures was ensured by the installation of thermal insulation pads around the radar transceiver heads (the head is visible without insulation in Fig. 5.2), and by the use of extra flexible silicone coated cables. These were also specified as sufficiently UV proof to temporally endure the harsh lighting conditions that can be found in Antarctic high altitude locations, which are strongly exposed to the ozone hole. For the same reason, UV proof ropes were chosen for securing all hardware on the crater rim against high winds.

To ensure the correct aim of the radar beam under rough field conditions, the existing aiming mechanism of the radar needed improvement. Traditionally, the radar was aimed onto a rotating[1] radar reflector consisting of two rotating steel balls, while improving the aim by trial and error until the reflector's echo signal was maximised. A telescopic sight attached to the radar (similar to the one visible on Fig. 5.2) was then adjusted and "locked" onto the reflector[2]. After this procedure (called *radar calibration*), the telescope's cross hairs indicated the centre of the radar beam, allowing the correct alignment of the beam onto any target of interest.

***Figure 5.3:* Radar calibration device with rotating corner reflectors.** *The ∼30 cm high device is typically powered by a 12 V battery.*

In the course of this study, the rotating reflector spheres were replaced by rotating corner reflectors (Fig. 5.3), resulting in a much stronger echo power, which allowed for a more precise adjustment. Additionally, the adjustment and lock mechanism of the telescope mount was newly constructed to allow for a better handling in the field while allowing for finer adjustments.

The data output stream of the fast MVR4 radar is typically transmitted through a 100 Mbit ethernet cable to an attached data logger. The older and slower MVR3 devices produce data output through a RS-232 serial port, which can either directly be connected to a serial port of a data logger, or to a serial-to-network converter (e.g. *Netbiter^{TM}*), which sends the data stream through a wireless network to a remote computer.

For the interpretation of results it is important to note that both MVR3 and MVR4 radars typically have a blind period in every sample, i.e. they do not measure reflected radar echoes during the entire sampling interval but have a short period of time when they are "blind". This time can partially be adjusted. A typical duration of the data measurement and integration period of an MVR3 radar is 300 ms out of every one-second sample interval. The device is therefore blind during the remaining 700 ms of every second, an effect that must be taken into account when interpreting MVR3 data of explosions. The MVR4 device, depending on its current sampling rate, has a typical blind time fraction of ∼75%, i.e. with a sampling period set to 0.07 s, the radar measures only during ∼0.018 s. Due to its higher sample rate compared to MVR3 radars, the blind time of MVR4 radars typically does not play an important role when interpreting explosion signals of volcanoes.

[1]The reflector needs to rotate, so its echo peak can easily be identified in the spectrum, moving at a non-zero velocity.

[2]taking into account a parallax error resulting from the telescope's position off the beam's centre axis.

Figure 5.4: *Data logger in operation.*

5.1.2 Data recording system

For on-site data storage, I developed a data recording system with a data logger as a central element. Maximised for reliability within the available resources, a variety of design criteria had to be met:

1. high reliability;
2. ruggedness;
3. wide operational temperature range (-40°C . . . +50°C);
4. gas and water proofness, and corrosion resistance to volcanic gases;
5. sufficient computing power to process the fast data stream from an MVR4 radar;
6. safe data storage despite low temperatures;
7. lightweight, easy to carry on foot;
8. easy to operate with gloves;
9. low power consumption;
10. easy to repair under field conditions;
11. wide power input range, power glitch, peak and reversal protection;
12. cost minimisation and availability of low-cost replacement parts;
13. lightning protection through electromagnetic shielding and grounding precautions.
14. impact protection from small volcanic bombs and from shrapnel from close impacts.

Criteria 2, 4, 7, 10, and 14 were met by using a rugged, commercially available, water- and gas proof synthetic *Peli*^{TM} case as housing for electronic elements (Fig. 5.4). All electronic elements (e.g. power supply, CPU board, connector board, see Fig. 5.5 left) were implemented

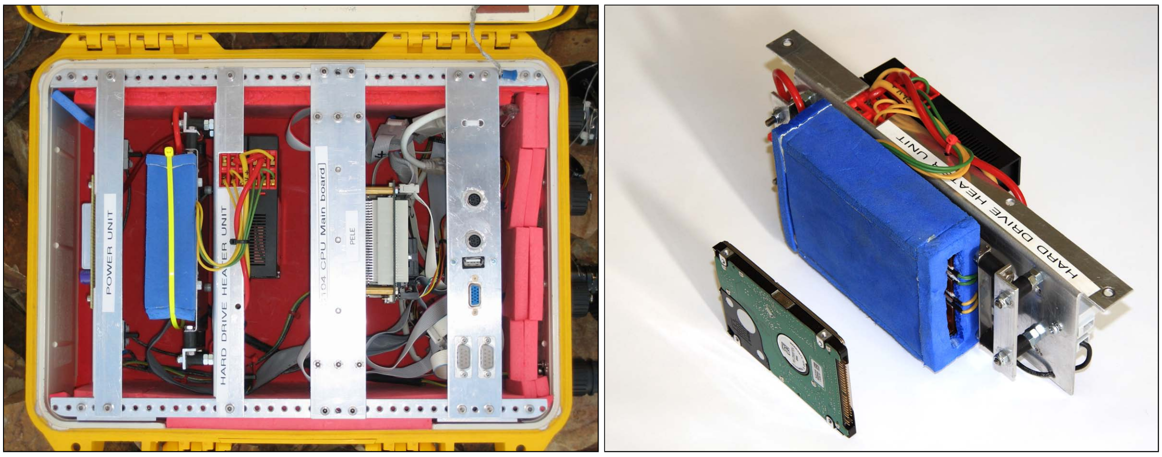

Figure 5.5:* Modular data logger. *Left: *Modules inside data logger (l. to r.): power module; hard drive module (also shown on right); CPU module; connector module for debugging.* ***Right:*** *Hard drive temperature stabilisation module with rubber shock absorbers, designed to house a standard 2.5″ laptop hard drive.*

as individual modules inside the logger. An aluminium rack was installed in the logger case as a structural backbone for all modules, allowing for quick and easy insertion or the replacement of individual modules even under field conditions (Fig. 5.5).

This modular approach was not only chosen for individual electronic components inside the data logger, but was adapted for the entire system. Accordingly, peripheral systems like the WLAN client, the timing servers, or the power distribution hub were implemented as individual and independent elements in their own respective cases, connected by cables (Fig. 5.1). This greatly simplified the identification of faulty elements, and allowed for their quick repair or replacement in the field. All elements are provided with power through cables from a central power distribution box, providing a power bus with a voltage choice of 12 and 24 V.

The core of the data logger is its central processing unit (CPU) module (Fig. 5.5 left), featuring an *AMD Geode*^{TM} ”Cool FrontRunner” single board computer (PC/104-Plus standard), providing a 366 MHz processor and 256 MB of memory at a power consumption of 6.5 W. While this computing power is sufficient to process the ∼1–2 Mbit/s data stream of a fast MVR4 radar, the CPU’s power consumption and therefore its heat generation is sufficiently low to refrain from using a cooling fan.

All used plugs, cables, and electronic parts are temperature rated down to at least -40°C, allowing for the wide operational temperature range specified in criterion 3. Additionally, the data logger provides space for a 2 cm thick foam padding layer that completely surrounds and insulates the logger’s interior. To test for the systems functionality at low temperatures, a multi-day full system test was performed at -30°C in a large laboratory freezer.

I refrained from the use of liquid crystal displays throughout, which typically cease functioning at low temperatures. Instead, for setting up the radar, for calibration, and for re-

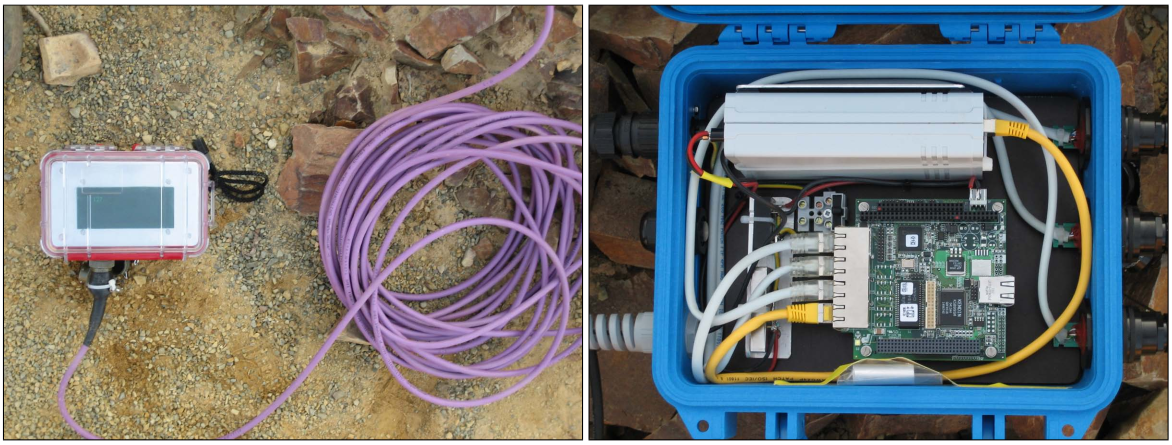

Figure 5.6: **Radar peripherals. *Left:*** *An all weather rugged control display for the radar system.* ***Right:*** *Field box with a GPS controlled NTP timing server and a network switch, providing precise timing information to the system.*

trieval of immediate state-of-health information, I developed a simple external display box that is easy to read in cold temperatures and in strong sunlight[3] (Fig. 5.6 left). The display box has four control buttons that are easy to use with thick gloves, and provide the necessary control over the instrument. Additionally, the entire system can fully be accessed and remote-controlled through a connection to a field laptop computer, either through a standard network cable or through a wireless WLAN connection.

Reliable data storage at low temperatures posed a particular challenge to the system design. This problem was solved in two ways, depending on the differing storage capacity requirements of the old and the new radars. For the older MVR3 radars, only a few GB of storage capacity was needed to accommodate several week's of radar data. In this case I decided against the use of conventional hard drives, replacing it with an 8 GB solid state disk (e.g. a *Compact Flash*^{TM} card) that served as a startup and data storage drive. Using such solid state disks, which are available as industry rated versions down to a temperature of -40°C, left the entire system without any moving parts.

For the faster MVR4 devices, a data storage capacity in the range of 100 GB was required. Since at the time of the experiment no solid state disk with such a capacity was available, the storage capacity requirements were met by using a standard 2.5″ hard drive that is commonly used in laptop computers. Unfortunately, due to their fragile movable parts, these drives typically have operational temperature ranges limited to >+5°C, and additionally are highly sensitive to shocks. Nevertheless, to allow for their usage, I constructed a temperature-stabilised, thermally insulated housing for the hard drive, which constantly monitors the hard drive temperature and provides heat if the drive temperature drops beneath +5°C (Fig. 5.5 right). The device also makes sure that after a potential power outage, the data logger only spins up the hard drive after heating it to a safe temperature. Pro-

[3]based on a vacuum fluorescence display with an attached green filter. Control commands between display and logger are transmitted through the CPU board's serial and parallel ports.

tection against potential mechanical shocks through moving or dropping the data logger is provided through a three-dimensional suspension of the drive and its copper block housing on rubber shock protectors.

In a field environment, the power supply is typically one of the major sources of problems. For example, if the available power sources (i.e. sun and/or wind) are not sufficient to meet the instrument's power needs, the voltage in the storage batteries drops. If uncontrolled, such a voltage drop can lead to a state of non-operation of connected electronic elements, which sometimes does not recover when the voltage rises back to normal, thus requiring a hard reset. Such a lockout scenario poses a major threat to data safety, especially in a remote-controlled system. A further source of power-related faults is, for example, the voltage drop over long power supply cables, or the accidental power reversal by a user.

To prevent any damage or data loss from power-related faults, a series of preemptive measures was taken. While the use of modern DC/DC power converters ensures a wide range of input voltages (9 – 36 V) at efficiencies >80%, an adequate reversal protection and additional fuses eliminate the danger from power peaks and reversals. Furthermore, the system was protected by so-called *watchdogs*, which are small independent electronic circuits that monitor the operation of the CPU, and perform a system reset in case of an undefined state. While the CPU board itself has two of them, another watchdog was manually installed in the data logger. The latter specifically monitors the state of the wireless network and is programmed to perform a power cycle of the network hardware in case of a problem (further described in Sec. 5.1.3).

Low-level protection against lightning and discharges of static electricity was achieved by the introduction of a single electrical ground potential for the whole system while avoiding grounding loops. Lightning protectors were introduced at all ethernet and antenna cable connections. A low-level electromagnetic shielding of the logger was achieved by applying a layer of specially conducting shield paint inside the logger case, which was electrically connected to the system ground. It must be noted that while these measures provide sufficient protection from static electricity and possibly from lightning strikes in the wider vicinity, they do not provide adequate protection from a direct lightning strike. Protecting from a direct strike would require an immense effort in grounding measures, and should be implemented on an individual basis, depending on the lightning hazards at the respective field location. In Antarctica, the danger from lightning strikes is relatively low in comparison to static voltage buildup due to blowing snow, thus I regarded further preemptive measures to the ones described above as unnecessary.

A minimisation of costs was achieved by the exclusive use of standard ("off-the-shelf") electronic parts. Mechanical hardware was manufactured by an in-house mechanical workshop, and special care was taken to keep all elements simple, easily replaceable, and reproducible.

5.1.3 Wireless telemetry, precision timing & power supply

When more than one radar is used at the same time, an effective time synchronisation and a centralised base station to control the different instruments is essential. Additionally, for data safety reasons in a hazardous environment, it is necessary to download and store data in real time at an off-site location. To accomplish this, all data loggers and radars in the system are connected through a wireless local area network (WLAN). This is realised through the use of several commercially available industrial wireless clients and access points that are rated to operate at low temperatures (for this study I used *Smartbridge*^{TM} products). Each radar-logger combination is connected through a LAN cable to either a client, an access point, or a repeater station, which in return is connected to a WLAN antenna (Fig. 5.1 inlay), effectively spanning a wireless network over the experiment site.

Commercially available products do not always hold what product advertising promises, and in accordance with this, occasional unexpected problems with the WLAN devices occurred during field tests, leading to unresponsive access points and therefore potentially to network outages and lockout situations. These can only be solved by a hard reset of the WLAN device, i.e. through a power cycle. To avoid these problems in the field, a special watchdog device (*iboot*^{TM}) was installed in the data loggers, continuously monitoring the status of the WLAN device. In case of a problem, such as an unresponsive device, the watchdog switches off the power to the WLAN device for a few seconds, therefore forcing a hard reset and resolving a potential freeze and the associated network outage.

Precision timing of all devices in the network is achieved by the use of two or more independent time servers in the network, which distribute precise timing information via the *Network Time Protocol (NTP)*. The devices, manufactured by *MTECH*® company, obtain the exact time from signals of the *Global Positioning System (GPS)*. NTP clients run on all data loggers and on the MVR4 radar, constantly querying the two NTP servers in the network, and by comparing network latencies, determining the precise time down to a few 100ths of a second. Ideally, one server is connected via cable to each data logger or radar (Fig. 5.6 right) so that precise timing is continued even in the case of a network outage.

The total power consumption of the radar system is strongly dependent on the choice of devices. A typical field station setup consists of a radar device (MVR3: ∼18 W[4]; MVR4: ∼23 W), a data logger (with hard drive: ∼13 W when writing; with flash drive:∼8 W), a GPS NTP server (3 – 5 W), and a WLAN client (4 – 6 W). In case of an MVR3 radar setup, this adds to a total of 33 W; a system with an MVR4 radar needs around 45 W. When power consumption is a critical constraint, the data logger and NTP server can be omitted, lowering the system's power consumption to around 25 W at the cost of data safety. As an example, such a reduced system can run for around 30 hours continuously on a standard 65 Ah car battery.

Even though it is the most important element in the system, an all-encompassing solution

[4]all given power consumptions are averages, and include the DC/DC voltage converters that transform the system input voltage of 9–36 V into the stabilised voltage needed by the respective device.

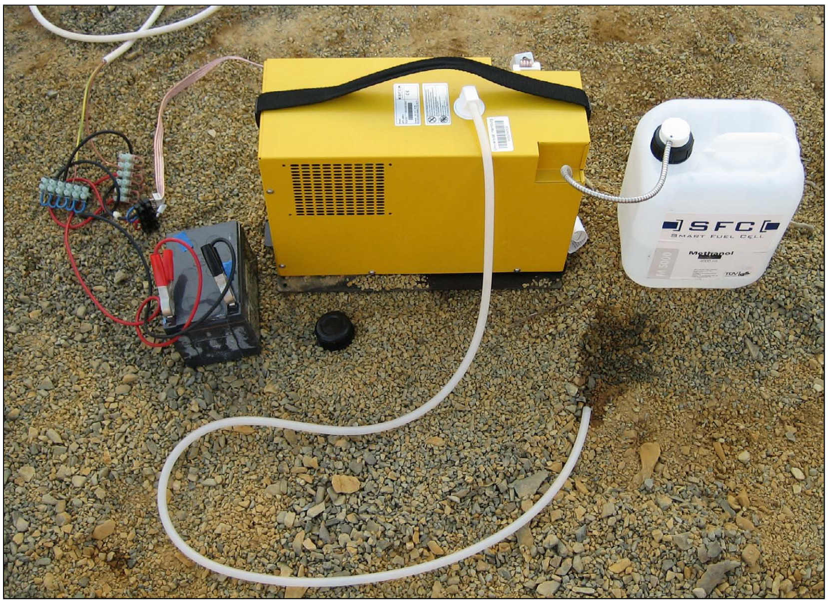

Figure 5.7: Power supply. *A methanol fuel cell providing 50 W continuous power.*

for the power supply does not exist. In most field experiments, the local setting dictates which power sources can be used. In the case of Antarctica, these choices are solar and wind power, simply because both of them are abundant in the Antarctic summer. Since they are not an explicit part of the system developed in this study, I will discuss them in Section 5.2.4 as part of the experiment description.

A very lightweight and versatile power source that was integrated into the system developed here, is a so-called *Methanol fuel cell* (Figs. 5.1 & 5.7), a small but powerful electric generator recently developed by *SFC Smart Fuel Cell AG®*. Weighing only 7 kg, it generates 50 W of continuous power by converting ~0.05 litres of methanol fuel per hour into water vapour and carbon dioxide. A 10 litre tank of methanol therefore lasts for more than a week when supplying a system that uses 50 W continuously, or for more than two weeks when supplying a 25 W system buffered by a small 12 V battery (Fig. 5.7).

Even though such a fuel cell would be an attractive alternative to the available energy sources in Antarctica, the technology was new at the time of the experiment and its reliability unproven under harsh environmental conditions, particularly under low temperatures. I therefore decided against using it in Antarctica in favour of the more established and proven solar and wind energy.

5.1.4 System test: monitoring a quarry blast with three radars

A quarry blast in Koschenberg, Germany, was observed with three radars on October 13, 2005, to test the setup of the radar system with precise timing capabilities, wireless data transmission and telemetry. The purpose of this section is to demonstrate the system setup in the field. The gained data will later be used to demonstrate a data processing method for calculating 3D velocity vectors (Appendix B.1.1).

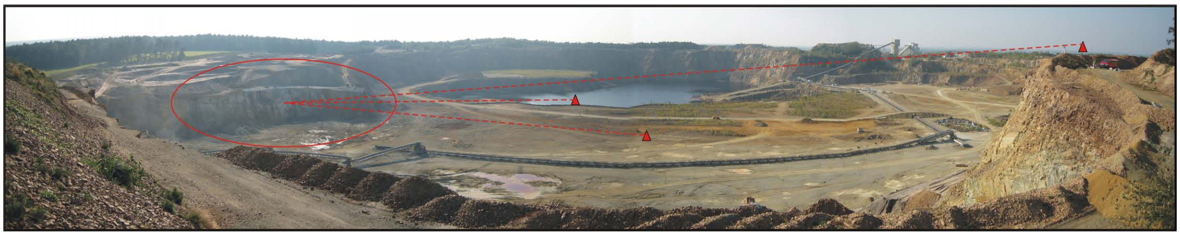

Figure 5.8: ***Quarry panorama*** *with radar locations (triangles) and blast wall (marked by an ellipse). The target region illuminated by the radars was much smaller than the wall, and is shown in Fig. B.2*

Figure 5.8 shows the setup of the blast site and indicates the position of the three radars. For the blast, 13 tons of explosives were placed in 60 vertical boreholes, aligned in three rows above the rock face. The ignition sequence was completed within around 0.5 seconds and moved from left to right (as seen from the radars), fracturing roughly 100,000 tons of rock.

The blast was observed by three radars at distances between 250 m and 320 m, sampling at 1 Hz (see Fig. 5.9 top). A laptop base computer was used for central data storage and to control the system. While the collocated base site and the MVR4 radar were powered by a 50 W methanol fuel cell, the other two radars ran off a car battery, respectively. The setup of the entire observation system took about half a day. All devices performed nominally during the test, nevertheless important information on necessary system improvements was gained. The obtained data and results can be found in Appendix B.1.1.

Figure 5.9: ***Radar pointing on the quarry wall after the blast.***

5.2 Multidisciplinary experiment at Erebus volcano, Antarctica

This section describes the experiment conducted at Erebus volcano (Figs. 1.2, 5.10 & 5.11) in the 2005/2006 field season, leading to the collection of a unique multidisciplinary dataset. While the collection of radar data (Sec. 5.2.1) was the responsibility of the author, the other elements of the dataset were collected by various working groups and individuals. *Jones et al.* (2008) installed and maintained a network of several acoustic infrasound microphones (Sec. 5.2.2), whereas staff of the Mount Erebus Volcano Observatory (MEVO, see *Aster et al.*, 2004) were responsible for the collection of infrared video data (Sec. 5.2.3).

The field campaign took place from 1 December 2005 until 3 January 2006, preceded by several weeks of preparation in the nearby McMurdo Base and a short altitude adaption period in an acclimatisation camp at medium altitude. The field camp was set up at the pre-existing *Lower Erebus Hut* (LEH, Fig. 5.12), located on the summit plateau of Erebus volcano at an altitude of 3400 m, which is about 170 m lower than the lava lake at $\sim$ 1.8 km distance.

A detailed elevation model of the crater region is given in Figure 5.10 (therefore supplementing Figure 1.2, which shows a satellite image of the whole volcano including the location of LEH). All relevant site coordinates are additionally given in Table 5.1.

Initial transport to and from the field camp was conducted by helicopters with additional frequent logistical support from McMurdo station (run by the US National Science Foundation) when weather conditions were appropriate. Transport in the field was accomplished by snowmobiles, allowing motorised travel to the base of the crater hill, some 150 vertical metres below the crater rim. From there, all instruments were carried on foot to their final location on the crater rim (Fig. 5.17).

Frequent blizzards and inclement weather conditions with temperatures down to -45°C restricted the number of opportunities for the setup of instruments. Working on the crater rim was only possible in good visibility conditions to reduce safety hazards originating from impacting explosion ejecta, which on several occasions travelled well beyond the crater rim (indicated by dots in Fig. 5.10). For the same reason, field teams were in close VHF radio contact with the field camp at LEH or with McMurdo station operations (MAC OPS) at all times, and operated in groups of at least two persons.

During the field season, explosions at Erebus typically occurred several times per day, and originated from the phonolitic lava lake (called Ray Lava Lake), which had a diameter of around 40 m the time. Ray Lava Lake was situated $\sim$ 200 m below the crater rim of a roughly 500 m wide crater (Fig. 5.15). Most explosions lasted for several seconds, with an impulsive main acceleration phase lasting for around one second. They often ejected a large number of decimetre to metre sized lava bombs (Fig. 5.14), covering distances up to several hundred metres from the lake.

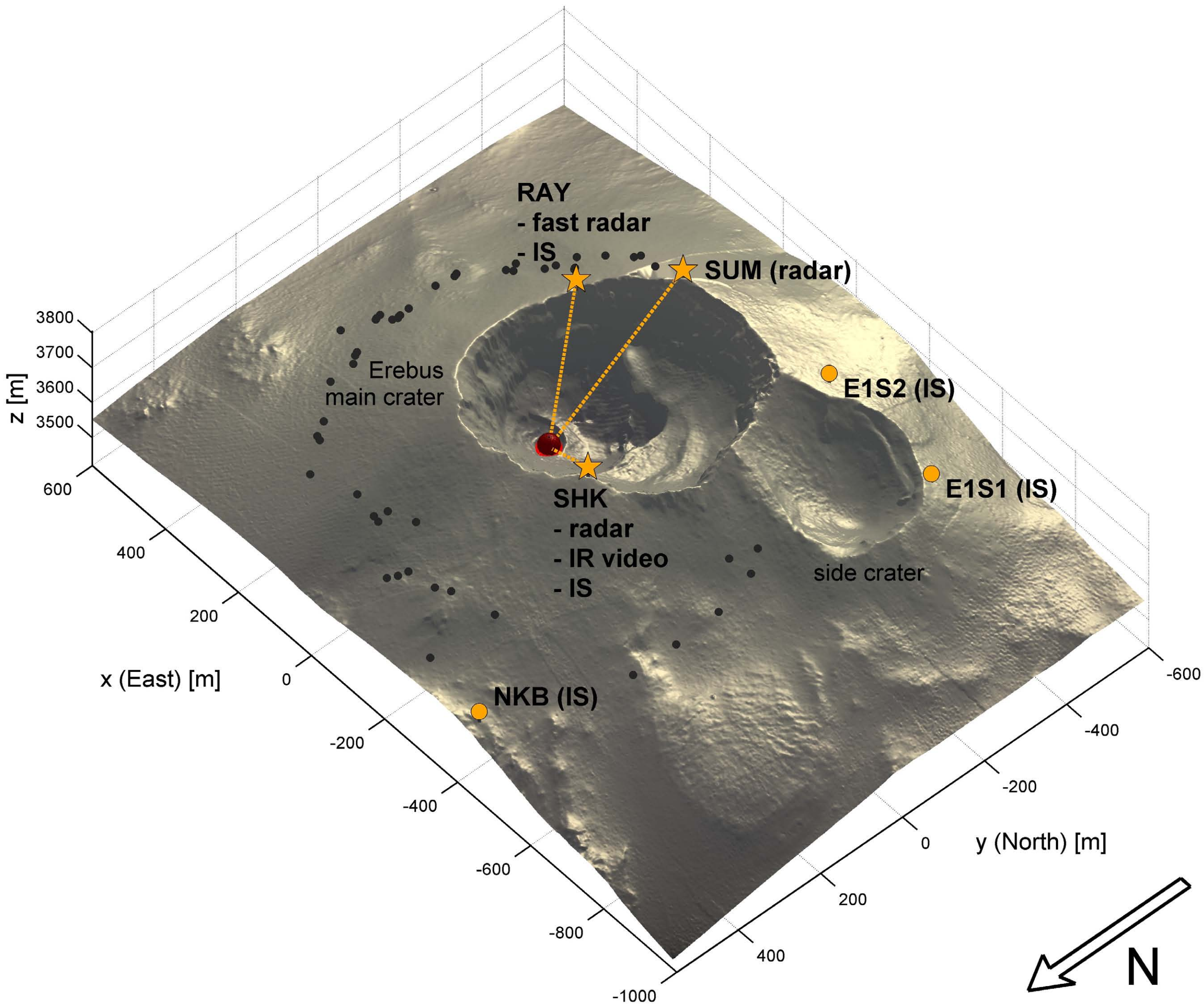

***Figure 5.10:* Digital elevation model of Mt. Erebus crater region.** *Radar and multi-instrument sites are shown as stars, all three of them are located on the crater rim with a direct line of sight to Ray Lava Lake (indicated as dashed lines). The lava lake is sketched as a red circle with an indicated, 40 m wide bursting bubble above. Orange circles show infrasound (IS) sites located at lower elevations on the crater flanks. The underlying horizontal grid is centred under the lava lake coordinates (Tab. 5.1), the vertical axis denotes elevation above sea level. Dark grey dots indicate the positions of the farthest flying bombs that were found (Bomb GPS locations were kindly provided by Nelia Dunbar, see also Gerst et al., 2008). The elevation model was acquired by airborne laser altimetry (Csatho et al., 2005).*

Name	Instrument type	Latitude	Longitude	Elevation
LEH (*Lower Erebus Hut*; base camp)	environmental monitoring	77.51039° S	167.14587° E	3400 m
RAY (*Ray's Site*)	fast radar	77.52857° S	167.17057° E	3769 m
	infrasound microphone	77.52856° S	167.17083° E	3769 m
SHK (*Shackleton's Cairn*)	radar	77.52605° S	167.15608° E	3774 m
	infrared video camera	77.52605° S	167.15608° E	3774 m
	infrasound microphone	77.52607° S	167.15585° E	3774 m
SUM (*Summit*)	radar	77.52991° S	167.16534° E	3790 m
NKB (*Nausea Knob*)	infrasound microphone	77.52199° S	167.14740° E	3627 m
E1S1 (*E1 Site*)	infrasound microphone	77.53045° S	167.13984° E	3712 m
E1S2 (*E1 Site*)	infrasound microphone	77.53034° S	167.15091° E	3769 m
Ray Lava Lake centre	none	77.52669° S	167.16528° E	3570 m

***Table 5.1:* Station locations (WGS84).** *The position of instrument sites were all determined by differential GPS (using Trimble receivers, supported by UNAVCO) with a precision better than +/- 10 cm (N. Dunbar, pers. comm.). Data were processed using a permanent base station at Lower Erebus Hut. The location of the lava lake centre was calculated using several distance measurements (not shown) with a Leica Vector GIS laser range finder relative to the crater rim station locations. The position of the permanent lava lake (named* Ray Lava Lake*) should be exact to within 10m, but it might not be stable over a time span of several years. The lake diameter was ∼40 m at the time. Note that inside Erebus crater there is another lava lake called* Werner Lava Lake*, which is transient in nature and much smaller than Ray Lava Lake.*

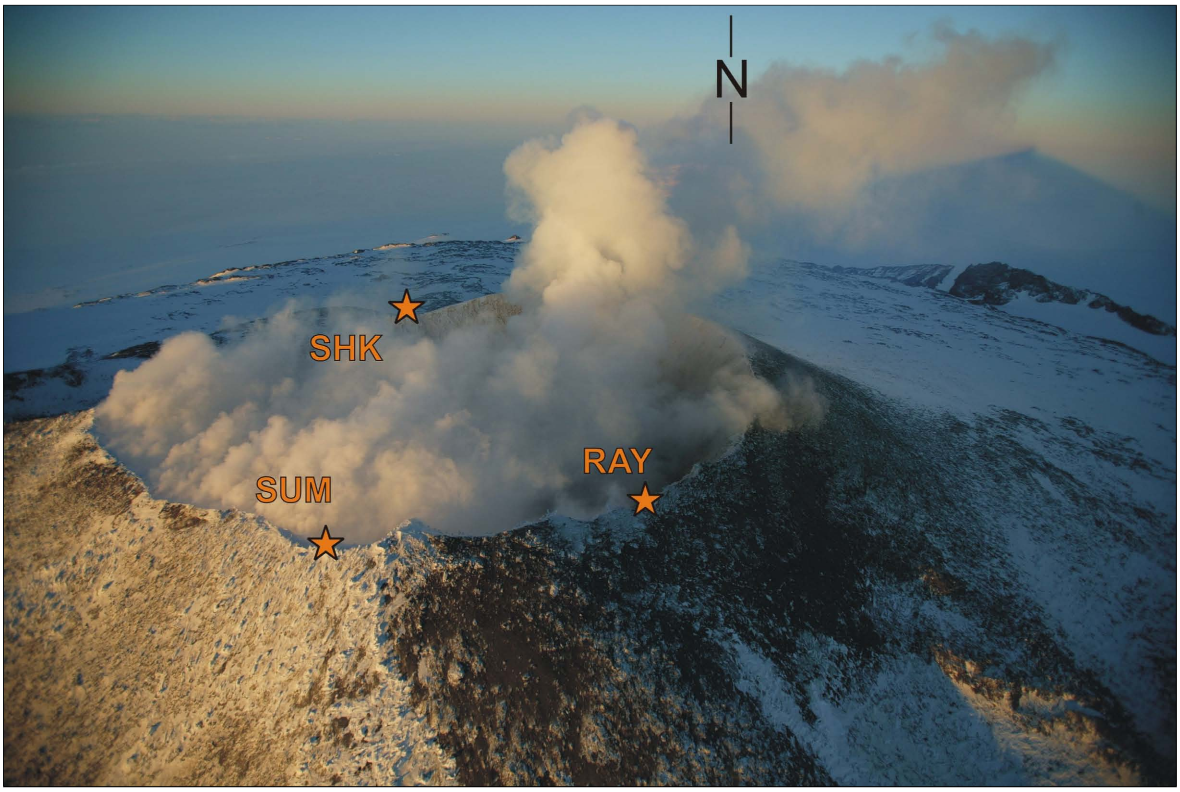

***Figure 5.11:* Photograph of Mt. Erebus crater region** *in the austral summer 2005/06, modified to include station locations. The location of Lower Erebus Hut on the summit plateau is obstructed by a volcanic plume of mainly water vapour and CO_2. This photograph was kindly provided by George Steinmetz ©.*

***Figure 5.12:* Field camp at Lower Erebus Hut,** *at an elevation of 3400 m. The mountains in the background are the* Transantarctic Mountains *at a distance of more than 100 km (A. Gerst, 2007).*

5.2.1 Doppler radars

The technical state of the Hamburg University Doppler radar monitoring system and the environmental conditions in the field allowed me to exceed the originally proposed experiment outline (DFG proposal HO1411-16/1) in two major points. Firstly, three radar devices were installed on the crater rim instead of one. Secondly, the timely completion of the development of a new and comparatively fast radar device called MVR4 (Sec. 5.1.1) not only increased the available sampling rate from 1 sps to ~14 sps, but also expanded the radar's velocity measurement range and resolution. These two additions allowed the observation of Strombolian explosions at Erebus not only in much more detail through the higher sampling rate, but also to observe them in three dimensions from three different observation points on the crater rim.

Three sites on the crater rim (RAY, SHK, SUM) were occupied with FMCW Doppler radar devices (technical information in Sec. 1.5 & 5.1.1), all of them with a direct line of sight to the lava lake, at an observation distance of ~300 – 400 m (leading to observation elevation angles between 31° and 41°, see Fig. 5.10 & Tab. 5.1). The fast MVR4 radar was installed at RAY site, operating with a sampling rate of ~14 sps. Two slower MVR3 radars were installed at sites SHK (Fig. 5.13) and SUM, operating at ~1 sps. The choice of sites was a tradeoff between optimal observation conditions (i.e. three maximally different azimuth angles from the lava lake), existing power supplies, and safety issues. While observation conditions were optimal at a site on the Northeast side of the crater rim, this location was avoided due to safety concerns regarding its frequent bombardment with volcanic ejecta (Fig. 5.10).

The centre areas of the radar beams observing the lava lake surface had a diameter of around 20 m, resulting from the beam spread angle of ~ 3° at -10 dB (Fig. A.1). The area of observation on an expanding bubble was large enough to ensure that its surface point that was moving fastest towards the radar was observed during at least the first second of each explosion, even when the bubble surface strongly bulged upwards during an explosion.

Figure 5.13: *Instruments at Shackleton's Cairn (SHK) site at an elevation of 3774 m.* *Left:* *The instrument in the foreground is a FTIR spectrometer (not used in this study), followed by a Doppler Radar and the thermal infrared video camera (C. Oppenheimer, 2005).* ***Right:*** *video camera closeup (A. Gerst, 2007).*

Figure 5.14: *Left:* *Alignment of the radar at SHK site. A directional Yagi WiFi antenna, as well as an omnidirectional dipole antenna is mounted on the pole on the left. The infrared video camera is located just out of view to the right.* ***Right:*** *fresh lava bomb, still partially molten and glowing inside (A. Gerst, 2005).*

Figure 5.15: *Ray Lava Lake seen from the Doppler radar's perspective* *on a day with good visibility from SHK site. The distance to the lake is ∼300 m.* ***Right:*** *Closeup view of currently ∼40 m wide Ray Lava lake (A. Gerst, 2005).*

All three radar devices sent their data directly through a wireless network to a database server located at the Lower Erebus Hut field camp. This allowed for a real-time monitoring of the data and the direct assessment of state of health information, as well as the issuing of control commands from the field camp. For additional data safety in the case of network outages, the radars at RAY and SHK had a custom built data logger (Sec. 5.1.2) directly attached, redundantly recording all data onto a temperature-stabilised hard drive. For weight and power saving reasons, the radar at SUM site, located at a relatively inaccessible place close to the summit of the volcano, did not have an additional data logger attached. While strongly reducing the power consumption of SUM site, the drawback of this practise was that its data could only be recorded as long as the wireless network was operating.

Precise synchronisation of the three radars down to a few milliseconds was ensured by the use of two independent, *M-TECH*® NTP servers in the network (Sec. 5.1.3), synchronised with the Global Positioning System, and located at SHK and RAY sites.

Before installation on their respective crater rim sites, all three radars were calibrated at Lower Erebus Hut, meaning that their radar beams were aligned with a telescopic sight attached to the radar, using a portable rotating radar reflector (Sec. 5.1.1). This practise allowed for the correct pointing of the radar beam onto the target simply by aiming through the telescopic sight (the mount for the telescope can be seen in Fig. 5.15; the telescope itself was not attached at the time). Subsequently, the radars were transported and anchored on the crater rim, using long ground pegs and special rope.

Valid radar data were obtained from 15 December 2005 to 2 January 2006, as will be described in more detail in the Data Section (an observation time overview is shown in Fig. 6.1).

5.2.2 Infrasonic acoustic microphones

A network of several acoustic microphones recording in the infrasonic frequency range (<20 Hz), was installed by *Jones et al.* (2008), complementing and replacing pre-existing microphones (*Aster et al.*, 2004). The network consisted of seven sensors, of which five were operating at the time of the radar experiment. They were installed at distances of $\sim$ 300 – 800 m from the lake (Fig. 5.10 & Tab. 5.1).

Two different sensor types were used (*pressure transducers* and *elecret condenser elements*; for further technical details see *Jones et al.*, 2008), mainly differing in their dynamical range. The more dynamical pressure transducers (installed at SHK site) have a dynamic range of $\pm$125 Pa and a flat frequency response down to 0.01 Hz (3 dB corner), controlled by a mechanical low pass filter attached to the microphone (*Jones et al.*, 2008). Elecret condenser elements (installed at RAY, NKB, E1S1 & E1S2) have a dynamic range of $\pm$50 Pa and provide useful data down to frequencies of 0.05 Hz, with a 3 dB attenuation corner at 0.5 Hz (*Aster et al.*, 2004).

***Figure 5.16:* Crater region seen from the field camp at Lower Erebus Hut,** *located on the summit plateau at a distance of about 1.7 km from the crater rim. From here, transport of equipment was accomplished by snowmobiles and by foot. All tents needed to be protected by snow walls to withstand the frequent and powerful Antarctic blizzards (A. Gerst, 2007).*

Figure 5.17:* Methods of transport (decreasing level of sophistication). Left:** *hooking up a cargo transport net to a hovering helicopter.* ***Centre: *Transport of gear to within 400 m of the crater rim is achieved via snowmobile.* ***Right:*** *The crater rim can only be approached on foot (A. Gerst, 2007 & 2005).*

5.2.3 Infrared video

A thermal camera was located on the crater rim, deployed by staff of the Mount Erebus Volcano Observatory (MEVO , see *Aster et al.*, 2004) at SHK site (Fig. 5.10), co-located with a Doppler radar. The camera recorded in an overlay mode of both the infrared and the visible spectrum and produced an analog video stream at a frame rate of 30 frames per second (fps). The analogue video stream was telemetered via a 900MHz radio link to a digitiser at *Lower Erebus Hut* (LEH), which produced a time stamped digital video stream of 640x480 pixel frames at a rate between 15 and 30 fps, depending on the variable quality of the radio link.

Relatively constant ambient lighting conditions were ensured by the polar latitude of 77.5° South, which prevented the sun from descending below the horizon even at "night" times in the Antarctic summer. In contrast to the microwaves used by Doppler radars, infrared radiation is strongly attenuated by clouds. Therefore, weather and volcanic plume conditions above and inside the crater strongly influence the quality of thermal video images.

Figure 5.18:* Field trouble. Left:** *Rime ice on instruments, typically building up in the final hours of large storms or blizzards before the weather improves.* ***Right: *RAY power site after a direct hit of a medium sized bomb. The large wooden battery boxes were only slightly scorched, thus narrowly escaping total destruction (A. Gerst, 2005).*

5.2.4 Power supply

Power for all stations was supplied by solar panels and wind generators. SUM site, a temporary installation that was only used for this experiment, had a portable array of solar panels installed with a total maximum power of ∼200 W[5]. Radars at SHK and RAY sites both tapped into the permanently installed MEVO power supply at the respective sites (*Aster et al.*, 2004). Each of these consisted of a solar array and a wind generator, located several hundred metres beyond the crater rim for operational safety reasons. Power was transferred to the crater rim via a cable. Despite its relatively safe location, RAY power site was partially destroyed by a direct hit from a medium sized volcanic bomb in mid December 2005 (Fig. 5.18 right).

5.2.5 Wireless network

The wireless local area network that was used for data transmission between radar sites and base camp consisted of commercially available *Smartbridge*® 2.4 GHz WLAN clients installed at sites RAY and SUM, as well as a repeater station ("XO_2^{TM}") installed at SHK site. SHK site allowed a direct line-of-sight connection to the base camp at Lower Erebus Hut, where a wifi access point provided the necessary network infrastructure. All sites used 20 dB directional Yagi antennae, the repeater site additionally used a 13 dB round dipole antenna for its connection to crater rim sites (as can be seen in Fig. 5.14). The used protocol was IEEE 802.11b, allowing for a maximum theoretical data transfer rate of 11 Mbps. However, during the experiment the typically achieved throughput was only a fraction of this (<2 Mbps).

[5] while this was the maximum achievable power output, the actual multi-day average output power was about 10% of that value.

The wireless architecture did not only provide a real time data downlink to the base camp, it also allowed remote access of all radar devices and their data loggers on operation system level, enabling the continuous download of state of health information of all involved instruments. A very useful additional feature of this wireless network architecture was that it could be easily accessed from a portable laptop computer (with a standard WLAN card) from virtually anywhere in the crater region, allowing a simple and wireless way to check recording instruments in the field.

The main cause for the occasional network outages that occurred during the experiment was found to be short power outages or voltage drops. These sometimes caused the WLAN devices to lock up until manually restarted by a power cycle. This problem was largely overcome by the introduction of small watchdog devices (installed in the data loggers) that continuously checked the network availability, and which automatically power-cycled the whole station in case of a device lock-up (see Sec. 5.1.3). Yet, despite these measures, the system occasionally locked up because even the watchdog devices proved to be vulnerable to power glitches under field conditions. Considering that severe weather conditions frequently eliminated the possibility of leaving the camp and servicing an instrument for time spans of up to a week, these lockout situations posed a potentially serious threat to data safety. To finally eradicate the problem, these vulnerable parts of the system were protected by a simple electromechanical timer, programmed to power cycle the connected devices every four hours.

An additional, entirely mechanical cause of network failures was the breaking of Yagi antennae through the buildup of rime ice (Fig. 5.18 left). However, this problem could quickly be overcome by a more sturdy suspension of the antennae by additional ropes.

CHAPTER 6

DATA

This section describes data that was collected in the frame of this study at Mt. Erebus volcano, Antarctica, from December 2005 to January 2006. It concentrates on data from a fast MVR4 Doppler radar device operating at location *Ray's* (RAY) on the crater rim, as well as data from an infrared video camera installed on the crater rim at position *Shackleton's Cairn* (SHK; see Tab. 5.1).

A short section will address data from two further, slower, MVR3 radar devices that were positioned at locations *Shackleton's Cairn* and *Summit* (SUM) on the crater rim. Additionally, I will briefly address recordings of acoustic infrasound that will be used later. The microphone setup and the acoustic data collection were not part of this study, but were carried out by *Jones et al.* (2008, see also Sec. 5.2.2). Likewise, infrared video data were collected by staff of the *Mount Erebus Volcano Observatory* (MEVO).

In Chapter 7 I will use the data from the fast radar to derive mechanical and energetic properties of typical bubble burst explosions with a high temporal resolution. The combined data from all three radar devices will be used in Chapter 8 to derive 3D vectors of explosion directivity, including a more detailed discussion of the data from the two slower radars.

Figure 6.1 gives a temporal overview of all explosions that were observed with the three radar devices, located at RAY, SHK and SUM sites. For an overview of all station locations and their coordinates, see Figure 5.10 and Table 5.1. A total of 55 explosions were recorded in 18 days of intermittent operation, classified into several different explosion types, as will be defined in the next sections.

For a better comparison between explosions detected by radar and explosions that were automatically detected by the infrasound network (*Jones et al.*, 2008), acoustic trigger events are included in Figure 6.1 as dashed lines. Their height indicates the relative sound pressure measured at the crater rim. Both the radar and the acoustic system were only intermittently operating, so not all explosions were detected by both systems together. Radar data were automatically and manually sighted for medium sized and large explosions, so the detection rate during radar operating hours should be close to 100%.

In general, operational failures were mainly caused by power outages due to severe polar storms covering solar panels with snow and depositing rime ice on wind generators,

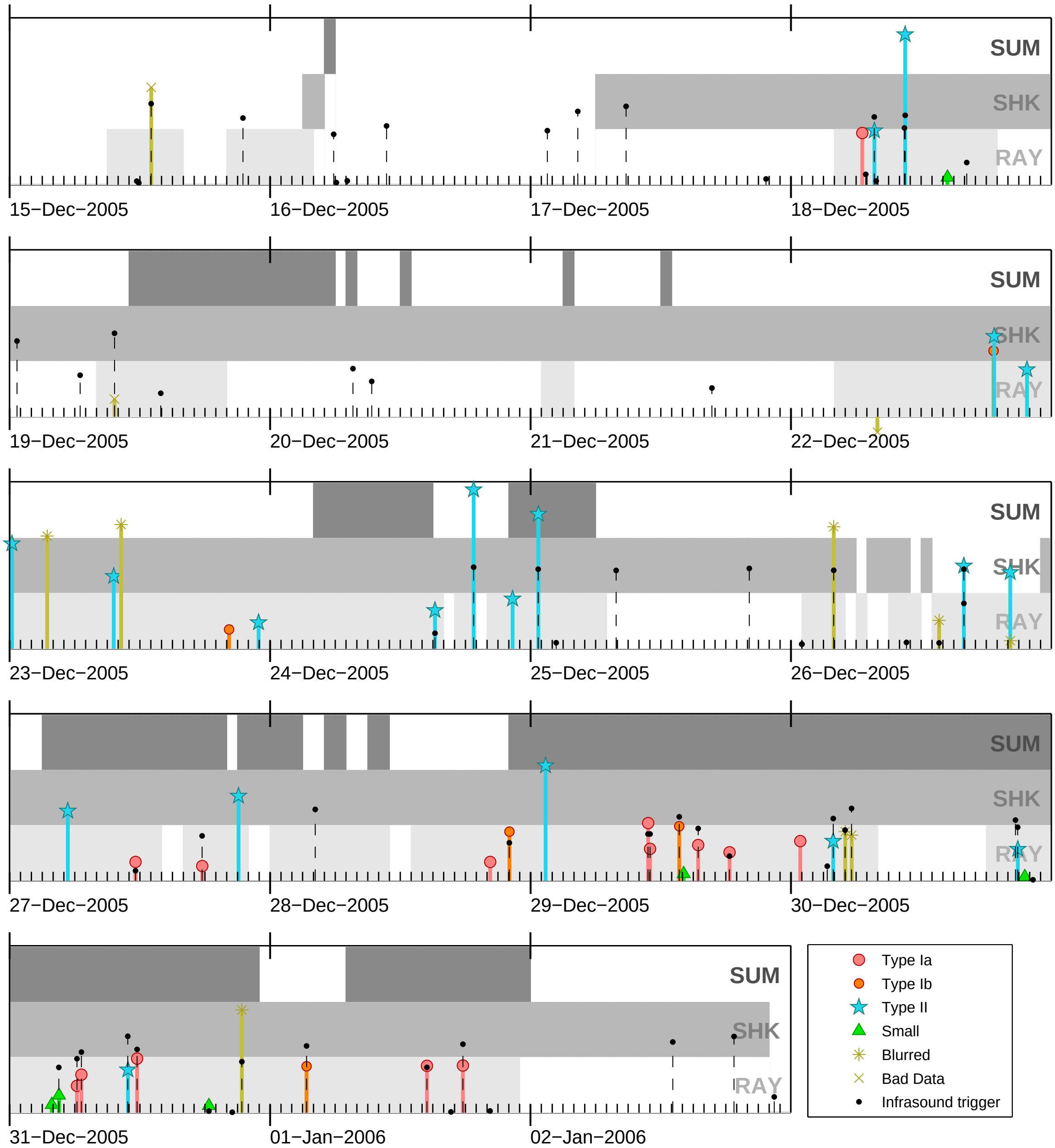

***Figure 6.1:* Overview of all explosions observed with radar.** *Underlying gray shades indicate the times at which the three radars were operating (located at SUM, SHK & RAY). Coloured vertical lines and symbols denote the kind of explosion that was detected, their relative height indicates the maximum detected velocity. Dashed black lines denote explosive events detected by the automatic infrasound triggering system (intermittently operating); the line heights are scaled with measured sound pressure. Major and minor tick marks indicate days and hours, respectively. Outages shorter than one hour are not explicitly shown. Note that at 16-Dec, the short operating period of SUM and SHK radars was an off-site calibration test only.*

sometimes for several days at a time. Additionally, occasional network outages sometimes prevented the recording of data from the radar located at SUM, because this device did not have a local data logger attached but transferred its data through the wireless network to a data logger at the base camp, located at the Lower Erebus Hut (LEH).

6.1 A visual overview

The thermal video camera installed at the crater rim (*Aster et al.*, 2004, see Sec. 5.2.3) allowed for the visual observation of explosions. However, weather and volcanic plume conditions permitted the video observation of only about half the explosions that were observed by radar. A characteristic snapshot of each of the visually observed explosions is shown in Figure 6.2 to provide an overview of explosions. The original video files are available in the supporting online material (*SOM*). Additionally, three sequences of several snapshots, each depicting one of the three different explosion types, are shown in Figures 6.10 to 6.12 below.

Explosion types. Explosions at Erebus were classified into four different types: *I*, *II*, *small*, and *blurred*, according to their explosion characteristics. Types *I* and *II* are by far the most frequent, and can be seen as the "standard" type explosions that are observed at Erebus. The main difference between them is the way bubbles expand. Their exact characteristics will be discussed in detail in the following sections. *Small* explosions, as the name suggests, resemble a smaller and lower energetic version of types *I* and *II*. This influences several of their characteristics, which will also be discussed. Finally, the naming of *blurred* explosions refers to their appearance in the radar velocity spectra, where they have a somewhat fuzzy, or blurred shape that prevents the picking of cutoff velocities (Sec. 4.1.2). Visually, *blurred* explosions are very similar to type *I* and *II* explosions, and might simply be a degenerated version of them. I will now successively describe the characteristics of all explosion types, shedding further light on their nature.

While type *I* and *II* explosions are equal in number (19 each), only six *small* and eight *blurred* explosions were detected. Video observations are more sparse, amounting to 11 type *I* and six type *II* explosions. Additionally, four *small* and one *blurred* explosion could be observed with a lower frame rate of 1 fps.

Video data show that type *I* & *II* explosions typically affected the entire surface of the lava lake[1]. *Small* explosions, due to a smaller bubble radius, only affected a part of the lake surface. In these cases the approximate radius of this affected area (i.e. their *footprint*) was determined from video (as annotated on the snapshots).

In addition to explosively bursting bubbles there were numerous very small gas bubbles ($R < 2$ m) that reached the surface of the lake without any sign of explosion. These very

[1] The snapshots in Figure 6.2 show some of the type *II* explosions in their early phase (e.g. II_P) before the explosion affects the whole lake surface.

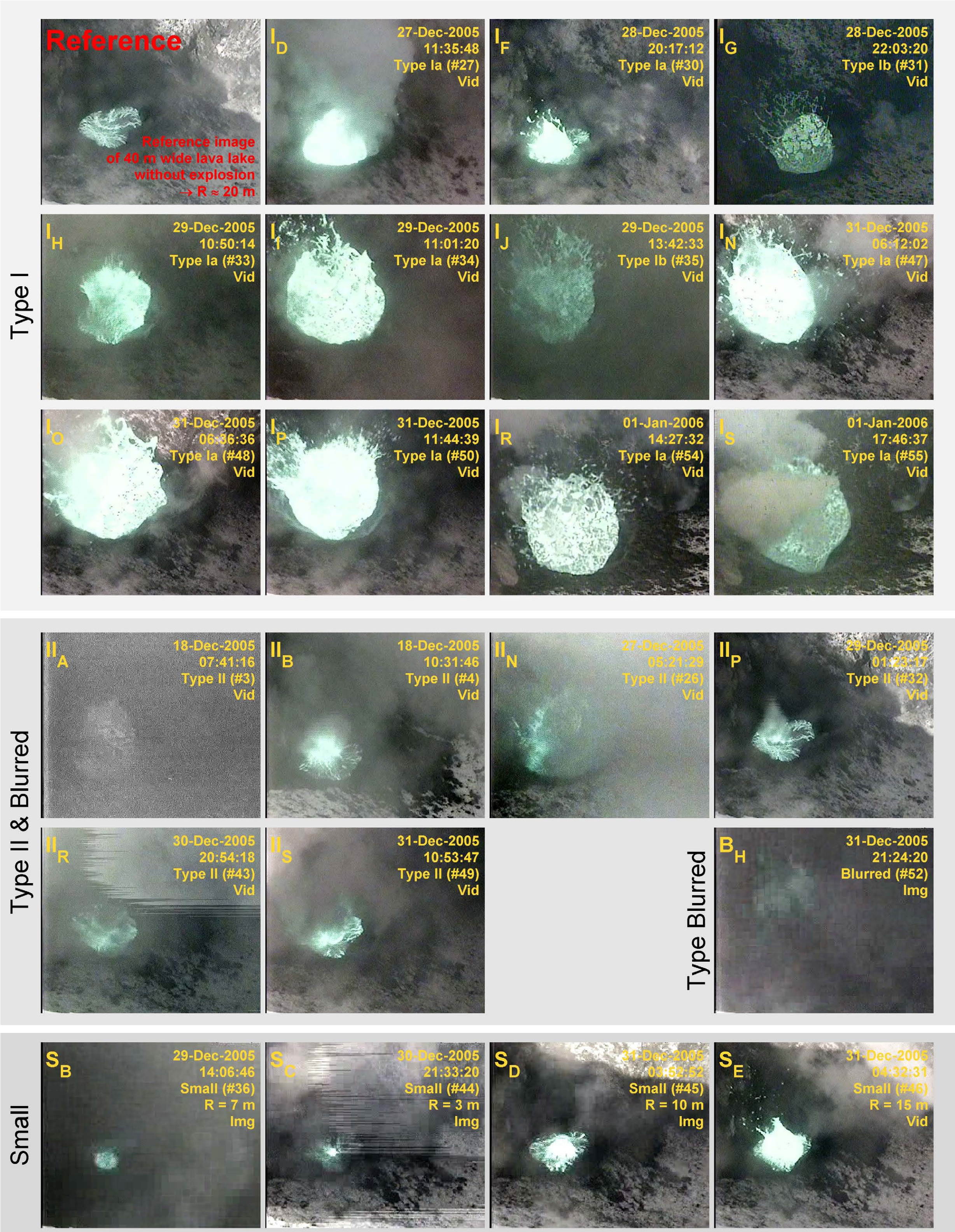

Figure 6.2: Thermal video snapshots of explosions *that were observed both by radar and the MEVO thermal camera (weather permitting). "Hot" pixels are shown in green, ambient tempered pixels are shown in their natural colours. All videos are available in the supporting online material (SOM). The unique identifier for each explosion (upper left corner) consists of a prefix showing the explosion type (I, II, S, & B), and an alphabetical index increasing in temporal order (see Fig. 6.6 below). Explosions that are annotated with "Img" are only available as low resolution video with 1 fps. Where stated, R denotes the approximate radius of the affected region of the lake surface (otherwise $R \approx 20$ m, i.e. the whole lake surface was affected for all but* small *explosions).*

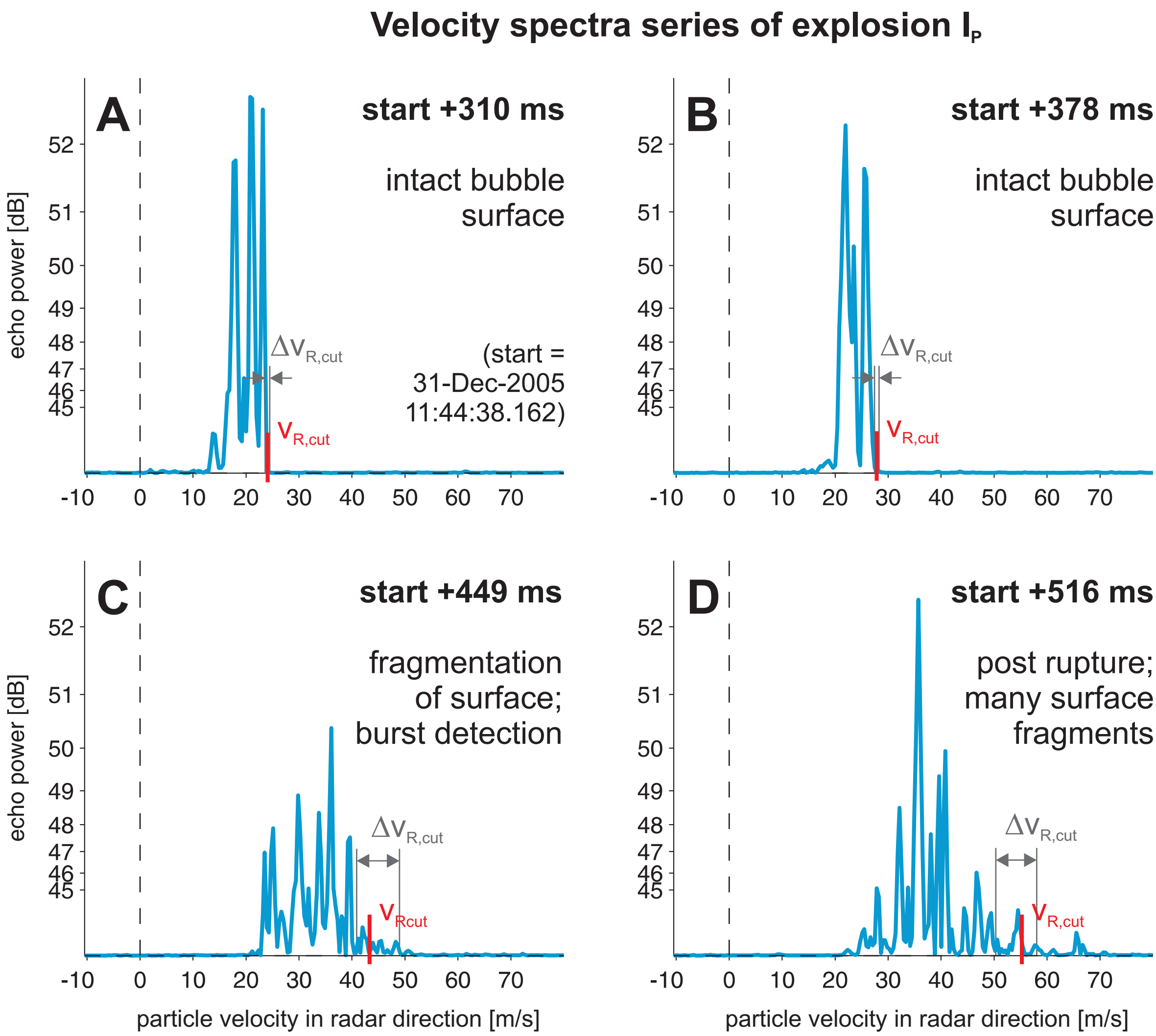

***Figure 6.3: Series of Doppler radar velocity spectra**, recorded during the rapid expansion phase of a typical type I bubble explosion (panel I_P in Fig. 6.2). The radar was of the fast type, located at RAY site. Each spectrum sums around 70 ms of Doppler velocity data (≈ 14 sps). Positive speeds mean a movement towards the radar. The small vertical lines show picked cutoff velocities and their error range.*

small bubbles obviously did not contain as much volume as their larger, explosive counterparts but occurred much more frequently. Typically, they reached the surface of the lava lake as benignly as an air bubble reaching the surface of water, and then slowly collapsed within a few seconds (see videos provided in *SOM*). Neither detectable audible sound nor infrasound was usually generated by these events.

6.2 Radar velocity spectra

Figure 6.3 shows an example series of radar velocity spectra, depicting four subsequent samples of a typical type *I* explosion at Erebus. The spectrum shown in Figure 6.3 A was recorded some 310 ms after the explosion started, with subsequent spectra following about every 70 ms. As discussed in Section 1.5, the spectra are a relative measure of how much material in the radar beam moved at which speed toward the radar. In case of Figure 6.3 A, this means that the bulk of material had a radar velocity component between 15 and 25 m/s at that time. I use the spectra for picking *radar cutoff velocities* ($v_{\mathrm{R,cut}}$, see Eq. 4.23), which allows the calculation of a bubble's surface velocity when applying the bubble expansion model (Sec. 7). Since they are the key parameter for all subsequent data processing, I will use the following paragraphs to describe the determination of $v_{\mathrm{R,cut}}$ in the necessary detail.

Surface points on an expanding bubble move in many different directions away from the centre. As was also discussed in Section 1.5, the direction of particle movement has a large influence on the measured velocity component pointing towards the radar (e.g. a particle moving perpendicular to the beam would appear to not move at all, having a radar velocity near zero). To demonstrate the consequences of this effect I have simulated the expected velocity spectra for four different stages of a bubble explosion. Figure 6.4 A shows the expected radar spectrum for an initial phase of an explosion, when the lake surface is still almost flat, but has already started to bulge up. In Figure 6.4 B and C the bubble grows, leading to an increasing radar cutoff velocity. As argued in Section 4.1.2, the typical peak in echo power just beneath $v_{\mathrm{R,cut}}$ is caused by the part of the bubble's surface area that is located around the point moving fastest towards the radar. The coherent and round shape of the bubble surface ensures that this area has a significant size, leading to the concentration of significant echo power in the spectrum just beneath the velocity of the point with the largest radar velocity. Consequently, $v_{\mathrm{R,cut}}$ is not only the upper cutoff velocity of this peak, but it is also the overall maximum velocity of which an echo can be observed in the spectrum (in the case of an intact bubble).

Figure 6.4 D shows a simulation of a post-burst situation (i.e. the expected velocity spectrum after the shell has ruptured) by using the same parameters as in C, with the addition that some of the individual reflector's speeds were increased by random values. This increase of speed simulates ejecta that have been randomly accelerated by escaping gas during shell rupture while most others still move close to their pre-burst velocity. Introducing this effect immediately broadens the simulated spectrum, and eliminates the distinct cutoff at the spectrum's right side. In real spectra, from this point on, picking the cutoff velocity is difficult because it is no longer equal to the spectrum's maximum velocity. In an extreme case it might even be entirely masked by the signature of the burst fragments, as indicated in this simulation.

Comparing the simulated spectra from Figure 6.4 to the real ones shown in Figure 6.3 allows us to understand their important features. As a first impression, the four spectra in Figure 6.3 illustrate that the shapes of velocity spectra can significantly change from one sample to the next. Velocity spectra of type *I* explosions typically started out showing one (or a group of) narrow but high peaks (Fig. 6.3 A & B), and then suddenly transformed into a broader group of peaks somewhat later in the explosion (Fig. 6.3 C & D). Consistent with

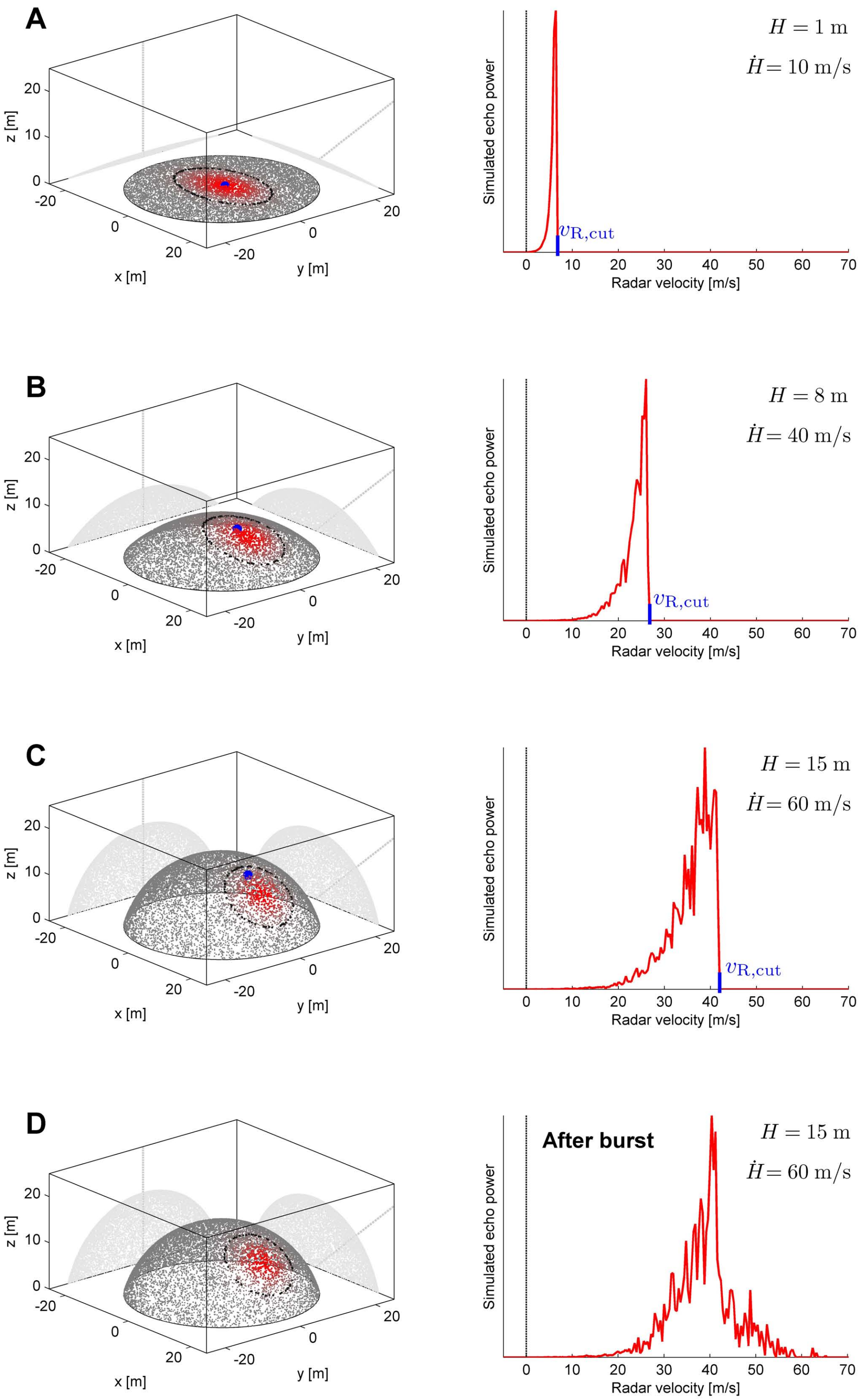

Figure 6.4: ***Simulated velocity spectra for different stages during a bubble explosion.*** *The simulation method is similar to the one used in Fig. 4.5. The radar's location was chosen to reflect the geometry at Erebus (ϕ_R = 39°, 300 m distance), illuminating only a part of the bubble surface (red). The black line marks where the radar's sensitivity reaches -10 dB, i.e. where the receivable echo power has fallen to 1/10 of that in the beam centre. The blue dot is the point on the bubble surface moving fastest towards the radar ($\rightarrow v_{\mathrm{R,cut}}$).* ***A-C:*** *Expansion of a bubble with an intact surface.* ***D:*** *Simulation of a post-burst spectrum, with otherwise similar parameters as were used in C.*

the simulation (Fig. 6.4 C), such a broadening of the spectrum is most likely caused by the change from a single intact surface in the radar beam to a situation where several (or many) objects move in the radar beam at significantly different radar velocities.

Additionally, comparison with explosion videos showed that this characteristic change of shape usually occurs around the time when bubble shell rupture can be identified on video. Accordingly, I interpret this change from a narrow to a broad radar spectrum as the detection of shell rupture from now on, transforming the single bulging lava lake surface into a group of individual ejecta fragments moving at different speeds. In the following figures, if observed, the detection time of this broadening effect will be marked as a star.

Picking of spectra. As mentioned above, for the later application of the bubble expansion model to the data it was necessary to identify the radar cutoff velocity $v_{\mathrm{R,cut}}$ in each explosion spectrum, a feature that allows the calculation of the speed of the bubble surface moving towards the radar (Sec. 4.1.2). Figure 6.3 gives an example of how the cutoff velocities were picked. In cases where the velocity spectra consisted of one single peak or a narrow group of peaks, the cutoff velocity was a very distinctive feature in the spectrum, and was additionally identical with (or close to) the maximum velocity in the spectrum. This made its identification trivial and easily obtained even by automatic methods (e.g. Fig. 6.3 A & B).

In the case of a broader group of peaks in the spectrum (Fig. 6.3 C & D), the automatic detection of $v_{\mathrm{R,cut}}$ proved to be unreliable due to the existence of many fragments instead of only one bubble surface in the radar beam. In this case, the original interpretation of $v_{\mathrm{R,cut}}$ does not hold, since there is no intact bubble surface any more. Instead, the closest analogy to that definition is to pick the maximum radar velocity of the bulk of material[2]. Picking this feature in post-burst spectra is very difficult for an automatic picking algorithm, since sometimes only a few fast fragments can cause an echo peak in the spectrum at a high velocity, but they do not represent the maximum speed of the bulk very well (e.g. small peak at far right in Fig. 6.3 D)[3]. Note that for further processing (e.g. for applying the bubble expansion model), only the pre-burst spectra are important. Even so, all available spectra (pre and post-burst) were manually picked to ensure a constant quality of picks. If necessary, this pick quality can be assessed in Figures 6.6 to 6.8 below.

To quantitatively include the quality of picks in the further processing, error ranges $\Delta v_{\mathrm{R,cut}}$ were introduced, embracing each pick of $v_{\mathrm{R,cut}}$ (shown in Fig. 6.3). The error ranges were manually picked with the aim of including the true cutoff velocity with a very high likelihood. Since this is a rather quantitative definition, the statistical analogy of a 95% confidence interval was aimed for, and is therefore considered an appropriate analogy. Consequently, the width of the error range was relatively large when the spectrum consisted of a broad

[2] defined as the maximum velocity at which a **significant** signal echo can be observed in the radar spectrum, caused by the main bulk of material.

[3] Next to manual picking, several types of automatic picking algorithms to determine cutoff velocities were investigated (not shown). While they all led to similar results, I found that the picking error rate is higher for automatic methods than when picking manually, so I refrained from using automated picks.

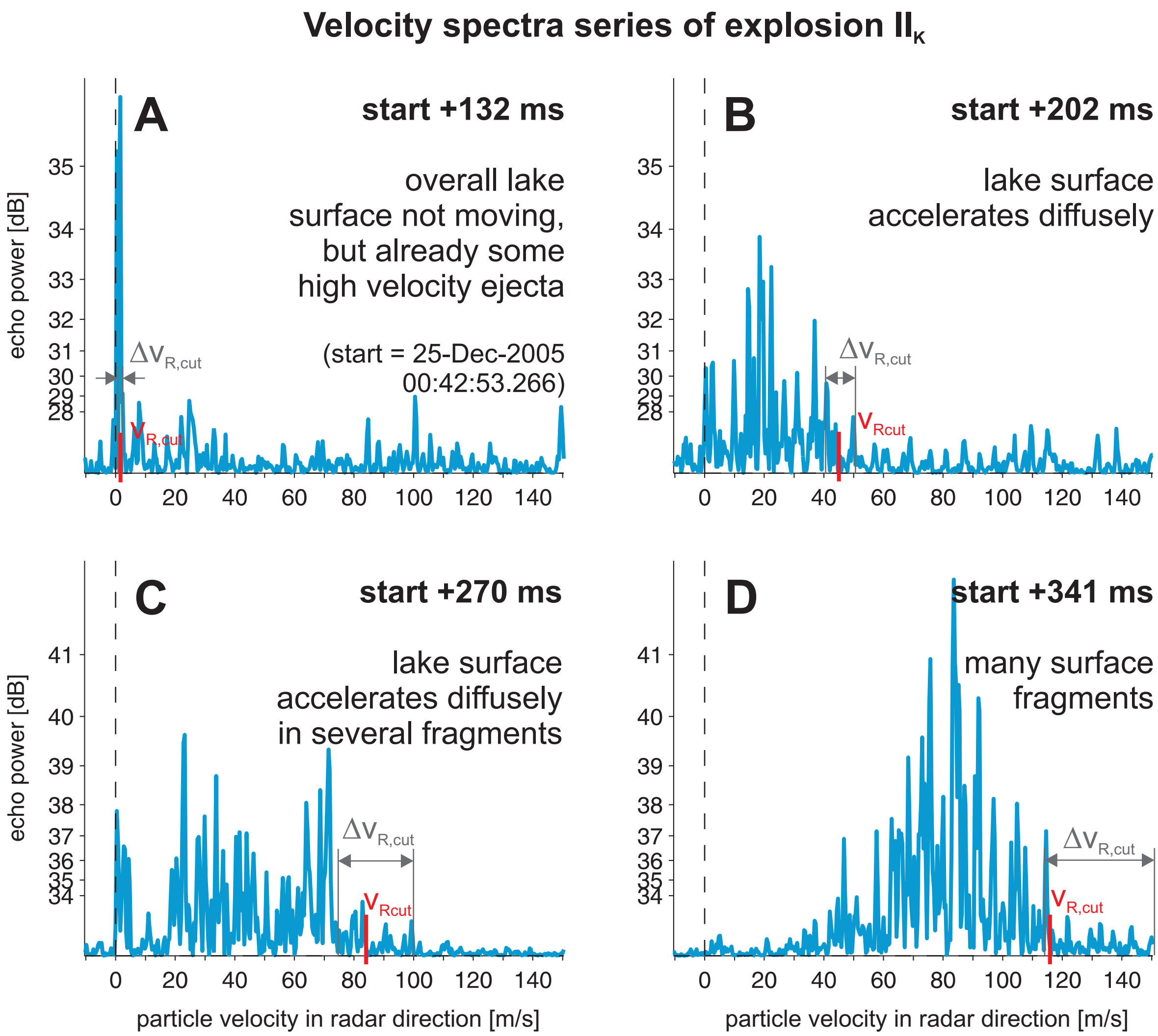

***Figure 6.5: Spectra series of a typical type II explosion**. Note the difference in vertical scale between A–B and C–D. Typical type II spectra show similar features as post-burst spectra from type I explosions (Fig. 6.3 D). In A & B, the echo power that can be seen to the right of $v_{\mathrm{R,cut}}$ is mostly ambient noise. Absolute dB values of type II explosions are typically smaller than those of type I explosions, most likely resulting from the fractured surface.*

group of peaks (e.g. post-burst spectra, Fig. 6.3 D), and sometimes it shrank down to the sample width of the velocity axis (i.e. the velocity resolution, in this case 0.39 m/s; e.g. Fig. 6.3 A). The pick of $v_{\mathrm{R,cut}}$ was not necessarily in the centre of the error range, caused by the asymmetrical shape of the falling upper flank in the spectrum.

Figure 6.5 shows a series of spectra from a typical type *II* explosion. In comparison to type *I* explosions (Fig. 6.3), type *II* explosions show higher velocities and a much broader and more diffuse spectrum, right from the start of an explosion. Similar to post-burst spectra from type *I* explosions (Fig. 6.3 D), type *II* spectra do not show the signature of an intact surface, i.e. a well defined peak. This typically leads to a large error range for the picked cutoff velocity. In contrast to type *I* explosions, radar and video observations of type *II* explosions suggest that the lava lake surface immediately ruptures when the first movement is detected, and before a significant bulging of the entire lake surface occurs.

In summary, cutoff velocities of type *II* explosions cannot be interpreted in the same way as those of type *I* explosions. While for type *I* explosions they are representative of the whole moving lake surface, they only represent a few (or many) explosion fragments for type *II* explosions. For this reason, cutoff velocities of type *II* explosions are not used in the further processing, apart for calculating their expected infrasonic acoustic signal.

Of the 55 recorded explosions, 44 allowed for the picking of radar cutoff speeds as a function of time. Eight explosions had a "blurred" radar velocity spectrum, i.e. they did not display a distinct maximum or cutoff velocity, but various widely dispersed velocity peaks with different heights. Cutoff velocities of *blurred* explosions could therefore not be picked. During three explosions the radar data showed short but significant gaps in the sampling, most likely due to a short overload of the radar's central processing unit. Cutoff velocities of these explosions (marked as "bad data") were therefore not picked, either.

The available radar data of explosions includes several hundred velocity spectra. Inspecting these one at a time does not allow for a clear overview of the data. Therefore, I will introduce a more adequate method to visualise a time series of several velocity spectra in one diagram.

6.3 Radar velocigrams

Figures 6.6 to 6.9 show radar velocity spectra for all measured explosions as so-called *velocigrams*. This type of illustration allows the visualisation of a time series of several velocity spectra in one plot, where their echo power is translated into a colour map, and their radar velocity is shown on the vertical axis. Therefore, brightly coloured areas in the velocigram allow the viewer to follow the temporal development of velocities of the material in the radar beam.

The velocigrams additionally show the cutoff velocities that were picked in each spectrum as white lines, and their respective error bars are indicated. This allows a judgement to be made on the correctness of fit between the picked cutoff velocities and the spectra. The figures show that generally, error bars ($\Delta v_{\mathrm{R,cut}}$) of type *II* explosions are significantly larger than those of type *I*.

For explosions of type *blurred* (Fig. 6.9) it was not possible to determine cutoff velocities because their velocity spectra typically did not show a distinctive peak or maximum velocity. It is therefore not possible to analyse their surface velocities. However, when comparing their velocigrams to the velocigrams of type *II* explosions (Fig. 6.7), they show important similarities, not only in their curve shape, but also in their velocity and echo power range. It is therefore likely that *blurred* explosions are very similar, if not identical, to type *II* explosions (this will be further discussed in Chapter 9).

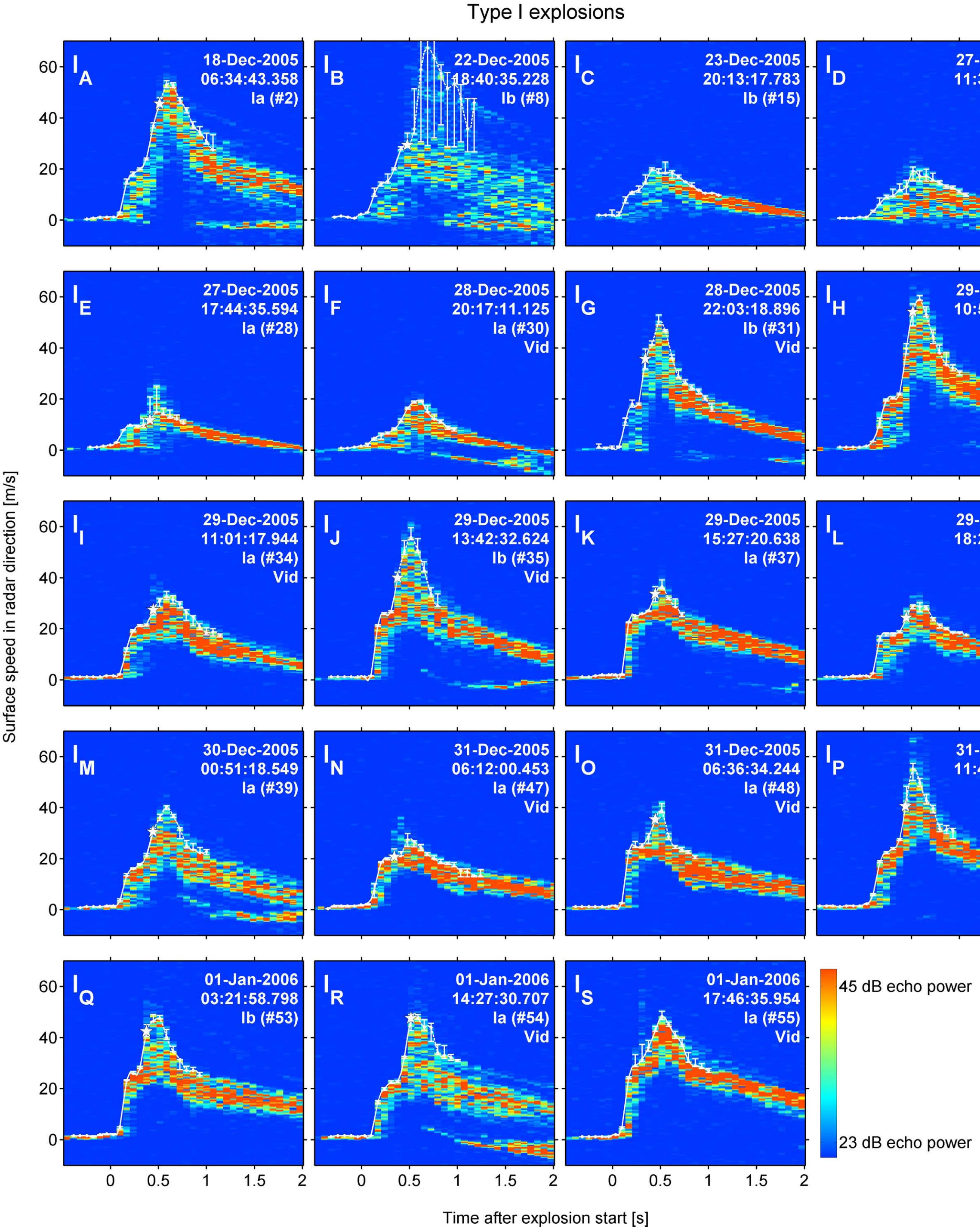

***Figure 6.6:* Radar velocigram of explosion type I.** *Each explosion was assigned a unique label (upper left), consisting of the explosion type and an index of subsequent letters of the alphabet. The text annotation shows the reference time of the explosion start and the explosion type (the meaning of types Ia and Ib will be explained in Sec. 6.4). Explosions for which a thermal video is available are marked with "Vid", explosions for which at least a single infrared snapshot image is available are marked with "Img". The colour map shows the echo power in dB that was measured by the radar at the respective time (scale is non-linear). White lines show the picked cutoff velocities and their error range.*

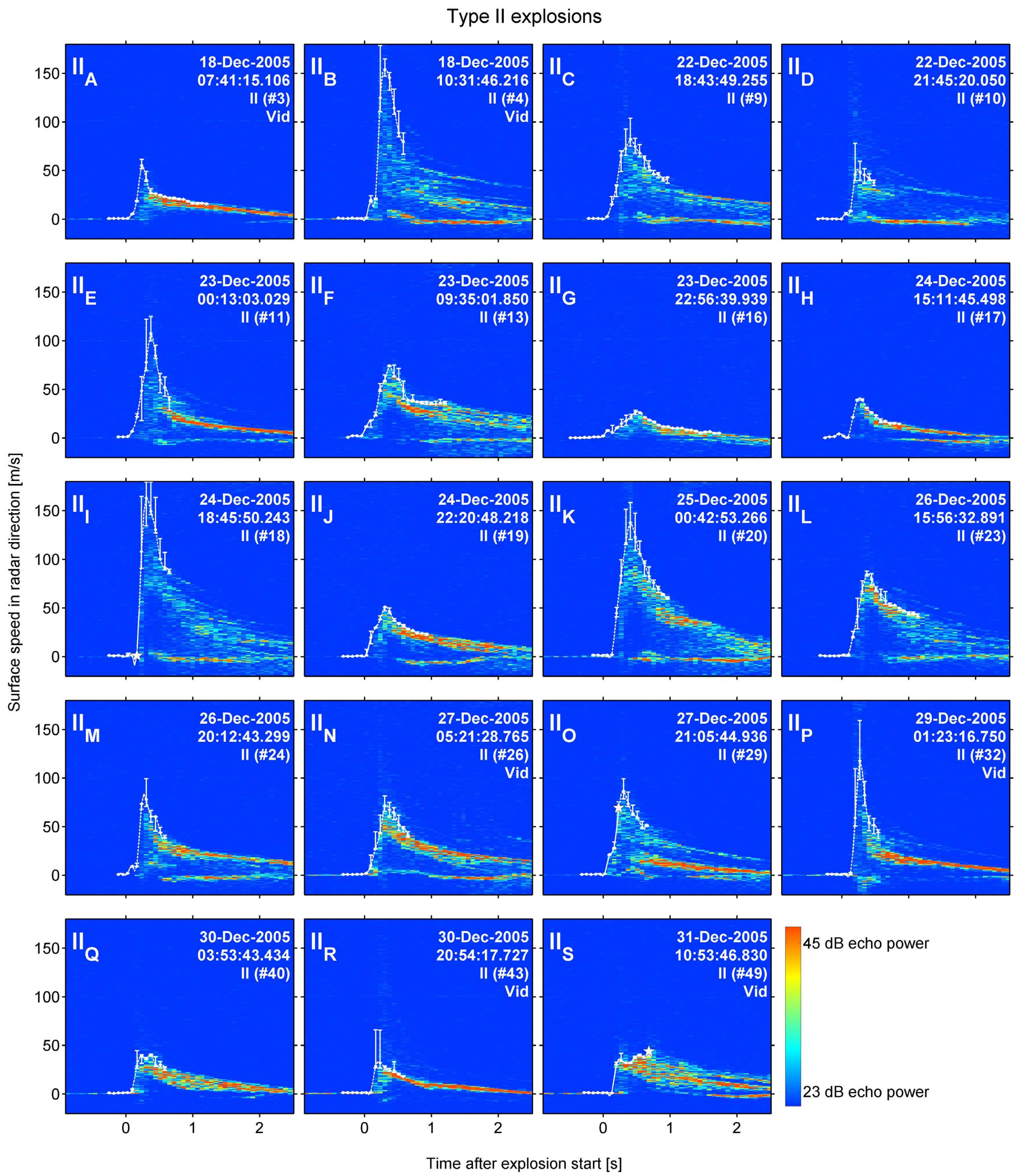

***Figure 6.7:* Radar velocigram of explosion type II.** *On average, type II explosions have radar velocities up to three times as high as type I explosions, but produce smaller echo powers (see Fig. 6.6 for further explanation).*

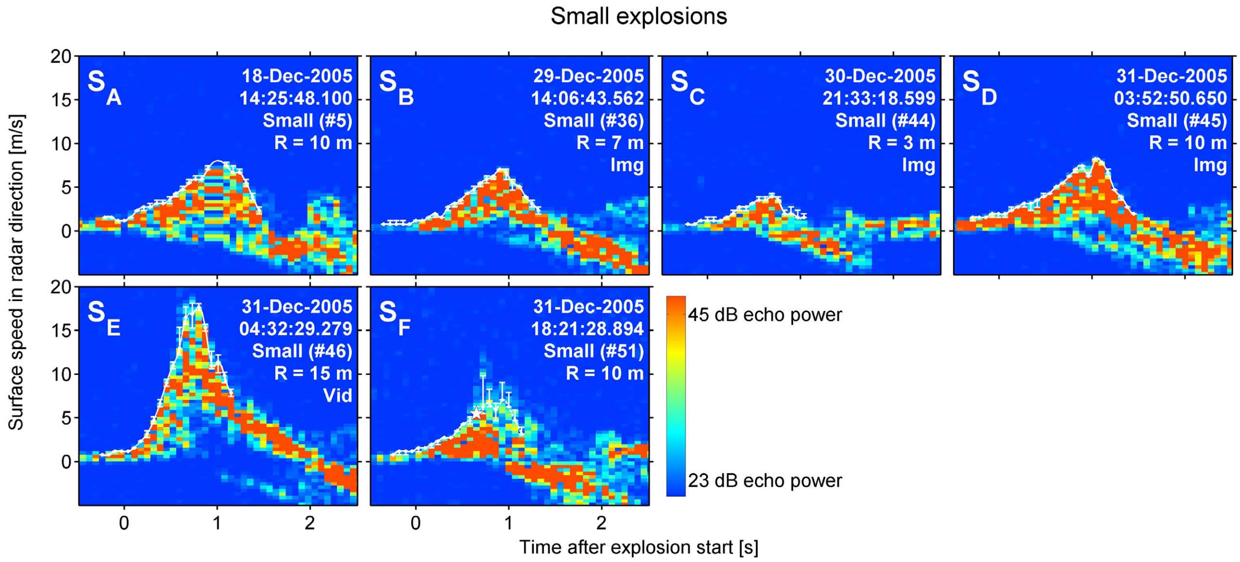

***Figure 6.8:* Radar velocigram of explosion type small.** *Note the difference in maximum radar velocities between* small *and type II explosions. R denotes the approximate radius of the affected region of the lake surface (in type I & II explosions $R \approx 20$ m, i.e. the whole lake surface was affected).*

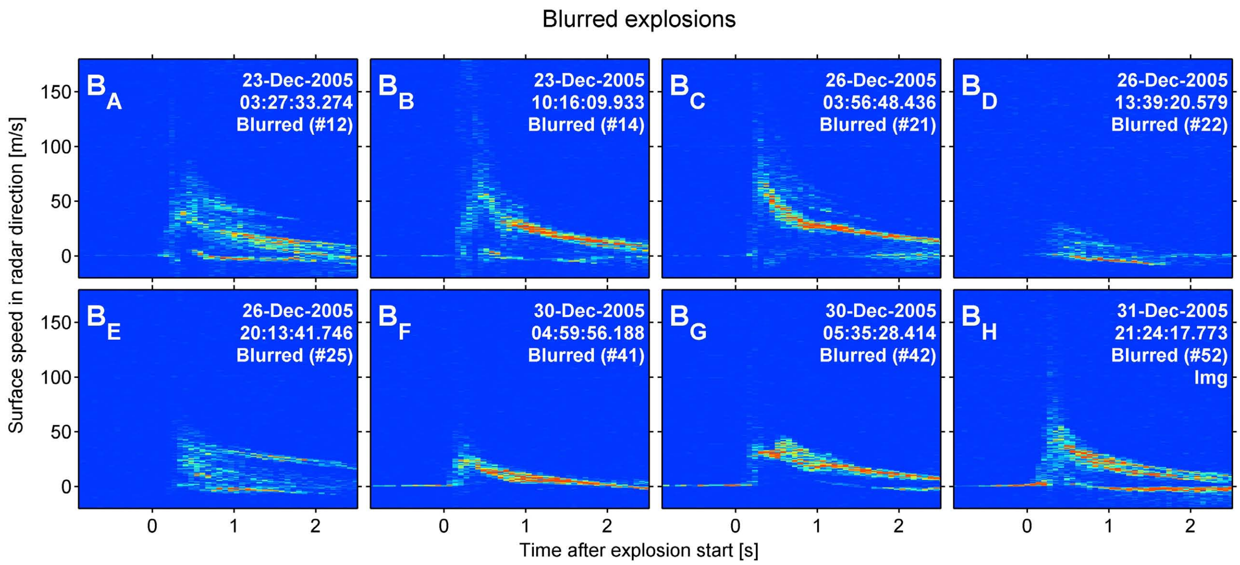

***Figure 6.9:* Radar velocigram of explosion type blurred.** *Due to a "blurred" upper end of the velocity spectrum, cutoff velocities could not be picked for this type. Despite this, spectra of* blurred *explosions appear very similar to those of type II explosions. The dB scale colour map is the same as was used in the other velocigram plots.*

When comparing the overall levels of echo power between explosion types, it is evident that type *I* and *small* explosions (Figs. 6.6 and 6.8) produce the highest echo powers, while type *II* and *blurred* explosions (Figs. 6.7 and 6.9) generally yield lower echo powers. This is partly because the echo power of type *II* and *blurred* explosions, due to their higher velocities, is distributed over a broader velocity range in the spectrum. However, it is likely that this effect is also partly caused by the early fragmentation of the bubble shell during type *II* and *blurred* explosions. Radar waves are expected to scatter much more strongly (therefore reducing echo power) when illuminating a cloud of fragments than when reflecting off an intact surface.

6.4 Surface velocities

As mentioned above, for the later application of the bubble expansion model it is necessary to further analyse the cutoff velocities picked from the spectra. According to Section 6.2, cutoff velocities in pre-burst spectra represent the speed of the bubble surface point moving fastest towards the radar. In post-burst spectra they represent the speed of the bulk of material moving fastest towards the radar.

Figures 6.10 to 6.12 (red traces) show the same cutoff velocity traces that were already shown as white lines in Figures 6.6 to 6.8 as a function of time. The difference is that now they are plotted into a single figure, grouped according to their explosion type. This allows the analysis of common properties of the curves as well as differences between explosion types. After their respective burst time (marked as star), the curves are plotted as dashed lines to account for the fact that after the shell has ruptured, the picked cutoff velocities do not represent a single surface velocity any more. I have shown in Section 6.2 that instead, at that time, they represent the maximum speed of bulk explosion fragments that are left over from the burst surface. In some cases, no shell burst could be determined, either because the shell did not burst within the plotted time range (as happened during several *small* explosions), or because the burst process happened so soon after the explosion start that the characteristic change of spectrum shape (Sec. 6.2) could not be uniquely identified (as in most type *II* explosions). In either case, the respective line was plotted fully solid.

Velocity curves were transferred into shell acceleration and displacement curves by performing simple calculus operations. Accordingly, the blue curves at the top of Figures 6.10 to 6.12 show the integrals of the respective cutoff velocity traces, allowing the judgement of the amount of maximum surface displacement towards the radar at any given point in time. Green curves at the bottom are the derivatives of cutoff velocity traces, i.e. they show the maximum surface acceleration towards the radar.

Lighter coloured shades behind the curves mark the estimated error range of every data point, showing one standard deviation around the expected value. As will be discussed in Section 7.1, this error range was determined with a Monte-Carlo type algorithm, and includes all significant sources of uncertainty, i.e. picking uncertainties as well as parameter

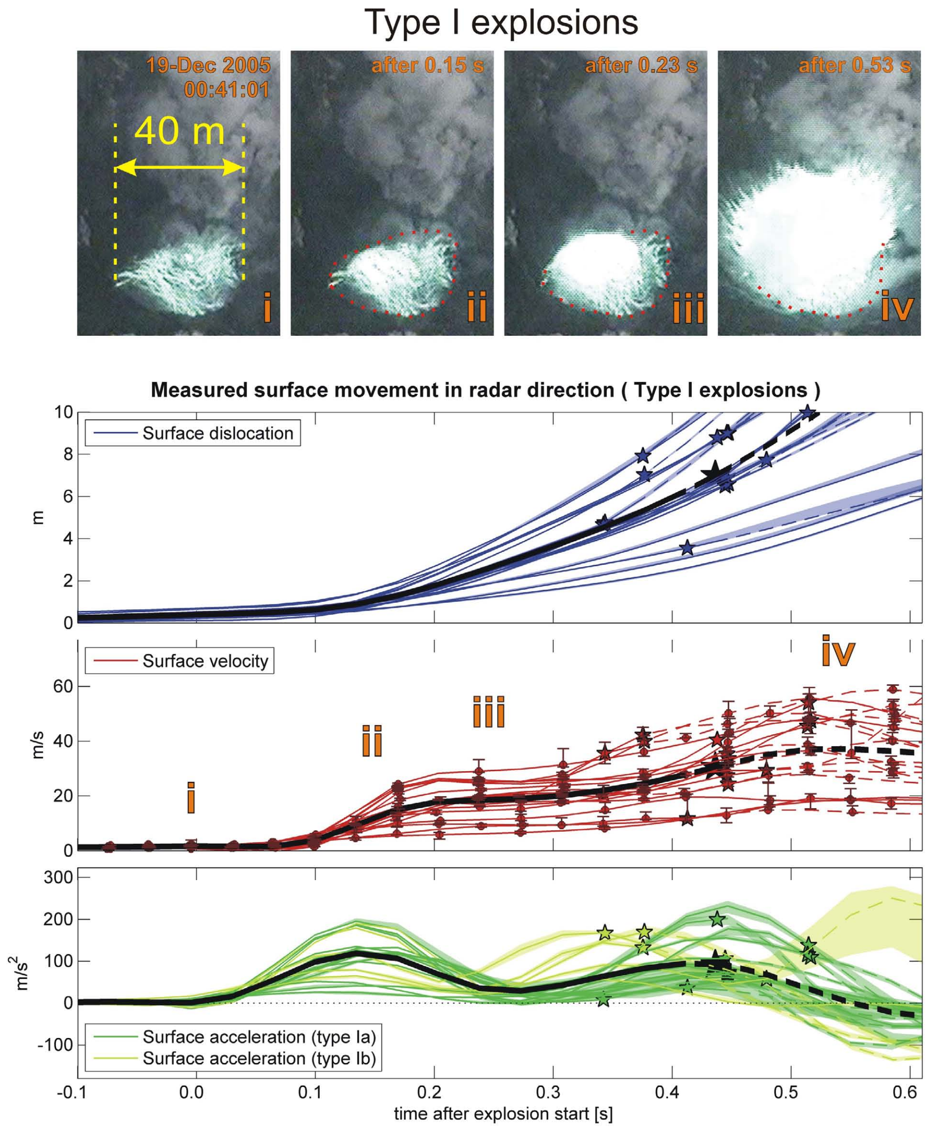

Figure 6.10: ***Measured surface movement of explosion type I. Image sequence:*** *infrared video snapshots of a typical type I explosion. Episodes are shown as Roman numbers.* ***Middle curves (red):*** *picked cutoff velocities ($v_{\mathrm{R,cut}}$) for all type I explosions. While the curves are oversampled (interpolated) by a factor of two, the true data points are marked as dots. Picked error ranges ($\Delta v_{\mathrm{R,cut}}$) are shown as error bars. Stars indicate the time when shell rupture was detected. The black solid line shows the mean of all curves, the black star marks the mean burst time.* ***Top curves (blue):*** *integrated velocity curves, representing surface displacement in radar direction. Propagated standard error ranges are marked as shades.* ***Bottom curves (green):*** *derivatives of velocity curves, representing the surface acceleration component pointing towards the radar. Type I acceleration curves show a* ***typical double peak*** *pattern. Curves are split into subtypes Ia & Ib, depending on the onset time of the second acceleration peak.*

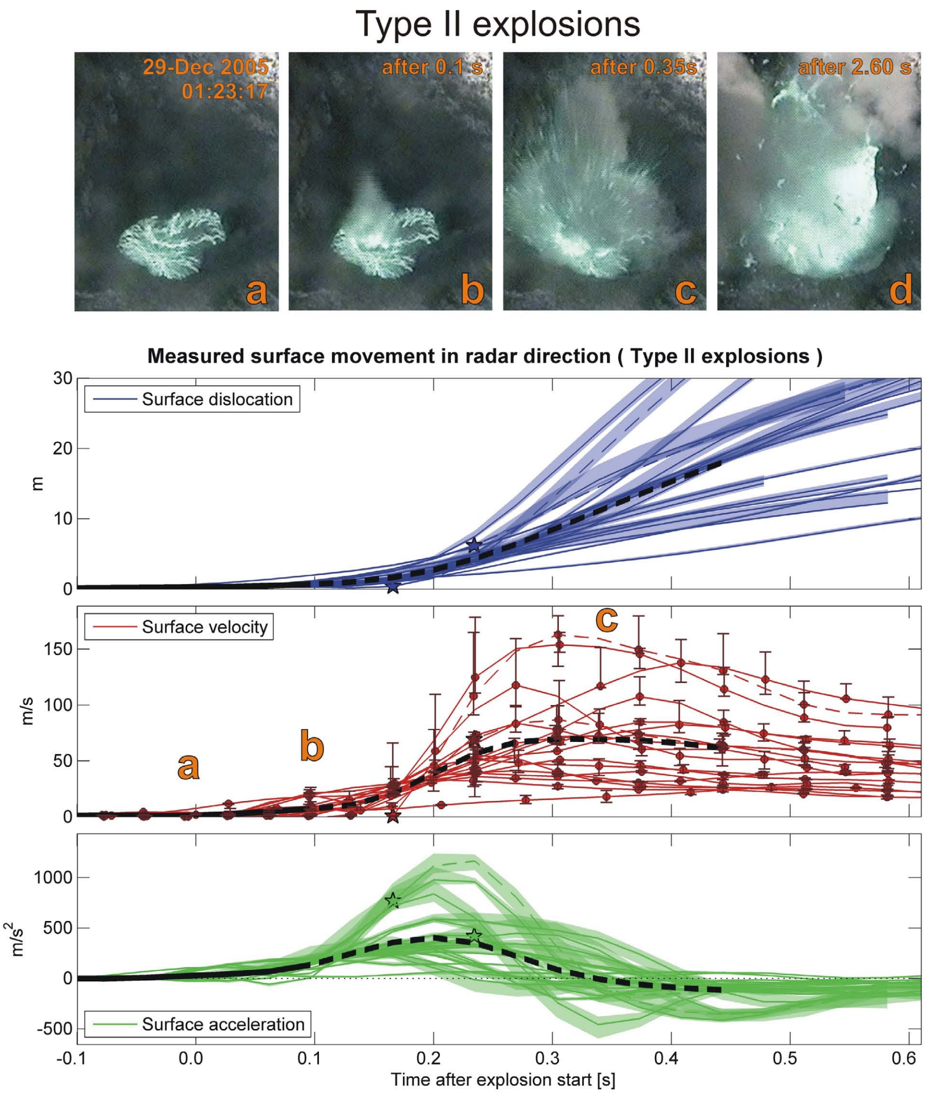

Figure 6.11:* Measured surface movement of type II explosions.** *Acceleration curves (bottom, green) typically show only a* ***single acceleration peak*. Shell burst usually occurred right at the start of the explosion.*

uncertainties. To minimise numerical errors during further processing, **after** calculating the derivatives and integrals, all curves were oversampled by a factor of two using a spline function. To allow for a quality assessment of this interpolation, all original data points are shown as dots in Figures 6.10 to 6.12 (red traces), together with the originally picked error bars ($\Delta v_{\mathrm{R,cut}}$).

There are significant differences between the curve shapes of the three different main explosion types. The most significant differences can be observed between type *I* and type *II* explosions. They can be best identified by comparing their respective acceleration curves: while type *I* explosions typically show a characteristic double acceleration peak separated by about a third of a second (Fig. 6.10), type *II* explosions show only a single but large accel-

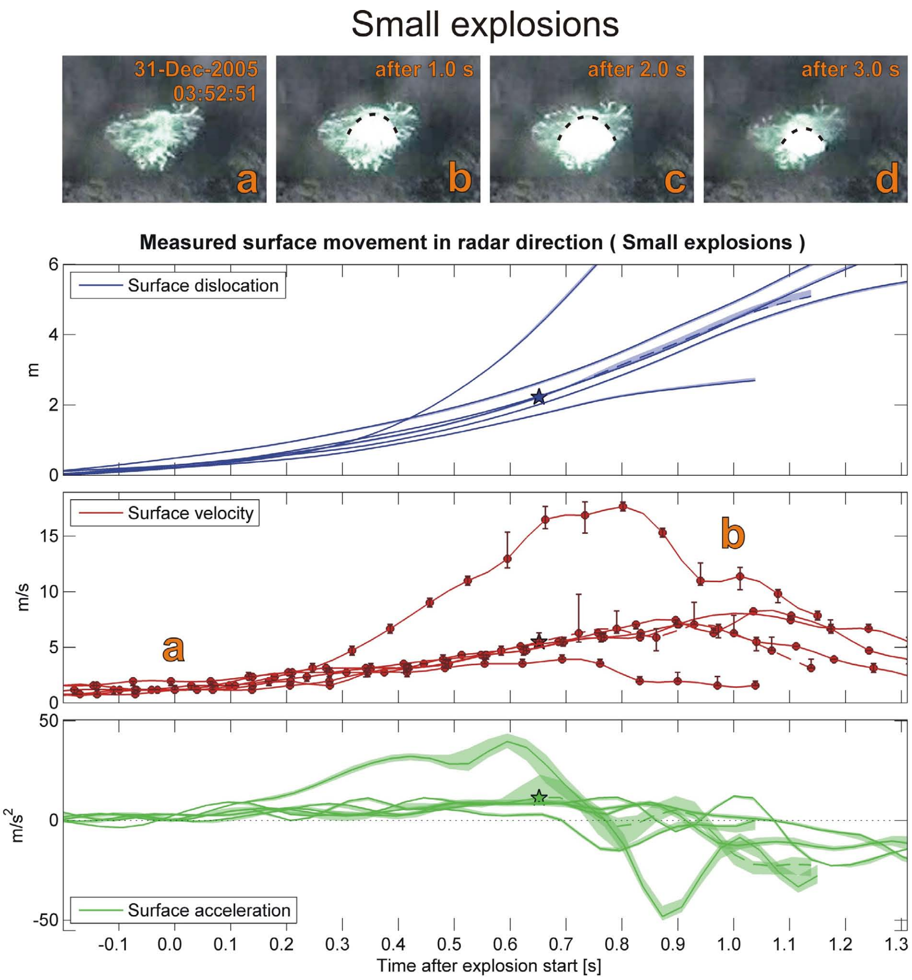

Figure 6.12:* Measured surface movement of type *small explosions. *Small bubbles tended to* ***slowly collapse*** *rather than burst.*

eration peak (Fig. 6.11). Generally, type *II* explosions show much larger surface accelerations and velocities (up to 1000 m/s^2 and 150 m/s in radar direction, respectively) than type *I* explosions (around 150 m/s^2 and 40 m/s). As suggested by their name, surface accelerations and velocities of *small* explosions are by far the smallest of the three types (around 20 m/s^2 and 10 m/s).

All explosions have in common that shortly after the explosion starts, the surface velocity of the bubble strongly increases, leading to a rapid expansion of the shell. This phase, which typically ends after 0.2 – 0.3 s for type *I* and *II* explosions, will be referred to as the ***rapid expansion phase*** of an explosion.

Video snapshots at the top of the figures further help to distinguish the different explosion types. The explosions chosen for the snapshots are typical examples of their respective group. For a more detailed analysis, all available videos can be found in the supporting online material (*SOM*). Precise time stamps in the snapshots and their respective annotations above the curves help to identify the snapshot times in the curves below (e.g. annotated as Roman numbers).

The start of an explosion is defined as the first detectable significant movement, which is also typically the onset of the rapid surface expansion phase. For type *I* explosions, video snapshots and burst detection times from radar suggest that the bulging lava lake surface typically stays intact until around 0.4 s after the explosion start. After the burst, the surface disintegrates into fragments whose velocities are measured by the radar. In contrast, the lava lake surface during type *II* explosions typically ruptures immediately upon its first detectable movement. Therefore, in all following figures for type *II* explosions, if shell rupture is not especially indicated by a star, it can be assumed to occur around time zero. This fundamental difference between type *I* & *II* explosions highlights that their acceleration curves must be interpreted differently. While for type *I* explosions they are representative of the accelerating lake surface, they represent accelerating explosion fragments for type *II* explosions.

Acceleration curves of type *I* explosions (Fig. 6.10, bottom) show a further noteworthy property: their characteristic double peak behaviour can be divided into two groups, according to the time between the peaks. While most explosions have a remarkably stable peak-to-peak time of ≈ 0.3 s (subsequently called subtype *Ia*, shown in dark green), some of them have a shorter peak-to-peak time of ≈ 0.2 s (subtype *Ib*, light green). It should also be noted that even though the acceleration curves are highly variable during the expansion phase of the bubbles, accelerations are always positive before the burst, meaning that both velocity and displacement grow monotonically. Eventually, after the burst, accelerations of fragments become negative, i.e. their speed component in radar direction decreases, but it does not decrease below zero in the time frame of interest. Therefore, even after the burst, the observed surface parts and fragments of type *I* and *II* explosions are **always moving away** from the explosion centre until their trajectories eventually turn towards the ground due to Earth's gravity.

Small explosions show a behaviour that is significantly different from both of the above types. Their video snapshot illustrates this (Fig. 6.12, top): while type *I* and *II* explosions affect the whole lava lake surface, bubbles of type *small* only fill a part of the lake surface, ranging from metre sized bubbles up to larger ones that are almost filling the entire lake. Another significant difference is that *small* bubbles do not explode as violently as type *I* and *II* bubbles. Instead, they grow for a certain time (typically for several seconds), and then slowly collapse and shrink without causing a large amount of ejecta or audible sound (although they do create infrasound, as will be shown later). While all of them monotonically grow at first and then subsequently shrink in one single cycle, the acceleration curves of *small* explosions typically show a subtle oscillation pattern superimposed on their (always positive) growth.

In summary, the main characteristics of the different explosion styles can be described as follows:

Type *I* explosions:	• Bubble expansion with an initially intact membrane. • Double acceleration peak. • Affects entire lava lake.
Type *II* explosions:	• Membrane ruptures right at start of explosion. • Single acceleration peak. • Higher velocities and accelerations than type *I*. • Affects entire lava lake.
Small explosions:	• Less violent than types *I* and *II*. • Affects only part of lava lake. • Membrane rupture is delayed or prevented.
Blurred explosions:	• Picking of cutoff velocities prevented by "blurred" spectra. • Similarity of velocigram to type *II* explosions.

CHAPTER 7

APPLICATION OF THE BUBBLE EXPANSION MODEL

In order to derive physical parameters of the bubble burst, such as energies, bubble pressures, and gas volumes, the model that was developed in Chapter 4 needs to be applied to the data measured at Erebus volcano (as described in the last Chapter). This application will be described in the following sections, starting with a short overview on how the necessary input parameters were chosen, and how the error analysis of results was accomplished.

Since the model describes an expanding bubble with an intact magma shell, its application is only valid when this condition is fulfilled. As shown in Section 6.2, only type *I* and *small* explosions can be considered as unfractured bubbles with an intact magma shell during the first moments of an explosion. Therefore, the model will only be applied to these two explosion types.

At the end of this chapter, the model's prediction of the acoustic signal generated by explosions will be compared to real acoustic data.

7.1 Error analysis & input parameters

The bubble expansion model includes a multitude of nonlinear dependencies, some of which need to be solved numerically. Additionally, its output is dependent on a variety of input parameters, which naturally have an uncertainty in their value. Both these properties make a reliable traditional error analysis (i.e. with a linear or squared approximation for error propagation) nearly impossible.

Therefore, to obtain reliable information on the propagation of errors in the model, I chose a statistical approach that can best be described as a *Monte Carlo* type. In this approach, all output parameters are computed a large number of times, while in each run all model input parameters were randomly varied within their known or presumed error ranges before entering the computations. By comparing the influence of a large number of these randomly varied computations on the output parameters (e.g. energies or pressure), it was possible to precisely determine the influence of known parameter uncertainties on the model results.

Symbol	Name	Expected value	Estimated 1σ uncert.	For source reference see	Main influence on
R_L	Lava lake radius	20 m	± 15 %	Tab. 5.1	All output parameters
ϕ_R	Radar elevation angle	39.1°	± 2°	Tab. 5.1	All output parameters
h_{burst}	Shell thickness at burst	0.75 m	± 0.2 m	this Sec.	All output parameters
ρ_m	Density of magma	2000 kg/m^3	± 15 %	this Sec.	All output parameters
μ_m	Viscosity of magma	5×10^4 Pa s	± 1 magn.	Sec. 4.2.5	Shell dissipated energy
c_a	Sound speed in air	313 m/s	± 10 %	Eq. 3.16	Sonic energy; IS signal
ρ_a	Density of air	0.86 kg/m^3	± 10 %	Eq. 3.14	Sonic energy; IS signal
$c_{p,m}$	Heat capacity of magma	1000 J/(kg K)	± 10 %	Sec. 4.2.9	Shell thermal energy
σ_m	Surface energy of magma	0.4 J/m^2	± 25 %	Sec. 4.2.6	Shell surface energy
v_p	P-wave speed in ground	2200 m/s	± 10 %	this Sec.	Seismic energy
v_s	S-wave speed in ground	1270 m/s	± 10 %	this Sec.	Seismic energy
ρ_{rock}	Surrounding rock density	2400 kg/m^3	± 10 %	this Sec.	Seismic energy

Table 7.1: Model input parameters with uncertainties. *When entering the model, the above parameters were randomly varied around their expected value, following a Gaussian distribution with a half width equal to the above uncertainty values (i.e. = 1 σ). Magma viscosity μ_m, due to its wide range, was varied by one order of magnitude in either direction (through a Gaussian distribution of its logarithm).*

All significant model input parameters are shown in Table 7.1. They were assumed to be statistically independent and normally (Gaussian) distributed around their expected value[1], with a 1 σ uncertainty range as shown in the Table. The distribution was truncated at 2 σ, i.e. the parameters were allowed to vary within the 2 σ range around their expected value.

In practice, a number of N computation runs with randomly varied input parameters typically led to a set of N results for each output parameter. The central 68.3% of this set of results thus depict a variation of one σ around the unvaried result. In all following graphs (with the exception of the picked radar velocities, see below), the extent of this 68.3% confidence interval is shown either as error bars or as colour shades in the background.

The stability of the solution was tested by investigating the influence of N on the resulting error ranges of output parameters. Error ranges were largely stable for $N > 100$, nevertheless $N = 10,000$ runs were used for the final computations to ensure a statistically significant number of runs.

Picking errors of cutoff velocities (see Fig. 6.3 and Sec. 6.3) entered the error estimation through the same principal mechanism as the other parameters (listed in Table 7.1), but followed a somewhat different distribution function. All values for cutoff velocities ($v_{\text{R,cut}}(t)$) that entered the model computation were randomly varied within their picked error boundaries ($\Delta v_{\text{R,cut}}$). Inside this range, their probability followed a *Laplacian* distribution, meaning that the highest probability was assigned to the expected value (i.e. the picked cutoff velocity $v_{\text{R,cut}}$), exponentially falling off towards the edges of the error boundary[2]. In contrast to the

[1]with the exception of magma viscosity, whose **logarithm** was assumed to be normally distributed.

[2]The symmetrical flanks were shaped so that the probability density function reached $\frac{1}{e^2}$ at the farther of the two boundaries, and additionally scaled so that the upper and the lower range had the same total probability (meaning that the median of all values is equal to the expected value).

parameters listed in Table 7.1, cutoff velocities were not allowed to vary beyond their picked boundary. It was found that the exact shape of the distribution does not have a significant influence on the results.

Magma density: *Dibble* (1994) used seismic ray path modelling and a vesicularity model to estimate magma densities at various depths in the magma column of Erebus. He argues that below a sufficient depth (i.e. > 50 m) the magma density approaches 2600 kg/m^3. His assumption is, however, that it will be significantly less at the surface of the lava lake due to vesicles in the magma, which can be observed in freshly ejected lava bombs (despite the low overall gas content of Erebus magma; *Sweeney et al.*, 2008). In this study, we assume a density of 2000 kg/m^3 for magma at the lake surface. The large uncertainty in this value is reflected in the assumed 1 σ uncertainty of $\pm$ 300 kg/m^3 entering the model.

The overall mass of accelerated magma was approximated through the thickness of the magma shell at burst, as can be estimated from typical fragment dimensions, found throughout the crater region. At Erebus, fragments that are ejected over the rim by bubble explosions usually have a flattened shape, likely representing near intact pieces of the ruptured magma shell. Often their "largest dimension" is in the range of a few metres. Yet, even these largest bombs rarely have a "smallest dimension" that is larger than one metre. The typical size of their smallest dimension is consistent for the majority of large bombs at Erebus, i.e. between half a metre and one metre. Assuming that these fragments resemble a cross section of the bubble shell, their smallest dimension is a rough estimate of the shell thickness at burst (an assumption that has already been made by others, e.g. *Vergniolle and Brandeis*, 1994, ; P. Kyle, *pers.comm.*, 2005). Accordingly, I assume that the shell thickness at Erebus at the time of burst is in the size range of 0.5 to 1 m (a number that is somewhat higher than, but in the same magnitude range as the 0.2 m estimated by *Dibble et al.*, 2008, from early video recordings).

Thus, for the following calculations, an average shell thickness of 0.75 $\pm$ 0.2 m was used, from which the overall magma volume in the shell was calculated (around 1800 m^3 for type *I* explosions, see Eq. 4.43). This is certainly a coarse simplification (e.g. videos suggest that bubble shells are usually thicker on the outside than in the centre part). However, since most of the momentum and the potential energy is carried by the centre part of the bubble, I regard this assumption as appropriate. From the shell magma volume, the shell mass can be easily calculated using the magma density discussed above, leading to a typical magma shell mass of around 3600 $\pm$ 1100 metric tons for a type *I* explosion.

Both the assumed shell thickness and the magma density influence the assumed mass of the shell in a near-linear way, and the shell mass influences most involved energy types. Therefore, it must be kept in mind that these uncertainties in mass estimation will result in a similarly sized error in the obtained pressures and energies (since mass influences the significant energy types in a linear way). Fortunately, it is unlikely that the error in mass estimation surpasses, or even approaches, a whole order of magnitude, meaning that the resulting error in energies and pressure will also remain in this limit. This is reflected in the overall error ranges of these parameters, as will be shown later in this chapter.

The lava lake radius used in the model was adopted from the true dimensions of the lava lake, as measured with a Leica Vector GIS LASER range finder (Tab. 5.1). Even though the lava lake had a somewhat elongated, or elliptical shape during the measurements (e.g. Fig. 6.2), the model approximates the lava lake as circular. For all explosions but those of type *small*, it was assumed that the radius affected by a bubble (i.e. the *bubble footprint*) equals the lake radius. However, as shown in Section 6.1, this assumption is not valid for *small* explosions. Therefore, footprint radii of *small* explosions were approximated from video by comparing their size with the known lake dimensions (as annotated in Fig. 6.2). For the error analysis they were assigned a 15% uncertainty.

Magma viscosity: phonolitic magmas from Erebus typically contain around 30% anorthoclase crystals (e.g. *Sweeney et al.*, 2008), which together with the magma water content and temperature have a large influence on the magma viscosity. *Sweeney et al.* (2008) estimate the magma's viscosity at depth (i.e. at a pressure exceeding 50 bars) to around 5×10^3 – 10^4 Pa s. Consistently, *Oppenheimer et al.* (2009) calculate the viscosity of Ray Lava Lake to 10^4 Pa s, based on a model by *Giordano et al.* (2008). The obtained viscosities are similar to those from andesite in the same temperature range (e.g. *Carmichael et al.*, 1974, Fig. 4.7, and P. Kyle, *pers. comm*, 2008). However, it is possible that the viscosity at the topmost lava lake surface layer could be approaching 10^6 Pa s, due to a slightly lowered surface temperature (in the order of 65°C lower, *Sweeney et al.*, 2008), and more importantly, due to a decreased water content (possibly down to 0.05 – 0.15 weight-%, *Sweeney et al.*, 2008, and K. Heide, *pers. comm. and unpublished data*, 2008). In this study, a surface viscosity of 5×10^4 Pa s was assumed for Erebus lava lake, with a 1 σ uncertainty range covering a whole order of magnitude in either direction (i.e. 5×10^3 to 5×10^5 Pa s).

Elastic parameters of the volcanic rock surrounding the lava lake (v_p, v_s and ρ_{rock}, see Tab. 7.1) were used to calculate the seismic energy created by bubble explosions. Estimates for these values were taken from *Dibble et al.* (1994) and are in accordance with more recent studies (e.g. *Aster et al.*, 2008). In all calculations, 10 % uncertainty was assumed for these parameters.

7.2 Bubble zenith velocities

The first bubble parameters that were determined from the model were the bubble's zenith height $H(t)$, zenith velocity $\dot{H}(t)$, and zenith acceleration $\ddot{H}(t)$ (these are not to be confused with the measured "raw" **radial** surface displacement, velocity and acceleration towards the radar, which were shown in Fig. 6.10. Instead, **zenith** parameters describe the vertical movement of the uppermost point of the dome). As described in Section 4.1.2, the zenith parameters were directly determined from cutoff velocities through simple geometrical conversions[3]. These traces are the basis for calculating all following parameters and predictions

[3]Similar to the surface movement parameters shown in Sec. 6.4, to minimise numerical errors during further processing, the $H(t)$, $\dot{H}(t)$, and $\ddot{H}(t)$ traces were oversampled by a factor of two **after** they have been calcu-

of the model.

Figure 7.1 shows these zenith parameters for all explosions of type *I*. The figure also shows a snapshot of different episodes of the explosion, together with a schematic illustration of the model to allow for a judgement of the validity of the model geometry. As expected from the angle of observation, zenith velocities are typically somewhat higher than the "raw" surface velocities shown in Figure 6.10.

Similar to the figures showing raw surface velocities (Fig. 6.10, middle), traces are continued as dashed lines beyond the times where shell fragmentation was detected by radar (marked as stars). At this time the traces do not represent intact surface properties any more, but those of the bulk of shell fragments. All important conclusions must therefore be deduced from the pre-burst part of the traces. Not surprisingly, zenith accelerations show the same double peak pattern as was already observed in the surface accelerations (Fig. 6.10 bottom), again split up in subtypes *Ia* & *Ib*.

The width of the zenith parameters' error range, shown as shades in the background, was mainly influenced by individual picking uncertainties ($\Delta v_{\mathrm{R,cut}}(t)$) and geometrical input parameters, such as the lava lake radius and the radar beam's elevation angle.

Figure 7.2 shows the zenith parameters of *small* explosions, which are significantly smaller in value than their counterparts of type *I* explosions. A bubble burst was detected for only one of the *small* explosions; for all others the shell remained mostly intact during the observation time displayed in the figure. Some of them supported an almost intact shell even when collapsing, while gas escaped through a relatively small hole in the shell (see videos in the supporting online material, *SOM*). In contrast to type *I* explosions, *small* explosions typically do not show a double acceleration pulse. Instead, while monotonically growing, their acceleration phase is often superimposed by a slight oscillation with a period between 0.2 – 0.3 s (Fig. 7.2 bottom).

7.3 Explosion energies

The relations derived in Section 4.2 allow the calculation of the amount of energy that was transferred from the gas internal energy into the different energy types associated with bubble expansion. Figure 7.3 shows a time series of these energies for type *I* explosions, allowing the assessment of the total released energy as well as its partitioning into different types. The main energy types that are involved are the kinetic energy of the accelerated magma shell, its potential energy in Earth's gravity field, the elastic energy radiated into the atmosphere by displacing the surrounding air, the elastic energy radiated into the ground as seismic waves, the frictional heating of the deforming magma shell, the energy needed to increase the surface area of the shell, and lastly the thermal energy output[4]. Since all of the above

lated from the original, non-oversampled cutoff velocities.

[4]This only refers to the heat that is carried by explosion fragments. Independently from this, eventually all of the involved types of energy will be transformed into thermal energy when ejecta have come to rest after an

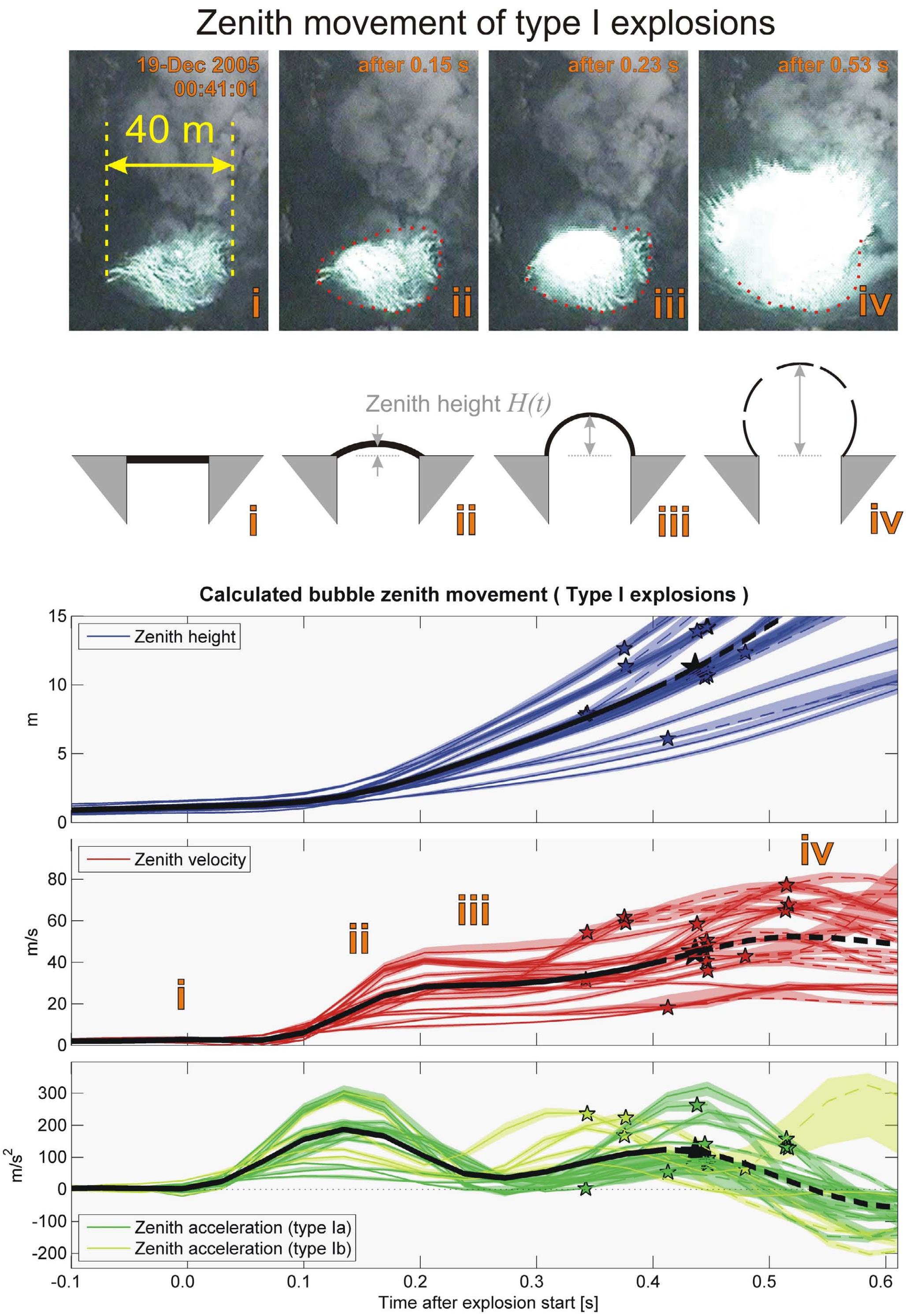

Figure 7.1: ***Calculated bubble zenith movement during type I explosions. Top:*** *Infrared snapshots of various stages of a typical explosion.* ***Middle:*** *Schematic sketch of the model geometry, depicting how each stage is reflected in the model.* ***Bottom:*** *Bubble zenith height above the original lake level (blue), its vertical velocity (red), and its vertical acceleration (green). Mean traces are shown as black lines; stars mark the burst time as detected by radar. Underlying colour shades show the standard deviation of the parameters, resulting from picking and parameter uncertainties.*

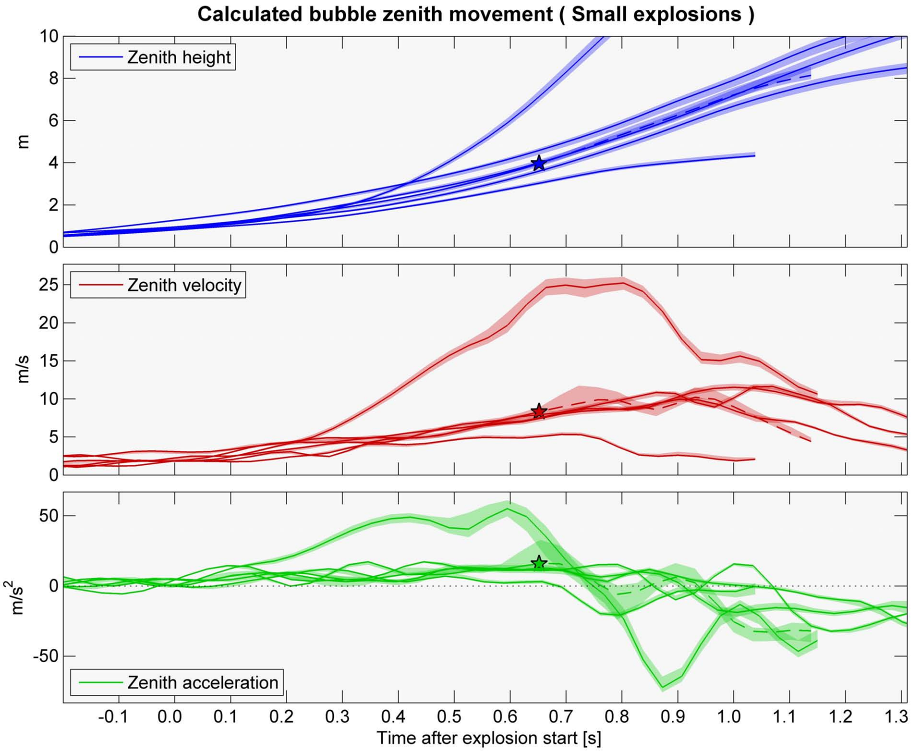

***Figure 7.2:* Bubble zenith movement during *small* explosions**

mentioned types of energy, apart from thermal energy, are powered by the dynamically expanding gas bubble, they are from now on referred to as ”dynamic” energies. Since thermal energy is not directly powered by the rapid gas expansion, it is considered as ”static”, or constant during an explosion. Also, on the timescales of interest, heat loss through radiation can be neglected.

All dynamic energy types show a similar temporal behaviour. Starting out from zero joule at rest, energies rise up to their pre-explosion level (i.e. before the time marked as *explosion start* in the figure), reflecting a small upward movement of the lake surface in the order of a few m/s that is usually preceding explosions. After the explosion start, during the rapid expansion phase, energies quickly increase by several orders of magnitude. After around 0.2 s, energies tend to level out and remain at their current order of magnitude until the shell bursts at around 0.4 to 0.5 s after the start of the explosion.

The energy partitioning figure (Fig. 7.3) shows that by far the most energy that is dynamically freed by gas bubbles is turned into **kinetic** and gravitational **potential energy** of the shell, making them the controlling factor for all parameters derived from the energy output (e.g. gas pressure and volumes). They add up to more than 1 GJ, or the energy equivalent

explosion

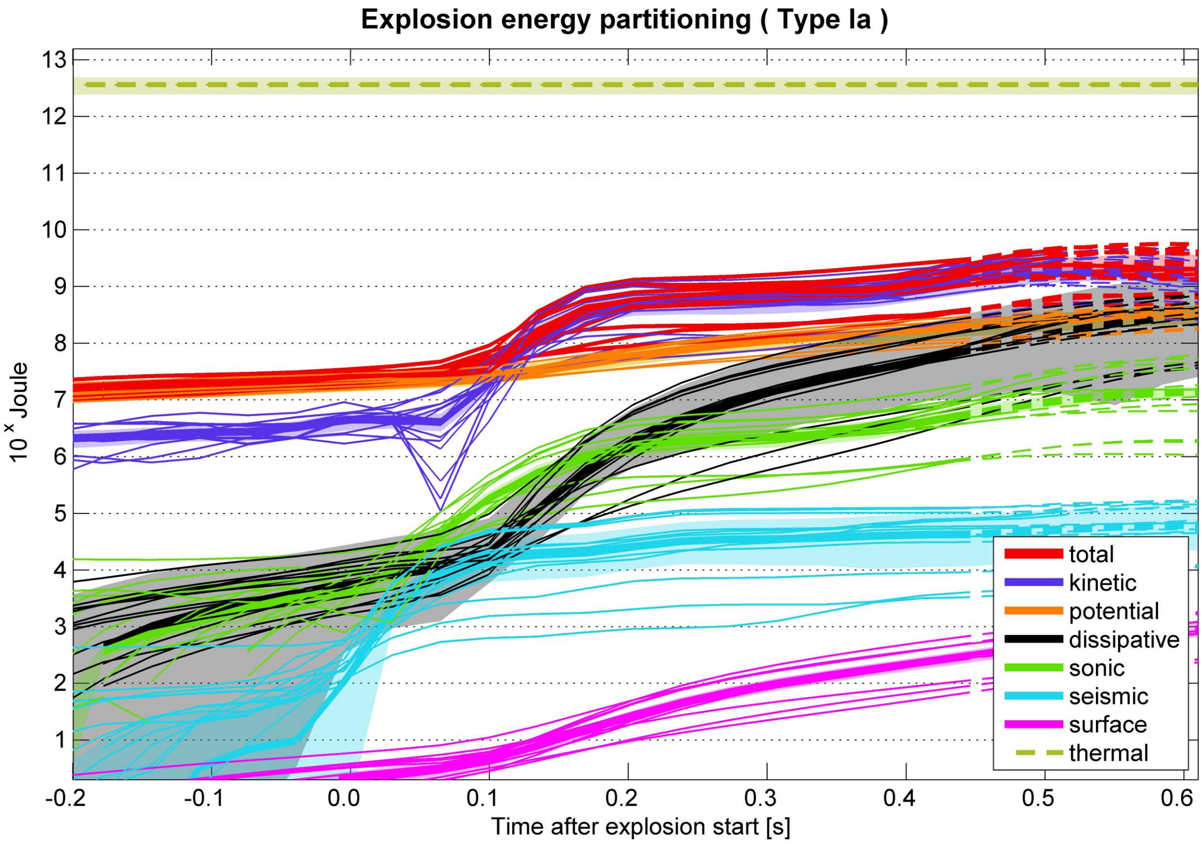

Figure 7.3: ***Explosion energy partitioning*** *for type I explosions. To keep the figure from cluttering, only type Ia explosions were plotted. Type Ib explosions are not substantially different, but have a slightly shorter rapid expansion phase. Note that even between explosions the lava lake surface is typically in (slow) motion, therefore some of the energy types do not start from exact zero during explosions (this effect is most prominent for kinetic and potential energies).*

freed by the explosion of several hundred kg of TNT[5]. Their uncertainty is mainly controlled by uncertainties in the mass estimate of the magma shell, and to a smaller degree by cutoff velocity picking errors.

The third largest type of dynamically freed energy, significantly smaller than the above types, is the shell's **dissipated energy** caused by viscous friction in the magma shell. This energy is immediately turned into heat, therefore raising the temperature of the magma shell while it expands. Yet, even though it exceeds 10 MJ just before the burst, it is hardly enough energy to heat the magma shell by more than a few 1000^{ths} of a kelvin, due to the enormous heat storage capacity of the magma shell (Eq. 4.61). As discussed in Section 7.1, the viscosity value for magma near the lake surface is only poorly constrained, leading to a large uncertainty in the dissipated energy output in the order of one magnitude. Nevertheless, Figure 7.3 shows that even in the most viscous assumption, the dissipated energy

[5]General unit definitions, including the *TNT equivalent*, can be found in *Thompson and Taylor* (2008)

during type *I* explosions remains about a magnitude smaller than the shell's kinetic energy. This ratio, however, is different for *small* explosions, as will be shown later.

Acoustic energy, i.e. the energy that is stored in, and radiated into the atmosphere by the expanding bubble, is the fourth largest dynamic energy type involved. Just before the burst of type *I* explosions it typically reaches 1 MJ. During the rapid expansion phase, the acoustic output *power* (or energy rate) often exceeds 10 MW (190 dB SWL; see Eq. 3.11), which is more than the acoustic output power of large spacecraft rockets (*Lighthill*, 1978, p. 17). The quality of the predicted acoustic energy output is mostly dependent on the knowledge of the bubble's surface area, which practically reduces to the correct estimation of the lava lake radius (or, for *small* explosions, the estimation of the bubble footprint radius).

Even though being about a magnitude smaller than the acoustic energy, a certain amount of energy is transferred into **seismic energy** that is radiated into the ground. At around 50 KJ, it surmounts to only one 100,000$^{\text{th}}$ of the kinetic energy of the shell, or as an everyday life analogy, to about the nutritional energy that is contained in a few grams of chocolate. This might seem surprising at first, given that the inertial forces of the accelerating heavy magma shell are in the 10^8 N range, as will be shown in Section 7.7. However, the process of force coupling to the ground is rather ineffective (Eq. 4.60), leading to such low energy values. The uncertainty in these value is mostly controlled by the knowledge of the mass of the shell, and by the elastic parameters of the ground surrounding the lava lake. Even less importantly, the amount of **surface energy** stored in the expanding bubble surface is less than 1 KJ, largely controlled by the magma's specific surface energy and the bubble's surface area.

Somewhat different to the dynamic energy types that are powered by the expanding gas, **thermal energy** is considered as constant during the burst since it is not freed by the expanding gas bubble but is passively carried by the $1000°$ C hot magma shell and the subsequent explosion ejecta. The thermal energy shown in Figure 7.3 assumes that the entire mass of the magma shell is ejected and lost to the system. In reality, most of the material eventually slips back into the lake, so only a part of the shell's mass and heat will actually be lost to the system (factor η_m in Eq. 4.61). But even if only a quarter of the material is available for cooling outside of the lava lake, the magnitude of the thermal energy output is unchanged, as can be seen in the logarithmic nature of Figure 7.3.

The amount of thermal energy transported by a single explosion lies in the order of 10^{12} J. This is equivalent to the energy release of $\approx$ 1 kiloton of TNT (about 5 – 10 % of the yield of a moderately sized nuclear weapon), or about fifty years worth of electricity for an average European five person household, therefore far exceeding the energy that is dynamically freed by the expanding gas ($\approx\ 10^9$ J).

Small **explosions**, as expected, released much less energy than type *I* explosions, yet their overall energy partitioning had similar characteristics to type *I* explosions. There are, however, some important differences between the types, as shown in Figure 7.4. While the total dynamic energy output of *small* explosions, due to small bubble sizes and low velocities,

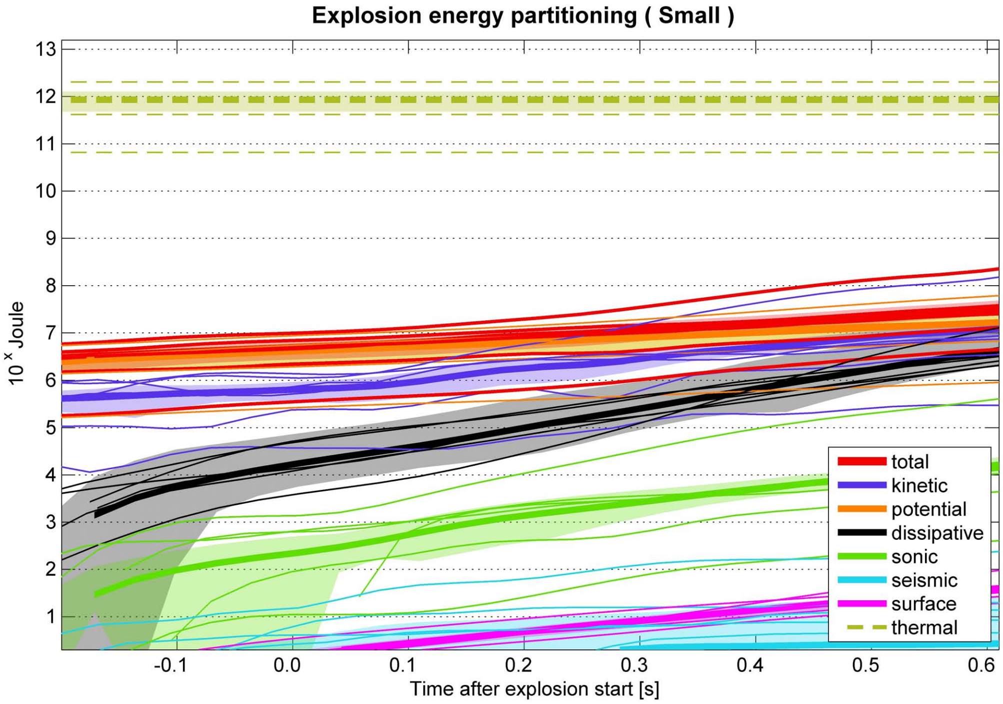

***Figure 7.4:* Explosion energy partitioning of *small* explosions.**

is only in the 10 MJ range, their kinetic and potential energies contribute about equally, if not in a reversed order than during type *I* explosions. It is also remarkable that magma viscosity, and therefore dissipative energy, plays a much larger role in *small* explosions than during type *I* explosions. At the bubble's maximum growth phase, the three aforementioned energies even contribute almost equally to the total amount of dynamic energy. A further striking feature of *small* explosions is that the amount of radiated seismic energy is in the 10–100 J range, which suggests that the seismic waves excited by *small* explosions are much weaker than that of the other types, and therefore most likely more difficult to detect.

Also, somewhat different than during type *I* explosions, it is difficult to quantify the amount of thermal energy that is passively transported by ejecta from *small* explosions, since many of their fragments immediately fall back into the lava lake and therefore remain in the system. It is also notable that *small* explosions do not show the sharp increase in dynamic energies that is prominent during the first moments of type *I* explosions. Instead, they show a more gentle and steady increase throughout the first half-second of explosions.

7.4 Gas pressure inside bubbles

In Section 4.3 I have shown how the gas pressure inside expanding bubbles can be derived from their rate of energy output. Figure 7.5 shows the result of Equation 4.63, calculated for

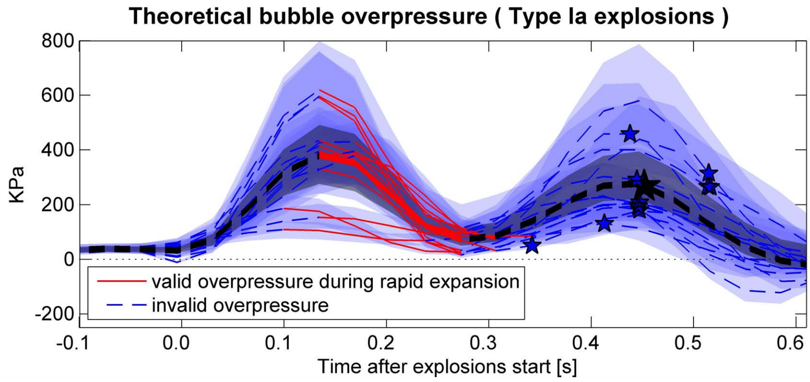

***Figure 7.5:* Calculating gas overpressure inside bubbles.** *The relevant part of the pressure curve is marked in red, an enlarged version is shown in Fig. 7.6.*

every available data point. The traces shown in the figure can therefore be interpreted as the relative gas overpressure in the bubbles above the ambient atmospheric pressure. However, care must be taken to only interpret these traces in their valid range (shown in red), which is only the time of pressure decrease following the first acceleration peak.

At times before the relevant section, the approaching bubbles have not yet reached the surface of the lava lake, therefore the magma shell mass is not yet fixed (but decreasing), while Equation 4.63 assumes a constant shell mass. This leads to an apparent pressure increase when in reality the gas pressure is ever decreasing at this stage due to the rise of the bubble in the conduit (i.e. by decreasing the hydrostatic load above the bubble). Shortly after, around the time when the shell acceleration reaches its first maximum, the shell mass can be considered constant because drainage from the shell is a significantly slower process (Sec. 2.2.1) than the shell expansion once the bubble shell has started moving. Therefore, during this phase, the calculated pressure values can be considered representative for the gas pressure inside the bubbles. It is interesting to note that at the time of the first acceleration maximum, the lava lake surface has only slightly bulged up (typically between 1 and 3 metres; compare Figs. 7.1 (blue traces) and 7.5).

The above gas pressures are meaningful, or valid, until the time when the bubble shell ruptures. Shell rupture is typically detected by radar only a short time after the pressure curve minima that follow the first peak. Considering that this detection of shell rupture by radar is probably somewhat delayed (most likely in the range of one sampling interval, i.e. ~ 0.07 s), I will interpret pressure curves only up to their minima, i.e. before the onset of the second peak. Therefore, the red area in Figure 7.5 ends there.

The cause of the second pressure/acceleration peak is not entirely clear at this stage. One possibility is that it is caused by a second bubble arriving at the surface just before the shell burst (this will be discussed in Chapter 9). In this case the calculated pressure is meaningful even beyond the minima, up until the burst time, as detected by radar. Another possible explanation for the second acceleration peak is that the true shell rupture is possibly detected

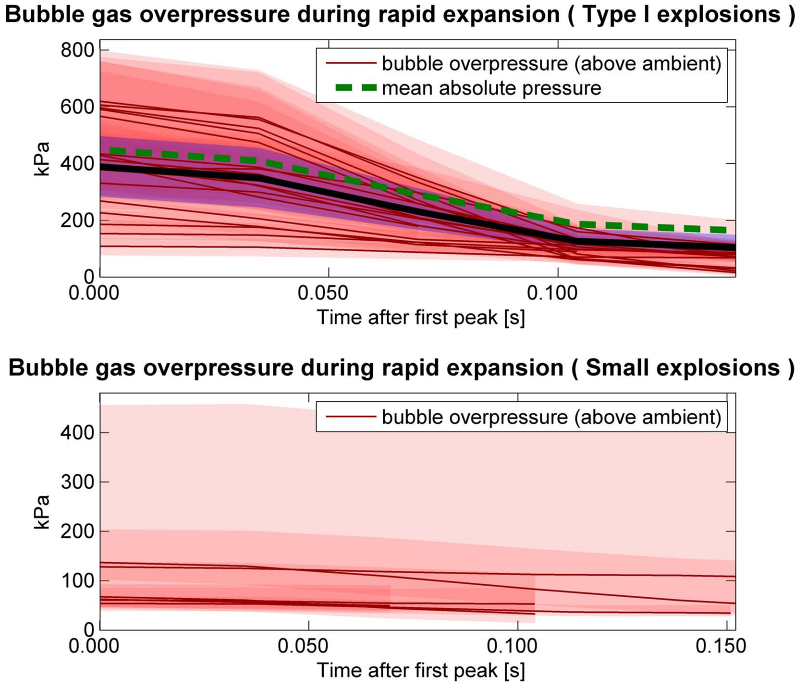

Figure 7.6: ***Gas pressure inside expanding bubbles.*** ***Top:*** *This figure shows the relevant part of Fig. 7.5 for type I explosions, i.e. the time between the start of the rapid expansion phase of every explosion and the time when the pressure reaches its minimum. Individual error ranges are shown as shaded areas in light red, the average error range is shown as the purple shaded area around the mean. An overpressure of 0 kPa means atmospheric pressure. In contrast, the green dashed line shows the mean* ***absolute*** *pressure.* ***Bottom:*** *similar plot for* small *explosions.*

by the radar with a more significant delay than previously assumed (i.e. > 0.1 s). In this case the second acceleration peak does not show the acceleration of an intact surface, but is merely "faked" by already accelerating shell fragments following the burst. In the second case the calculated pressure would not be correct after its minimum. To avoid this ambiguity, I refrain from interpreting the ambiguous part of the pressure curve.

Figure 7.6 (top) shows only the relevant part of Fig. 7.5, i.e. the relative overpressure during the time between the start of the rapid expansion phase of every explosion, and the time when the pressure reaches its minimum between the peaks. The figure shows that at the start of the rapid expansion phase of type *I* explosions, the gas overpressure lies between 100 and 600 kPa, with a mean of $\sim$400 kPa (4 bars) above ambient, i.e. the range of a few atmospheres only, or merely about the pressure in a bicycle tyre. Due to the large surface area on which the pressure acts (i.e. the inner surface of the bubble shell), this relatively low pressure is sufficient to produce the large observed energy output.

Towards the end of the rapid expansion phase, the overpressure typically drops to about 100 kPa (1 bar) or less, being lowest at the onset of the second acceleration peak. After that time, the meaning of the pressure curve is ambiguous, depending on the reason for the second peak, as was discussed above. If the first discussed possibility is true, then at this time the remaining pressure will be topped up by a newly arriving bubble from below, or, if the second possibility is true, it will immediately be freed by the rupture of the bubble shell.

Error ranges of pressure traces are shown as red shades in Figure 7.6. Due to their width, error shades of individual explosions overlap and are therefore hard to distinguish. Thus, the median width of all pressure error shades is shown as a single darker shade behind the mean trace, allowing judgement of the average standard deviation of the traces. This lies in the order of several 10s of percent, reflecting the large uncertainty in the shell mass. Despite this large uncertainty, the figure shows that even in the worst case the gas overpressure at the start of the rapid expansion phase is unlikely to exceed 1,000 kPa (10 bars).

The bottom part of Figure 7.6 shows the pressure drop calculated for *small* explosions. As can be expected, the overpressure found in *small* bubbles is far less than in type *I* explosions, only ranging around 100 kPa. The large extent of error shades in this figure shows that the relative size of errors for *small* explosions is much larger than for type *I* explosions (most prominent for one single trace, which belongs to explosion S_C, see Fig. 6.8). This is mainly the result of the relatively large influence of dissipated energy on the total energy output rate of *small* bubbles (as discussed in Sec. 7.3). As shown, dissipated energy has a large uncertainty due to uncertainties in the magma viscosity, which reflects on the pressure uncertainties. This means that a better constraint on magma viscosities would significantly reduce the error on gas pressures during *small* explosions.

7.5 Gas volume

It was shown in Section 4.4 that there are three separate methods to determine the gas volume of exploding bubbles, namely *i)* from the shape of the pressure decay in bubbles, *ii)* from the energy output, and *iii)* from video observations. Results from these three methods will now be shown and compared.

Method A): Gas volume from pressure decay. In the last section, the bubble's gas pressure decay was determined as a function of time during their rapid expansion phase. At the same time the amount of volume expansion of the bubble cap is known from radar measurements. Section 4.4.2 describes how these two properties can be used to calculate the initial gas volume of the bubble just before the onset of the rapid expansion phase. It needs to be noted that in the case of several bubbles erupting in quick succession, this method would yield only the initial volume of the first approaching bubble.

Figure 7.7 (top) shows the pressure decay of all type *I* explosions, in a different style than shown in Figure 7.6. The used diagram style is similar to Figure 4.8, which was used to introduce the technique. It relates the amount of gas pressure decay to the amount of gas volume expansion. Red curves show data derived from radar, while blue curves show how an ideal gas is expected to behave when it expands adiabatically. Not surprisingly, the shape of the pressure drop in the ideal gas is highly dependent on its starting volume (which is

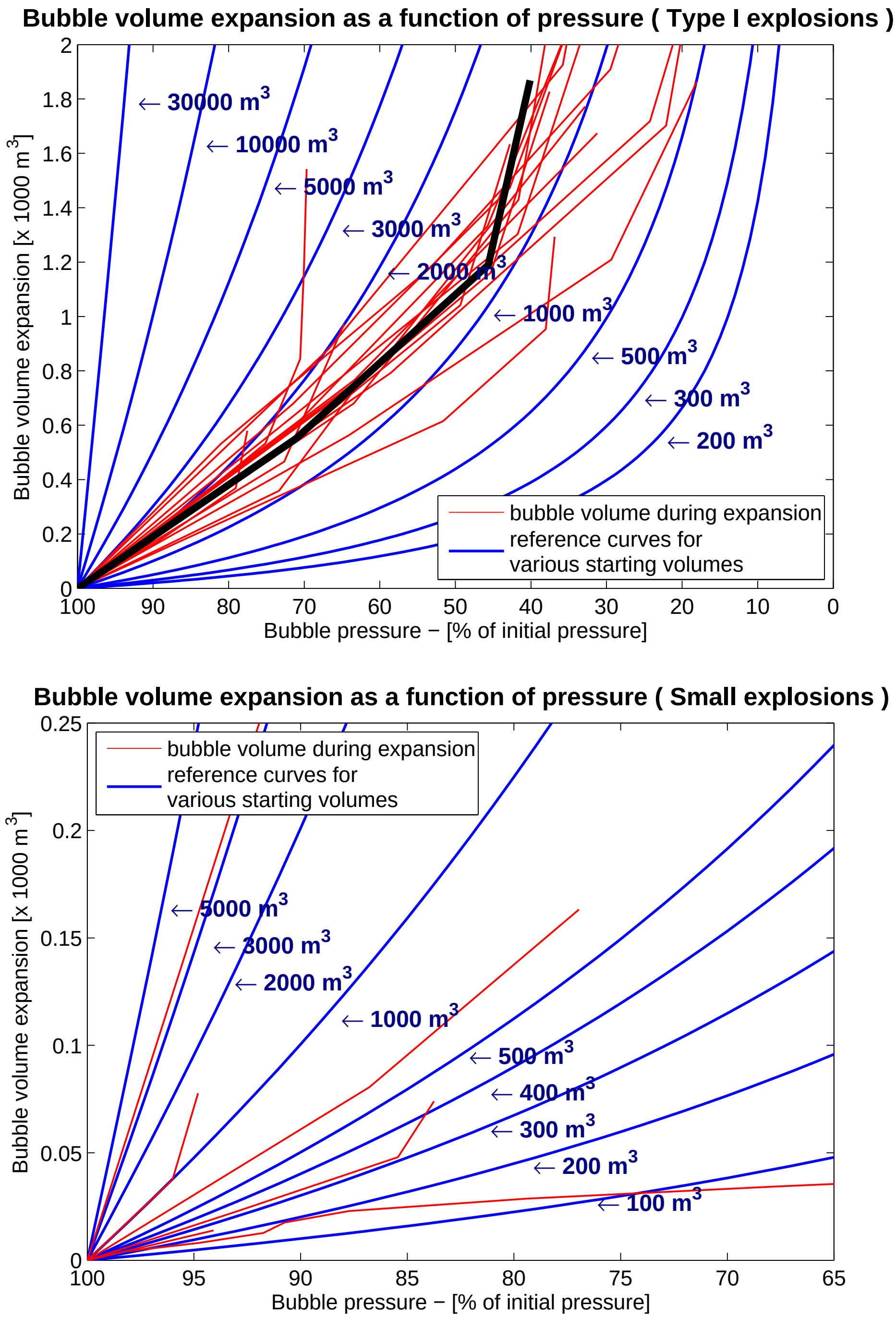

Figure 7.7:* *Estimating bubble gas volume from expansion speed. *These figures are similar to Fig. 4.8, now with real data included. The top plot shows data from type I explosions, the bottom plot shows* small *explosions. Red curves show the pressure drop inside the bubble vs. volume increase during the bubble expansion phase. The volume increase is derived from the bubble size change measured by the radar. Blue curves show the expected behaviour of an adiabatically expanding ideal gas bubble with different initial volumes (as annotated). The black line shows the mean trace of all type I explosions.*

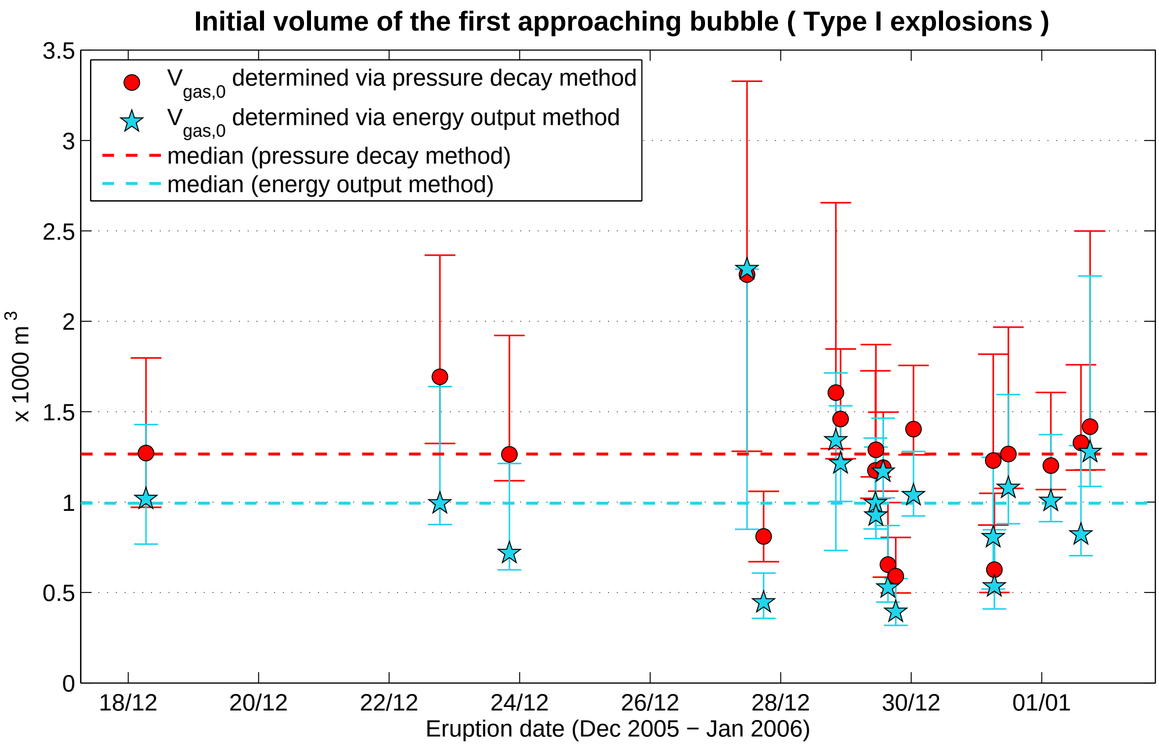

Figure 7.8: Bubble volumes of Type I explosions. *Blue stars show initial gas volumes ($V_{gas,0}$) determined with the energy output method, red dots show initial gas volumes of the same explosions determined with the pressure decay method. Error bars indicate one standard deviation. Dashed lines show the median of the respective group.*

annotated in the figure). For example, when an initial gas volume of 10,000 m^3 is expanded by 1,000 m^3, it will only slightly lower its pressure, while an initial gas volume of 1,000 m^3 will just about half its pressure when it is expanded by 1,000 m^3.

Two things can be read from Figure 7.7 (top). First, most red traces follow the curvature of a blue curve, meaning that the assumption of an adiabatically expanding ideal gas was appropriate. If this assumption were unjustified, a differently shaped expansion behaviour would be expected. Second, the red curves tend to group between the reference curves for 1,000 m^3 and 2,000 m^3, respectively. This suggests that the gas volume of type *I* bubbles at the start of the rapid expansion phase lies in that range.

The bottom part of Figure 7.7 shows the same plot as the top part, but for *small* explosions. As can be expected, their average gas volume is smaller than that of type *I* explosions, but the volumes are also more scattered. This high relative variation in the gas volumes of *small* explosions results from the large uncertainties of their pressure curves, as was discussed in the last section.

Method B): Gas volume from energy output. This technique makes use of the knowledge about the bubble's total energy output during the rapid expansion phase; its details were described in Section 4.4.1. Figure 7.8 shows initial bubble volumes of all type *I* explosions determined from the energy output method as blue stars, including error bars. To allow a comparison with the previous method, results from the pressure decay method are also included in the figure, shown as red dots. Similar to the previous method it needs to be noted that in the case of several bubbles erupting in a quick succession, this method would yield only the initial volume of the first approaching bubble.

The figure shows that there are minor but systematic differences between the two pressure determination methods. While the median of type *I* initial volumes determined with the pressure decay method lies around 1,250 m^3 (dashed red line), their median as determined from the energy output method lies around 1,000 m^3. This difference in the order of a few tens of percent is within the expected error range, reflecting the uncertainties involved with the different methods (see error bars). Given that the two methods are largely independent, the result can be considered a very good agreement. Nevertheless, the difference shows that the energy output method systematically tends to yield somewhat smaller initial volumes than the pressure decay method

Error bar sizes of both methods are mostly influenced by uncertainties in the pressure values, and therefore largely controlled by uncertainties in the shell mass estimates. To a minor degree, error bars on the energy output method are controlled by bubble energies, which are again largely dependent on the shell mass. Error bars determined with the pressure decay method are, to a minor degree, dependent on errors in the cap volume, which are controlled by radar velocity picking errors.

Method C): Gas volume estimation from video. This method makes use of the assumption that after an explosion, the void volume inside the lava lake and the conduit (i.e. the volume that was filled with magma before the explosion) equals the total volume of ejected material, i.e. gas plus magma. Contrary to methods A) and B), in the case of several bubbles erupting in quick succession, this method does **not** yield the volume of the first bubble, but the overall amount of gas erupted during the entire explosion.

Figure 7.9 shows infrared video snapshot sequences from three different typical explosions at Erebus. The respective first snapshot was taken immediately before the explosion. The other(s) were taken as a comparison just after the explosion. As a reference scale, the lava lake diameter is annotated as ≈ 40 m. *Dibble et al.* (2008), when observing Erebus explosions in 1987, noticed that the lake level sometimes continued to drop for several seconds after an explosion (most likely caused by inertia of the magma column, which was accelerated downward by the explosion). Such effects were not observed on the video data available for this study.

The first sequence (Fig. 7.9, top) shows a very large type *I* explosion. Right after the explosion, the lake level has dropped out of view, i.e. it dropped by at least 30 m, as can be approximated from the figure. Assuming a roughly circular lake surface, this amounts to a void volume larger than 37,000 m^3. It was argued in Section 7.1 that the magma volume of a

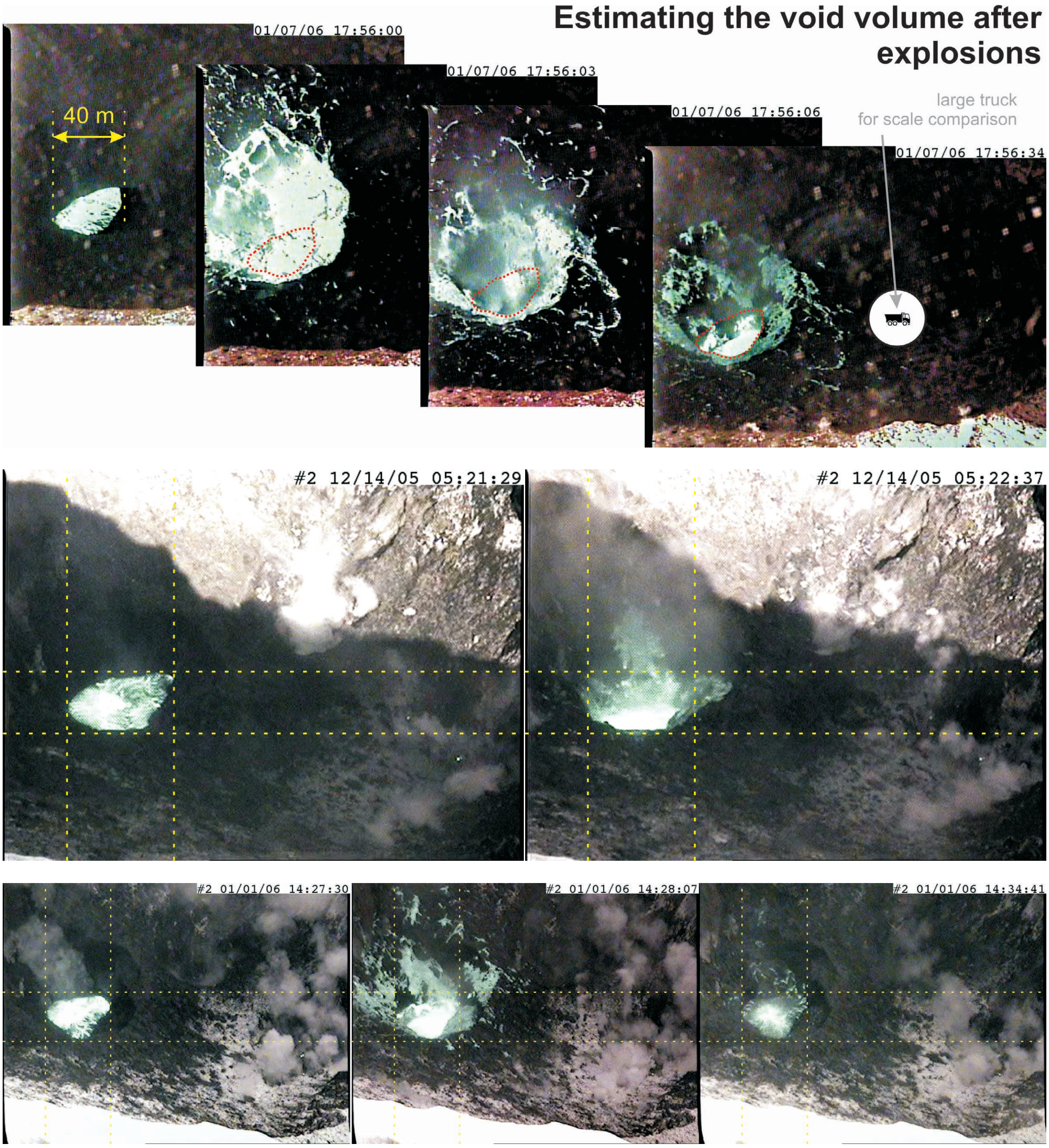

Figure 7.9: ***Estimating total erupted gas volume from video snapshots.*** *These three sequences of infrared video snapshots show the lake level drop caused by three different explosions. Since the size of the lake is known (approximately 40 m on its largest horizontal dimension), the erupted gas volumes were estimated to* $> 35{,}000\ m^3$ *(top),* $\sim 17{,}000\ m^3$ *(middle), and* $\sim 8{,}000\ m^3$ *(bottom).*

large type *I* explosion lies in the order of 1,800 m^3. Assuming that just before the start of the explosion, this void volume was filled with pressurised gas[6] and the ejected magma shell, this means that the total ejected (pressurised) gas volume during this explosion amounted to **at least** 35,000 m^3.

The second sequence (Fig. 7.9, middle) shows a typical type *II* explosion. In this case, the lake level dropped by around 15 m, suggesting a total gas volume of $\sim$ 17,000 m^3. The third sequence (Fig. 7.9, bottom) shows a medium sized type *I* explosion (I_R). In this case the lake level dropped by about 8 m, which corresponds to a total gas volume of $\sim$ 8,000 m^3. During other type *I* explosions (not shown), the lake level was mostly found to drop in the range between 10 and 15 m, and no significant systematic differences were found between type *I* and *II* explosions. During small explosions (not shown) the lake level typically dropped by an insignificant amount only, showing that the ejected gas volume is highly variable between explosions, strongly depending on their type.

When comparing the three available methods for estimating gas volumes, the video method is a rather coarse technique, carrying a large amount of error that mainly arises from uncertainties in the lake dimensions and the observation geometry. Nevertheless, it clearly shows that the **total** gas volume ejected by explosions is significantly higher (i.e. by a factor of 5 – 10) than **initial** gas volumes determined from the two former methods. This discrepancy will be further discussed and interpreted in Chapter 9.

7.6 Acoustic signals caused by explosions

The methods derived in Section 4.5 allow the calculation of the expected acoustic signal caused by bubble explosions up to the time of shell fragmentation. Following arguments from Section 3.4, the bulging lava lake should be regarded as a non-compact source in the frequency band of interest (i.e. acoustic infrasound around 1 Hz). Therefore I calculated its predicted infrasound signal by adding up the expected infrasound signal of a large number of random monopole sources on the surface of the bulging lake (Fig. 4.9), effectively using the *Green's function* method described in Section 3.6. To demonstrate the difference between using the equations for the compact and non-compact case, I have included an example figure in Appendix A that shows the predicted signals for both cases (Fig. A.3).

Red lines in Figure 7.10 show the expected infrasound signals of all type *I* explosions, as they would be observed on the crater rim at a line-of-sight distance of 300 m and an elevation angle of 39°. The effect of atmospheric absorption (*Pierce*, 1981) on the pressure amplitude was neglected, which is a common practise for such a short distance (e.g. *Vergniolle et al.*, 1996; *Johnson et al.*, 2008). Each explosion is plotted in a separate box (similar to the

[6]Gas volumes are highly dependent on their current gas pressure, so they are only comparable at similar pressures. The gas pressure **here** is similar to the gas pressure that was assumed for the previous estimates of the initial gas volumes, i.e. it is the typical bubble pressure just before the rapid expansion phase, as shown in Fig. 7.6. Therefore, the volume numbers are comparable.

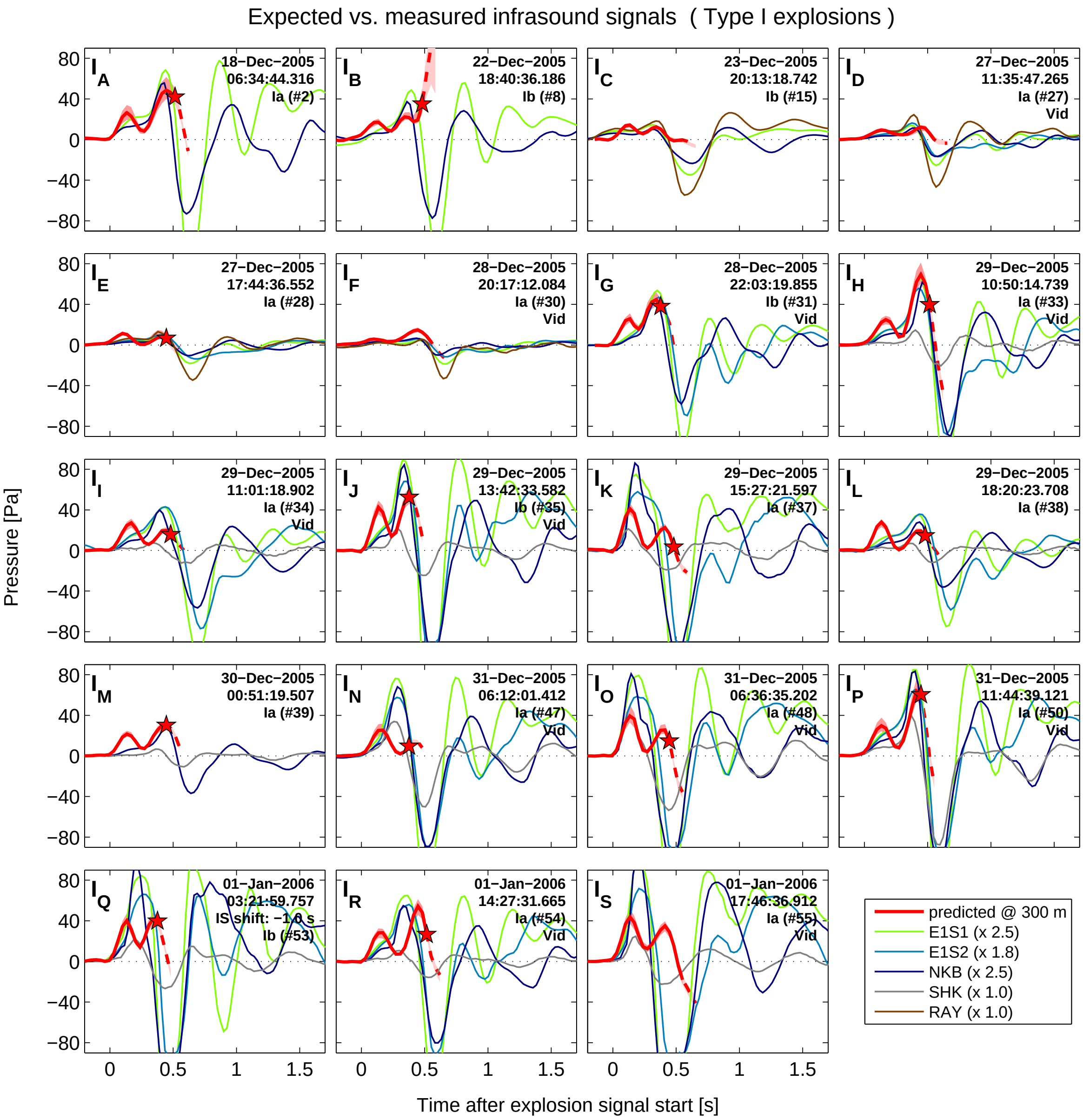

Figure 7.10: ***Expected vs. measured infrasound signals (type I).*** *Thick red lines show the acoustic pressure signal predicted by the model, calculated from radar data. Underlying red shades depict their error range (sometimes hidden behind thick red line). Thin lines show recorded unfiltered infrasound signals from different microphone sites. Since the microphones all have different distances from the lava lake, the traces were shifted and scaled in their amplitude to a common virtual distance of 300 m (apart from SHK and RAY, which already fulfill that criterion). The text information is similar to Fig. 6.6, with the difference that the time axis origin refers to the explosion signal start as observed on the crater rim, i.e. shifted by the signal's travel time.*

velocigrams shown in Fig. 6.6) to allow for a comparison with the underlain real acoustic recording of the respective explosion (thin coloured lines).

Red error shades under the red lines show uncertainties in the prediction of the acoustic signal. Their main contributors are uncertainties in the volumetric acceleration of the lava lake surface, caused by uncertainties in the lava lake diameter and in the radar velocity picks. Other contributors are uncertainties in the surrounding air density and the atmospheric sound speed.

Acoustic data were recorded by *Jones et al.* (2008) with two different types of infrasound microphones, distributed around the crater rim (see also Sec. 5.2.2). Due to the crater geometry, individual microphones have different distances from the lava lake. Therefore, for better comparison of real and predicted acoustic signals, I have shifted all recorded acoustic signals by a fixed amount of time to represent a recording on the crater rim at 300 m distance from the lake centre. This time shift was not adjusted for individual explosions, but was determined only once per station and remained fixed for the entire data set (signal travel times from lake to receiver were found to be 0.93 s, 0.99 s, 1.74 s & 2.43 s for RAY, SHK, E1S1 & E1S2 sites, respectively). Additionally, I have scaled the recorded amplitudes to that same distance, using the $^1/_r$ law, where r is the distance from the source. This practise allows for a direct comparison between predicted and real acoustic recordings, with respect to travel time as well as to the signal's true amplitude.

Figure 7.10 shows that the model predicts an infrasonic wave to be emitted during explosions even before the burst of the shell (marked as star), merely through the bulging of the lava lake surface. The expected signal starts with a compression of the atmosphere, caused by the bulging of the lake surface, followed by an expansion when the bulging slows down. The pressure waves are very powerful (several tens of Pa at the crater rim), yet they are located mainly in the infrasonic spectrum and thus largely outside the human audibility range. Radar data are only valid for describing the acceleration of the magma shell before the burst, thus the predicted sound traces end at burst time.

One of the most notable features of Figure 7.10 is that despite being determined in an entirely different way, predicted and measured acoustic pressure signals match very well for most type *I* explosions, not only in amplitude but also in the shape of the signal up until the burst time. Both of them agree in that a significant amount of acoustic energy is radiated before the bubble bursts, simply by introducing and accelerating volume into the surrounding atmosphere. This effect will be further discussed in Chapter 9, supplemented by a simple explanation for the acoustic signal that can be measured **after** the burst.

When looking at the match in detail, it is striking that the typical double peak pattern in the predicted acoustic pressure signal (resulting from the double acceleration peak that is typical for type *I* explosions) often correlates with a distinctive plateau, or a bank, before the main onset of measured acoustic signals from type *I* explosions. This plateau was previously observed in acoustic recordings at Erebus (*Johnson et al.*, 2004), it is therefore likely to be a distinctive feature of current Erebus explosions. When comparing the waveforms, the first

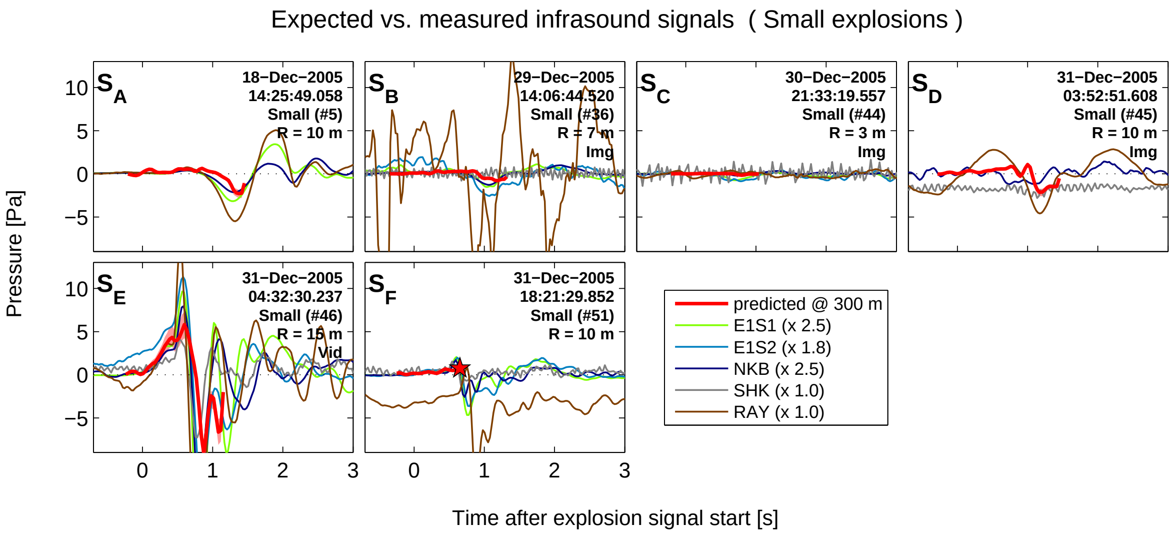

***Figure 7.11:* Expected vs. measured infrasound signals (small explosions).** *R denotes the approximate radius of the affected region of the lake surface (in type I & II explosions $R \approx$ 20 m, i.e. the whole lake surface was affected).*

and smaller one of the two predicted pressure peaks typically aligns very well with the plateau in the recorded pressure (e.g. Fig. 7.10 $\mathrm{I_A}$). However, the predicted trace rarely matches the plateau's exact shape. Thus, despite the good overall fit during the explosion's main phase and the very good temporal correlation between predicted peak and recorded plateau, the model is not fully sufficient to reproduce the exact acoustic waveform at the very start of explosions.

The most likely reason for this is that the model tends to overestimate the acoustic signal early in the explosion. It assumes that right from the start, the **entire** lava lake surface bulges upwards, while in reality, in those first moments only a fraction of the lake surface is bulging up. This means that a small upward bulging of the model lava lake early in the explosion generates a relatively strong predicted acoustic signal (i.e. the first of the two peaks in Fig. 7.10 $\mathrm{I_A}$), which is much stronger than the real acoustic signal generated by the partly bulging lake at that time. Even though this effect diminishes quickly into the explosion when the affected area grows to engulf the entire lake surface, it leads to an overestimation of the first of the two typical predicted acoustic pressure peaks of type *I* explosions. While it would be possible to eliminate this effect in the model by introducing additional parameters, I refrained from doing so to keep the model simple and to avoid introducing arbitrary parameters.

Yet, as a demonstration, Figure A.5 (Appendix A) shows the same data as Figure 7.10 but uses the spectra's mean velocity instead of their cutoff velocity to predict the acoustic traces. Even though being a somewhat arbitrary procedure, the fit between real and predicted traces increases significantly for some explosions.

Figure 7.11 shows a similar plot for *small* explosions. The calculation takes into account

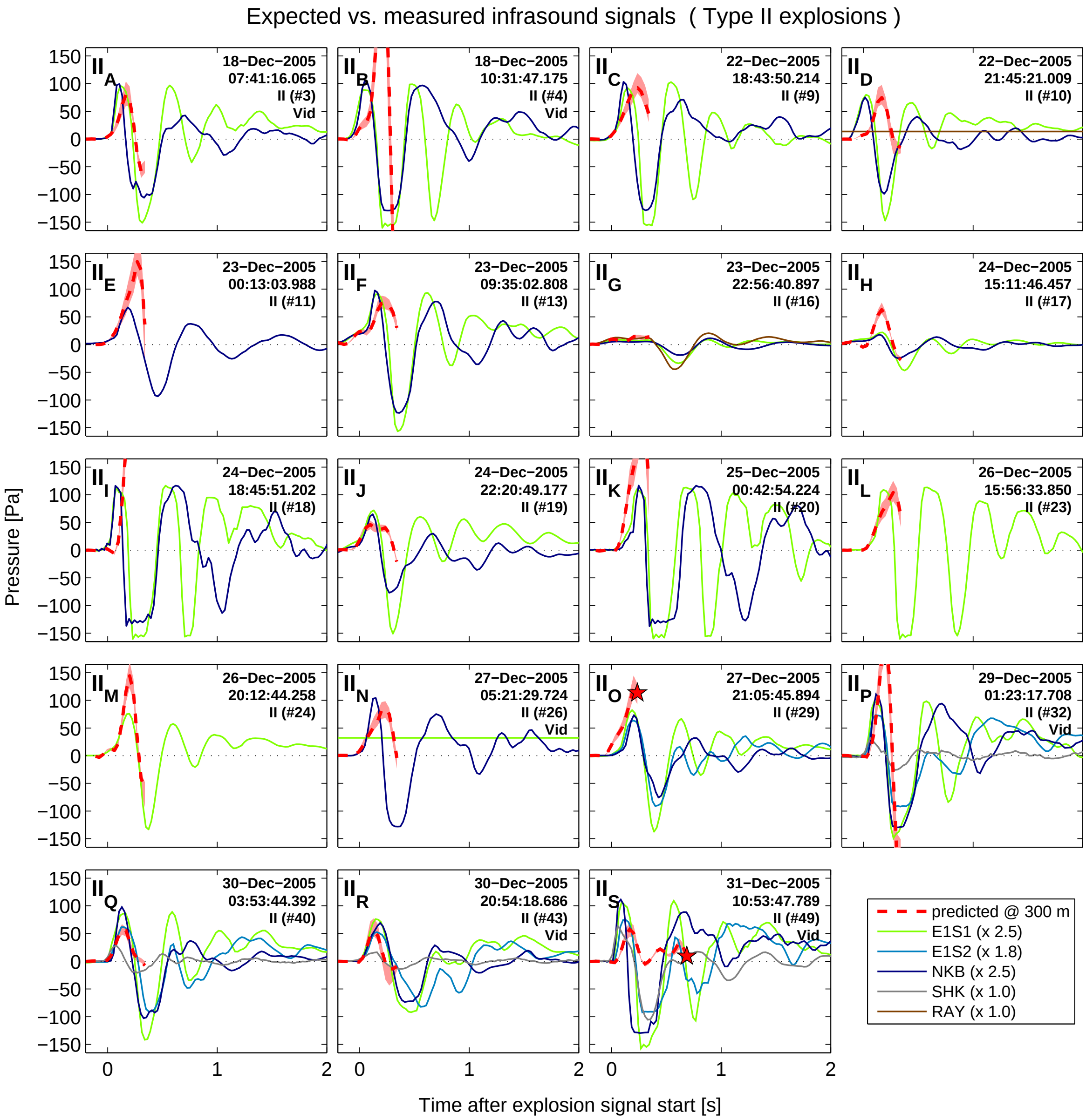

***Figure 7.12:* Expected vs. measured infrasound signals (type II).** *The predicted acoustic traces are fully dashed because shell rupture typically occurs right at the start of type II explosions, therefore not fulfilling the conditions for a valid use of the bubble expansion model. Nevertheless, the model was used to calculate these traces as a demonstration of its capabilities even outside its valid range. Note that some of the traces are clipped (e.g. II_L).*

that the area of affected lava lake surface is much smaller than during type *I* explosions (see parameter R in Fig. 7.11). As expected, *small* explosions cause significantly weaker pressure waves than type *I* explosions, reflected not only in the model prediction but also in the measured signal. Similar to type *I* explosions, predicted acoustic traces of *small* explosions match the recorded signals very well, not only in amplitude but also in shape. This not only indicates that the bubble expansion model is a good description of the real process, but also that the size estimates (R) obtained from video are reasonable.

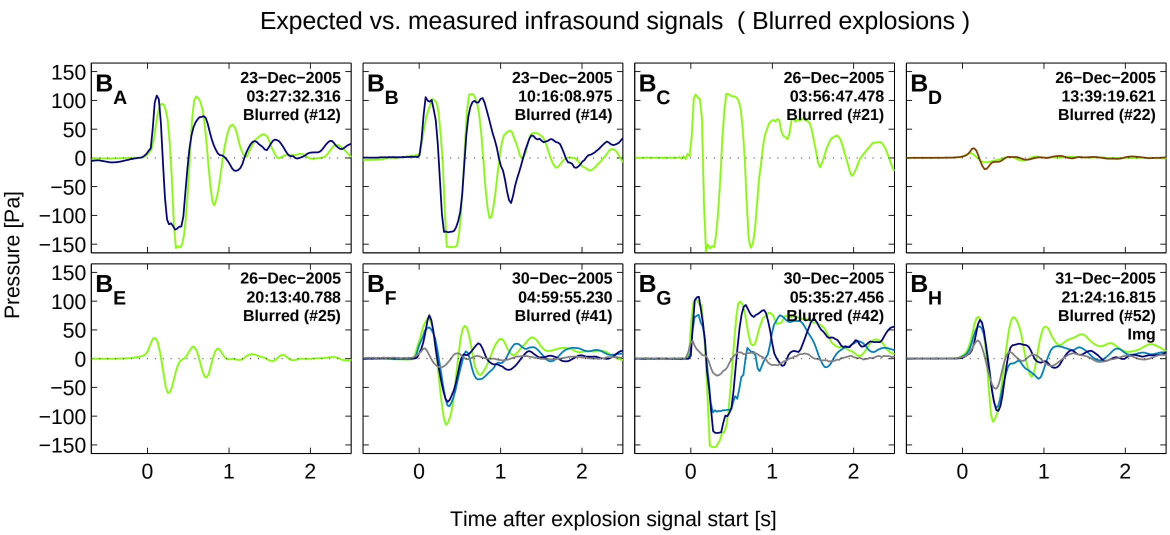

Figure 7.13: Measured infrasound signals (blurred explosions). *No acoustic traces can be predicted from the model, since blurred explosions did not allow for the picking of radar cutoff velocities. Note that similar to Fig. 7.12 some of the traces are clipped (e.g. B_C).*

As an additional demonstration, Figure 7.12 shows the same kind of comparison as the above figures, adapted for type *II* explosions. The predicted traces are fully dashed because as argued before, the bubble shell during type *II* explosions tends to rupture immediately at the start of the explosion. Therefore, applying the bubble expansion model to predict the acoustic signal of type *II* is not strictly valid. However, doing so regardless of these concerns leads to a surprisingly good fit between predicted and measured signals. This indicates that even though being outside of its valid range, the bubble expansion model successfully predicts the acoustic signals of type *II* explosions. A possible explanation for this is that after the burst of type *II* bubbles, the resulting two-phase flow of fragments and gas behaves somewhat similarly to an intact shell with regard to infrasound generation.

The main difference between type *I* and *II* acoustic signals is that type *II* signals generally have the much larger pressure amplitudes. Accordingly, Figure 7.12 shows that some of the recorded signals are clipped, which usually occurs at pressures exceeding $\pm$ 125 Pa at the microphone. This is in agreement with qualitative video observations, giving the impression that type *II* explosions are more violent than type *I* explosions. Another interesting feature of type *II* acoustic signals is that on both the predicted and the measured traces, they entirely lack the characteristic plateau, or double peak signature that is typical for type *I* explosions. This is in agreement with Figure 6.11, showing that type *II* signals only have one acceleration peak.

Lastly, Figure 7.13 shows the measured acoustic signals for *blurred* explosions. Since no radar cutoff velocities were picked for these events, no predicted acoustic signal can be shown. The figure nevertheless reveals some useful properties of *blurred* explosions. Their amplitudes are similarly high as those of type *II* explosions, and even their shapes are very

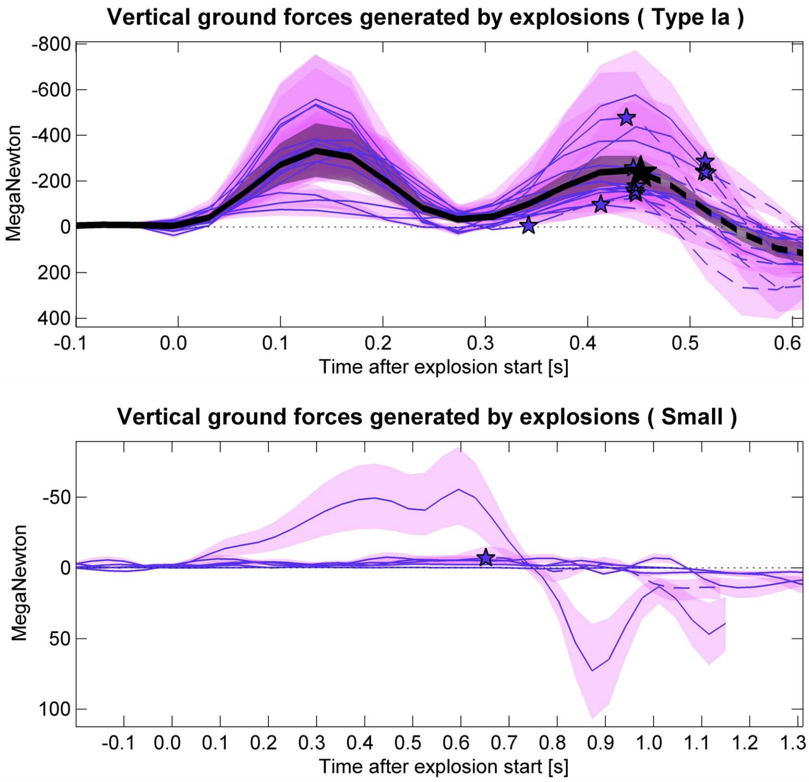

Figure 7.14: Vertical ground forces generated by explosions. Top: *type Ia explosions. The black line shows the mean of all traces, its gray error shade indicates the median width of all error shades. Note that type Ib explosions were not plotted here to avoid cluttering and to allow a better comparison with Fig. 7.1 (bottom).* ***Bottom:*** *small explosions.*

similar to type *II* signals. This supports the conclusion drawn in Section 6.3 that type *II* and *blurred* explosions are very similar to each other.

In summary, the above data show that predicted and measured acoustic pressure signals agree very well for type *I* and *small* explosions, and they even show a surprising match for type *II* explosions, outside the model's range of validity. This overall agreement is remarkable, given that the respective traces were determined from entirely different data types, i.e. one from radar velocity data using a geometrical expansion model, and the other from direct acoustic pressure measurements on the crater rim.

7.7 Ground force caused by explosions

Vertical ground forces resulting from bubble explosions were calculated from Equation 4.55. As argued in Section 4.2.8, following Newton's second law, the ground force is mainly controlled by the inertial forces of the shell mass during its acceleration. Accordingly, the ground force mimics the zenith acceleration function (Fig. 7.1), scaled by a geometrical factor and the shell mass. Since the acceleration is mainly upwards, the ground force is expected to be directed downward, i.e. its value should mostly be negative.

Figure 7.14 (top) shows the vertical ground force for type *Ia* bubble bursts, which is indeed mainly negative, i.e. directed downwards. Its peak values vary between $\sim 100 - 800$ MN, i.e. they mainly lie in the 10^8 N range. Similar to the previous parameters, the calculated ground force is only valid until the burst of the bubbles, i.e. it does not include post-burst effects.

The bottom part of Figure 7.14 shows ground forces for *small* explosions, which are naturally much smaller than those of type *I* explosions. This should reflect in a much smaller seismic signature, as was already argued in Section 7.3 when discussing the seismic energy output of small explosions (Fig. 7.4).

The error shades shown in Figure 7.14 partially overlap, therefore their median width is indicated as a dark error shade around the mean trace (solid black). Error ranges of ground forces are generally relatively large compared to other model output parameters because they directly depend on uncertainties of the shell mass, which, as argued before, is less constrained than other parameters. Additionally, uncertainties in the picked radar cutoff velocities influence the zenith acceleration and therefore the ground force uncertainties, but only to a minor degree compared to mass errors.

CHAPTER 8

MEASURING THE DIRECTIVITY OF EXPLOSIONS IN 3D AND 4D

Note: parts of this chapter were already published in Gerst et al. (2008)

In the last chapters, physical properties of bubble explosions were derived from Doppler radar data coming from a single high resolution instrument. By applying the expansion model (Chapter 7), the assumption of a vertically symmetrical process was made. Yet, some of the explosion videos show a slight directivity of explosions towards one side, therefore breaking vertical symmetry. When measuring the surface speed of such an asymmetrically exploding bubble, the result will depend on the observation azimuth of the radar (i.e. depending on whether the explosion is directed towards the radar or away from it). It will be argued in Chapter 9 that this effect is averaged out when measuring and analysing several explosions, which are likely to show a variety of different explosion directivity. However, this assumption is yet to be shown as being valid, which will be one of the purposes of this chapter.

My approach to do so will make use of data from three different radar devices, which recorded several explosions simultaneously from three different observation azimuths. This combined data set allows for the calculation of the directivity of explosions in three dimensions.

The knowledge of the directivity of explosions is not only important for supporting the overall conclusions that will be drawn in this study. It also plays a fundamental role when interpreting infrasonic recordings of volcanic eruptions in general, which is a very powerful tool in volcanology. Several studies (e.g. *Vergniolle et al.*, 1996; *Johnson et al.*, 2004) were aimed at gaining information about the source process of a Strombolian eruption by analysis of the infrasound signal. In most previous cases of infrasonic near-source recordings, only one or two sensors were used, which were often placed at locations determined by practical reasons, assuming that source directivity effects and path effects were negligible. Practically, this means that the assumption of a monopole sound source was made. As shown in Chapter 3, an acoustic monopole is a source with an isotropic emission pattern, i.e. the generated acoustic pressure is independent of the direction of observation. It can be realised by a spherically symmetric volume source, or, in a half space, a hemisphere located right on the boundary. A dipole source, i.e. a source with a certain direction-dependent emission pattern (Sec. 3.5), can be generated, for example, by either a directional expansion of a bubble shell or by a moving sphere. In other words, if there is a significant amount of directivity in an explosion, then the assumption of a monopole source can become invalid, leading to a possibly erroneous interpretation of acoustic data.

Recent studies of volcanic infrasound signals support this assumption. With the development of new instruments it became possible to observe the source of a volcanic eruption with a whole network of acoustic microphones. *Jones et al.* (2008), just shortly after the radar experiment, deployed a network of three acoustic sensors on the crater rim of Erebus volcano, with a special emphasis on determining the source signature. Using these data, *Johnson et al.* (2008) conclude that infrasonic signals from explosions from the active lava lake on Erebus contain a significant non-monopole part, which is interpreted as an asymmetric (i.e. non-isotropic) expansion of the bursting bubble. However, sound distortions along the path could not be fully ruled out as a possible explanation.

This raises the question of when the assumption of a monopole source is valid, and whether this can be determined by means that are independent from acoustic recordings. I will show that one possibility to achieve this is via the three dimensional recording of radar data from an explosion. Using velocity measurements from three radars allows the calculation of the directivities of explosions in 3D as they evolve in time, effectively providing a 4D observation. Non-symmetrical explosions can be identified on the basis of their directivity vector.

As this 3D radar technique is relatively new, I initially derive the theoretical background for calculating the directivity of a moving projectile, a volcanic jet, and eventually that of an expanding bubble (shown in Appendix B.1). On the basis of this theory I will present the directivity of 10 explosion recorded at Erebus.

8.1 The synchronous measurement with three Doppler radars

As shown in previous chapters, most explosions in 2005/06 at Erebus lasted for several seconds, with an impulsive main acceleration phase lasting for around one second. The 3D radar system at Erebus was set up so that the devices were located at the sites RAY, SHK & SUM (see Table 5.1 and Fig. 5.10), which are all located on the crater rim with a direct and unobstructed view of the lava lake inside the crater. The area of observation on the bubble surface (i.e. illuminated by the radar) had a diameter of around 20 m, resulting from the spread angle of the radar beam (Fig. 6.4). This is large enough to ensure that the point on the bubble surface that is moving fastest towards the radar was always within the area of observation during the first seconds of each explosion, even if the bubble centre moved somewhat away from the centre of the lake[1] (the videos show that even for explosions that

[1] Even though the radially decreasing sensitivity of the radar beam causes reflected signals to decrease towards the lake borders, the correct measurement of velocities is not compromised by this effect (Sec. 1.5).

showed some directivity, this lateral displacement was indeed small during their first few seconds).

To make the data of the three radar devices comparable, the data of the fast radar (∼14 sps; RAY site) had to be adapted to simulate the data output style of the two slower radars (∼1 sps; SHK & SUM sites). Internal technology of the two slower radar devices limited the observation time during every sample interval, so that for the chosen setup, the target could only be observed during the last 250 ms of every full UT (universal time) second. Therefore, to provide a uniform and unambiguous dataset, data from the faster radar were accordingly cut and downsampled, such that 3D velocity data of the target exist for every 250 ms in every full UT second (see Fig. 8.1). This obviously means that the sampling process was sparse, and that the system was blind for processes occurring within the first 750 ms of every full UT second. Since the typical expanding phase of an intact bubble at Erebus took about a second, one sample can be expected from that phase.

Samples from times before the shell burst show the surface velocity of the expanding bubble, while samples from times after the burst show the velocities of large shell fragments. In contrast to the more sophisticated model used in Chapter 7, due to the low sampling rate of 1 sps, a very simple expansion model was chosen for this purpose (Sec. B.2). This means that during an explosion, material is considered as mainly moving radially away from the lake in all directions, thus the cutoff velocities obtained at that time are considered to represent the explosion's expansion velocity (i.e. without any geometrical corrections for the shape of the bulging lake, and not considering if the shell has already burst). Accordingly, I do not distinguish between explosion types here, as was done in Chapters 6 and 7, but I include explosions of all types that allow the picking of cutoff velocities (i.e. all but *blurred* explosions). While these assumptions would be too crude for determining detailed physical properties of explosions, they are fully sufficient to determine the directivity of an explosion, since data from the three radars are all similarly processed, i.e. using the above made geometrical simplification. In summary, the necessary information for the directivity of explosions can almost directly be derived from the difference in measured surface velocity of the different radars. However, the used simplifications put limits on the interpretation of the obtained directivities, as will be discussed later.

8.2 Results

To obtain the 4D explosion directivity at Erebus, radar cutoff velocities (as explained in Fig. 6.3) were determined for each explosion and plotted in Figure 8.1. As a picking criterion, care was taken to only consider the maximum speed of the bulk material (i.e. the shell surface), and not to pick the maximum speed of small amounts of fast ejecta, which could have been the result of gas jets from the fracturing of the shell. I then used the technique described in Appendix B.2 to calculate the directivity vector as a function of time for every explosion.

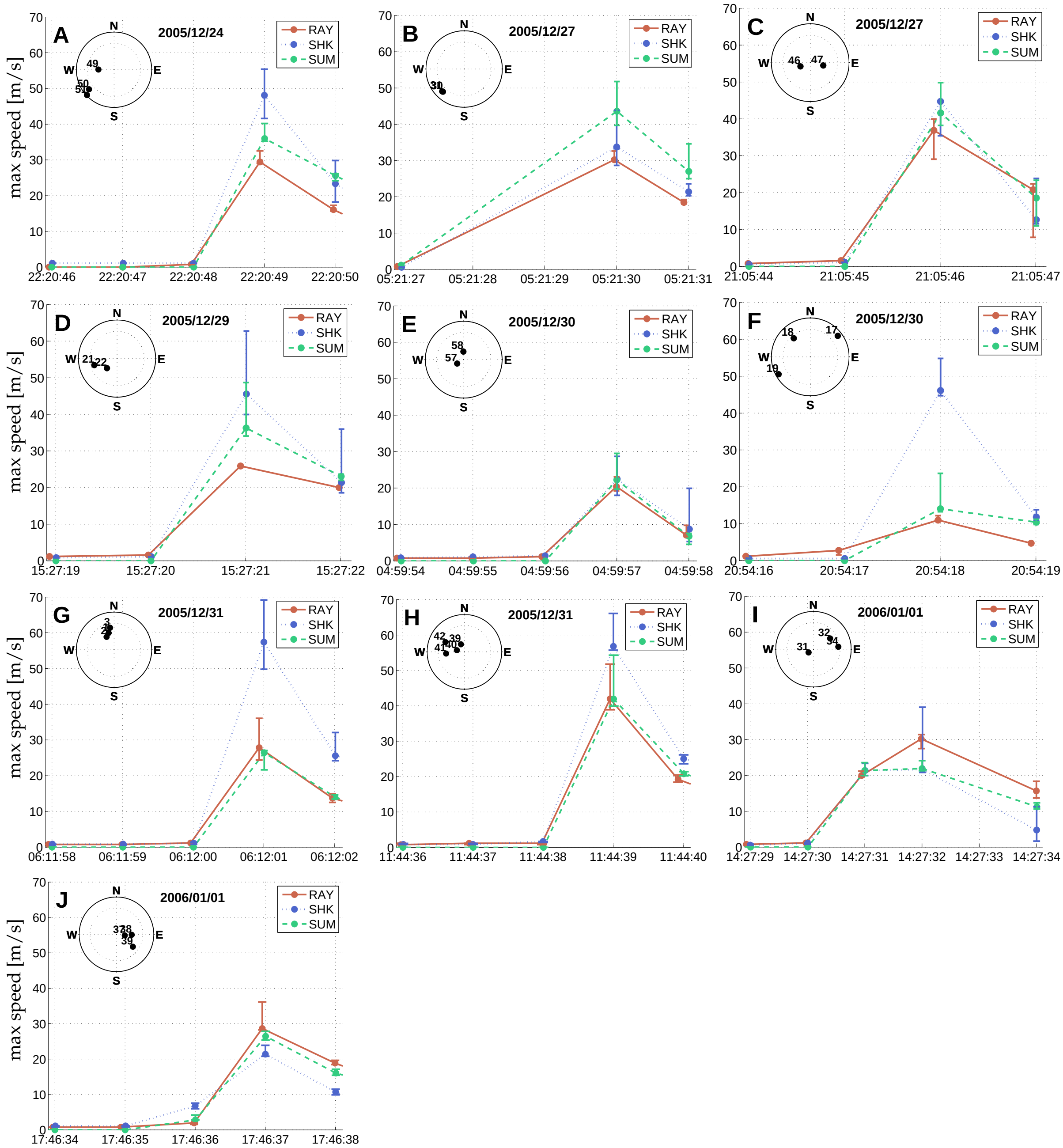

Figure 8.1: ***Picked cutoff velocities of three radars*** *for 10 explosions, including error bars. The vertical axis shows the speed [m/s] of the bubble shell (before burst) or its fragments (after burst), the horizontal axis shows time of day [hh:mm:ss UT] until one second after the main part of the explosion. Data from later times are not shown in the diagram, since velocities are usually small. The inlay plot shows a stereographic projection of the directivity vectors, annotated with the respective second. The circular grid line marks an inclination of 45°, with the centre representing a vertical vector (meaning* ***no*** *directivity). Note that the length of the vectors is not accounted for in the stereographic plot, therefore vectors with a small absolute velocity will be visually overestimated.*

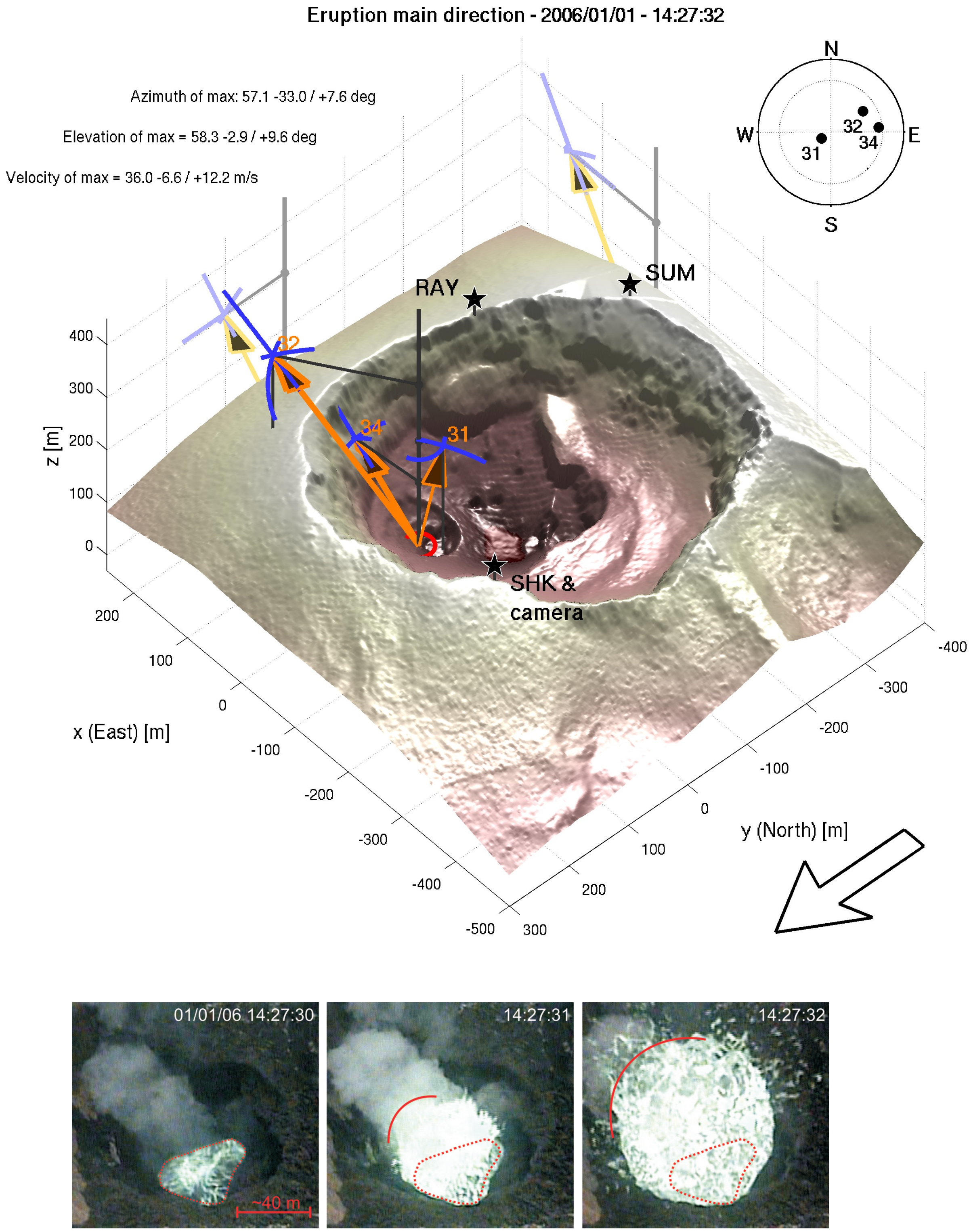

Figure 8.2: ***Top: 3D radar directivity vectors for a Strombolian explosion at Erebus.*** *The three orange arrows show the main explosion direction for three seconds (01/01/2006, 14:27:31, 32, 34), where the thickness of the vector is scaled with the strength of the radar signal, which is a relative measure for the amount of moving material in the radar beam. The length of the vector in m is scaled by a factor of 10 from its absolute value in m/s (i.e. 300 m length equals 30 m/s). Blue lines indicate error boundaries for azimuth, inclination and absolute value. Station and camera locations are marked as stars; the 40 m wide Ray Lava Lake is indicated as a red circle on the crater bottom. Numbers at the arrow tips indicate the second of their occurrence. For better orientation, the projection of the longest directivity vector and its error bars is drawn on the sides of the box. Note that unlike in Fig. B.2, a vertical arrow here means* ***no*** *directivity, i.e. purely symmetrical expansion. The stereogram in the corner shows the direction of the respective vectors in the same fashion as in Fig. 8.1 I).*
Bottom: infrared video sequence of the explosion*, recorded by the MEVO camera from the crater rim at position SHK. The images show that the explosion is not symmetrical, but has a preferred direction towards the upper left of the picture. This direction fits very well with the explosion directivity vector derived from the radar observations.*

During the deployment time of the radar system, 24 eruptive events were recorded simultaneously on all three radars (Fig. 6.1), 10 of which yielded velocity spectra that allowed the determination of cutoff velocities, and therefore the calculation of one or more successive explosion directivity vectors. The other 14 explosions did not allow for the determination of directivity vectors, mainly due to short time gaps in the spectra, resulting from a temporarily slow network (as mentioned in Sec. 5.2.1, the radar located at SUM did not have a local data logger for storage, but directly transferred its data to the base camp). Three explosions produced velocities that were too high for the sensitivity range of the two older radar instruments (> 72 m/s), so cutoff velocities could not be picked. Figure 8.2 shows the directivity vectors that were obtained during one of the 10 processable explosions. Of these 10 explosions, six were recorded on video; all of them with a good to very good fit between video and directivity (see Table B.1, Fig. 8.2 and *SOM*).

Error boundaries around the cutoff velocities were picked as described in Section 7.1, resulting in a positive and a negative error boundary for each radar measurement, i.e. leading to a total of six error boundaries for the three radars. Assuming the validity of this relatively simple model (Appendix Sec. B.2), these six error boundaries were propagated to the azimuth, inclination, and absolute value of the final derived velocity vector (App. B.2). The propagated error boundaries were grouped in positive and negative errors. Subsequently, their squares were added inside each group, since the errors from the different radars are considered statistically independent. The resulting error boundaries on azimuth, inclination, and absolute value of the final derived velocity vectors are given in Table B.1, and are also shown as blue bars in Figure 8.2.

Figure 8.1 shows not only the picked radar velocities of explosions, but also a small stereographic plot showing the resulting directivity vectors in their temporal order. For all but one (Fig. 8.1 F) of the 10 explosions, the directivity vectors of subsequent seconds are grouped, allowing for the conclusion that the main directivity remains stable within a certain region throughout an explosion even though shell rupture usually occurs after the first sample of the explosion (i.e. around the time of the peak). However, when taking a closer look, even though the vectors are grouped, they show significant changes (or a rotation) of direction during the time of an explosion. Especially interesting is the event shown in Figure 8.1 F. Its directivity vectors show a large variation in the stereogram, indicating a non-uniform explosion directivity. And indeed the video footage of this explosion shows that the initial movement of the bubble is significantly different to the movement in the main expansion phase (see *SOM*).

Figure 8.3 is a stereogram containing all explosion directivity vectors obtained from the 10 explosions that allowed for the calculation of directivities. The figure shows that explosion directivities have a large variation, and even though vectors from single explosions are grouped together, they change strongly from explosion to explosion. The average azimuthal error on the directivity values is 32.5°, and the average inclination error is 15.6°. The closeness of the mean direction to the centre (= **no** directivity) shows that the explosions do

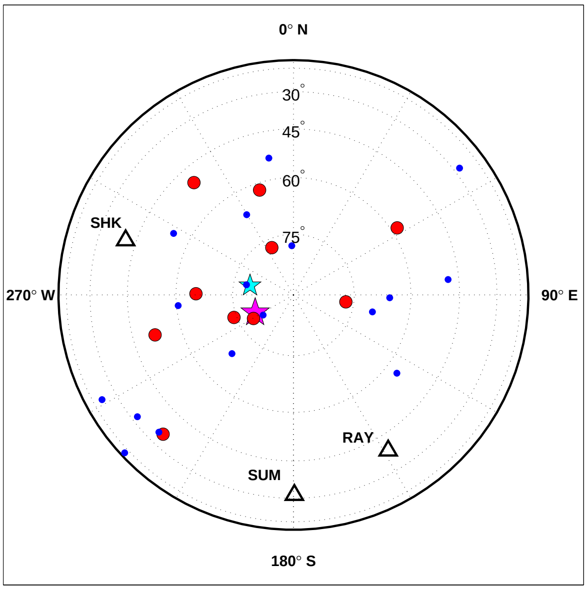

Figure 8.3: ***Directivities (azimuth/inclination pairs) derived from radar measurements plotted on a hemisphere****, where the centre point (i.e. the vertical) indicates an explosion with no directivity. This plot combines the stereograms in Fig. 8.1 A – J. Big dots mark the direction of the longest vector of each explosion, which can be considered as the "main direction" of each explosion. Small dots show all other directivity values. The big star marks the mean direction of the longest vector of all explosions, calculated by adding up all unit vectors of all longest vectors (i.e. all large dots). The small star marks the mean direction of all other vectors. Radar locations, as seen from the source, are marked as triangles.*

not have a single preferred direction. Only a directional sector around SSW appears to be avoided, although I do not consider this as statistically significant at this stage, i.e. without further evidence. Note that error ranges are too small to be fully responsible for the large variation of directivities. Therefore, the variation of explosion directions must be a true feature of the volcanic system.

Figure 8.4 is a map of locations of fresh volcanic bombs that were found **farthest** from the lava lake. It shows that on all but the west side of the crater, the farthest reaching bombs are distributed close to the 400 m distance line from the lake. The exact distribution is, to a large part, expected to be influenced by the elevation angle of the crater rim as seen from the lava lake, which at Erebus is changing significantly with azimuth, being smallest on the South and East sides of the crater. Nevertheless, the figure shows that no strong trend of bomb directivity is present at Erebus, consistent with the widely scattered explosion directivities shown in Figure 8.3.

8.3 Implications of the 3D observations

I have shown in Chapter 7 that with the help of a geometrical bubble expansion model, explosions at Erebus bear a wealth of physical parameters that can be determined, allowing for an interesting insight into their mechanism. In contrast, the aim of this chapter is restricted to the determination of directivity effects of explosions, using a strongly simplified expansion model. Naturally, the choice of model complexity has positive and negative effects on the gained results, some of which are discussed in detail in *Gerst et al.* (2008). At Erebus, the system of three radars recorded three independent parameters. Accordingly, a simplified model with three degrees of freedom was chosen as the best compromise between model simplicity and information gain, leaving the model neither under- nor over-determined. It is therefore not necessary to guess any of the parameters, which would introduce a strong

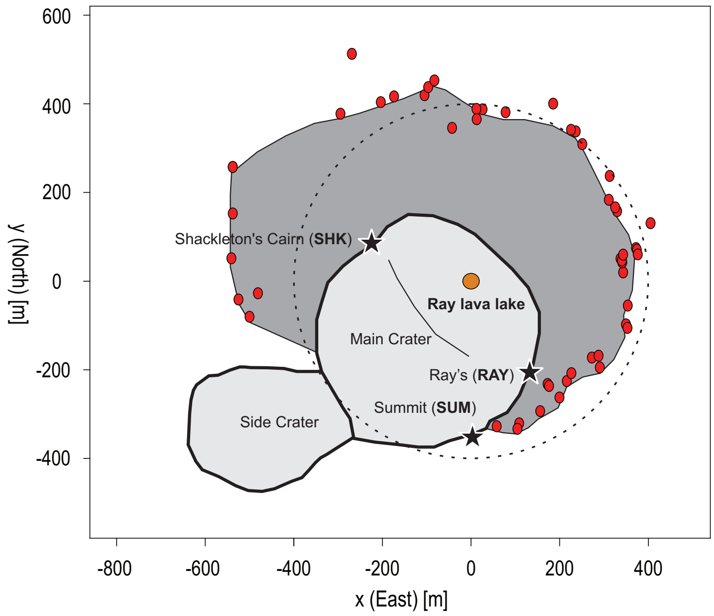

Figure 8.4: ***Map of farthest reaching volcanic bombs on the volcano slope*** *that were ejected in the months before January 2006 (red dots; also shown in Fig. 5.10). The darker shaded area represents the typical area of bomb fall for the time period measured. A dashed circle marks the 400 m distance line from Ray Lava Lake for comparison. Stars indicate the locations of radar devices (Tab. 5.1). GPS Locations were generated using Trimble 5700 receivers operated in differential mode with the base station receiver located roughly 2 km away at Lower Erebus Hut. Note that there was no access to the two craters (thick black line) in that season, so no bombs could be located therein. Source: Nelia Dunbar, pers. comm.*

bias to the results. And indeed, the good correlations between radar measurements, video observations and infrasound recordings suggest that in the case of Erebus, such a simple (and qualitative) model is a valid first order description of the real process. Additionally, even if doubt should remain whether the system can be sufficiently described by an expanding, horizontally moving bubble, the derived directivity vectors still have significance. This is because the radar velocities can indicate the presence of a preferred (i.e. asymmetrical) expansion direction of the volumetrically expanding body, independently of its assumed shape in the model.

The above results show that explosions often show a strong directivity, i.e. the expanding bubble has a significant horizontal velocity component and therefore a favourite expansion direction. It is therefore likely that the assumption of an exclusive monopole sound source is insufficient for these explosions, and that at least a dipole component has to be added to adequately describe the acoustic source. This conclusion is strongly sustained by the observation made by *Johnson et al.* (2008) that infrasound signals from explosions at Erebus often inherit a significant dipole (if not quadrupole) signature. Even though sound waveform distortions along the path might be causing similar effects, they are not necessary to explain the good agreement between radar and infrasound data (*Johnson et al.*, 2008).

A good correlation between video observations and radar explosion directivity measurements was found, as well as a significant grouping of directivity vectors during single explosions. This indicates that the method presented here is a stable and reliable method of determining 4D directivities of explosions. A more detailed analysis of the directivity behaviour during single explosions shows that even though being grouped, some directivity vectors display a change or rotation during the explosions. This behaviour is consistent with variations of infrasound dipole axes during single explosions (*Johnson et al.*, 2008), which is expected when the preferred direction of expansion slightly varies during explosions. Unfortunately, the (now permanent) network of infrasound microphones used by *Johnson et al.* (2008) was not yet fully operational at the time of the radar experiment, so a direct comparison of explosions directivities and acoustic dipole axes of individual explosions is not possible due to the lack of temporal overlap.

Rotations of explosion directivity are possibly caused by the rupture of the magma shell, which usually occurs after the first sample of the main part of an explosion. After the rupture, the radar is tracking the largest shell fragments, the velocities of which are probably influenced not only by their velocity shortly before the rupture, but also by the rupture process itself. Considering this, a change of the explosion directivity, accompanied by a rotation of the infrasound dipole axis is not surprising. Additionally, the system is expected to inherit a further mechanism for the rotation of infrasound dipole axes, resulting from the expected cavity resonance after the burst of the magma shell (as will be discussed in Sec. 9.5). While the dipole axis of the expanding bubble is expected to be influenced by the directivity of the explosion, the cavity resonance after the burst is expected to generate a mostly vertical dipole, controlled by the orientation of the conduit axis. Thus, acoustic dipole axes of explosions can be expected to systematically rotate towards the vertical after the shell burst.

When examining the behaviour of several explosions, a large variety of explosion directivities was observed (Fig. 8.3). Since measurement errors cannot account for such a large variation, I conclude that eruptive events at Erebus in 2005/06 had a wide range of main directions. The relatively uniform distribution pattern of directivity vectors agrees well with the locations of the farthest volcanic bombs ejected from the explosions, and suggests that the preferred direction of an explosion is mainly random. The implication of this is that a systematic bias of results obtained in Chapter 7, caused by a possibly preferred main direction of explosions, can be ruled out. Therefore, even though **single** traces of the shown physical parameters are possibly biased by the directivities of individual explosions, their **average** can be expected to be free of such influence.

What are the possible causes for such a randomness in explosion directions? Generally, such behaviour can be expected if the source region does not force the explosion in a certain direction. In this case, the point of first rupture will most likely be controlled by the geometry and the physical properties of the magma shell of the bubble, which at the point of rupture spans the entire surface of the lake. Since the momentum of the gas inside the expanding bubble is negligible compared to the momentum of the dense magma shell, the point of rupture will most likely be determined by the fastest expanding (or the thinnest) point in the expanding magma shell, the position of which can be considered as largely random from the current perspective.

This is an important observation, since it suggests that despite its somewhat non-circular surface footprint, the internal geometry of Ray Lava Lake and the immediate region underneath is largely symmetrical with a vertical axis of symmetry, i.e. non-inclined. For example, if the conduit mouth were strongly inclined, a predominant explosion direction would be expected. Again, this behaviour is consistent with observations by *Johnson et al.* (2008) of a wide direction range of infrasound dipole axes.

Additionally, this assumption is supported by the observation that the point of first expansion at the start of each explosion is variable but mainly located in the middle of the lake (in case of an inclined conduit directly beneath the lake surface, the points of first expansion would most likely be expected to predominantly appear at one side of the lake, indicating the dip direction of the conduit). This point is further supported by the symmetrical shape of the empty lava lake immediately after an explosion, which is visible in some of the videos. From a thermodynamic point of view it is not surprising that a circular geometry is favoured by a system that is stable over a long period of time, since round shapes generally provide the smallest ratio of surface to volume, therefore minimising cooling effects (*Bruce and Huppert*, 1989).

Part III

WHAT DID WE LEARN ABOUT STROMBOLIAN ERUPTIONS?

CHAPTER 9

DISCUSSION OF BUBBLE MODEL RESULTS

Results from Chapter 7 show that the application of the bubble expansion model developed in Chapter 4 leads to very well constrained conclusions on important eruption parameters such as explosion speeds, energies, gas pressures, bubble volumes, expected infrasonic signals, and therefore on the explosion mechanism in general. I will now discuss these results in a broader frame, analysing their credibility and consistency with results from other studies.

9.1 Limitations & constraints of the used model

While the model developed in this study provides important insight into the dynamics of explosions at Erebus, it has a few important limitations that should be kept in mind when interpreting the results shown in Chapter 7:

- The most significant constraint of this method is that the model results are only valid at times before the burst of the bubble, which means that at Erebus, the model is only valid for explosions of type *I* (and *small* explosions). Only during these explosions does the surface of the lava lake bulge up as assumed in the model (Fig. 4.1). Explosions of this type represent around half of the explosions at Erebus recorded in 2005/06. However, it was argued in Chapter 7 that while type *II* explosions appear visually different through their early shell rupture, all explosion types most likely have strong similarities in their important parameters.
- It is also important to keep in mind that the model results, such as forces, pressures and energies, represent physical properties that are averaged over the whole area of the doming shell. In the real system, these properties will vary across this large area, therefore they will exceed the average in certain areas or at certain times. Additionally, the exact geometry of the doming shell varies from explosion to explosion, and the true lake geometry is slightly elliptical instead of circular. Therefore, this simple geometrical model does not serve as a detailed source of information on **single** explosions, but attempts to capture the common and characteristic parameters of the whole **set** of explosions at Erebus.

- Somewhat similar to the last point, the expansion model cannot (yet) resolve the influence of the directivity of explosions (which were determined in Ch. 8), since up to now it only incorporates data from one fast radar device (the other two devices used in the 3D experiment described in Ch. 8 are too slow to capture the detailed processes of a bubble explosion). Therefore, depending on the explosion direction, results from **single** explosions might be systematically biased by the explosion's directivity, whereas such an influence is not expected when considering the bulk of explosions together (this will be further discussed below).

9.2 Explosion types

Independently from the applied model, raw radar data (Sec. 6.3 and 6.4) show that explosions at Erebus can be divided into two main groups. Video observations and the shape of radar spectra suggest that type *I* explosions expand with an initially intact magma shell until they burst some 0.4 seconds later. Type *II* explosions do not show this behaviour, but violently burst right at the time of the first detected movement on the lava lake surface, inferred from radar spectra and thermal video. While type *I* explosions are suitable for the application of the bubble expansion model, and therefore reveal information about gas pressures, energies and volumes, type *II* explosions unfortunately do not. With the given data it is therefore impossible to directly compare these parameters between the two explosion types.

Due to the lack of more conclusive data on this matter, reasons for the early rupture of type *II* explosions can at this point only be speculated upon. The most likely explanation for an early rupture of the magma shell are heterogeneities in the surface structure of the lava lake, possibly caused by local differences in temperature (and therefore viscosity) or by the structure of convection cells that are constantly reworking the lake surface.

The range of surface and ejecta velocities measured at Erebus, 5 – 160 m/s (Figs. 6.6 – 6.9), is wider and higher than that of comparable volcanoes but nevertheless similar. Velocities at Stromboli are in the range of 20 – 80 m/s, as obtained through a variety of measurement techniques (e.g. *Chouet et al.*, 1974; *Weill et al.*, 1992; *Seyfried and Hort*, 1999; *Urbanski et al.*, 2002; *Hort et al.*, 2003; *Vöge et al.*, 2005). Indeed, the vast majority of particles during Erebus explosions is in that same range (Figs. 6.10 – 6.11), and only a few fragments exceed this, accelerating up to 160 m/s or more. New data from Yasur volcano, Vanuatu, and from Stromboli measured with the same advanced Doppler radar device that was developed for this study revealed that even during Strombolian explosions from these volcanoes, a small but significant fraction of particles was found travelling at similarly high speeds and was most likely missed before (unpublished data and *T. Meier & M. Hort, pers. comm.* and *Meier et al.*, 2009).

Two further explosion types were identified at Erebus, subsequently named *small* and *blurred* to reflect their main characteristics. *Small* explosions are most likely caused by the same process as type *I* explosions, with the main difference being a significantly smaller gas volume, leading to less powerful explosions.

Blurred explosions are somewhat more difficult to characterise, due to the fact that cutoff velocities could not be identified and picked for this type. Their velocigrams look very similar to type *II* explosions, suggesting that the two types are largely similar.

The difference between type *II* and *blurred* explosions is possibly caused by a simple observational effect: as shown in Chapter 8, explosions at Erebus often show a significant directivity in their expansion. While this has only a slight effect on the observation of intact bubbles, it might be a crucial factor when observing the initial jet of exploding shell fragments in type *II* explosions. It is possible that *blurred* explosions simply have an initial jet direction that is by chance pointed towards the radar device, thus causing a high number of fragments moving at different speeds in the radar beam early in the explosion. This would cause the radar spectra to "blur". If this is the case, then the only difference between type *II* and *blurred* explosions is the direction of their first jet of particles. This hypothesis is further sustained by the small number of *blurred* explosions in comparison to type *II* explosions, reflecting the relatively low statistical likelihood that an initial explosion jet is directed towards the radar device.

9.3 Explosion energies

Results in Section 7.3 show that bubble explosion dynamics at Erebus are mainly controlled by the kinetic and potential energy of the heavy magma shell, as well as to a lesser degree by viscous dissipation inside the shell. Type *I* explosions often release energies of up to one gigajoule within 0.2 seconds after the explosion start, which amounts to a short time power output of 5 gigawatts, or several times the power output of a large nuclear power plant.

It must be noted that the energy output presented here only accounts for explosions, and is meant to illuminate their dynamics. The values presented are not intended to represent a long-term energy budget, which would have to include the steady-state heat and gas output between explosions (e.g. *McGetchin and Chouet*, 1979).

Furthermore, even though the energy output of type *II* explosions cannot be determined with the method presented here, it is likely to be in the same order of magnitude as type *I* explosions. The fact that type *II* explosions visually appear more energetic and have higher radar velocities and accelerations does not mean that their energy is higher than that of type *I* explosions. The high velocities belong to a few explosion fragments, which are indeed faster than those observed during type *I* explosions, but their mass is significantly less than that of the entire lake surface moving during type *I* explosions.

Directivity effects are certainly expected to have an influence on the apparent energy output of a bubble, in that a bubble expanding towards the radar will appear more energetic than a bubble with a main expansion direction away from the radar. Therefore, the energy

Figure 9.1: ***Strombolian explosion at Yasur volcano, Vanuatu, 2007.*** © *A. Gerst.*

values of **single** explosions should only be interpreted with this effect in mind. Yet, since it was shown in Chapter 8 that the directivities of **multiple** explosions are largely random, this effect does not play a significant role when interpreting the average trace of all explosions. The same argument is valid for the other derived properties, such as pressures and volumes.

The energy values obtained for Erebus explosions are an impressive display of the breadth of magnitude scales that are covered by volcanic eruptions. While seismic energies radiated into the ground can be as low as $10^3 - 10^5$ J, dissipative and potential energies lie in the 10^7 and 10^8 J range, respectively, topped by the shell's kinetic energy, which reaches 10^9 J. Even though these dynamic energy types are comparable to the impressive amount of energy freed by the explosion of several hundred kilograms of TNT (Sec. 7.3), they pale in comparison to the thermal energy that is passively transported by fragments, which is another 1000 times larger. Located in the 10^{12} J range, the thermal energy released by a single explosion at Erebus would take an entire hour to be produced by a large nuclear power plant (at 1 GW).

Such observations of magnitude-spanning energy output, and especially the importance of thermal energy, are consistent with estimations of volcanic energy output at volcanoes with a different eruption style (see Sec. 1.4, e.g. *Minakami*, 1942; *Yokoyama*, 1956; *Hédervári*, 1963; *Nakamura*, 1965; *Gorshkov and Dubik*, 1970; *Woulff and McGetchin*, 1976, ...). As discussed in Section 1.4, *Yokoyama et al.* (1992) derived a partial energy budget of the 1982 El Chichon explosive lava dome eruption in Mexico. Even though the large scale and explosive nature of this eruption is based on entirely different mechanics than the ones at Erebus, making it impossible to conduct a time-dependent analysis of the eruption energies, their estimated relative energy partitioning is very similar to the one determined at Erebus. Consistently, they report that by far the most energy is contained in the thermal output ($> 10^{17}$ J in this case), followed by kinetic energy, which was two orders of magnitude smaller. *Zobin et al.* (2009) determined kinetic explosion energies at Volcán de Colima based on seismic recordings, and suggest that kinetic energies of single explosions are in the 10^9 J range, which is, despite the different explosion mechanisms, very similar to those obtained at Erebus.

Even though they are not the controlling factors of explosions, energy types with smaller magnitudes provide important clues about the mechanism of explosions. Two important ones are the acoustic and seismic energy output of explosions.

Acoustic and seismic energies. An overview of typical acoustic energies at different volcanoes is provided by *Johnson* (2003) and *Johnson et al.* (2003), concluding that the acoustic energy output from single pulse explosions at a variety of volcanoes lies in the $10^5 - 10^7$ J range. *Heki* (2006) found a similar value ($\sim 1.2 \times 10^7$ J) for the acoustic energy generated during the 2004 eruption of Asama volcano, Japan. These values match closely with the acoustic energy output of Erebus determined in Section 7.3. It is important to note that the values in the above studies were all determined directly from acoustic measurements. In contrast, the estimate for the acoustic energy output in *this* study, shown in Figure 7.3, is solely determined from radar measurements in combination with the simple expansion model developed here, without the involvement or adjustment of any free parameters. Thus, the agreement of the two methods supports the validity of the method presented here.

Johnson and Aster (2005), in 1999 and 2000, measured seismic energies at Erebus volcano in the range of $10^4 - 10^6$ J, and infrasound energies in the order of 10^5 to 10^7 J. They found a stable ratio of ~10 between acoustic and seismic[1] energy, which they named the *volcano acoustic seismic ratio*, (*VASR*). Both their observations align very well with the results of our radar measurements combined with the explosion model (in absolute and relative terms, see Fig. 7.3), providing additional confidence in the model presented here.

Johnson and Aster (2005) show that the VASR varies greatly from volcano to volcano[2], allowing for clues on the source depth and explosion mechanism. Values can even become smaller than one (e.g. at Karymsky volcano), meaning that the seismic energy output is greater than the acoustic energy output. Typically, high VASR values are expected for explosion sources that are located close to the surface, as is the case in many Strombolian systems (*Johnson and Aster*, 2005). This is consistent with the findings of this study, and with the conclusions drawn by *McGetchin and Chouet* (1979) on Stromboli (although their VASR

[1]SP & LP, ~0.5–12 Hz

[2]and sometimes it varies with explosion size. Consistently, Figs. 7.3 and 7.4 show that during *small* explosions, seismic energies are much more reduced than acoustic energies, an effect that was already noted by *Rowe et al.* (2000).

is probably strongly overestimated due to limited technical possibilities at the time, and through their time averaging).

Overall, the above results show that the energy partitioning obtained from radar measurements at Erebus is not only much more detailed than that of previous studies, it is also consistent with the energy partitioning estimated for other volcanoes and with previous findings at Erebus. This creates additional confidence in the technique used here, and provides us with additional knowledge about in-situ parameters of Strombolian explosion mechanics.

9.4 Gas pressure

A time series of the in-situ bubble gas pressure was determined (Fig. 7.6) from the dynamic rate of energy that was released during bubble explosions, exploiting the fact that the higher the bubble pressure, the higher the energy output rate. For type *I* explosions, overpressures at the beginning of the rapid expansion phase were found in the range of 100 – 600 kPa, or 100 – 800 kPa when including the estimated uncertainty of the values. This means that even in the "worst case", bubble overpressures do not exceed 800 kPa. These findings show that a moderate amount of overpressure in the order of a few atmospheres is sufficient to account for the observed energy release. The obtained pressure curve also predicts the amount of overpressure that is left over at burst time of type *I* explosions, about one atmosphere. The energy stored in this remaining pressure is mainly converted into heat and an infrasonic wave pulse. Since type *II* bubbles were shown to burst earlier in the process than type *I* bubbles, they are expected to have a burst overpressure somewhere in between these values, which means that the burst pressure of type *II* explosions is higher than that of type *I* explosions.

While the method applied here gives very detailed results, its correct magnitude can easily be checked using Newton's second law. It states that the acceleration force F of the heavy magma shell must be equal to the driving overpressure p times the surface A on which the pressure acts: $F = m\,a = p\,A$. Friction effects are not considered in this simple comparison, an assumption that is considered adequate due to the minor influence of friction on the overall dynamics (Fig. 7.3). While the determination of the exact values is rather difficult, using an approximation for $A = \pi R_L^2 \approx 1257\ \mathrm{m}^2$, $m \approx 3.6 \times 10^6$ kg (Sec. 7.1) and $a \approx 100\ \mathrm{m/s}^2$ (around half of the peak accelerations shown in Fig. 7.1, giving the average acceleration for the whole shell instead of the zenith only) leaves us with an estimated overpressure of $p \approx 290$ kPa. Comparing this value to Fig. 7.6 shows that the two methods give consistent results.

Even though the pressure values determined here are valid for Erebus volcano only, the underlying mechanism will be similar at other Strombolian-type volcanoes. It can be expected that pressures correlate strongly with ejecta velocities, which are, for example, relatively similar between Erebus and Stromboli volcano (Sec. 1.2, or e.g. *Blackburn et al.*, 1976).

Therefore, the relatively precise overpressure determined here considerably narrows down the large variety of pressure estimates suggested for Strombolian explosions in general.

Superstatic slug pressures in the order of up to 10 MPa have been suggested to explain infrasonic data obtained at Stromboli (e.g. *Vergniolle*, 1998). Yet to the knowledge of the author no mechanism has been proposed to date that could account for a sustained overpressure of such magnitude in an open basaltic system (e.g. as discussed by *Massol and Jaupart*, 1999; *Morrissey and Chouet*, 1997). At the opposite end of the scale, *Blackburn et al.* (1976), by using cine film recordings of explosions, suggested an overpressure of only 600 Pa (0.006 atmospheres) for bubble explosions at Stromboli (also suggested by *Chouet et al.*, 1974), and 25 kPa (0.25 atmospheres) for Heimaey. *Ripepe and Marchetti* (2002), using a method similar to that used by *Vergniolle and Brandeis* (1994), suggested 50 – 400 kPa for explosions at Stromboli. *Wilson* (1980) suggests initial overpressures of around 20 – 400 kPa for Strombolian explosions. For Shishaldin, *Vergniolle et al.* (2004) suggest vibrating and bursting bubbles with an overpressure of $\sim$150 – 1400 kPa.

The results obtained here suggest that, with respect to the above-mentioned studies, pressures on the extreme ends of the scale are unrealistic. While a bubble overpressure that is significantly below one atmosphere cannot account for the ejecta velocities observed, an overpressure of several MPa (i.e. several tens of atmospheres) does not only lack a convincing generation mechanism, it would also result in a much more violent explosion than the ones typically observed at Strombolian volcanoes (*Morrissey and Chouet*, 1997). The data presented here, together with the physical bubble expansion model suggest that pressures of one to several atmospheres are indeed the most realistic, both accounting for the observed bubble expansion and being in accordance with estimates from several other studies. It is important to note that at no stage in the process are bubbles at Erebus underpressurised (i.e. with a gas pressure lower than the ambient atmospheric pressure; see *Vergniolle and Brandeis*, 1996), showing that bubble oscillations as proposed by *Vergniolle and Brandeis* (1994, 1996) do not occur at Erebus.

To support the credibility of the pressure values obtained here it is necessary to check if such overpressures can indeed be generated by a slug rising in a liquid magma conduit. The main hinderance for pressure buildup in a slug is that whenever the slug has an overpressure (i.e. a gas pressure that is higher than the hydrostatic pressure of the surrounding liquid), it simply expands, therefore lowering the pressure inside (Sec. 2.2). The most effective process for a pressure buildup in a slug despite this mechanism is the so-called *"viscous overpressure"*, which results from the viscosity and mass of the liquid preventing a fast enough expansion of the rising slug, therefore resulting in a small but significant slug overpressure.

Vergniolle and Brandeis (1996) argue that, while they suggest gas pressures at Stromboli in the order of 20 – 600 kPa, viscous overpressure can only explain 3 kPa of that, but fail to explain where the rest comes from. They speculate that during the bubble's rise in the conduit, these might keep an initial excess pressure, which they possibly acquired when being formed at a depth of several hundred metres. As was shown in Section 2.2, this is a rather

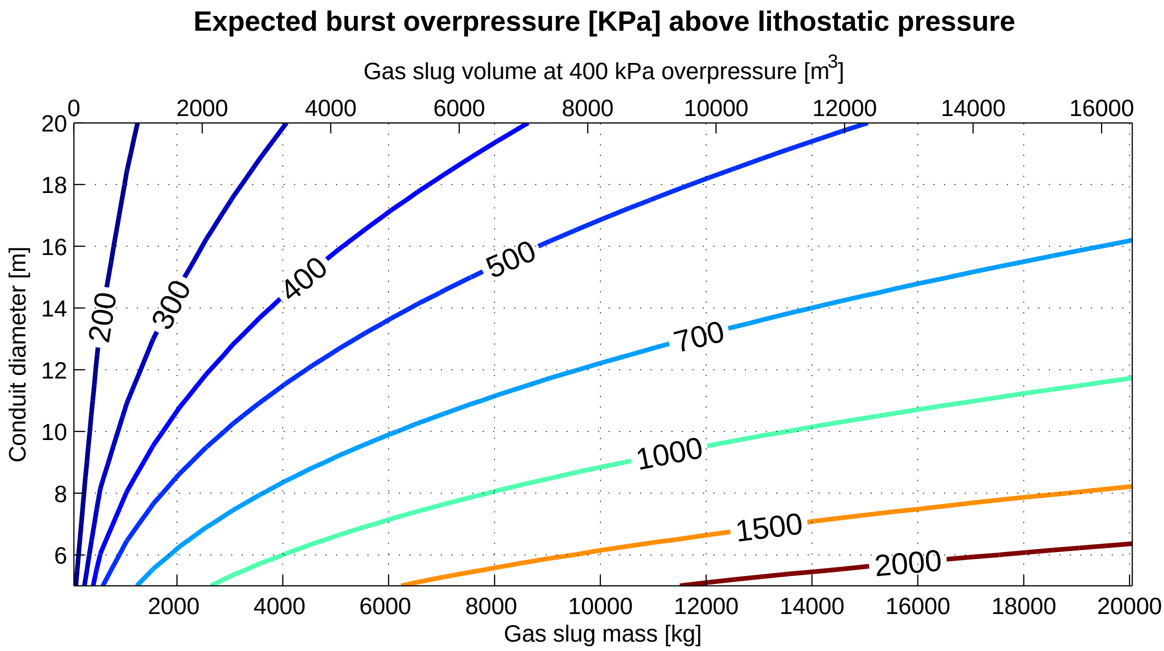

Figure 9.2: ***Expected overpressure of a gas slug at burst.*** *Obtained by calculating conduit rise parameters (similar Figs. 2.2 & 2.3, based on James et al., 2008) for a grid of slug masses and conduit diameters. The lower horizontal axis denotes slug gas masses, the upper axis denotes the respective slug volume at 400 kPa overpressure. Burst overpressures (isolines) are given in kPa for a moment shortly before the burst, when the liquid magma head has decreased to a thickness of 1.4 m (which is assumed to be the thickness at the start of the rapid expansion phase). Geometry and fluid parameters are those assumed for Erebus (Sec. 2.2), although the widening of the conduit into the lake is not incorporated.*

unlikely scenario when considering the fluid dynamic laws that govern the pressure development in a rising gas slug, meaning that the slug will rapidly equalise such an overpressure by expansion.

James et al. (2008) developed both a 1D and a 3D slug ascent model that was verified in laboratory experiments (see also *James et al.*, 2004, and Sec. 2.1). Their results clearly show that a slug rising in a volcanic conduit is not able to effectively sustain an initial overpressure, i.e. the overpressure that it initially acquired during its formation deep in the conduit, regardless of the exact mechanism. Upon release of the slug, any initial overpressure rapidly leads to an expansion of the slug, which either ends in a neutralisation of the pressure by the time it reaches the surface, or in a damped longitudinal oscillation of the liquid head above the slug (*Vergniolle et al.*, 1996; *James et al.*, 2004).

The above discussed model by *James et al.* (2004, 2008) nevertheless predicts a significant amount of overpressure for slugs that approach the surface of the liquid, based on viscous and inertial effects initiated by the slug's volume expansion. Figure 9.2 is a plot of the expected overpressure of a slug at Erebus approaching the surface, obtained in a similar way to Figure 2.2, using parameters that are assumed representative for Erebus (see Sec. 2.2). It shows that expected overpressures can be as high as 400 kPa for a 10 m wide conduit and a slug mass of 2,000 kg (translating into a slug volume of $\sim$1,700 m^3 at 400 kPa overpressure), which is similar to this study's findings at Erebus (Sec. 7.4). For the simplicity of calculations, the conduit was assumed to retain its diameter up to the surface instead of widening into a lava lake (which I will argue later has a profound effect on slug dynamics). Thus, despite their remarkable match, these values can only serve as a demonstration of magnitude rather than as an exact calculation of burst overpressures. Yet, in summary, a sufficient overpressure can indeed be explained by the simple model of a slug rising in a conduit, making it unnecessary to explain the overpressure of a slug approaching the surface with an initial overpressure at depth, as proposed by *Vergniolle and Brandeis* (1996); *Vergniolle et al.* (2004); *Vergniolle and Caplan-Auerbach* (2004).

9.5 Source of the acoustic signal

The results from Section 7.6 show that radar measurements in combination with an explosion model match acoustic data from the same explosions very well. This provides the basis for interpreting acoustic signals at Erebus and other Strombolian volcanoes. The variety of possible source models (as discussed in Sec. 1.3) can be collapsed to a dual mechanism at Erebus, namely the strictly monotonic final expansion of a large gas bubble beneath the surface of the lava lake, followed by a cavity resonance mechanism after the burst of the bubble. I will now discuss various aspects of this dual mechanism, starting with general atmospheric propagation effects.

As discussed in several studies (e.g. *Buckingham and Garcés*, 1996; *Garcés and McNutt*, 1997; *Garcés et al.*, 1998; *Matoza et al.*, 2007; *Fee and Garcés*, 2007), propagation effects of acoustic waves in the atmosphere need to be ruled out or accounted for. *Johnson et al.* (2008), in accordance with earlier studies (e.g. *Vergniolle et al.*, 1996; *Pierce*, 1981), argue that acoustic path effects such as dispersion, multipathing, diffraction, and non-linearities are negligible when certain conditions are given, such as measuring infrasonic frequencies with a moderate amplitude directly at the crater rim of a volcano, and when considering only the first moments of an explosion signal.

As shown in Figure 5.10, two of the infrasonic stations at Erebus are located significantly behind the crater rim, therefore diffraction effects[3] cannot completely be ruled out for these stations. Yet, at Erebus, with typical frequencies around 2 Hz and all stations located well within 1 km of the source, no evidence was found that would suggest such effects (*Johnson et al.*, 2008; *Jones et al.*, 2008).

Multipath effects such as echoes from the crater wall are not expected to influence the explosion signal before about 1.7 s after the initial onset (*Johnson et al.*, 2003), consistent with the actual crater dimensions. Therefore, I do not assume that these effects play a signifi-

[3] as reported by *Johnson* (2004) for frequencies around 20 Hz at Stromboli

cant role here[4]. Using environmental data collected by the MEVO network at Erebus (*Aster et al.*, 2004), *Johnson et al.* (2008) show that environmental influences such as wind speed and direction only play a small or even negligible role in sound propagation at Erebus during non-storm conditions. Finally, the linear propagation of sound appears to be an adequate assumption for Erebus, given that acoustic pressure signals at the crater rim are typically within 0.25% of the ambient atmospheric pressure (*Dowling and Williams*, 1983, p.12). Of course non-linear effects in the close vicinity of the lava lake cannot be ruled out, but are beyond the scope of this study.

9.5.1 Pre-burst acoustic signal: a volumetric source

As demonstrated in Figure 7.10, pre-burst waveforms predicted from radar data match the true waveforms closely, both in amplitude as well as in shape. This match, together with the simplicity of the expansion model that was used for the prediction, suggests that the responsible process for the generation of the initial infrasound signal during Erebus explosions is indeed the bulging surface of the lava lake, which acts as a non-compact volumetric source of sound by displacing the atmosphere. Consequently, several alternative models must be discarded.

Vergniolle and Brandeis (1994) suggest that most of the acoustic energy is released due to vibrations of the bubble around its equilibrium at the magma-air interface before the bubble bursts (a process that has never been directly or visually observed during Strombolian explosions). They also claim that the signal of the actual bubble burst is merely a small high frequency disturbance of the acoustic wave. The data presented here show that both these assumptions are certainly not valid at Erebus, where bubbles neither deflate nor vibrate once they have reached the surface, and where the generated waveforms (which are highly similar to those at Stromboli) can be fully explained by the expansion of a volumetric source (i.e. a bulging lava lake) up to the point of the bubble's burst. This is consistent with findings by *Ichihara et al.* (2009), measuring atmospheric acoustic waveforms created by shallow underwater explosions. They showed that the generated acoustic air waves are mainly created by the interaction of the bulging liquid surface with the atmosphere - a situation that is geometrically very similar to the expanding lava lake surface at Erebus.

One of the reasons why bubble vibrations might seem intuitive to some could be that sufficiently deep underwater explosions typically generate bubbles that oscillate for several cycles before equilibrium sets in (e.g. *Ichihara et al.*, 2005, 2009). While they are deep enough and therefore far enough from the liquid's surface, these bubbles do not have the possibility of equalising their pressure by bursting through the surface – they are therefore stable and oscillate around their equilibrium pressure. However, this situation drastically changes when the amount of liquid between the bubble and the surface decreases. In this

[4] A reflection from the bottom of the crater cannot be ruled out for large bubbles, possibly enhancing the strong rarefaction that is typically observed in Erebus waveforms (Figs. 7.10 and 9.4). Yet, this effect would only affect the post-burst waveform.

case, which is somewhat similar to that of Strombolian bubbles right at the surface of a magma column, explosion bubbles do not oscillate any more[5] but expand violently through the liquid's surface (*Ichihara et al.*, 2009). Consequently, a strongly overpressured gas slug or a bubble rising in a magma conduit can freely oscillate around its equilibrium pressure only until it approaches the surface. In the last seconds of its rise it acquires a large overpressure (compared to ambient air pressure) due to the relatively high viscosity and mass of magma (Fig. 2.2). Shortly before reaching the surface, its expansion will quickly accelerate, leading to a rapid and monotonic volume expansion followed by the bubble's burst[6] before reaching equilibrium *James et al.* (2004, 2008, 2009).

Additionally, the above observations also rule out that the acoustic wave is merely generated by wave transmission at the magma surface, i.e. resulting from a pressure wave travelling through the liquid magma to the surface. While such a scenario is now easy to disprove for Erebus, where visual data are abundant, such mechanisms have been proposed to explain acoustic signals at other Strombolian-type volcanoes (e.g. *Buckingham and Garcés*, 1996; *Garcés and McNutt*, 1997; *Hagerty et al.*, 2000). In the light of results from this study, however, this mechanism is likely to play only a minor role in similar style Strombolian explosions.

A certain influence on predicted acoustic waveforms is expected by the directivity of explosions, as discussed in Chapter 8, and as observed by *Johnson et al.* (2008), leading to a variation of the partial dipole signature in the infrasound signal. However, since this variation was shown to be random (Sec. 8.3), I expect no overall systematic influence on the obtained waveforms.

9.5.2 Post-burst acoustic signal: a cavity resonance

An important observation arising from the comparison of calculated and real acoustic signals (Fig. 7.10) is that the largest part of the pressure peak occurs **after** the burst of the bubble (as detected by radar and confirmed by video), meaning a process occurring after the burst must be responsible for its generation.

Spiel (1992) showed that small bubbles bursting at the surface of water behave like Helmholtz resonators, because their neck opens slowly compared to their resonance period. *Vidal et al.* (2006), in contrast, use a model that was geometrically adapted to that of an elongated volcanic gas slug, and show in theory and experiment that a "$\lambda/4$" resonator is formed when a membrane above a pressurised, gas-filled cylindrical cavity suddenly bursts (Fig. 9.3). The sudden pressure release excites a resonance whose fundamental wave length λ is four times the cavity depth (*Vidal et al.*, 2006).

Assuming that this mechanism is present when volcanic gas slugs burst at the top of a lava column, I now calculate its expected resonance properties. Accordingly, I expect a strong

[5] At a certain depth, shallow underwater explosions can generate a double acceleration pulse, which is **not** an oscillation of the surface (i.e. the surface has no deflation phase), see *Ichihara et al.* (2009) and Sec. 9.8.2 below.

[6] accelerated by the lack of sufficient elasticity in the magma membrane

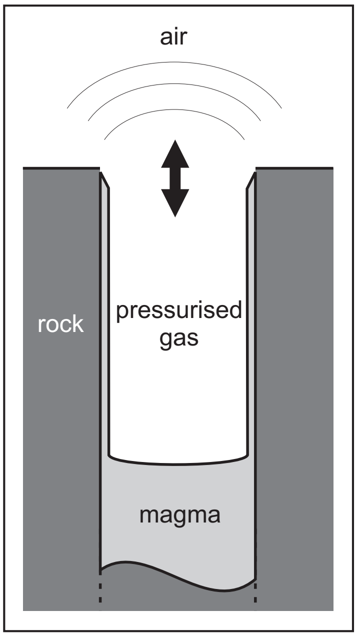

Figure 9.3: ***Cavity resonance principle.***

vibration signal caused by the resonance of hot magmatic gas contained in the cylindrical cavity that is formed by the gas slug after its top lid is suddenly removed by the burst of the magma shell.

From the total slug volume that I infer from video observations[7], i.e. in the order of 10,000 – 40,000 m^3, final slug lengths in the order of 100 m are expected when assuming a conduit width between 10 and 20 m. However, this assumption neglects the width of the lava lake, which is ∼40 m at the top, therefore overestimating slug lengths just before the burst. Figure 7.9 shows that after large explosions, cavities occupy the whole lake volume to at least a depth of 30 – 40 m or possibly even deeper. The actual depth of the point where the lake narrows to a conduit is therefore not known in 2005 (in contrast to 1987, where it was in the range of 30 – 40 m; *Dibble et al.*, 2008). Therefore, from video observations alone, it is only possible to constrain slug lengths to a range of around 40 – 100 m.

Assuming that the cavity formed by a slug contains a 60/40 mol mixture of water vapour and CO_2 at a temperature of 800°C, the speed of sound inside the cavity is around 600 m/s (Sec. A.2). For a 100 m deep cavity this leads to an expected fundamental resonance frequency of ∼1.5 Hz. Due to radiation at the cavity mouth and dissipation through the cavity walls, strong damping of the resonance wave is expected. From *Vidal et al.* (2006, Eq. 4), I estimate[8] a characteristic damping time of $\tau \approx 3.4$ s (fundamental mode), for a 100 m cavity with a 40 m wide mouth that is filled with hot magmatic gas (Sec. A.2). The true damping time will possibly be even shorter due to the presence of shell fragments around the resonator mouth.

[7] at the start of the rapid expansion phase of an explosion (Sec. 7.5)
[8] assuming a kinematic viscosity of 2×10^{-4} m^2/s (hot steam at 800°C) and a *Prandtl number* of 0.8.

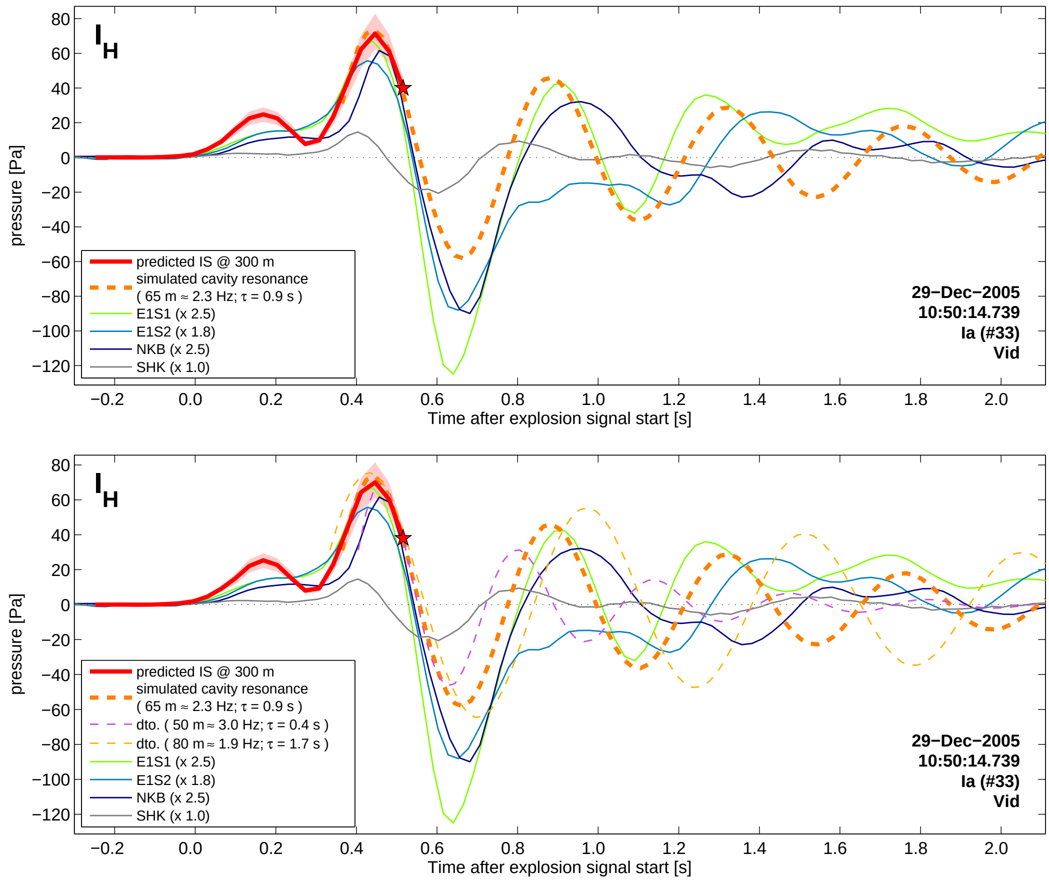

Figure 9.4: ***Cavity resonance generating an acoustic signal.*** *The Figure is similar to Fig. 7.10 (I_H), showing a typical explosion at Erebus. Accordingly, the thick red line shows the signal as predicted by radar measurements up to the time of burst. Thin lines show recorded unfiltered infrasound pressure signals of four stations around the crater rim, scaled and shifted to a common distance of 300 m.* ***Top:*** *the thick orange dashed line shows the expected acoustic pressure signal of a 65 m deep resonating cavity.* ***Bottom:*** *by slightly varying the cavity length (thin dashed lines) the influence of the cavity length on the signal can be demonstrated, suggesting a cavity length in the order of 60 – 80 m. Note that the E1S1 microphone provides the most consistent waveforms, see Fig. 7.10.*

Laboratory experiments (*Vidal et al.*, 2006) show that for slowly bursting membranes (i.e. membranes with high inertia, such as the bubble's heavy magma shell), the measured resonance amplitude scatters strongly even with consistent initial conditions. It is typically only a small fraction of the expected outward propagated initial cavity pressure (i.e. corrected by $1/r$, where r is the distance between source and receiver), and is almost impossible to predict without knowing details of the membrane rupture process[9]. Thus, as a demonstration, I assume a 65 m deep cavity and a resonance amplitude of around 80 Pa at the crater rim, knowing this is a somewhat arbitrary but not an unreasonable assumption for a highly inert bursting magma shell. Figure 9.4 (top) shows the expected waveform of such a resonator, with its calculated damping time of $\tau = 0.9$ s (again using *Vidal et al.*, 2006, Eq. 4). It was

[9]i.e. during the membrane rupture, a Helmholtz resonator is formed for a short period of time, quickly developing into an open cavity resonance once the membrane has burst.

superimposed on the calculated infrasound signal just before the burst was detected by the radar.

Figure 9.4 (bottom) shows the same data as shown in the top part, but includes two additional hypothetical resonator signals obtained by a slightly altered resonator length. Its purpose is to demonstrate the influence of the bubble length on the match between expected and real acoustic pressure signals.

Waveforms in Figure 9.4 show that with the above made simple estimates on expected slug lengths and damping time (based on gas volume data and thermodynamic considerations), a cavity resonance signal can be predicted that matches the observed acoustic signal reasonably well. Even though a difference in the match quality between individual receivers exist, the main waveform characteristics are reproduced.

For the explosion shown in Figure 9.4, a resonating cavity (and therefore slug length at burst time) of 65 m is the most adequate assumption. Even the decay of the signal is well reproduced by the expected damping time of 0.9 s, although some low frequency noise on the signals prevents an ideal fit without filtering the signal. Thus, when using infrasonic signals to obtain information about a resonating gas-filled conduit, the frequency of the signal provides information on the length of the cavity, while the conduit mouth width can be estimated from the signal's damping time. This property can possibly be used as a surprisingly simple and effective tool for the remote analysis of Strombolian-type volcanoes.

According to the theory, harmonic overtones are expected at $(2n + 1)$ times the fundamental frequency $[n > 0]$ (*Vidal et al.*, 2006). At Erebus, the first harmonic overtone would therefore be expected around 6 Hz. However, harmonics are not clearly visible in spectrograms (not shown), most likely due to noise and very short signal lengths, and the fact that higher harmonics are damped much faster than the fundamental mode (*Vidal et al.*, 2006). A more sophisticated search for these harmonic frequencies, and an investigation of the correlation between resonance frequencies and explosion size (or slug size) would therefore be an interesting goal for a future study at Erebus.

When analysing the quality of the match between the two waveforms it must be kept in mind that crater echoes are likely to play a role in the acoustic signals starting at about 1 s after the signal onset. This means that a detailed match of the waveform after the first second is unlikely without the detailed incorporation of these echoes in the atmospheric transport model. The echoes are strongly dependent on the crater geometry, and are expected to vary between receiver sites. Their incorporation will thus be a promising challenge for future studies. Even so, Figure 9.4 shows an impressive match between a simple cavity resonance waveform and the real acoustic signals.

Since resonance effects have been previously proposed to cause acoustic signals after Strombolian explosions, I will briefly discuss two alternative mechanisms.

Alternative I: the model of an excited Helmholtz resonator in the gas-filled conduit (e.g. *Spiel*, 1992; *Vergniolle and Caplan-Auerbach*, 2004; *Cannata et al.*, 2009) is very similar to the above mechanism, and might possibly fit the real waveforms just as well as the cavity resonance model discussed above. However, it requires additional variables to be determined or guessed, such as the neck length and neck width of the Helmholtz resonator. It therefore adds additional complexity and ambiguity without providing more information on the actual mechanism. I therefore suggest the use of the much simpler cavity resonance model presented by *Vidal et al.* (2006), unless or until new data might necessitate the use of more complex models for resonance generation.

Alternative II: the above discussed cavity resonance model is also somewhat similar to that of a resonating open organ pipe, as proposed by *Chouet et al.* (1974), who observed oscillating gas velocities during explosions at Stromboli. For the same resonating frequency, the $\lambda/4$ model discussed above suggests a resonator that is only half as long as that of an open organ pipe. This is because an *open* organ pipe has two open ends as a boundary condition (the exciting end of an organ pipe is always open), leading to a $\lambda/2$ type resonance (*Hall*, 2001). However, the cavity formed by a burst gas slug in a conduit has only one open end, and is therefore more similar to that of a *closed* organ pipe instead of an *open* one (*Hall*, 2001), leading once again to a $\lambda/4$ type resonance (i.e. eliminating alternative II). Thus, in the case of Stromboli, this suggests a resonating conduit that is roughly only half as long as that resulting from the "open organ pipe" formula used by *Chouet et al.* (1974). Additionally, contrary to some previous studies, it is important to use the correct speed of sound for the hot magmatic gas that is located inside and outside the conduit after a burst, which is typically almost twice as high as the commonly used atmospheric sound speed at ambient temperatures (Eq. A.2).

Volcanic acoustic waveforms are far from the purity of laboratory waveforms, influenced by a variety of poorly constrained parameters, such as echoes and details of the source geometry. Therefore, since some of the above proposed resonance mechanisms produce similar resonance patterns, the question about the correct mechanism is difficult to resolve by simply comparing waveforms.

In summary, the $\lambda/4$ type cavity resonance (as discussed by *Vidal et al.*, 2006) that was proposed in this study as the predominant mechanism for Erebus post-burst waveforms is by far the most simple and straightforward of the above proposed mechanisms. It keeps unconstrained parameters at a minimum while explaining the waveforms and observed effects just as well or even better than the other mechanisms. I thus propose to use *"Ockham's razor"* (e.g. *Gernert*, 2007), meaning that more complex models than the simplest sufficient one should be discarded until they provide testable predictions that justify their increased complexity, ideally offering a better understanding of the phenomena in question.

For example, using the cavity resonance model to interpret the 7–9 Hz signal measured at Stromboli by *Vergniolle and Brandeis* (1994) and *Vergniolle et al.* (1996) would lead to a slug lengths of 16–21 m. Accordingly, the 2 Hz signal measured by *Vergniolle and Caplan-Auerbach* (2004) at Shishaldin volcano would lead to slug lengths of $\sim$75 metres. This is slightly longer than what the authors of the study proposed based on a Helmholtz resonator model, and it is very similar to the value obtained for slugs at Erebus.

Naturally, all of the above models, including the one proposed here, have their limitations. In the case of bubble bursts, as long as details of the shell rupture process are unknown, the results of *Vidal et al.* (2006) clearly show that it is impossible to calculate the initial bubble pressure from post-burst infrasound alone. It is prevented because the amplitude of the cavity resonance after the burst is strongly dependent on the details of the burst process. Therefore, without the development of even more sophisticated bubble models, this spoils the ability of using post-burst acoustic amplitudes for calculating the gas energy. Even though this was attempted in the past, doing so leads to incorrect values. This also explains reports of the typically weak correlation of seismic and infrasonic amplitudes during volcanic explosions (*Johnson et al.*, 2005), again highlighting that it is impossible under most conditions to estimate the bubble parameters at volcanoes from distant pressure recordings alone.

Fortunately, the data presented here show that, despite the model's simplicity, radar measurements in combination with an explosion model provide the necessary information to successfully predict the acoustic signal from Strombolian explosions at Erebus. The properties of the waveform match, without the adjustment of arbitrary parameters, provide confidence in the interpretation of acoustic signals not only at Erebus but also at other Strombolian volcanoes. Therefore, by using the frequency of acoustic explosion signals, the technique presented here offers a surprisingly simple tool to judge the length of Strombolian gas slugs, and possibly to estimate the width of the conduit mouth. This new tool should therefore be tested at other Strombolian volcanoes.

9.6 Source of the seismic signal

As discussed in Sections 4.2.8 and 7.7, Strombolian bubble bursts are expected to generate a large, mainly vertical downward force on the ground. They therefore generate seismic waves in the short period range, in addition to the very long period signal associated with the bubble's rise in the conduit. The explosion forces are expected to couple into the ground at regions of conduit discontinuities (e.g. *Chouet et al.*, 2008), of which the most obvious and closest one to the surface is the transition zone between the wide lava lake and the more narrow conduit (see Sec. 9.8.1 below). While the relative amount of seismic energy radiated into the ground was already discussed in this Chapter (Sec. 9.3), I will now discuss the ground forces that are generating these short period seismic waves.

Figure 7.14 shows that peak vertical ground forces are expected between 100 and 800 MN, i.e. in the 10^8–10^9 N range. As a comparison, this force is about equal in its absolute value to the force needed to lift a large cruise ship[10]. The frequency of this force signal is around

[10] e.g. the R.M.S. Queen Mary II, which at its construction in 2003 was the worlds largest passenger ship, has a mass of ≈ 76,000 metric tons, i.e. its weight is around 750 MN in Earth's gravity.

3 Hz; it therefore lies in a frequency range similar to that of typical volcanic *long period (LP)* signals (e.g. *McNutt*, 2005).

These above calculated forces are two orders of magnitude higher than what was previously assumed and modelled for slug ascents and bursts (*James et al.*, 2004, 2008). Yet intriguingly, they are very similar to forces determined by seismological field studies. For example, forces in the 10^8 N range were suggested for mechanisms causing *very long period* (VLP) signals at Stromboli (*Chouet et al.*, 2003, 2008), Popocatépetl volcano (*Chouet et al.*, 2005), and also at Erebus itself (*Aster et al.*, 2008). Forces in the 10^9 N range were suggested at Hawai'i (*Ohminato et al.*, 1998) and small explosions at Volcán de Colima (*Zobin et al.*, 2009), topped by 10^{10} N for vulcanian explosions at Asama volcano (*Ohminato*, 2008) and for large explosions at Popocatépetl (*Zobin et al.*, 2009). In most of these cases, however, the frequency of the measured signal lies in the *very long period (VLP)* range, having significantly longer periods than the 3 Hz force signal inferred for explosions at Erebus.

As discussed in Chapter 7, type *II* explosions do not allow for the application of the bubble expansion model. Therefore it is not possible to determine their ground forces in the same way as for type *I* signals. Type *II* explosions appear visually more violent than type *I* explosions, have higher ejecta velocities (Sec. 6.3), and also generate stronger acoustic signals (Sec. 7.6). Nevertheless, it is possible that they generate a weaker ground force and therefore a weaker seismic signal than type *I* explosions, resulting from their very localised point of shell rupture early in the explosion. This "pinpointing" leads to a violent gas outbreak and generates fast ejecta, but it does not lead to a comprehensive acceleration of the entire lava lake surface. Therefore, a strong acoustic signal might be generated, but not necessarily accompanied by a strong ground force or seismic signal. If present, this effect should reflect in a systematic VASR difference (see Sec. 9.3 and *Johnson and Aster*, 2005) between type *I* and *II* explosions.

Seismic energies of *small* explosions turned out to be very small, due to the small masses and accelerations involved. It can therefore be expected that the generation of seismic waves during *small* explosions is negligible, which should reflect in weak, or even in a lack of, seismic recordings of *small* explosions on the local seismological network. Similar observations were made by *Rowe et al.* (2000), who report a significantly increased VASR (i.e. decreased seismic energy) for small explosions at Erebus.

Due to its high frequency, the above proposed force function for bubble bursts cannot serve as an alternative generation mechanism for previously proposed VLP source mechanisms. VLP events have periods between 2 and several 100 s (e.g. *McNutt*, 2005), and are assumed to emerge during the rise of the slug in the conduit, i.e. several seconds before the burst and at depths of a few 100 metres (as discussed in Sec. 2.2.2, and e.g. *Chouet et al.*, 1997, 1999, 2003, 2005, 2008; *Rowe et al.*, 1998, 2000; *Ripepe and Gordeev*, 1999; *Ripepe et al.*, 2001; *Seyfried and Freundt*, 2000; *Aster et al.*, 2003, 2008; *James et al.*, 2004, 2006). In contrast, the ground forces inferred for Erebus are expected to generate a strong signal around 3 Hz right at burst time, and should be easily observable in the volcanic edifice, although typically strongly altered by reverberations.

Intriguingly, *Rowe et al.* (1998, 2000) analysed seismic events from Erebus explosions and find signals around 3 Hz, which have long codas that prevent a detailed waveform analysis, but which are radially polarised towards the lava lake (*De Lauro et al.*, 2009). Thus, despite the effects of attenuation and complex path effects that are typically found at volcanoes, I propose that seismic amplitudes and frequency contents of explosion signals from other Strombolian volcanoes should be compared to force functions determined from respective radar measurements.

9.7 Bubble gas volume

Bubble gas volumes were determined in Section 7.5 in three different ways. The first two methods (A & B), based on thermodynamic considerations, agree very well in suggesting that approaching bubbles have an initial volume of around 1,000 – 1,250 m^3 at the start of their rapid expansion phase. Such plain numbers of volume are relatively hard to visualise. To provide the reader with a more imaginable figure, this volume is similar to about twice the cabin volume of a large passenger aircraft[11].

The third method (Sec. 7.5, C), based on video observations, yields much higher estimates for the total gas volume expelled during the entire explosion. These are in the range of 8,000 – 35,000 m^3, and strongly varying from explosion to explosion. Gas volumes of large explosions could even be greater than 35,000 m^3. In all cases they are much larger than volumes determined from the first two methods. Error bars on the plots show that this difference cannot be explained by systematic errors, e.g. by having selected wrong values for shell thickness or magma density (see parameter errors, Sec. 7.1).

While this systematic difference seems odd at first, it can be explained by a simple mechanism. The first two methods (A & B) only constrain the volume of the gas bubble that is **initially** pushing up the lava lake surface, whereas the video estimation method (C) takes into account the **total** volume of gas ejected during the **entire** explosion. If only a single bubble rises and expands to form an explosion, these two volumes are expected to be similar. However, if there is more than one bubble involved, or if it is a fragmented bubble whose fragments arrive at the surface in quick succession, then the initial volume of the first approaching bubble is expected to be significantly smaller than the combined volume of all bubbles. In that case, the different volumes measured by methods A/B and C are consistent with the theory, bearing important information on the explosion mechanism.

Figure 4.7 gives another hint that supports the above reasoning. When not only the first acceleration peak is taken into account, as was done for methods A & B, but when estimating the initial volume from the amount of energy that is freed between the start of an explosion and the moment of burst, then a new picture arises. The amount of freed energy before the

[11] The combined cabin volume of both passenger decks of a Boeing 747-400 aircraft is $\sim$700 m^3.

moment of burst is around $5{\times}10^9$ J for large type *I* bubbles (Fig. 7.3). Therefore, at least this amount of energy must have been stored in the combined bubbles at the beginning of the rapid expansion phase, plus the unknown amount of gas energy that was still contained in the bubble(s) at the moment of the (first) bubble's burst. At the start of the rapid expansion, the bubble had an overpressure of around 400 kPa, dropping by about 300 kPa before bursting (Fig. 7.6). The simple thermodynamics plotted in Figure 4.7 show that in order to release this amount of energy at that specific pressure drop, the bubbles must have had a combined volume of at least 12,000 m^3 at the beginning of the rapid expansion phase.

The above consideration shows that, as soon as more than only the first approaching bubble is taken into account, the various methods for determining bubble volumes match much more closely. Nevertheless, the information on the volumes of the respective first approaching bubbles is a very useful resource, as will be shown and further discussed in Section 9.8.

I will now compare the obtained bubble volumes to values obtained with other methods and at other volcanoes. *Johnson et al.* (2008) determined gas volumes at Erebus from acoustic records, and estimate bubble volumes of 1,000 m^3 – 24,000 m^3. Interestingly, this covers the total range of bubble volumes determined here, including the relatively small volumes of the first approaching bubble of each explosion, as well as entire explosion gas volumes. *Johnson et al.* (2004), based on infrasonic measurements, estimated the gas mass of Erebus bubbles to the order of 10^3 kg per explosion, which translates into a volume in the order of 1,000 m^3 when assuming an overpressure of 400 kPa and 1000°C at the start of the rapid expansion phase.

Gas volumes estimated for Stromboli are naturally much smaller than those inferred for Erebus, given the smaller scale of Stromboli's explosions. *Vergniolle and Brandeis* (1996) suggest gas volumes at Stromboli in the order of 2 – 100 m^3 (however, based on the assumption of bubble vibrations, the existence of which seem unlikely in the light of this study). To make these numbers comparable, assuming an average overpressure of 400 kPa at burst, the bubbles would need to have volumes between 0.5 and 20 m^3, the lower end of which appears rather small despite Stromboli's moderate sized explosions. More realistically, airborne COSPEC measurements at Stromboli volcano (*Allard et al.*, 1994) suggest a gas output of a few hundred kilograms per second during explosions, which translates into a few hundred cubic metres per explosion (at 400 kPa) when assuming an average explosion duration of one second. This is consistent with early photoballistic measurements by *Chouet et al.* (1974), suggesting gas masses in the order of a few hundred kg per explosion.

For the much larger explosions at Shishaldin, *Vergniolle et al.* (2004), also based on assumed bubble vibrations, suggest slug diameters of 5 m at lengths of 10 – 60 m (sometimes 80 m) with an overpressure of ~150 – 1400 kPa. They suggest an overall gas volume at atmospheric pressure of ~10,000 m^3 per bubble, which translates into ~2,000 m^3 at 400 kPa overpressure.

Gas volumes are likely to be highly dependent on the individual properties of the volcanic system, therefore gas volumes from different volcanoes cannot easily be compared. Nevertheless, the above values show that gas volumes determined from radar measurements at Erebus are in a similar magnitude range than that of comparable volcanoes. Furthermore, the results obtained here (Sec. 7.5, C) show that gas volumes are strongly dependent on the explosion type. A more causal way to express this relation is that, most likely, the available gas volume determines the explosion type.

9.7.1 Slug expansion: a volume problem?

Due to the volume expansion experienced by a rising gas slug in a volcanic conduit, the liquid head above a slug is pushed upwards, constantly raising the surface level until the moment when the slug reaches the surface. This effect was already indicated in Figure 2.2, simulating a typical slug rise at Erebus, although for only one possible conduit diameter and not taking account of the widening of the conduit into the lava lake.

In contrast, video and visual observations at Erebus show that the level of Ray Lava Lake does not rise strongly in the last moments before an explosion (*SOM*, 2010; *Dibble et al.*, 2008). Only in the last few seconds before an explosion, the lake level rises by a few metres and eventually starts to bulge and explode.

If the predicted lake level rise cannot account for the observed one, then the proposed slug rise model for Erebus does not adequately represent the real processes. For example, a very small lake level rise before explosions might suggest a very shallow source of gas instead of a bubble rising in a long conduit. I will therefore test the compatibility of the proposed conduit rise model with the observed lake level rise. To do so, I have repeated the simulation shown in Figure 2.2 for a variety of conduit diameters and gas slug masses, but also incorporated the effect that the large cross sectional area of the lava lake has on the expected conduit rise (i.e. for a given volume input, the level rise decreases by a factor of $(R_c/R_L)^2$, where R_c and R_L are the conduit and lake radii, respectively. This cross-section ratio is independent from the lake depth).

Figure 9.5 shows the result of this simulation. It shows that the lake level rise is indeed only moderate when including the effect of the large surface area of the lake, but it depends on the conduit diameter. *Dibble et al.* (2008) observed in 1987, under favourable viewing conditions after a large explosion, that the hole at the bottom of the (then emptied) lava lake has a diameter of around 10 m. Due to the changeability of a magmatic system, this might not necessarily represent the conduit diameter nearly 20 years later, but the observed general steadiness of conditions at Erebus suggests that this value is still in the correct range. The figure suggests that the expected lake level rise for a 10 m conduit is indeed below 3 m for slug masses up to 12,000 kg, which corresponds to a slug volume of ~10,000 m^3 at 400 kPa overpressure above ambient.

Vergniolle et al. (2004, and references therein) give an overview of vent and conduit diameters for various volcanoes, such as Etna (2–10 m), Kilauea (~20 m), Stromboli (~2 m), and estimate a conduit radius of 12 m for Shishaldin. The above suggested 10 m for Erebus is

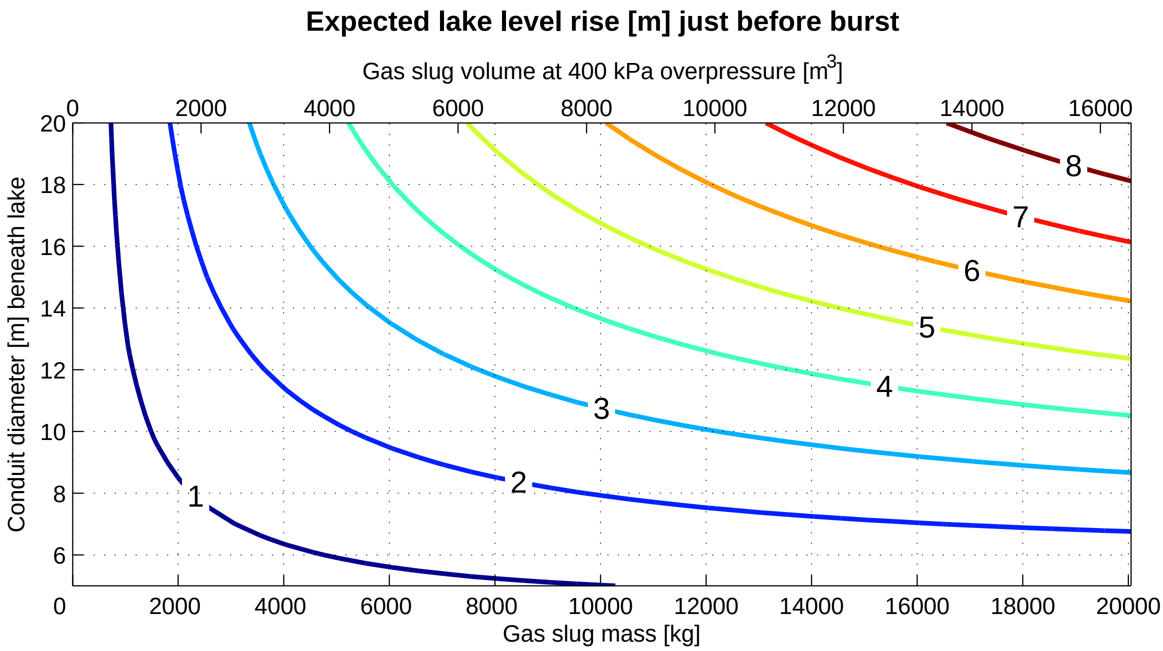

Figure 9.5: ***Expected lake level rise before burst.*** *This plot is similar in style to Fig. 9.2, but shows the expected level rise in Ray Lava Lake shortly before the burst, which is caused by the expansion of the rising slug in the conduit in the seconds before reaching the surface (Figs. 2.2 & 2.3). The lower horizontal axis denotes slug gas masses, the upper horizontal axis denotes the respective slug volume at 400 kPa overpressure above atmospheric pressure. While the slug expansion was calculated for the respective conduit diameter shown on the vertical axis, it was converted into the expected lake level rise for a lava lake of 40 m diameter (isolines). The large area of the lava lake in comparison to the conduit cross section dampens the expected level rise compared to that of a pure conduit.*

therefore within the range spanned by other Strombolian volcanoes, and is consistent with thermal considerations by *Calkins et al.* (2008), who calculate a minimum conduit diameter of ~4 m for Erebus. *Wallis* (1969) observe that in a slug flow regime, slug lengths are typically within 10 times the conduit diameter. At Erebus, even though highly dependent on scaling laws, this would allow for slug lengths of ~100 m. When neglecting the film thickness, it would infer slug volumes at depth in the order of 8,000 m^3 (while still at a high pressure), which is consistent with the above determined final slug volumes at the beginning of the rapid expansion phase.

The expected lake level rise shown in Figure 9.5 is thus fully compatible with video observations (*SOM*) and those of other authors (*Dibble et al.*, 2008), therefore fully accounting for the slug volume expansion. As a consequence, the slug rise model is not compromised by observations of only a moderate pre-explosion lake level rise.

9.8 Constraints on the conduit shape - generating "double bubbles"?

Figures 6.10 and 7.1 illustrate that type *I* bubbles at Erebus show a very consistent double acceleration peak. This means that the lake surface accelerates in two pulses, separated by about 0.3 s. In between the pulses the expansion acceleration almost stagnates, so that the expansion velocity remains constant for some fractions of a second before resuming acceleration. While a possible explanation for the first peak is evident, i.e. the rapid expansion of an overpressured gas bubble under the surface of the lava lake leading to a pressured drop in the bubble, the explanation for the second peak is not so simple.

As a first hypothesis, it is possible that the second acceleration peak is merely caused by the increased velocities that the radar measures after the bubble has burst. Since the burst process accelerates many small fragments, it is possible that the radar spectrum is dominated by their fast velocities after the burst, appearing as a second acceleration peak while in reality the large shell fragments do not accelerate a second time. Even though this would be a convenient explanation for the phenomenon, existing evidence points in another direction. Figure 6.10 shows that the bubbles' burst is consistently detected $\sim 0.1 - 0.15$ s after the onset of the second peak by the radar. While it is possible to imagine a systematic delay time between the actual burst and its detection by radar, it would be hard to explain why the radar would nevertheless detect the resulting high velocities immediately after the burst without a delay.

Furthermore, radar velocigrams as shown in Figure 6.6 (e.g. I_{I}) suggest that after the velocity stagnation in between the two acceleration phases, not only a few fragments but the **bulk** of the material continues to accelerate. This evidence suggests that the second acceleration phase indeed concerns the entire, still intact magma shell before the burst. Additionally, estimated bubble volumes (as discussed in Sec. 9.7) suggest that the bubble that is responsible for the first acceleration peak only has a volume in the range of 1,000 m^3, while the total amount of gas expelled in an explosion is ten times higher. If only one bubble is involved in the explosion, then it remains unclear where the large total gas volume comes from. I thus conclude from the combined evidence above that the double acceleration peaks are indeed a real phenomenon.

Consistently, double explosions have been suggested as possible explanations for peculiar phenomena at Stromboli (from video data *Chouet et al.*, 1974; *Ripepe et al.*, 1993; *Harris and Ripepe*, 2007). *Chadwick et al.* (2008) observed submarine Strombolian-style eruptions at the submerged "NW Rota-1" volcano in the Mariana arc, and find hydroacoustic evidence for multiple gas slugs arriving at the magma surface in rapid succession. And at Erebus, almost 10 years before the data for this study was recorded, *Rowe et al.* (2000) found acoustic wave forms that they attribute to double explosions. Consistent with the findings in *this* study, they report time lags in the order of $0.15 - 0.3$ s between the explosion peaks. Yet, until now, no satisfying explanation was given as to their generation mechanism.

The above evidence necessitates a physical explanation for the generation of at least two acceleration peaks[12]. Since the curve shapes are very similar between different explosions that are weeks apart, there must be a non-destructive and highly repetitive underlying mechanism. As a possible explanation I suggest the arrival of two or more slugs at the surface in rapid succession. Their generation mechanism can simply be explained by the fluid dynamic effects that are typically caused by a sudden widening of the conduit only a few tens of metres beneath the surface of the liquid column. I will now discuss this phenomenon in detail.

9.8.1 The effects of an abrupt change in conduit diameter

A mechanism that is capable of introducing a significant pressure disturbance in an ascending slug is the passage of a sudden change in conduit diameter. While this was suspected soon after volcanological models for slug flow were proposed (e.g. *Seyfried and Freundt*, 2000; *Aster et al.*, 2003), it was systematically investigated by *James et al.* (2006), who found astonishing results.

James et al. (2006), on the basis of detailed laboratory experiments, found that it is not a conduit **constriction** that generates the greatest disturbance to a rising slug, but a **sudden widening** of the conduit diameter, a so-called *"flare"*. The experimenters demonstrate that the passage of even a minor widening of the conduit (i.e. an increase of the conduit diameter as small as a factor of 1.3 – 2.1) leads to a severe disruption of the slug ascent. Typical effects are the occurrence of superstatic pressure peaks, net forces on the system, and a sudden acceleration of the slug accompanied by a violent disruption of the slug shape, which often tears the slug into two or more separated sections. Figure 9.6, adapted from real data by *James et al.* (2006), sketches such a flare passage. The severity of these effects was found to increase with the amount of diameter change. The effects even occurred when the widening concerned only a small section of the conduit at depth (i.e. a spatially confined "bulge" in the conduit).

These highly dynamic effects are caused by the abrupt change of slug rise speed (*James et al.*, 2006), which generally strongly increases with the tube diameter (Eq. 2.6). A higher rise speed in the wider, upper part of the tube leads to an acceleration of the downward flux of liquid on the side of the slug as soon as its nose enters the upper part. During the passage of the flare, this relatively fast downward flowing liquid film above the flare is entering the lower (narrower) tube, leading to a thickening of the film there, accelerating and "squeezing" the slug into the upper tube. When the slug is sufficiently long, this thickening occurs before the slug has completely passed the flare, eventually closing off the ascending gas for a moment and cutting the slug in two separate sections, which then typically reach the surface in rapid succession (Fig. 9.6).

[12] Possibly, even more than two acceleration peaks exist, which could occur after the bubble has burst, i.e. when the radar cannot track the velocity of the intact shell any more.

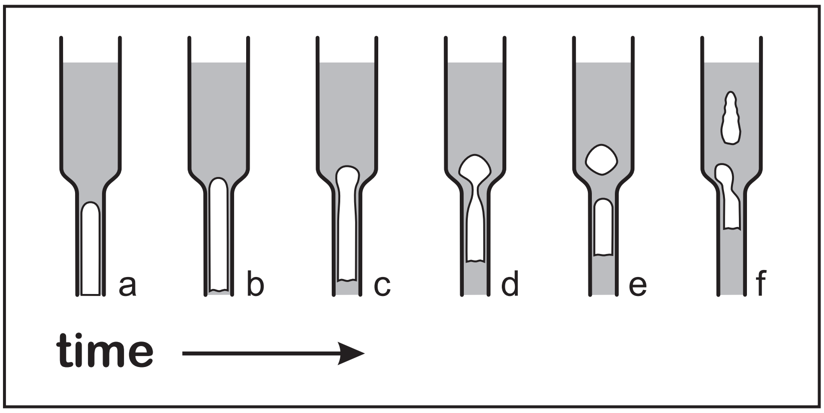

Figure 9.6: ***A gas slug passing a section of a sudden conduit widening*** *(also called a* ***"flare"****). (adapted from James et al., 2006). During the passage, a slug of sufficient length typically gets cut into several sections, accompanied by strong shape distortions and an acceleration of the slug's rise speed. A similar geometry is expected under lava lakes. Even though the scaling behaviour of this effect is not entirely clear, the experiments suggest that it occurs in a wide range of flow regimes, including the one inferred for Erebus' magma viscosity and conduit geometry.*

James et al. (2006) found that the effects of such a flare passage are highly repeatable, and strongly depend on the depth of the flare and its profile, i.e. the widening of the cross-sectional conduit area. Shallow positioned[13] sections of severe tube widening (i.e. a doubling of the diameter[14]) were observed to cause the largest disruption in the slug's final approach to the surface.

Interestingly, such a geometry is very likely to be present at the bottom of most existing lava lakes, with a relatively narrow conduit feeding into a wider, fluid-filled lava lake. Such a funnel-shaped vent geometry is common at volcanoes (*Sparks et al.*, 1997), and recent literature has noted that it is also present at Erebus (e.g. *Dibble et al.*, 2008; *Calkins et al.*, 2008). This is not surprising, given that such a geometry is very likely to be enhanced by convectional erosion in the lava lake, where constantly circulating hot magma generates a downward flow along the lake walls (*Calkins et al.*, 2008).

Even though *James et al.* (2006) point out that the usually applied scaling laws fail in such a dynamic regime, the mechanisms observed during a flare passage of a laboratory slug are likely to have a great similarity to larger natural systems. Therefore, if such a flare is situated just beneath the surface of a lava lake, it is likely to have a significant influence on the slug rise in the last moments before reaching the surface, possibly influencing the gas overpressure just before the explosion.

The phenomenon of slug separation into two or more sub-bubbles deserves a closer look.

[13] shallow in this respect means that the flare is not submerged significantly deeper than about three times the upper conduit diameter. Numerical and analogue models of fluid dynamics show that the "active" part of liquid flow field above the slug occupies a volume that is about equal in length and width, i.e. it is not much longer than the conduit is wide, possibly even less (*Polonsky et al.*, 1999a; *James et al.*, 2006).

[14] the used widening profiles were relatively gentle-shaped, i.e. it is not necessary to have a step-like widening of the profile to observe this effect.

James et al. (2006) found that when slug separation occurs in slugs that are just longer than the critical cutoff length, the respective first segments experience the strongest acceleration towards the surface. In contrast, slugs that are just under the critical length are accompanied by strong shape elongations. Depending on several different parameters, laboratory slugs temporarily increase their ascent velocity by up to a factor of 10 after the passage of a flare (*James et al.*, 2006). Shape disruptions occur during the entire high-speed phase of the slug (i.e. just above the conduit widening) and sometimes lead to a very narrow and pointed slug nose, which ascends to the surface in a jet-like manner.

Intriguingly, in the natural system, this shape alteration mechanism can sufficiently explain the two main types of explosion styles found in the Ray Lava Lake of Mt. Erebus. The violent type *II* explosions emerge at a relatively small and defined spot on the lake surface. Thus, they could be caused by slugs that are just under the cutoff length, which have experienced a strong elongation, possibly causing a strongly pointed slug nose. In contrast, type *I* explosions, with their double acceleration peak might be caused by slugs that are beyond the critical length and therefore get cut in two (or more) sections. Consistently, *small* explosions could result from bubbles that are much too small to be cut in half or to be significantly disturbed, therefore not generating a double peak.

The length or volume of the first bubble is partly determined by the geometry of the flare and the liquid properties, both of which are expected to be reasonably stable at Erebus (*Kelly et al.*, 2008b). Therefore, if this mechanism plays a role, sizes, pressures and volumes of the respective first bubble of explosions can be expected to be similar to each other. In contrast, the combined volume of the **following** bubbles is dependent on the initial slug length, which varies between explosions. Therefore, this mechanism can conveniently explain why the bubble pressures and volumes of the respective first bubble of different type *I* explosions are so similar to each other, while the overall expelled gas volume varies greatly from explosion to explosion (Fig. 7.9).

James et al. (2006) show that acceleration forces and changes in flow pattern associated with a slug passage act as net vertical forces on the whole system (typically a small-magnitude upward force acting on the flare neck, followed by a stronger downward force acting on the bottom of the tube). Depending on the geometry and the pressure wave velocity of the system, these pressure perturbations can stimulate longitudinal oscillations ("standing waves") of the conduit.

A testable expected consequence of this mechanism is therefore the excitation of seismic waves. The signals are expected to emerge a few seconds before the burst from the flare neck and possibly from the bottom of the conduit, potentially capable of exciting the entire conduit to resonance. While this has the potential for an in-depth future investigation, it is so far consistent with existing seismic studies conducted at Erebus (*Rowe et al.*, 1998, 2000; *Aster et al.*, 2003, 2008).

9.8.2 Alternative explanation: an explosive gas injection

An alternative explanation for the double acceleration peak during bubble explosions at Erebus is that bubbles are not the result of gas slugs that have risen in the conduit, but the result of a sudden explosive degassing into a shallow area of the lava lake. Such an explosive injection of highly pressurised gas into the liquid magma could generate a hydrodynamic phenomenon that is very similar to that caused by shallow underwater explosions.

Ichihara et al. (2005) and *Ichihara et al.* (2009) have conducted underwater explosion experiments showing that shallow explosions cause the bulging of the water surface above, which acts as a volumetric source for the generation of an acoustic signal. They found that for a certain depth of the explosion relative to their size, the water surface above the explosion accelerates in two separate pulses. The first acceleration pulse is caused by the massive displacement of volume through the explosion itself, followed by a deceleration of the displacement when the gas pressure drops due to the bubble's expansion. Then, a second peak in the acceleration of the water surface is caused by the top of the bubble approaching the surface (while the bottom part of the bubble continues to decelerate). Even though the surface level does not oscillate (i.e. there is no surface retraction phase during shallow explosions), these two acceleration peaks of the water surface typically generate an acoustic M-wave (*Ichihara et al.*, 2009) by volumetrically expanding into the atmosphere.

If the above mechanism is present at Erebus, it could account for the double acceleration peak observed at the surface. The resulting typical plateau in the acoustic signal, could then be interpreted as a degenerated form of an M-wave. If existing, this mechanism would have profound consequences for the currently accepted model for Erebus explosions. Instead of rising gas slugs inside the conduit, it would imply that the conduit is more or less slug-free. Additionally, a persistent source of explosive gas release would have to be present in the shallow part of the lake.

The presence of an active gas vent in Erebus' crater next to Ray Lava Lake, which sporadically and sometimes explosively ejects a gas jet (*Calkins et al.*, 2008; *Jones et al.*, 2008), shows that an explosive source of gas injection into Ray Lava lake is possible. *Oppenheimer and Kyle* (2008b) show that gas released from Ray Lava Lake has a significantly different CO_2/H_2O composition than gas released from the other vents at Erebus, suggesting that at least two different gas supply mechanisms exist in Erebus' crater.

Furthermore, after observing explosions in 1987, *Dibble et al.* (2008) reported that right after some explosions, *"... new lava entered the empty basin through a small vent at the top of the wall on the side away from the camera wall."* This observation suggests that even though the system is overall stable, the magma supply to Ray Lava lake is not always exclusively feeding into the lake from the bottom, thus providing a possible source of a gas injection on the side.

Aster et al. (2003) suggest that a shallow summit magma reservoir could exist at Erebus, in that case being the source of magma and gas feeding into the lava lake. In the case of a reservoir roof that is possibly located only a few tens of metres beneath Erebus' crater floor, gas would be expected to accumulate at the roof of the reservoir and beneath structural barriers in the shape of coalescing foam. When such a barrier is finally surmounted by the gas, depending on the geometry, it would either rise up the (in that case very short) "conduit" into the lava lake, or it could rise through cracks, causing a direct gas explosion, as can frequently be observed in Erebus' active ash vent.

Such a geometry is supported by observations by *Dibble et al.* (2008), who report that after some large explosions at Erebus, the lava lake continued to drain down the conduit for several seconds after an explosion. This was most likely caused by inertia of the magma column, which was pushed downward by the explosion's force (Sec. 7.7). Due to the large mass of magma in a long conduit, the presence of such a strong effect suggests a rather short conduit length, which is consistent with a very shallow magma reservoir. Additionally, a short conduit length strongly promotes the stability of a conduit-lake system (*Witham and Llewellin*, 2006), and might explain why Ray Lava Lake shows such a high degree of long-term stability, which is generally hard to obtain (*Witham and Llewellin*, 2006).

In summary, the alternative model for the shallow Erebus conduit system and the associated explosion mechanism discussed in this section is interesting, but it is not backed up by many quantitative observations, thus I do not regard it as the most likely scenario at this point. However, while it opens up a variety of new questions, it answers some others, and the rationales presented here suggest that it should nevertheless be further discussed and considered in future studies.

9.8.3 No alternative: bubble vibrations

As discussed in Section 2.2, the liquid head above a rising slug can act as a mass bouncing on a gas spring, resulting in longitudinal oscillations of the slug (e.g. *Vergniolle et al.*, 1996; *James et al.*, 2008). It is tempting to attribute the double acceleration peak that is observed during bubble expansion to such an oscillation (similar to the model developed by *Vergniolle and Brandeis*, 1994). *Vergniolle et al.* (1996, Eq. 5) provide a formula for the expected oscillation period of a slug **at depth**, which was confirmed in laboratory experiments by *James et al.* (2004).

Figure 9.7 shows this expected pre-burst oscillation period for a variety of conduit diameters and gas masses expected for Erebus, using the same model as was used for Figures 2.2, 9.2 & 9.5 (*James et al.*, 2008), and using the formula provided by *Vergniolle et al.* (1996). The period is shown for the moment when the liquid head above the slug has decreased to 1.4 m thickness, representing the thickness of the magma shell (Sec. 7.1) above the slug at the beginning of the rapid expansion phase, i.e. at the time when the first acceleration peak occurs.

The expected period for a longitudinal slug oscillation at Erebus, depending on the conduit diameter, lies in the range of several seconds even for small slugs just before the burst

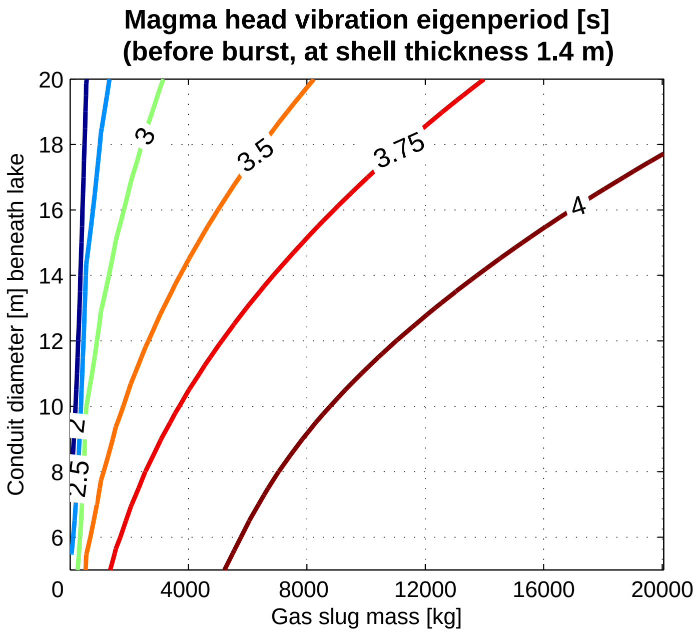

Figure 9.7: ***Expected oscillation period of a magma head above a slug.*** *This plot is similar in style to Fig. 9.2, but shows the expected oscillation eigenperiod of the liquid magma column above the slug, bouncing on the pressurised gas and therefore acting like a mass-spring system. Periods are given for the moment just before the burst, when the liquid has only a remaining thickness of 1.4 m (which is assumed to be the thickness at the start of the rapid expansion phase). The periods are even lower when the slug is still deep.*

(Fig. 9.7). It increases substantially for larger slugs, and is much higher for slugs that are still deep, due to the larger mass of magma above the slug. Even though the model considers the existing amount of overpressure in the slug, which strongly decreases the oscillation period, the predicted period is still much higher than the ~0.3 s period that can be inferred when interpreting the double acceleration peaks as an oscillation (Fig. 6.10).

Furthermore, if such a longitudinal oscillation is so strongly excited in that phase of an explosion, its excitation would be expected to slowly emerge in the seconds before the burst, with a constantly decreasing period due to the ongoing mass decrease above the slug (as observed by *James et al.*, 2004). Surface accelerations obtained from radar data do not show any signs for such a slowly emerging oscillation of the lake surface. Consistent with the above, in laboratory experiments, *James et al.* (2004) find evidence suggesting the presence of such longitudinal oscillations when the slug is still deep, but they do not find any evidence for shape oscillations of the membrane once the bubble has approached the surface.

9.9 Long term energy balance and mass flux

Section 4.2 shows that the overall (static and dynamic) explosive energy output at Erebus is dominated entirely by the thermal energy transported in magma fragments ejected from the lake. The general observation that thermal energy by far exceeds all other types of energy is in accordance with earlier observations at other volcanoes (e.g. *Yokoyama*, 1956; *Hédervári*, 1963; *McGetchin and Chouet*, 1979).

On Erebus, each large explosion (of all types but *small*) ejects hot fragments carrying around 4×10^{12} J of heat. With an estimated daily average of about 3 – 4 large explosions (Fig. 6.1), and assuming that a quarter of the hot shell material remains outside the lake long enough to cool before slipping back (factor η_m in Eq. 4.61), this amounts to a daily thermal output of $\sim 3 \times 10^{12}$ J during an active phase of the volcano, such as the field season 2005/06. On average, this is equivalent to a constant power output of ~35 MW, but this value neglects the additional steady-state radiative and convective heat output from the lava lake occurring in between the explosions.

Calkins et al. (2008), by using a temporally deployed ground-based thermal camera[15], estimate the steady-state radiative and convective thermal output of Ray Lava Lake in 2004 to about 36 $\pm$ 3 MW, which is about the same amount of energy that is transported through explosions (as estimated above). Therefore, by including power output by mass loss, the estimated thermal energy loss is significantly greater than previously assumed. This must be considered when, for example, estimating minimum reservoir sizes through thermal heat loss (e.g. *Calkins et al.*, 2008).

The additional non-steady power output caused by explosions is difficult to detect or determine with satellite-based methods (e.g. *Harris et al.*, 1999; *Davies et al.*, 2008; *Wright and Pilger*, 2008a,b), since they are typically sampling only once in several days. Therefore, satellites are likely to simply miss the short time period after an explosion where the ejected and dispersed lava significantly adds to the radiated heat, and might even introduce an *aliasing* effect. Consistently, *Wright and Pilger* (2008a) measure a highly variable heat flux at Erebus at the end of 2005 with an average of ~17 MW, but with single measurements as high as 100 MW (e.g. MODIS, 10 April 2006, with the satellite possibly sampling shortly after an explosion).

I have argued in Section 7.1 that the mass of magma removed from the conduit during a large explosion in the austral summer of 2005/06 was in the order of ~3,600 metric tons. If an average of three explosions per day is assumed of which a quarter remains permanently outside the lake, this surmounts to a mass loss of ~2,700 tons/day, or an average mass loss of ~30 kg/s. This mass loss is in the same order of magnitude as the assumed magma supply rate that is necessary to deliver (via thermal convection in the conduit) the required heat to counterbalance the heat loss through radiation. *Wright and Pilger* (2008a) estimate the average convective magma supply rate of Erebus at 14 - 118 kg/s, or 1,200 – 10,000 tons per day on the basis of satellite measured heat flux. *Calkins et al.* (2008), using a ground-based thermal camera, estimate this value at 140 - 400 kg/s, while *Davies et al.* (2008), using satellite-based measurements in the austral summer of 2005/06, suggest a convective magma supply rate of 64 – 93 kg/s.

Given that both the amount of mass ejection through explosions, and the thermally necessary magma supply rate (*Calkins et al.*, 2008; *Davies et al.*, 2008) are based on a number of assumptions, their agreement is remarkable. The consequence of this is that during a phase as active as December 2005 and January 2006, the magma supply rate in the conduit must accommodate for both the radiative heat flux between explosions, as well as for the net mass

[15] The permanently installed thermal infrared camera at Erebus (*Aster et al.*, 2004) is not calibrated, and can therefore not be used for calculating the energy output.

loss by explosion ejecta. Another possibility is that, rather than being strongly convective, the conduit feeding Ray Lava Lake might almost be a ”one way street” during such phases, delivering just as much magma to the top as is removed by the explosions, and still providing enough heat to support a permanent lava lake. An investigation of this effect will be an interesting target for a future study.

CHAPTER 10

CONCLUSIONS AND OUTLOOK

This study derives and analyses a multi-parameter dataset using Doppler radar and seismic, infrasonic and video observations collected in 2005/06 at Erebus volcano, Antarctica. The results show that such a multi-parameter dataset can provide novel and important information about the start of Strombolian eruptions, therefore enhancing our understanding of Strombolian-type volcanoes. We now have a tool at hand to determine in-situ parameters during the critical first second of an eruption in real-time, and during all weather and light conditions. It provides information on the eruption mechanism in unprecedented detail, and for the first time allows the calculation of energy that is freed during the first second of a volcanic eruption as a detailed function of time. Similarly, the history of gas pressure during an explosion can now be derived as a function of time, thus allowing for a detailed analysis of the physical state of the vent system at any given time during the important first moments of an explosion. Serving as a basis for future studies, these parameters deliver the necessary boundary conditions for sophisticated conduit modelling at Erebus and most likely at other Strombolian volcanoes. Furthermore, the obtained results not only enhance confidence in the used explosion models and measurement techniques, but also provide us with profound knowledge about the source of acoustic signals from Strombolian eruptions.

I will summarise the outcome of this study, as discussed in Chapter 9, by answering the questions stated in the introduction of this manuscript (Sec. 1.1). While the complexity of the process makes it impossible to include all aspects of the respective answers in just a few sentences, there are several key findings that stand out:

1. *What happens during a Strombolian explosion, and how do bubbles burst?*

   At Erebus, the first second of an explosion is characterised by several time episodes, developing from an undisturbed lava lake surface into an episode of a rapidly bulging and accelerating lake surface up to the point of violent rupture. During about half of the explosions, the acceleration of the lake surface shows two peaks that are separated by about 0.3 s. Results suggest that this type of bulging of the lake is caused by the adiabatic expansion of two or more gas bubbles reaching the surface of the lake in rapid succession. Conduit modelling data from other studies suggest that this is caused by the breakup of a large approaching gas slug, most likely only several tens of metres beneath the surface of the lava lake, caused by the geometry of the conduit-lake transition. For this type of explosion, the bubbles' burst usually occurs 0.4 – 0.5 s after the first significant movement of the lake surface. During the other half of Erebus' explosions, bubbles burst immediately after reaching the lava lake surface. In all cases, bubbles expand strictly monotonic, and do not vibrate before their burst.

2. *What are the energies involved, and what is their partitioning?*

   Due to the new techniques and instruments that were applied in this study, the energy partitioning obtained from radar measurements at Erebus is comprehensive and much more detailed than that of previous studies. At the same time it is consistent with the sparsely available, partial attempts to acquire energy partitioning estimates for other volcanoes, and it agrees with previous findings at Erebus, providing additional confidence in the results. The data show that of all energy types that are involved in Strombolian eruptions, only the thermal energy together with two dynamic types of energy are significant for the overall energy budget: the kinetic energy of the ejecta, as well as their potential energy in Earth's gravity field. The dynamic energy types are powered by large pressurised gas bubbles rising in the conduit and exploding at the top, whose sheer size makes up for their moderate overpressure of only a few atmospheres. At Erebus, the **dynamic** energy released during an explosion (i.e. not counting thermal energy) is equivalent to the explosion of several hundred kilograms of TNT, around one gigajoule. Most of this energy release occurs within 0.2 seconds. For a short time this is equivalent to the power output of five large nuclear power plants. Yet at the same time this dynamic energy output is almost negligible in comparison to the thermal energy that is passively carried by the hot ejecta. This thermal energy is in the terajoule range, or equal to about fifty years worth of electricity for an average European five person household. This relation emphasises the importance of the ejecta's thermal energy in the long-term energy budget of volcanoes.

3. *What are the gas overpressures of a rising gas bubble just before its explosion?*

   Calculated overpressures of gas bubbles were in the range of several atmospheres during the start of the explosion ($\sim$200 – 600 KPa, about the pressure in a bicycle tire), dropping to about one atmosphere (100 kPa) just before the burst. Even when including all parameter uncertainties, no overpressure was found to be larger than 800 kPa. These findings are consistent with state of the art theoretical considerations and recent laboratory models undertaken by others.

4. *How large are the gas volumes of exploding bubbles?*

   As described above, about half of the explosions show a double acceleration peak that is most likely caused by the breakup of rising gas slugs in two or more parts. Gas volumes of the **first** approaching bubble of each explosion were found to be very stable at around 1,000 m^3 (about the cabin volume of two large passenger aircraft), and were determined through two semi-independent thermodynamic methods. The **total** gas volume of each explosion was found to be highly variable, and exceeded 35,000 m^3 during some large explosions.

5. *What causes the acoustic signal that is typically observed during Strombolian explosions, and what can we learn from it?*

   Doppler radar data, together with a simple eruption model, is now capable of explaining the acoustic signal generated by Strombolian eruptions at Erebus, providing confidence for the validity of this source mechanism at other Strombolian volcanoes, which was a constant source of debate in the past. At Erebus, the infrasound signal can be explained by a dual mechanism consisting of a short volumetric expansion before the burst, and a simple "$\lambda/4$-type" resonance generated by the gas slug cavity once the bubble has burst. Results show that the post-burst part clearly dominates the explosion's acoustic signal, both in amplitude and duration.

   To be more precise, results show that real acoustic signals match their simulated counterparts closely until the time of the bubbles' burst. This means that acoustic amplitudes scale robustly with the explosions' volumetric expansion, determined from radar data through the explosion model developed here. While this scaling relationship is very clear until the time of the bubbles' burst, post-burst signals cannot be explained by this mechanism any more. Following *Vidal et al.* (2006), I propose a resonance of the suddenly depressurised gas remaining in the cavity formed by the slug, with a wavelength that is four times the length of the cavity. While the **shape** of the measured acoustic waveform matches very well with this mechanism without the adjustment of arbitrary parameters, *Vidal et al.* (2006) show that the **amplitude** of the cavity resonance after burst is strongly dependent on the details of the burst process and cannot easily be predicted. Consistently, recorded acoustic amplitudes at Erebus generally scaled with explosion velocities and energies, but included considerable scattering.

   Therefore, without the development of even more sophisticated bubble models, Vidal's results and the outcome of this study strongly suggest that it is not possible to determine eruption pressures or energies from post-burst infrasound alone. The results shown here do, however, suggest a very simple tool for determining gas slug lengths at the time of burst, simply by measuring the cavity resonance wavelength and dividing it by four. If the conduit diameter can be estimated, either by measuring the decay time of the resonance signal or by visual observations, this value easily translates into bubble gas volumes.

6. *What are the associated ground forces, and can they explain the seismic signals that usually accompany Strombolian explosions?*

   Vertical ground forces generated by explosions, as predicted by the model presented here, are in the 10^8 N range. This is about the force needed to lift a large cruise ship in Earth's gravity. This magnitude of force is in the same range as the forces proposed by existing models as the source of VLP seismic signals at Strombolian volcanoes.

10.1 What can we learn about other volcanoes?

The above results provide a new perspective for interpreting data from Strombolian eruptions, not only at Erebus but also at other volcanoes. The results constrain important physical eruption parameters, and they serve to improve existing models for the generation of acoustic signals during explosions.

Even though the model presented in this study was developed primarily for Erebus, it can be applied to other Strombolian-type volcanoes. Naturally, magmatic and geometric parameters at other Strombolian volcanoes are likely to be different from those at Erebus. For example, estimates for magma viscosities at Stromboli volcano range from 100 Pa s (*Williams and McBirney*, 1979; *Vergniolle and Brandeis*, 1994) to 1250 Pa s (*Vergniolle et al.*, 1996), which is roughly an order of magnitude less than the viscosity inferred for Erebus magma. Similarly, the estimated magma viscosity at Shishaldin is around 500 Pa s (*Vergniolle et al.*, 2004). These parameter differences can easily be adjusted in the model. Therefore, as long as the geometry of the volcano in question allows the observation of a bubble burst with a Doppler radar instrument, the model is suitable to provide conclusive information about the explosion processes at other volcanoes.

Unfortunately, the number of volcanoes that allow the observation of Strombolian bubble bursts directly from the crater rim is limited to only a handful of cases worldwide, mainly due to geometry and safety constraints. Nevertheless, the results obtained in this study allow for conclusions even on those Strombolian eruptions that cannot easily be observed with instruments on the crater rim. For example, explosions at Erebus and Stromboli have very similar acoustic waveforms (*Vergniolle et al.*, 1996; *Rowe et al.*, 2000; *Johnson et al.*, 2003), therefore it is likely that the underlying mechanisms are also similar. The same characteristics can be found in acoustic signals recorded at other Strombolian volcanoes, such as at Klyuchevskoi (*Firstov and Kravchenko*, 1996), Shishaldin (*Vergniolle et al.*, 2004), Arenal (*Hagerty et al.*, 2000), and Karymsky (*Johnson et al.*, 2003).

The clarity and simplicity of the causal connection between the bubbles' monotonic volumetric expansion at Erebus, their early burst, and the resulting acoustic signal strongly suggests a similar mechanism for other volcanoes with a similar eruption style. Therefore, from the results obtained at Erebus we can learn how to interpret acoustic signals at these volcanoes. Once tested at such volcanoes, the technique can provide a very simple method for determining gas slug lengths, conduit mouth widths, and erupted gas volumes. One of the factors whose influence needs to be tested is the geometry of the upper part of the conduit, which in the case of many other volcanoes is not as unobstructed as at Erebus, therefore possibly influencing the acoustic signal shapes. I therefore propose that this theory be tested and volumetric expansion and cavity resonance signals be investigated at other Strombolian volcanoes.

In a similar manner, the technique of determining the ground force history of explosions from radar observations provides a simple source function for propagation models of seismic waves, and should be tested against seismic recordings at Erebus and other Strombolian volcanoes. The results have great potential to increase our understanding of seismo-acoustic measurements at volcanoes, and they provide additional confidence when interpreting data from volcanoes where one of the sensor types are not available for various reasons.

What else do the results obtained at Erebus tell us about other volcanoes? A parameter of interest is the bubbles' gas pressure just before the burst. Studies show that pre-burst bubble gas pressures are expected to be strongly dependent on magma viscosities and conduit diameters (*James et al.*, 2008). Even for volcanoes with different geometries and magma compositions, these values can often be estimated, allowing for an order of magnitude estimation of pre-burst gas pressures at other Strombolian-type volcanoes.

Similar to the gas pressure of bubbles, the energy partitioning during explosions depends on several factors and will therefore vary from volcano to volcano. Yet, observed differences of several magnitudes between the principal energy types (thermal, kinetic, potential and dissipative) suggest that the partitioning order obtained for Erebus is fairly robust and therefore possibly valid for many other volcanoes of Strombolian eruption type. Furthermore, the above results suggest that the absolute value of all involved energies mainly depends on the total mass of ejected magma fragments, and can therefore be determined at other volcanoes. Usually, this total mass can be estimated by accounting for the ejected material after an explosion, either by a physical investigation or potentially with the help of a thermal camera, as is currently in use at many volcanoes worldwide.

Moreover, the results show that the directivity of volcanic explosions, i.e. the direction of the main acceleration of mass during a blast, can be monitored by three Doppler radar instruments in 3D, and even in 4D when the process spans more than one sampling interval of the recording system.

10.2 Future outlook

In addition to the testing of the above techniques at other Strombolian volcanoes, I suggest the further use of the unique possibilities that arise from the almost ideal observation conditions given at Erebus volcano. Despite the sometimes challenging logistical conditions, Erebus serves as an outdoor laboratory and a Strombolian model volcano. Studying this volcano will not only result in improved knowledge on Erebus itself, but more importantly it will enhance our knowledge about Strombolian volcanoes in general, some of which are potentially dangerous, and are located in populated areas in Europe and other continents.

For future activities at Erebus I suggest establishing a system of four or more radars, fully surrounding the explosion source. In this case the setup will allow the use of a more sophisticated eruption model. A great improvement would be the exclusive use of the newer and faster types of radar with a sampling rate of 20 samples per second or more, offering a far more detailed insight into eruption processes. Furthermore, this would greatly enhance the capability of a direct comparison of radar measurements to the now continuously operating network of infrasound microphones.

An open question at Erebus is the actual length of the conduit, and the processes that form or release a gas slug. The rapidly progressing technological capabilities of the MVR radar system now allow for a detailed measurement of even small changes in the lava lake surface level in between explosions. This not only offers the possibility of monitoring small scale oscillations of the lake level, it also allows the determination of the precise rate at which the lava lake refills after an explosion. Using a fluid dynamic model, this refill rate can provide clues on the deeper conduit geometry, such as the overall conduit length and width, and would help the interpretation of existing seismic data associated with conduit resonances and slug formation (*Aster et al.*, 2008).

The suggestions made in the last two sections merely represent a brief list of possible uses of Doppler radar measurements in combination with a multi-parameter experiment, and it is likely to be biased and narrowed by the limited perspective of a single person's point of view. The potential of the method is much greater than this, most likely allowing the determination of a wide range of information that is of interest to scientists at various volcanoes worldwide. While several interesting projects are currently under way to solve the riddles of some of these volcanoes (e.g. *Scharff et al.*, 2007, 2008, 2009; *Meier et al.*, 2009), it is up to the imagination of the reader to make even more use of this potential in the future.

ACKNOWLEDGEMENTS

A huge thanks goes to Matthias Hort, Phil Kyle, Rick Aster, Malte Vöge and the *University of Hamburg* for providing the unique and magnificent possibility to conduct this study, as well as for providing an incredible amount of advice, inspiration and resources. Without them, this study would have not even started.

Likewise, I would not have been able to conduct this study without the generous technical support and help in the field from Bill McIntosh, Nelia Dunbar, Clive Oppenheimer, Peter Kelly, Julie Calkins, Kyle Jones, Ashley Davies, Christine Kimball, Elizabeth Morton, Sarah Krall, Lea Scharff, Sonja Hofmann and Sebastian Heimann, or without the logistical support from the staff at the Antarctic McMurdo station.

I would like to express my special thankfulness to Jeff Johnson, Joachim Wassermann, Clive Oppenheimer, Gerhard Peters, Bernd Müller, Lea Scharff, Phil Kyle, Rick Aster, Dirk Gajewski, Mike James, Valerie Vidal, Maurizio Ripepe, Torsten Dahm, Milton Garcés, Sylvie Vergniolle, and Mie Ichihara for very thoughtful discussions that added great value to this study. Furthermore, inspiring comments by Matthew Hall and Kristina Meier greatly improved the quality of this manuscript. Not less importantly, I would like to thank Christel Mynarik for her always friendly words, an unlimited supply of pieces of yellow sticky paper, and for keeping our institute together.

Thanks to Bill and Nelia for teaching me how to drive a snowmobile on a forty-five degree slope, how to cook a delicious three-course dinner in a tent at -40°C in high altitude, how to abseil into a 20 metre deep ice cave (and to get out again), how to dodge large hot lava bombs, and for cutting the *"woop"* with my freshly sharpened Leatherman tool. Likewise, thanks to Sarah Krall for showing me how to attach a sling load to a four ton helicopter hovering above. My respect goes to Paul Murphy and his colleagues from *Petroleum Helicopters, Inc.*, not only for flying tons of my gear to the top of a four kilometre high active volcano in rarely perfect Antarctic conditions, but also for making beautiful contrails.

This project was funded by the German Science Foundation (DFG) through project HO1411-16, and field work at Erebus was supported by funding from the Office of Polar Programs, National Science Foundation grants OPP-0229305 and ANT-0538414. Acoustic and visual data were kindly provided by the *Mount Erebus Volcano Observatory*, with special help from Phil Kyle, Bill McIntosh, Kyle Jones and Jeff Johnson. A map with GPS data of bomb locations was kindly provided by Nelia Dunbar from *New Mexico Tech*, and a detailed analysis of Erebus lava samples was provided by Klaus Heide from the *University of Jena*. I thank the

Thank you - I couldn't have done this without you!

Basalt-Actien-Gesellschaft / Norddeutsche Hartsteinwerke for the friendly permission to perform measurements in their quarry, and the *Alfred Wegener Institute for Polar and Marine Research (AWI)* for the possibility of letting me test my field equipment in their freezer. Major hardware construction and updates were accomplished with great support from the mechanical workshop of the *Centre for Marine and Climate Research* of the University of Hamburg. Thanks also to *METEK* company and Gerhard Peters for providing unbureaucratic help with our radar instruments when needed.

Last but not least I would like to express my great thankfulness to the girl with the sun in her head, to my family and to my dear friends who unselfishly supported me over many years, a task which certainly was not always easy.

Die Weichen sind gestellt
in einer Welt,
deren Umriss uns gefällt.

Wir sind gewillt zu übersehn,
was wir jetzt noch nicht verstehn.
Wir müssen gehn.

Tocotronic

Part IV

APPENDIX

APPENDIX A

SUPPORTING FIGURES AND CALCULATIONS

A.1 Radar antenna gain pattern

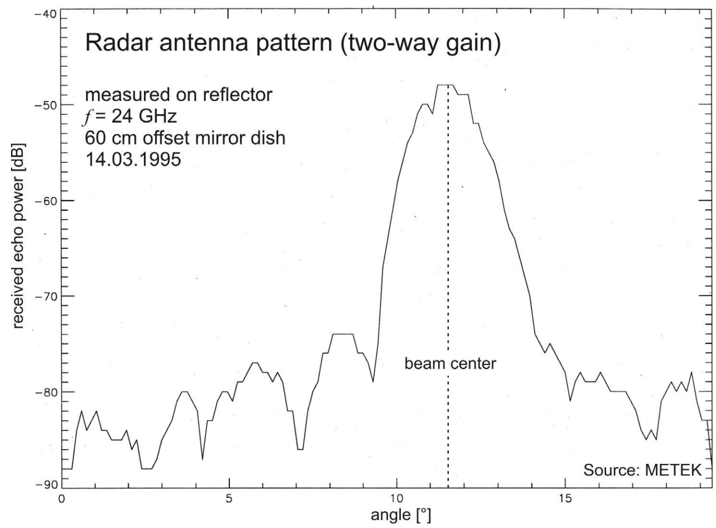

***Figure A.1:* Doppler radar squared antenna gain pattern (two-way gain).** *The pattern was obtained by slowly turning the radar beam horizontally, sweeping the beam over a distant reflector. The diagram shows the measured reflected echo power vs. the radar beam angle (both with arbitrary offsets). The echo power peaks where the radar beam aims right on the reflector, and falls off rapidly towards the side, dropping to -10 dB at ≈ 1.5° off the beam centre. Since the radar waves passed through the antenna twice (for sending and receiving), the measured pattern is the square of the pure antenna gain pattern (i.e. dB values are doubled).*

Despite the effect of a radially decreasing sensitivity of the radar beam, the correct measurement of velocities of reflectors at the beam edge is not compromised by this effect (i.e. a reflector's echo peak in the spectrum will still appear at the correct velocity, even though its signal is weaker than the signal of a reflector that is closer to the beam centre). There is, of course, a limit to this, since beyond a certain distance from the beam centre, the echo power drops too low to allow for a significant contribution of echo power to the spectrum. In practise, the -10 dB line (Figs. 1.8, 4.5) is a good indicator for this corner, therefore defining an area with a significant echo contribution to the spectrum. Accordingly, the -10 dB line can be considered as the practical "beam edge".

A.2 Temperature and sound speed of an adiabatically expanding gas

When hot gas expands adiabatically, its temperature drops. Therefore, such a temperature decrease also takes place in a rapidly expanding magmatic gas bubble. It can be determined through (*Kinney and Graham*, 1985):

$$T_{\mathrm{gas},1} = T_{\mathrm{gas},0} \left(\frac{\hat{p}_{\mathrm{gas},1}}{\hat{p}_{\mathrm{gas},0}} \right)^{\frac{\gamma-1}{\gamma}} \tag{A.1}$$

where $T_{\mathrm{gas},0}$ is the initial temperature of the gas at the beginning of the expansion process. It is assumed to be equal to the temperature of the lava lake, around 1000°C (*Kelly et al.*, 2008b). It is worth noting that at the time of the burst, the gas has cooled down by only a few hundreds of K (see Fig. A.2).

In order to calculate the speed of sound in a gas, its molar mass must be known (Sec. 3.2). *Oppenheimer and Kyle* (2008b) determined the typical gas composition at Erebus (Sec. 1.6), and find that the gas is mainly composed of water vapour and carbon dioxide (CO_2). I thus approximate the molar mass of the magmatic gas by using that of a gas mixture consisting of 60 mol % water vapour M_{gas} ($\approx$ 0.0180106 kg/mol) and 40 mol % CO_2 ($\approx$ 0.044010 kg/mol). This leads to a molar mass of $M_{\mathrm{gas}} \approx$ 0.028 kg/mol, which is very similar to that of dry air (Sec. 3.2).

By using Equation 3.16 with an adapted γ parameter (i.e. a ratio of specific heats $\gamma = 1.1$ for hot magmatic gas instead of 1.4 for dry air), the speed of sound of the hot magmatic gas can be estimated to

$$c_{\mathrm{gas}} \approx 18.07\sqrt{T_{\mathrm{gas}}} \,, \tag{A.2}$$

which gives a speed of sound of $c_{\mathrm{gas}} \approx$ 650 m/s at 1000°C and 600 m/s at 800°C.

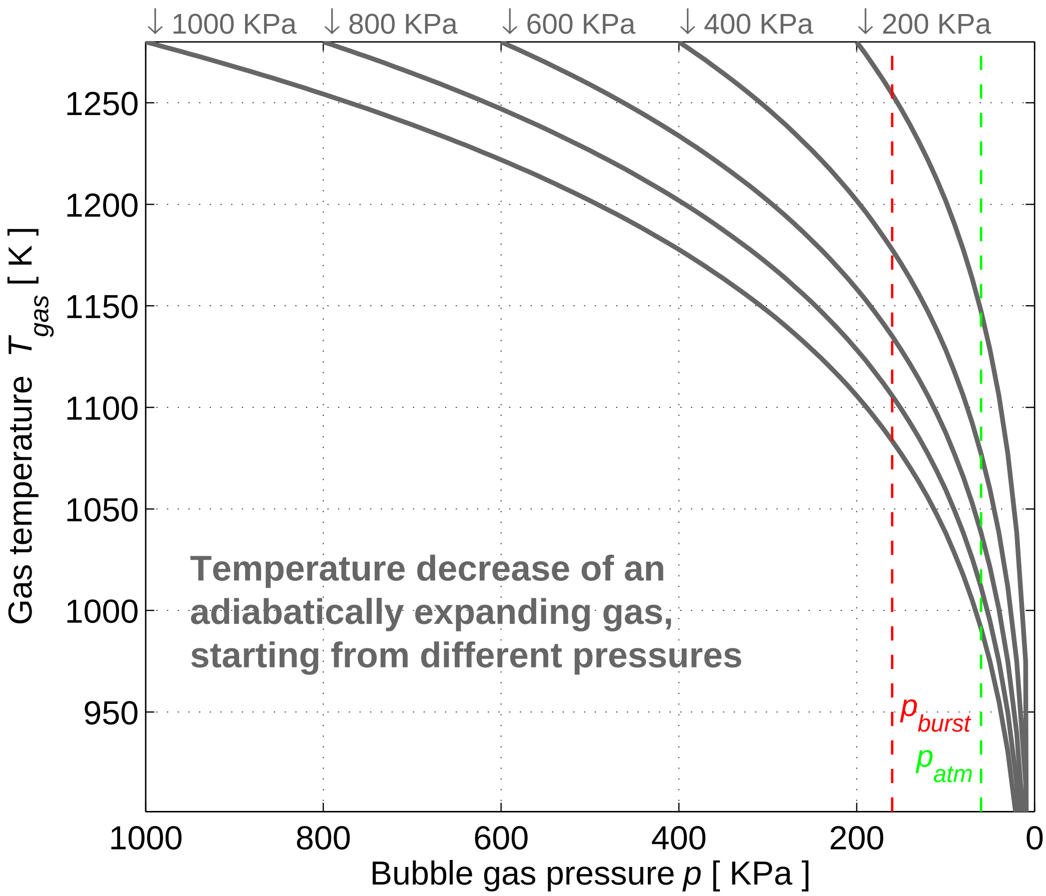

Figure A.2: *Temperature change of an adiabatically expanding gas, with an initial temperature of 1000°C (∼1273 K). Note that depending on the initial pressure, the gas looses only 50 K to 150 K during its expansion phase before the burst, and about the same amount again once it has expanded enough to assume ambient atmospheric pressure.*

A.3 Compact vs. non-compact lava lake

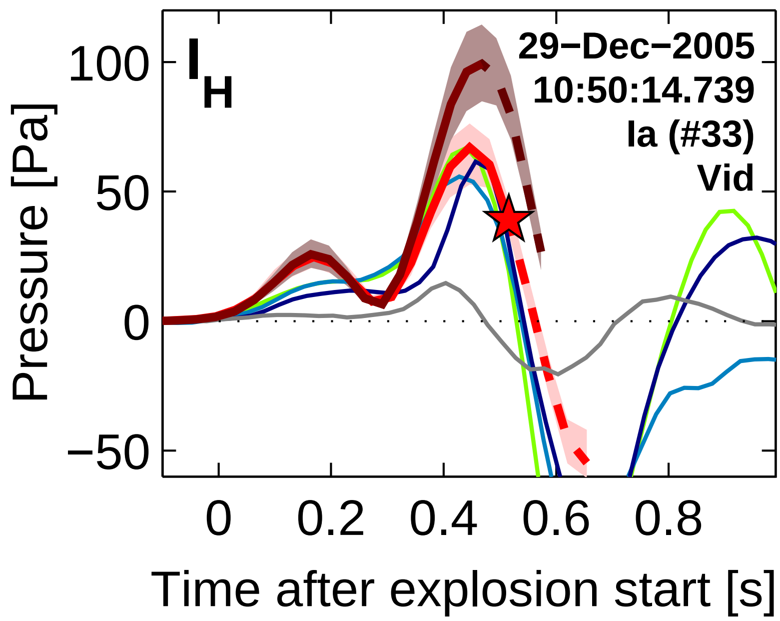

Figure A.3: ***Erebus lava lake as a compact vs. non-compact infrasound source*** *The figure is similar to Fig. 7.10 (I_H). Analogous to that figure, the lower red line shows the predicted acoustic signal when using the Green's function method for a* ***non-compact*** *source. Additionally, the upper (dark red) line shows the predicted sound output of a* ***compact*** *acoustic monopole with the same volumetric properties (i.e. the same volumetric acceleration at any given time). Thin lines show real acoustic signals as measured around the crater region, scaled to a common reference distance. In accordance with the conclusions drawn in Sections 3.4 & 7.6, the non-compact source is more adequate for reproducing the real sound output of explosions from Ray Lava Lake on Erebus volcano.*

A.4 Calculating acoustic waveforms using mean radar velocities

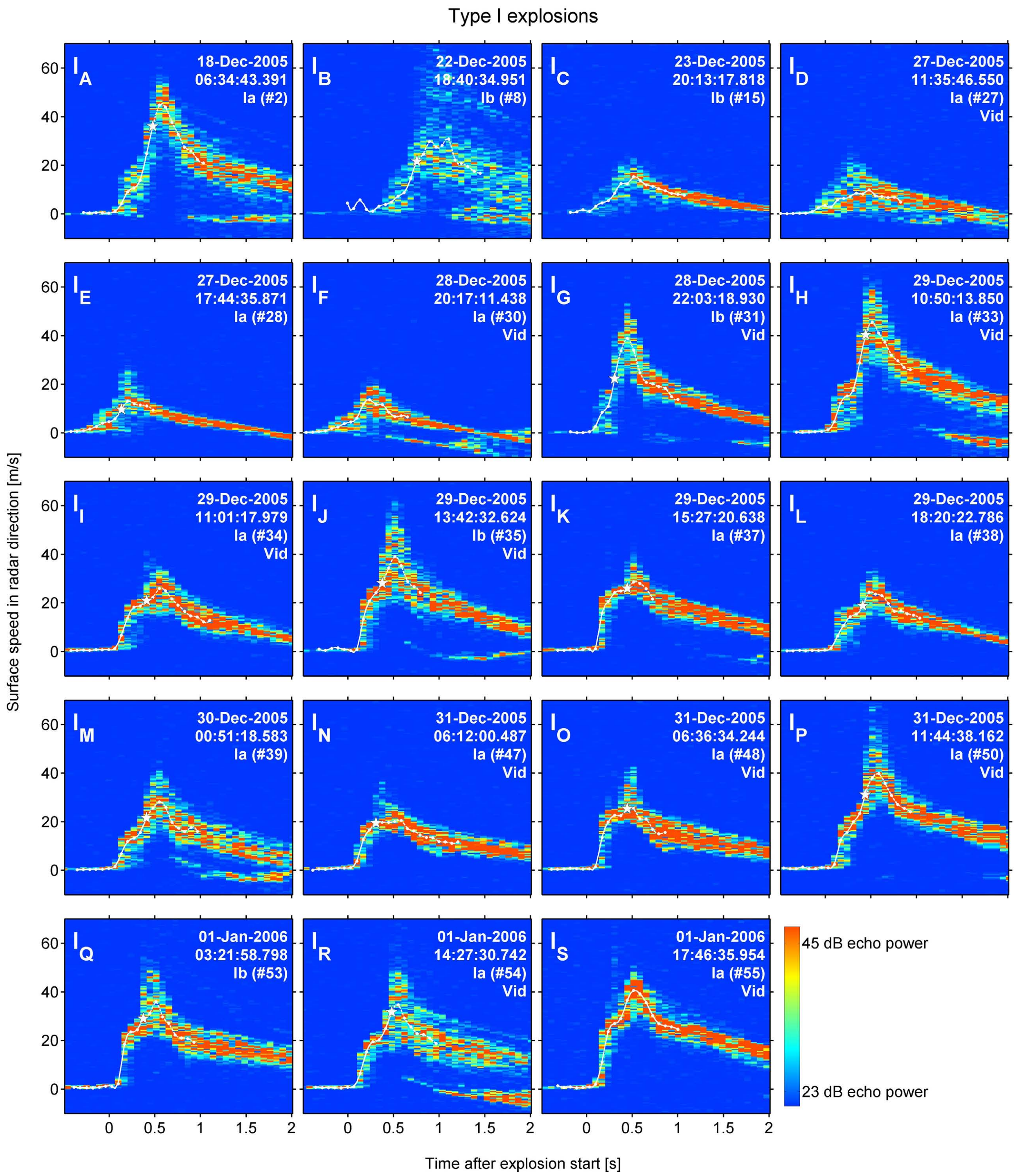

Figure A.4: ***Radar velocigram of explosion type I, showing automatically picked mean velocities instead of cutoff velocities.*** *This Figure is largely similar to Fig. 6.6, the only difference is that the white lines do not show the manually picked cutoff velocities, but automatically picked* ***mean velocities****. These will be used in Fig. A.5 to demonstrate their effect on the fit between predicted and expected acoustic traces.*

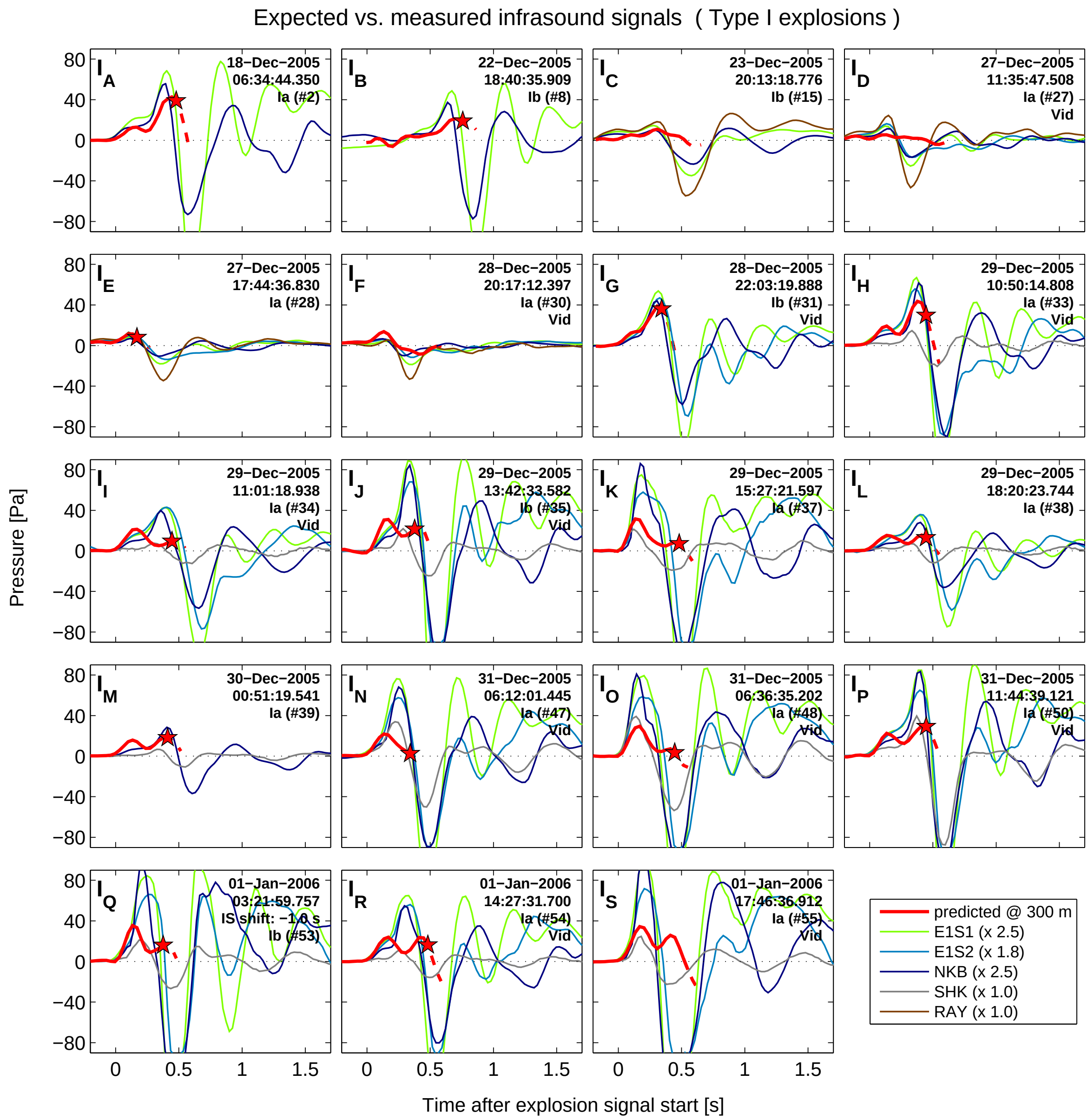

Figure A.5: ***Expected vs. measured infrasound signals (type I), when using mean velocities instead of cutoff velocities.*** *This Figure is largely similar to Fig. 7.10. The difference is that here, instead of using manually picked cutoff velocities to predict the acoustic pressure traces, automatically picked* ***mean velocities*** *were used (see Fig. A.4). Practically, even though the reason is not entirely clear, this increases the fit between real and predicted acoustic traces, especially for the typical small plateau before the main peak (see explosions I_A to I_H). A possible explanation is that mean velocities, which are always smaller than cutoff velocities, provide a better description of the volumetric expansion process when the bubble is still small, therefore not overestimating the first plateau (as discussed in Sec. 7.6).*

Note that using mean velocities instead of cutoff velocities only has a minor scaling effect on the other explosion parameters (e.g. energies, pressures, volumes) that can be obtained from the model (not shown).

APPENDIX B

DERIVING 3D EXPLOSION DIRECTIVITY

Note: parts of this chapter were already published in Gerst et al. (2008)

To obtain a 3D velocity vector, at least three linear independent velocity components of the moving object have to be measured. This can be achieved by aligning three radar beams to overlap in the region in which the object is located, i.e. the target region. In order to understand the meaning of radar velocity data, it is important to be aware of the nature of such a measurement. Most importantly, the radar will only measure the Doppler shift of scattered reflections from the target surface, i.e. only the velocity component in beam direction will be measured. Because the beam has a finite angle of spread (around 3°, depending on the used antenna type; see Fig. A.1) several objects in the target region are observed simultaneously, represented in a velocity spectrum (Fig. 6.3).

Depending on the nature of the target there are two ways to extract the target's velocity from the spectra, which is subsequently needed to calculate its velocity vector. For a single particle in the radar beam this is trivial, since it will lead to only a single line in the spectrum, the radar velocity of which can be easily identified. In case of several objects in the radar beam, moving at different speeds, a representative average speed can be obtained by calculating the median velocity of the spectrum. In this case, care must be taken to ensure similar illumination areas of the different radars. If not all three radars observe the same group of particles at the same time, their median velocities will be biased by this, leading to a systematical error in the obtained velocity vector. When calculating the directivity of an expanding bubble, median velocities are of no use because they are strongly influenced by the area of illumination on the bubble surface, and therefore by parameters like the radar's distance to the source etc. In this case, as will be shown below, cutoff velocities need to be picked (Fig. 6.3), allowing for the determination of the bubble's current surface speed.

FMCW Doppler radars typically integrate the received echo power over a certain time interval, which typically is shorter than the sampling interval (see Sec. 5.1.1). For a temporally precise measurement, it is best to minimise the sampling interval, or, if this is technically impossible, to minimise the integration interval time within the sampling interval. In this study, controlled by the two slower MVR3 radars with a sampling period of 1 s, the integration interval was 300 ms for the man-made explosion (Sec. B.1.1) and 250 ms for the Erebus setup.

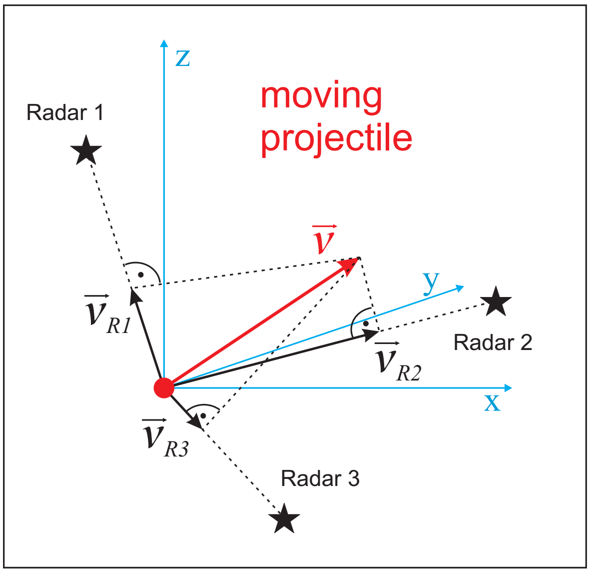

Figure B.1: ***Directivity of a projectile.*** *When observing a projectile (large dot) in the target region moving with velocity $\vec{v}$, all three radars "see" the same object, therefore measuring different components of the same velocity vector $\vec{v}$. These are projections of $\vec{v}$ onto the respective unit vectors pointing towards the radars.*

I will first derive the theoretical background for calculating the direction of a **single projectile, jet, or directed explosion** from three linear independent Doppler radar observations. This technique was originally used by *Hort et al.* (2003), but without an introduction of the mathematical background of the technique. I will qualitatively verify this technique by processing a non-volcanic data set from a quarry blast where the direction of the material is known a priori (Sec. B.1.1 below). Then I will modify the theory such that it becomes applicable to the **explosion of bubbles** on active volcanic lava lakes (Sec. B.2 below).

B.1 The directivity of a moving projectile

I start with the simplest scenario, which assumes either i) a single object moving through the three radar beams (e.g. a projectile of an explosion) or ii) several projectiles that are distinguishable in each of the different spectra recorded by the different radars (while this might be possible for a few objects, it is impossible in the case of thousands of particles moving simultaneously through the beam) or iii) many moving objects in the radar beam with similar trajectories, i.e. behaving like one large particle. Figure B.1 shows that in this case the measured velocity components v_{Ri} in the three radar directions are simply projections of the original projectile velocity $\vec{v}$ onto the radar beams, i.e. onto the unit vectors $\hat{\vec{r}}_{Ri}$ pointing towards the radar i ($i = [1, 2, 3, ...]$):

$$v_{Ri} = \vec{v} \cdot \hat{\vec{r}}_{Ri} \ . \tag{B.1}$$

With three radars measuring, this can be expressed as the following system of equations:

$$\begin{pmatrix} v_{R1} \\ v_{R2} \\ v_{R3} \end{pmatrix} = \begin{pmatrix} \hat{r}_{1,x} & \hat{r}_{1,y} & \hat{r}_{1,z} \\ \hat{r}_{2,x} & \hat{r}_{2,y} & \hat{r}_{2,z} \\ \hat{r}_{3,x} & \hat{r}_{3,y} & \hat{r}_{3,z} \end{pmatrix} \begin{pmatrix} v_x \\ v_y \\ v_z \end{pmatrix} \tag{B.2}$$

or, simply

$$\vec{v}_R = \bar{R}\,\vec{v}\,, \tag{B.3}$$

where $\vec{v}_R$ is the vector with all three observed radar velocities. Equation B.3 can be solved by inverting the matrix $\bar{R}$:

$$\vec{v} = \bar{R}^{-1}\,\vec{v}_R\,. \tag{B.4}$$

B.1.1 Directivity example: a quarry blast in 4D

A quarry blast in Koschenberg, Germany, was observed with three radars on October 13, 2005, to test the setup of the radar system with precise timing capabilities, wireless data transmission and telemetry. A detailed description of the field setup was given in Section 5.1.4, where it served as a system test and demonstration. The blast, in which 13 tons of explosives were used to remove a ∼100,000 ton rock face, was measured at distances between 250 m and 320 m by the three radars sampling at 1 Hz (see Fig. B.2 top).

In this setup, the radar target was a wall of rock. This means that the assumption of a single projectile in the target region does not hold. However, the three radars observed the rock face from the front (Fig. 5.8), allowing them all to observe the same target region, which, due to the beam width of $\sim 3°$ was significantly smaller than the moving rock face. Thus, the assumption can be made that all particles in the target region (circle in Fig. B.2 A) moved with approximately the same velocity and initially parallel trajectories, so the above calculation of $\vec{v}$ is valid. As suggested above, median velocities were calculated from the spectra and used for the calculation of velocity vectors.

Figure B.2 (bottom) shows that during the first second after detonation, the material moved almost horizontally. Yet it did not simply move away from the rock face, but moved mostly parallel to it (towards the right). This parallel movement was very likely caused by a delayed ignition of the borehole charges (a technique deliberately used by the blast crew), which also moved from left to right within 0.5 s. A second later the parallel movements have slowed down significantly, and a rapid downward movement is observed, obviously caused by gravity. Three seconds after the detonation, downward movement was fastest, with a speed of almost 25 m/s (second "3", and image at top centre). From this point on, material started to slow down, until almost all material came to rest at about seven seconds after the ignition.

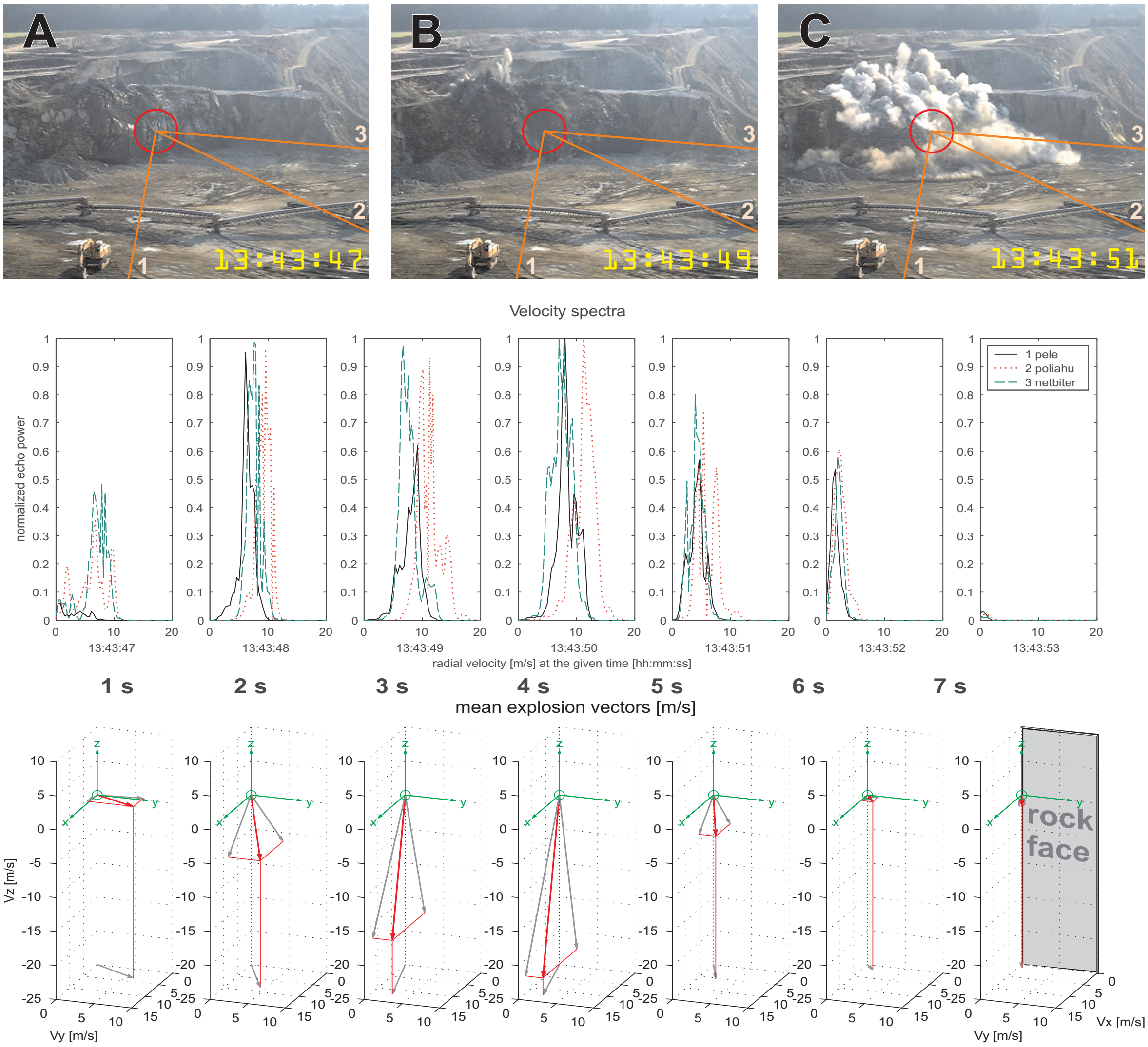

***Figure B.2:* Monitoring the directivity of a quarry blast.**
Top row: *snapshot images from the explosion sequence, with a time difference of two seconds each. The first movement in the target area (indicated by circle) on the front of the rock face was detected at 13:43:46.7 [hh:mm:ss.s UT]. Lines show the approximate location of the radar beams, annotated with numbers. Radar no. 1 is located right next to the camera. From snapshot A and B it is visible that some of the boreholes blew out during the blast (outside the target region, so this was not observed by the radars).*
Middle row: *individual velocity spectra of the three different radars are shown for each second after the ignition (as annotated). Each plot contains integrated velocity information about the last 300 ms of the previous UT second. The width of the peaks indicates that some material moves at speeds different to the median speed (main peak) or in different directions inside the radar beams, as can be expected in such a scenario.*
Bottom row: *combined true velocity vectors of the bulk material in the target area for each second after the ignition. In this visualisation, the rock face roughly coincides with the back part of the box (y-z plane), and the x-axis approximately points along beam 2 (top).*

The above data show that 3D radar observations of the quarry blast agree very well with the true target movements, which are, in this case, known a priori, and additionally supported by video observations. This shows that it is possible to successfully track 3D directivities of an explosion evolving with time with Doppler radars.

B.2 The directivity of an expanding bubble

At Erebus, the dynamics of explosions substantially differ from those at a quarry blast. Explosions at Erebus occur from the surface of a lava lake, which is visible from the crater rim in a direct line of sight, caused by the expansion of a large overpressured gas bubble (or slug) just beneath the surface. These explosions are not constrained by surrounding walls, so ejecta can freely follow their original trajectory. Additionally, at Erebus the dynamically expanding surface of the lava lake stays intact during the first moments of bubble expansion, gradually evolving to an almost hemispherical magma shell. The growing cap causes the different radars to "see" slightly different parts of the bubble, i.e. there is no single target region any more. Thus, the assumption made in Section B.1 that the target behaves as a single projectile with a single velocity vector $\vec{v}$ is not valid any more. The model needs to take into account that the radial expansion of the bubble always leads to a positive contribution to the measured radar velocity, independent of the observation azimuth (this is not the case when observing a single projectile). Thus, the technique developed in Section B.1 has to be slightly modified to account for this different geometry.

For this task, a very simple eruption model was used to limit the number of free parameters. The model assumes that during an explosion, when the head of a pressurised gas slug approaches the surface of the lava lake, the magma shell that develops from the lake surface expands with a hemispherical shape, and with its centre remaining close to the centre of the lava lake. Such an assumption is an adequate first order description of the majority of explosions at Erebus (see video caption in Fig. 8.2 and *SOM*).

To account for a possible directivity of an explosion in the model, the radially expanding hemisphere is allowed to possess a velocity component in the horizontal plane, i.e. the radially expanding sphere is allowed to move horizontally while keeping its expanding spherical shape (see Figure B.3). Such behaviour is assumed to be a good first order approximation for the observed asymmetric, or non-isotropic expansion of bubbles. To keep the model simple and to avoid additional free parameters, the bubble centre is not allowed to move vertically (only when the expanding bubble is observed by more than three radars, a vertical movement of the bubble can be included without an under-determination of the model). For the intended task, such an assumption is reasonable for a simple model, and video observations show that the bubble centre does not rise far above the lake level during an explosion.

The three radars need to be aligned to observe the same area on the lake surface when it is still flat (i.e. before an explosion). When an explosion takes place and the lake surface

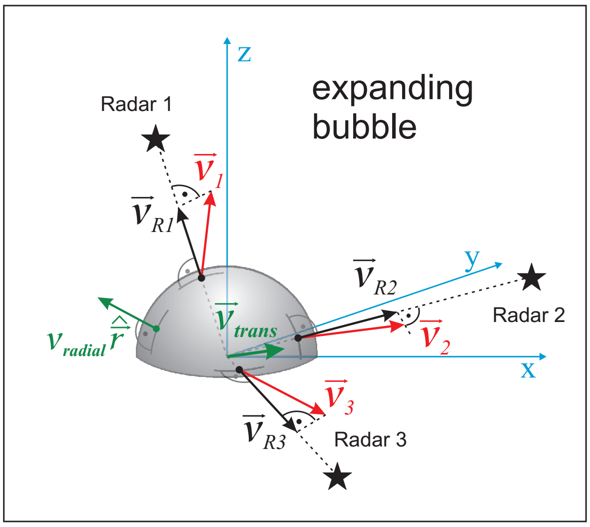

Figure B.3: **Directivity of a bubble burst.** *When observing a bubble burst, all three radars will "see" a slightly different (but possibly overlapping) part of the bubble surface, due to different observation angles.*

bulges upwards the three radars will "see" increasingly different parts of the evolving hemispherical surface due to their different observation angles. Naturally, for the given geometry and with a slow horizontal movement of the bubble compared to the expansion velocity, the surface point moving fastest towards the radar will be located close to the point where the radar beam has a 90° angle of incidence on the surface. Therefore, both points will move at a similar velocity towards the radar. In the special case that the sphere has no lateral velocity, each radar will in fact measure the true radial expansion velocity (so in this case all three radar spectra are equal, i.e. the explosion has no directivity). To obtain the speed of the above mentioned point from a radar spectrum, not the median but the cutoff velocity in each radar spectrum (see Fig. 6.3) must be picked, which represents the beam-parallel component of the shell velocity.

The velocity of an arbitrary point on the magma shell during an eruptive event at Erebus can be expressed as

$$\vec{v} = \vec{v}_{trans} + v_{radial}\,\hat{\vec{r}}\,, \tag{B.5}$$

where $\vec{v}_{trans}$ (Figure B.3) is the horizontal movement of the magma shell ($\vec{v}_{trans}$ has no vertical component, i.e. $v_{trans,\mathbf{z}} = 0$), v_{radial} is the absolute value of the radial velocity of the hemisphere, and $\hat{\vec{r}}$ is the normal vector on the surface at the point of interest.

To calculate the velocity component v_{R1} in beam direction at a point where the beam of radar no. 1 is perpendicular to the surface, the velocity of this point has to be projected onto the surface normal unit vector $\hat{\vec{r}}_{R1}$ pointing towards the radar, since the radar is only measuring the component along the beam:

$$v_{R1} = \left(\vec{v}_{trans} + v_{radial}\,\hat{\vec{r}}_{R1}\right)\,\hat{\vec{r}}_{R1} = \vec{v}_{trans}\cdot\hat{\vec{r}}_{R1} + v_{radial}\,. \tag{B.6}$$

Under the above made assumption ($|\vec{v}_{trans}| \ll v_{radial}$) and with a distance to the radar source that is significantly larger than the bubble radius, the point of 90° incidence can be considered identical with the point moving fastest towards the radar. Thus, v_{R1} for this point can be identified in the spectrum as the cutoff velocity $v_{R1,cut}$.

When three radars are installed, three of the above equations can be set up, resulting in an equation system

$$\begin{pmatrix} v_{R1,cut} \\ v_{R2,cut} \\ v_{R3,cut} \end{pmatrix} = \begin{pmatrix} \hat{r}_{1,x} & \hat{r}_{1,y} & 1 \\ \hat{r}_{2,x} & \hat{r}_{2,y} & 1 \\ \hat{r}_{3,x} & \hat{r}_{3,y} & 1 \end{pmatrix} \begin{pmatrix} v_{trans,x} \\ v_{trans,y} \\ v_{radial} \end{pmatrix} \tag{B.7}$$

or,

$$\vec{v}_{R,cut} = \tilde{\bar{R}}\, \vec{v}_{dir} \ , \tag{B.8}$$

where $\vec{v}_{R,cut}$ is the vector with all three observed radar cutoff velocities. The equation can, once again, be solved by inverting the matrix, in this case $\tilde{\bar{R}}$ (which is significantly different to the matrix $\bar{R}$ from Section B.1, since the z-coordinates of the radar locations do **not** contribute to $\tilde{\bar{R}}$):

$$\vec{v}_{dir} = \tilde{\bar{R}}^{-1}\, \vec{v}_{R,cut} \ . \tag{B.9}$$

The resulting vector $\vec{v}_{dir}$, which consists of the two horizontal components and the radial component of the hemisphere movement, represents the **velocity vector of the uppermost point of the hemisphere**, therefore providing a measure of the directivity of the explosion (Fig. 8.2). It is important to note that a purely vertical vector means that the expanding spherical cap does not move horizontally, i.e. it has no directivity. Also note that at this stage, with three recording instruments, a purely vertical directivity (e.g. like a vertically accelerating cannon ball) can be detected for a single projectile, but not for an expanding bubble. In future deployments with more than three radars, such additional parameters can be resolved.

Date	Time [UT]	v_{RAY} [m/s]	v_{SHK} [m/s]	v_{SUM} [m/s]	Dir Azimuth [°]	Dir Inclination [°]	AbsVel [m/s]	Video
2005-12-24	22:20:49	29.43 -0.40 / +3.10	48.09 -6.50 / +7.30	36.00 -0.80 / +4.20	-89.3 -26.6 / +26.0	65.5 -11.9 / +8.7	39.8 -4.2 / +5.7	-
2005-12-24	22:20:50	16.09 -0.40 / +1.20	23.34 -5.10 / +6.50	25.59 -1.40 / +0.60	232.0 -9.6 / +13.5	32.6 -7.8 / +11.3	26.2 -2.7 / +2.2	-
2005-12-24	22:20:51	7.06 -0.40 / +1.20	11.25 -0.30 / +7.00	15.75 -0.60 / +0.60	226.9 -1.7 / +15.3	10.4 -2.3 / +13.0	21.0 -2.7 / +1.6	-
2005-12-27	05:21:30	30.21 -0.40 / +2.40	33.75 -5.10 / +10.10	43.59 -3.90 / +8.20	223.1 -6.9 / +13.9	35.7 -17.8 / +17.4	40.1 -6.1 / +16.2	yes
2005-12-27	05:21:31	18.44 -0.40 / +0.80	21.38 -1.10 / +2.20	27.00 -2.00 / +7.60	224.4 -3.7 / +4.9	35.1 -21.9 / +11.5	25.2 -3.1 / +15.6	yes
2005-12-27	21:05:46	36.88 -7.80 / +3.10	44.72 -9.30 / +0.30	41.62 -3.40 / +8.20	249.3 -41.4 / +56.6	74.3 -39.1 / +12.7	39.9 -4.8 / +5.7	-
2005-12-27	21:05:47	20.79 -12.90 / +1.60	12.66 -1.10 / +11.20	18.56 -7.60 / +4.80	102.1 -96.2 / +150.6	69.9 -69.3 / +3.9	18.5 -0.8 / +16.8	-
2005-12-29	15:27:21	25.89 -0.40 / +0.40	45.56 -5.60 / +17.20	36.28 -2.20 / +12.40	253.9 -22.6 / +28.5	52.2 -29.2 / +7.1	38.9 -3.0 / +21.5	-
2005-12-29	15:27:22	20.01 -0.40 / +0.40	21.38 -2.80 / +14.60	23.06 -1.10 / +0.60	226.3 -14.7 / +71.2	68.8 -7.0 / +8.5	20.2 -1.2 / +9.7	-
2005-12-30	04:59:57	20.40 -1.20 / +2.70	22.50 -4.50 / +6.20	22.22 -2.50 / +7.30	239.5 -41.7 / +220.0	78.6 -44.9 / +7.6	20.9 -2.3 / +8.1	-
2005-12-30	04:59:58	7.06 -0.40 / +2.70	8.72 -3.40 / +11.20	6.75 -2.20 / +0.80	-2.0 -87.3 / +134.2	77.9 -38.7 / +2.8	8.5 -2.2 / +11.5	-
2005-12-30	20:54:17	2.75 -1.20 / +0.40	0.56 +0.00 / +0.00	0.00 +0.00 / +0.00	52.6 -2.9 / +0.5	27.2 -0.3 / +1.5	7.2 -3.0 / +1.0	yes
2005-12-30	20:54:18	10.99 -0.40 / +1.20	46.12 -1.40 / +8.70	14.06 -0.80 / +9.60	-41.5 -48.9 / +8.5	50.3 -13.8 / +1.5	39.0 -1.3 / +8.3	yes
2005-12-30	20:54:19	4.71 -0.40 / +0.40	11.81 -0.80 / +2.00	10.41 -0.60 / +0.80	241.3 -4.1 / +7.5	21.8 -5.6 / +6.7	13.9 -1.3 / +1.8	yes
2005-12-31	06:12:01	27.86 -3.50 / +8.20	57.38 -7.60 / +11.80	26.44 -4.80 / +0.60	-17.9 -19.2 / +36.0	62.0 -8.3 / +3.8	52.7 -7.7 / +18.0	yes
2005-12-31	06:12:02	13.73 -1.20 / +1.20	25.59 -1.40 / +6.50	14.06 -0.60 / +0.60	-30.2 -19.9 / +19.0	66.7 -6.7 / +1.9	22.4 -1.7 / +5.9	yes
2005-12-31	06:12:03	8.24 -0.80 / +0.80	22.22 -15.80 / +0.60	6.75 -0.60 / +0.00	-10.2 -7.8 / +71.5	53.7 -1.6 / +13.8	21.9 -13.1 / +1.6	yes
2005-12-31	11:44:39	41.98 -3.10 / +9.80	56.81 -1.10 / +9.30	41.91 -2.00 / +12.40	-24.5 -100.8 / +58.5	77.2 -24.0 / +0.8	52.2 -3.3 / +16.6	yes
2005-12-31	11:44:40	19.22 -0.80 / +1.20	25.03 -1.40 / +1.10	20.81 -0.60 / +0.60	-77.8 -23.0 / +42.3	78.2 -4.9 / +4.1	22.1 -1.1 / +1.3	yes
2005-12-31	11:44:41	11.77 -0.40 / +1.60	20.25 -2.50 / +0.00	15.19 -1.70 / +0.80	264.7 -16.2 / +35.8	60.5 -6.3 / +14.1	16.7 -1.5 / +0.5	yes
2005-12-31	11:44:42	6.67 +0.00 / +1.60	18.84 -1.70 / +0.00	9.00 -0.60 / +0.00	-62.8 -6.0 / +26.8	55.0 -0.0 / +6.9	15.1 -1.4 / +0.9	yes
2006-01-01	14:27:31	20.01 -0.40 / +1.20	21.38 -1.40 / +2.00	21.38 -1.40 / +2.20	236.5 -21.4 / +105.5	81.1 -16.3 / +9.9	20.2 -0.8 / +1.8	yes
2006-01-01	14:27:32	30.21 -2.70 / +1.20	21.66 -0.80 / +17.40	21.94 -0.60 / +2.20	57.1 -33.0 / +7.6	58.3 -2.9 / +9.6	36.0 -6.6 / +12.2	yes
2006-01-01	14:27:34	15.69 -2.00 / +2.70	4.78 -3.10 / +6.50	11.25 -0.60 / +1.10	84.3 -30.2 / +24.6	48.6 -9.8 / +11.5	16.1 -4.4 / +6.8	yes
2006-01-01	17:46:37	28.64 -0.40 / +7.50	21.38 -0.60 / +2.50	26.44 -1.10 / +1.40	97.5 -40.1 / +37.1	77.0 -20.4 / +2.9	26.4 -1.3 / +14.0	yes
2006-01-01	17:46:38	18.83 -0.40 / +0.80	10.69 -0.80 / +0.80	16.03 -0.60 / +1.10	91.7 -12.0 / +23.0	65.8 -4.3 / +3.6	17.3 -1.4 / +1.7	yes
2006-01-01	17:46:39	11.77 -0.40 / +0.40	4.22 -1.10 / +17.70	10.69 -0.80 / +0.60	127.1 -139.1 / +19.2	56.5 -6.5 / +6.7	9.6 -0.5 / +11.3	yes

Table B.1: *Picked cutoff velocities from three radars (RAY, SHK, SUM), showing 10 explosions and their respective directivity vectors. When the bubble expansion phase lasted for more than one second, several directivity vectors were calculated. Error boundaries on the picked velocities were determined manually, and their propagation on the directivity vectors were calculated. See Fig. 8.3 for a graphical display of the results. Note that errors due to unprecise station locations are negligible compared to errors resulting from picking uncertainties.*

References

Abramowitz, M., and I. Stegun (1965), *Handbook of Mathematical Functions with Formulas, Graphs, and Mathematical Table*, Courier Dover Publications.

Aki, K., and P. Richards (1980), *Quantitative Seismology: Theory and Methods*, W.H. Freeman and Company, San Francisco, California.

Allard, P., J. Carbonelle, N. Métrich, H. Loyer, and P. Zettwoog (1994), Sulphur output and magma degassing budget of Stromboli Volcano, *Nature*, *368*, 326–330, doi:10.1038/368326a0.

Allard, P., M. Burton, and F. Muré (2005), Spectroscopic evidence for a lava fountain driven by previously accumulated magmatic gas, *Nature*, *433*(7024), 407–410, doi:10.1038/nature03246.

Aster, R., S. Mah, P. Kyle, W. McIntosh, N. Dunbar, J. Johnson, M. Ruiz, and S. McNamara (2003), Very long period oscillations of Mount Erebus Volcano, *J. Geophys. Res.*, *108*(B11), 2522, doi:10.1029/2002JB002101.

Aster, R., W. McIntosh, P. Kyle, R. Esser, B. Bartel, N. Dunbar, B. Johns, J. Johnson, R. Karstens, C. Kurnik, et al. (2004), Real-time data received from Mount Erebus Volcano, Antarctica, *Eos Trans. AGU*, *85*(10), 97–101, doi:10.1029/2004EO100001.

Aster, R., D. Zandomeneghi, S. Mah, S. McNamara, D. Henderson, H. Knox, and K. Jones (2008), Moment tensor inversion of very long period seismic signals from Strombolian eruptions of Erebus Volcano, *J. Volc. Geotherm. Res.*, *177*(3), 635 – 647, doi:10.1016/j.jvolgeores.2008.08.013.

Baker, B. B., and C. T. Copson (1953), *The Mathematical Theory of Huygens Principle*, Clarendon, Oxford.

Bannister, S., R. Snieder, and M. Passier (2000), Shear-wave velocities under the Transantarctic Mountains and Terror Rift from surface wave inversion, *Geophys. Res. Lett.*, *27*(2), 281–284.

Batchelor, G. (1967), *An Introduction to Fluid Dynamics*, Cambridge University Press.

Behrendt, J. (1999), Crustal and lithospheric structure of the West Antarctic Rift System from geophysical investigations – a review, *Global Planetary Change*, *23*, 25–44.

Blackburn, E., L. Wilson, and R. Sparks (1976), Mechanism and dynamics of strombolian activity, *J. Geol. Soc. London*, *132*, 429–440, doi:10.1144/gsjgs.132.4.0429.

Blackstock, D. (2000), *Fundamentals of Physical Acoustics*, 1st ed., 121 pp., John Wiley, Hoboken, NJ, ISBN 0-471-31979-1.

Brown, G., H. Rymer, J. Dowden, P. Kapadia, D. Stevenson, J. Barqero, and L. Morales (1989), Energy budget analysis for Poás crater lake: implications for predicting volcanic activity, *Nature*, *339*, 370–372.

Brown, G., H. Rymer, and D. Stevenson (1991), Volcano monitoring by microgravity and energy budget analysis, *J. Geol. Soc. London*, *148*, 585–593.

Brown, R. (1965), The mechanics of large bubbles in tubes, I-bubble velocities in stagnant liquids, *Can. J. Chem. Eng.*, *43*, 217–23.

Bruce, P., and H. Huppert (1989), Thermal control of basaltic fissure eruptions, *Nature*, *342*(7 December 1989), 665–667, doi:10.1038/342665a0.

Buckingham, M. J., and M. A. Garcés (1996), Canonical model of volcano acoustics, *J. Geophys. Res.*, *101(B4)*, 8129–8151, doi:10.1029/95JB01680.

Burton, M., P. Allard, F. Mure, and C. Oppenheimer (2003), FTIR remote sensing of fractional magma degassing at Mount Etna, Sicily, *Geol. Soc. Special Publ.*, *213*(1), 281.

Burton, M., P. Allard, F. Mure, and A. La Spina (2007), Magmatic Gas Composition Reveals the Source Depth of Slug-Driven Strombolian Explosive Activity, *Science*, *317*(5835), 227 – 230, doi:10.1126/science.1141900.

Caldwell, D., and P. Kyle (1994), Mineralogy and geochemistry of ejecta erupted from Mount Erebus, Antarctica, between 1972 and 1986, in *Volcanological and Environmental studies of Mount Erebus, Antarctica*, *Antarct. Res. Ser.*, vol. 66, edited by P. Kyle, pp. 147–162, Am. Geophys. Union, Washington, D.C.

Calkins, J., C. Oppenheimer, and P. Kyle (2008), Ground-based thermal imaging of lava lakes at Erebus volcano, Antarctica, *J. Volc. Geotherm. Res.*, *177*(3), 695 – 704, doi:DOI:10.1016/j.jvolgeores.2008.02.002.

Calvari, S., L. Spampinato, L. Lodato, A. Harris, M. Patrick, J. Dehn, M. Burton, and D. Andronico (2005), Chronology and complex volcanic processes during the 2002-2003 flank eruption at Stromboli volcano (Italy) reconstructed from direct observations and surveys with a handheld thermal camera, *J. Geophys. Res.*, *110*, 23–47.

Cannata, A., P. Montalto, E. Privitera, G. Russo, and S. Gresta (2009), Tracking eruptive phenomena by infrasound: May 13, 2008 eruption at Mt. Etna, *Geophys. Res. Lett.*, *36*(5), L05,304, doi:10.1029/2008GL036738.

Carmichael, I., F. Turner, and J. Verhoogen (1974), *Igneous petrology*, McGraw-Hill New York.

Carn, S., J. Pallister, L. Lara, J. Ewert, S. Watt, A. Prata, R. Thomas, and G. Villarosa (2009), The Unexpected Awakening of Chaitén Volcano, Chile, *Eos Trans. AGU*, *90*, 24.

Carniel, R., M. D. Cecca, and D. Rouland (2003), Ambrym, Vanuatu (July-August 2000): Spectral and dynamical transitions on the hours-to-days timescale, *J. Volc. Geotherm. Res.*, *128*, 1–13.

Chadwick, W., K. Cashman, R. Embley, H. Matsumoto, R. Dziak, C. de Ronde, T. Lau, N. Deardorff, and S. Merle (2008), Direct video and hydrophone observations of submarine explosive eruptions at NW Rota-1 volcano, Mariana arc, *J. Geophys. Res.*, *113*, B08S10, doi:10.1029/2007JB005215.

Chouet, B., N. Hamisevicz, and T. McGetchin (1974), Photoballistics of volcanic jet activity at Stromboli, Italy, *J. Geophys. Res.*, *79*, 4961–4976, doi:10.1029/JB079i032p04961.

Chouet, B., G. Saccorotti, M. Martini, P. Dawson, G. De Luca, G. Milana, and R. Scarpa (1997), Source and path effects in the wave fields of tremor and explosions at Stromboli volcano, Italy, *J. Geophys. Res.*, *102*(B7), 15,129–15,150.

Chouet, B., P. Dawson, T. Ohminato, M. Martini, G. Saccorotti, F. Giudicepietro, G. De Luca, G. Milana, and R. Scarpa (2003), Source mechanisms of explosions at Stromboli volcano, Italy, determined from moment-tensor inversions of very-long-period data, *J. Geophys. Res.*, *108*, 2019, doi:10.1029/2002JB001919.

Chouet, B., P. Dawson, and A. Arciniega-Ceballos (2005), Source mechanism of Vulcanian degassing at Popocatépetl Volcano, Mexico, determined from waveform inversions of very long period signals, *J. Geophys. Res.*, *110*(B07301), doi:10.1029/2004JB003524.

Chouet, B., P. Dawson, and M. Martini (2008), Shallow-conduit dynamics at Stromboli Volcano, Italy, imaged from waveform inversions, in *Fluid Motion in Volcanic Conduits: A Source of Seismic and Acoustic Signals*, vol. 307, edited by S. J. Lane and J. S. Gilbert, pp. 57–84, Geol. Soc., London, Special Publications, doi:10.1144/SP307.5.

Chouet, G., B. Saccorotti, P. Dawson, M. Martini, R. Scarpa, G. De Luca, G. Milana, and M. Cattaneo (1999), Broadband measurements of the source of explosions at Stromboli volcano, Italy, *Geophys. Res. Lett.*, *26*(13), 1937–1940.

Csatho, B., T. Schenk, W. Krabill, T. Wilson, G. McKenzie, C. Hallam, S. Manizade, and T. Paulsen (2005), Airborne laser scanning for high-resolution mapping of Antarctica, *Eos Trans. AGU*, *86*(25), 237 – 238.

Csatho, B., T. Schenk, P. Kyle, T. Wilson, and W. B. Krabill (2008), Airborne laser swath mapping of the summit of Erebus volcano, Antarctica: Applications to geological mapping of a volcano, *J. Volc. Geotherm. Res.*, *177*(3), 531 – 548, doi:DOI:10.1016/j.jvolgeores.2008.08.016.

Davies, A., S. Chien, V. Baker, T. Doggett, J. Dohm, R. Greeley, F. Ip, R. Castano, B. Cichy, G. Rabideau, et al. (2006), Monitoring active volcanism with the Autonomous Sciencecraft Experiment on EO-1, *Remote Sens. Environ.*, *101*(4), 427–446.

Davies, A., J. Calkins, L. Scharenbroich, R. Vaughan, R. Wright, P. Kyle, R. Castaño, S. Chien, and D. Tran (2008), Multi-instrument remote and in situ observations of the Erebus Volcano (Antarctica) lava lake in 2005: A comparison with the Pele lava lake on the jovian moon Io, *J. Volc. Geotherm. Res.*, *177*(3), 705–724, doi:10.1016/j.jvolgeores.2008.02.010.

Davies, R., and G. Taylor (1950), The mechanics of large bubbles rising through extended liquids and through liquids in tubes, *Proc. Roy. Soc. London*, *200*(1062), 375–390.

De Lauro, E., S. De Martino, M. Falanga, and M. Palo (2009), Decomposition of high-frequency seismic wavefield of the Strombolian-like explosions at Erebus volcano by independent component analysis, *Geophys. J. Int.*, *177*(3), 1399–1406, doi:10.1111/j.1365-246X.2009.04157.x.

Demant, A., P. Lestrade, R. Lubala, A. Kampunzu, and J. Durieux (1994), Volcanological and petrological evolution of Nyiragongo Volcano, Virunga volcanic field, Zaire, *Bull. Volc.*, *56*, 47–61.

Dibble, R. (1989), Infrasonic recordings of Strombolian eruptions of Erebus, Antarctica, March – December 1984, covering the jump in activity on 13 September 1984, in *Volcanic Hazards, Assessment and Monitoring*, edited by J. Latter, pp. 536–553, Springer-Verlag, Berlin.

Dibble, R. (1994), Velocity modeling in the erupting magma column of Mount Erebus, Antarctica, in *Volcanological and Environmental studies of Mount Erebus, Antarctica*, *Antarct. Res. Ser.*, vol. 66, edited by P. Kyle, pp. 17–33, Am. Geophys. Union, Washington, D.C.

Dibble, R., J. Kienle, P. Kyle, and K. Shibuya (1984), Geophysical studies of Erebus volcano, Antarctica, from 1974 December to 1982 January, *New Zealand J. Geol. Geophys.*, *27*(4), 425–455.

Dibble, R., B. OBrien, and C. Rowe (1994), The velocity structure of Mount Erebus, Antarctica, and its lava lake, in *Volcanological and Environmental studies of Mount Erebus, Antarctica, Antarct. Res. Ser.*, vol. 66, edited by P. Kyle, pp. 1–16, Am. Geophys. Union, Washington, D.C.

Dibble, R., P. Kyle, and C. Rowe (2008), Video and seismic observations of Strombolian eruptions at Erebus volcano, Antarctica, *J. Volc. Geotherm. Res.*, *177*(3), 619 – 634, doi:10.1016/j.jvolgeores.2008.07.020.

Dingwell, D., N. Bagdassarov, G. Bussod, and S. Webb (1993), Magma rheology, in *Experiments at high pressure and applications to the Earth's mantle*, vol. 21, edited by R. Luth, pp. 131–196, Mineral. Assoc. Canada.

Divoux, T., V. Vidal, F. Melo, and J. Géminard (2008), Acoustic emission associated with the bursting of a gas bubble at the free surface of a non-Newtonian fluid, *Phys. Rev.*, *77*, 056,310.

Donn, W., and N. Balachandran (1981), Mount St. Helens eruption of 18 May 1980: Air waves and explosive yield, *Science*, *213*(4507), 539–541, doi:10.1126/science.213.4507.539.

Donnadieu, F., G. Dubosclard, R. Cordesses, T. Druitt, C. Hervier, J. Kornprobst, J. Lénat, P. Allard, and M. Coltelli (2005), Remotely monitoring volcanic activity with ground-based Doppler radar, *Eos Trans. AGU*, *86*, 21, doi:10.1029/2005EO210001.

Dowling, A. (1998), Steady-state radiation from sources, in *Handbook of Acoustics*, edited by M. Crocker, pp. 99–117, Wiley-Interscience.

Dowling, A., and F. Williams (1983), *Sound and Sources of Sound*, Horwood, Chichester, England.

Dubosclard, G., R. Cordesses, P. Allard, C. Hervier, M. Coltelli, and J. Kornprobst (1999), First testing of a volcano doppler radar (VOLDORAD) at Mount Etna, Italy, *Geophys. Res. Lett.*, *26(22)*, 3389–3392, doi:10.1029/1999GL008371.

Dubosclard, G., F. Donnadieu, P. Allard, R. Cordesses, C. Hervier, M. Coltelli, E. Privitera, and J. Kornprobst (2004), Doppler radar sounding of volcanic eruption dynamics at Mount Etna, *Bull. Volc.*, *66*, 443–456, doi:10.1007/s00445-003-0324-8.

Dunbar, N., K. Cashman, and R. Dupre (1994), Crystallization processes of anorthoclase phenocrysts in the Mount Erebus magmatic system; evidence from crystal composition, crystal size distributions, and volatile contents of melt inclusions, in *Volcanological and Environmental studies of Mount Erebus, Antarctica*, *Antarct. Res. Ser.*, vol. 66, edited by P. Kyle, pp. 129–146, Am. Geophys. Union, Washington, D.C.

Ehrenfried, K. (2003), Skript zur Vorlesung: Strömungsakustik I, Technische Universität Berlin.

Esser, R., P. Kyle, and W. McIntosh (2004), 40 Ar/39 Ar dating of the eruptive history of Mount Erebus, Antarctica: volcano evolution, *Bull. Volc.*, *66*(8), 671–686, doi:10.1007/s00445-004-0354-x.

Fabre, J., and A. Liné (1992), Modeling of two-phase slug flow, *Ann. Rev. Fluid Mech.*, *24*(1), 21–46, doi:10.1146/annurev.fl.24.010192.000321.

Fee, D., and M. Garcés (2007), Infrasonic tremor in the diffraction zone, *Geophys. Res. Lett.*, *34*, L16,826, doi:10.1029/2007GL030616.

Firstov, P., and N. Kravchenko (1996), Estimation of the amount of explosive gas released in volcanic eruptions using air waves, *Volcanol. Seismol*, *17*, 547–560.

Ford, R. (1970), *Introduction to Acoustics*, 154 pp., Elsevier, New York.

Francis, P., C. Oppenheimer, and D. Stevenson (1993), Endogenous growth of persistently active volcanoes, *Nature*, *366*, 554–557.

Francis, P., L. Horrocks, and C. Oppenheimer (2000), Monitoring gases from andesite volcanoes, *Phil. Trans.*, *358*(1770), 1567–1584.

Garcés, M., and S. McNutt (1997), Theory of the airborne sound field generated in a resonant magma conduit, *J. Volc. Geotherm. Res.*, *78*(3-4), 155–178, doi:10.1016/S0377-0273(97)00018-8.

Garcés, M., R. Hansen, and K. Lindquist (1998), Traveltimes for infrasonic waves propagating in a stratified atmosphere, *Geophys. J. Int.*, *135*(1), 255–263, doi:10.1046/j.1365-246X.1998.00618.x.

Garcés, M., S. McNutt, R. Hansen, and J. Eichelberger (2000), Application of wave-theoretical seismoacoustic models to the interpretation of explosion and eruption tremor signals radiated by Pavlof volcano, Alaska, *J. Volc. Geotherm. Res.*, *105*, 3039–3058.

Garcés, M., A. Harris, C. Hetzer, J. Johnson, S. Rowland, E. Marchetti, and P. Okubo (2003), Infrasonic tremor observed at Kilauea Volcano, Hawai'i, *Geophys. Res. Lett.*, *30*(20), 2023, doi:10.1029/2003GL018038.

Gernert, D. (2007), Ockham's razor and its improper use, *J. Sci. Exp.*, *21*(1), 135–140.

Gerst, A., M. Hort, P. Kyle, and M. Vöge (2006), The first second of a Strombolian eruption: velocity observations at Erebus volcano, Antarctica, *Eos Trans. AGU, Fall Meet. Suppl.*, *87*(52), Abstr. V31G–04.

Gerst, A., M. Hort, P. Kyle, and M. Vöge (2008), 4D velocity of Strombolian eruptions and man-made explosions derived from multiple Doppler radar instruments, *J. Volc. Geotherm. Res.*, *177*, 648–660, doi:10.1016/j.jvolgeores.2008.05.022.

Giggenbach, W., P. Kyle, and G. Lyon (1973), Present volcanic activity on Mt. Erebus, Ross Island, Antarctica, *Geology*, *1*, 135–136.

Giordano, D., J. Russell, and D. Dingwell (2008), Viscosity of magmatic liquids: A model, *Earth and Planetary Sci. Lett.*, *271*(1-4), 123–134, doi:10.1016/j.epsl.2008.03.038.

Gorshkov, G. (1960), Determination of the explosion energy in some volcanoes according to barograms, *Bull. Volc.*, *23*(1), 141–144, doi:10.1007/BF02596639.

Gorshkov, G., and Y. Dubik (1970), Gigantic directed blast at Shiveluch volcano (Kamchatka), *Bull. Volc.*, *34*(1), 261–288, doi:10.1007/BF02597790.

Gouhier, M., and F. Donnadieu (2008), Mass estimations of ejecta from Strombolian explosions by inversion of Doppler radar measurements, *J. Geophys. Res.*, *113*, B10,202, doi:10.1029/2007JB005383.

Hagerty, M., S. Schwartz, M. Garcés, and M. Protti (2000), Analysis of seismic and acoustic observations at arenal volcano, Costa Rica, 1995-1997, *J. Volc. Geotherm. Res.*, *101*, 27–65, doi:10.1016/S0377-0273(00)00162-1.

Hall, D. E. (2001), *Musical Acoustics*, 3rd revised edition ed., Brooks/Coole.

Harris, A., and M. Ripepe (2007), Synergy of multiple geophysical approaches to unravel explosive eruption conduit and source dynamics–A case study from Stromboli, *Chemie der Erde - Geochemistry*, *67*(1), 1–35, doi:10.1016/j.chemer.2007.01.003.

Harris, A., R. Wright, and L. Flynn (1999), Remote monitoring of Mount Erebus volcano, Antarctica, using polar orbiters: Progress and prospects, *Int. J. Rem. Sens.*, *20*(15), 3051–3071.

Harris, A., R. Carniel, and J. Jones (2005), Identification of variable convective regimes at Erta Ale Lava Lake, *J. Volc. Geotherm. Res.*, *142*(3-4), 207–223.

Harris, D., and W. Rose (1983), Estimating particle sizes, concentrations, and total mass of ash in volcanic clouds using weather radar, *J. Geophys. Res.*, *88*(No. C15), 10,969–10,983.

Harris, D., W. Rose, R. Roe, and M. Thompson (1981), Radar observations of ash eruptions, *USGS Professional Paper*, *1250*, 322–333.

Haskell, N. A. (1964), Total energy and energy spectral density of elastic wave radiation from propagating faults, *Bull. Seismol. Soc. Am.*, *54*(6), 1811–1841.

Hédervári, P. (1963), On the energy and magnitude of volcanic eruptions, *Bull. Volc.*, *25*(1), 373–385.

Heki, K. (2006), Explosion energy of the 2004 eruption of the Asama Volcano, central Japan, inferred from ionospheric disturbances, *Geophys. Res. Lett.*, *33*, L14,303, doi: 10.1029/2006GL026249.

Henderson, D. (2007), Analysis of seismic similarity in Strombolian eruptions from Mount Erebus, Antarctica, Master's thesis, New Mexico Institute of Mining and Technology.

Hort, M., and R. Seyfried (1998), Volcanic eruption velocities measured with a micro radar, *Geophys. Res. Lett.*, *25(1)*, 113–116, doi:10.1029/97GL03482.

Hort, M., R. Seyfried, and M. Vöge (2001), Monitoring volcanic eruption velocities in three dimensions: First results from Doppler radar measurements at Stromboli volcano, *Eos Trans. AGU Fall Meet. Suppl.*, *82*(47), F1400.

Hort, M., R. Seyfried, and M. Vöge (2003), Radar Doppler velocimetry of volcanic eruptions: theoretical considerations and quantitative documentation of changes in eruptive behaviour at Stromboli Volcano, Italy, *Geophys. J. Int.*, *154*, 515–532, doi:10.1046/j.1365-246X.2003.01982.x.

Hort, M., M. Vöge, R. Seyfried, and A. Ratdomopurbo (2006), In situ observation of dome instabillities at Merapi Volcano, Indonesia: A new tool for hazard mitigation, *J. Volc. Geotherm. Res.*, *153*, 301–312, doi:10.1016/j.jvolgeores.2005.12.007.

Hurst, A., H. Bibby, B. Scott, and M. McGuinness (1991), The heat source of Ruapehu Crater Lake; deductions from the energy and mass balances, *J. Volcanol. Geotherm. Res*, *46*, 1–20, doi:10.1016/0377-0273(91)90072-8.

Ichihara, M., K. Tanaka, H. Oshima, A. Goto, and H. Taniguchi (2005), Wave generation and formation in the air by underwater explosions, in *Proc. 25th International Symposium on Shockwaves*, p. Paper No. 1137 3a.

Ichihara, M., M. Ripepe, A. Goto, H. Oshima, H. Aoyama, M. Iguchi, K. Tanaka, and H. Taniguchi (2009), Airwaves generated by an underwater explosion: Implications for volcanic infrasound, *J. Geophys. Res.*, *114*(B3), B03,210, doi:10.1029/2008JB005792.

Jaeger, J. (1964), Thermal effects of intrusions, *Rev. Geophys.*, *2*(3), 443–466.

James, M., S. Lane, B. Chouet, and J. Gilbert (2004), Pressure changes associated with the ascent and bursting of gas slugs in liquid-filled vertical and inclined conduits, *J. Volc. Geotherm. Res.*, *129*(1-3), 61–82, doi:10.1016/S0377-0273(03)00232-4.

James, M., S. Lane, and B. Chouet (2006), Gas slug ascent through changes in conduit diameter: Laboratory insights into a volcano-seismic source process in low-viscosity magmas, *J. Geophys. Res.*, *111*(B5), 5201, doi:10.1029/2005JB003718.

James, M., S. Lane, L. Wilson, and S. Corder (2009), Degassing at low magma-viscosity volcanoes: Quantifying the transition between passive bubble-burst and Strombolian eruption, *J. Volc. Geotherm. Res.*, *180*(2-4), 81–88, doi:10.1016/j.jvolgeores.2008.09.002.

James, M. R., S. J. Lane, and S. B. Corder (2008), Modelling the rapid near-surface expansion of gas slugs in low-viscosity magmas, in *Fluid Motion in Volcanic Conduits: A Source of Seismic and Acoustic Signals*, vol. 307, edited by S. J. Lane and J. S. Gilbert, pp. 147–167, Geol. Soc., London, Special Publications, doi:10.1144/SP307.9.

Jaupart, C., and S. Vergniolle (1988), Laboratory models of Hawaiian and Strombolian eruptions, *Nature*, *331*, 58–60, doi:10.1038/331058a0.

Jaupart, C., and S. Vergniolle (1989), The generation and collapse of a foam layer at the roof of a basaltic magma chamber, *J. Fluid Mech.*, *203*, 347–380, doi:10.1017/S0022112089001497.

Johnson, J., and R. Aster (2005), Relative partitioning of acoustic and seismic energy during Strombolian eruptions, *J. Volc. Geotherm. Res.*, *148*(3-4), 334–354, doi:10.1016/j.jvolgeores.2005.05.002.

Johnson, J., and J. Lees (2000), Plugs and chugs: Seismic and acoustic observations of degassing explosions at Karymsky, Russia and Sangay, Ecuador, *J. Volc. Geotherm. Res.*, *101*, 67–82.

Johnson, J., M. Ruiz, J. Lees, and P. Ramon (2005), Poor scaling between elastic energy release and eruption intensity at Tungurahua Volcano, Ecuador, *Geophys. Res. Lett.*, *32*, L15,304, doi:10.1029/2005GL022847.

Johnson, J., R. Aster, K. Jones, P. Kyle, and W. McIntosh (2008), Acoustic source characterization of impulsive Strombolian eruptions from the Mount Erebus lava lake, *J. Volc. Geotherm. Res.*, *177*(3), 673 – 686, doi:DOI:10.1016/j.jvolgeores.2008.06.028.

Johnson, J. B. (2003), Generation and propagation of infrasonic airwaves from volcanic explosions, *J. Volc. Geotherm. Res.*, *121*, 1–14, doi:10.1016/s0377-0273(02)00408-0.

Johnson, J. B. (2004), Source location variability and volcanic vent mapping with a small-aperture infrasound array at Stromboli Volcano, Italy, *Bull. Volc.*, *67*, 1–14, doi:10.1007/s00445-004-0356-8.

Johnson, J. B., R. C. Aster, M. C. Ruiz, S. D. Malone, P. J. McChesney, J. M. Lees, and P. R. Kyle (2003), Interpretation and utility of infrasonic records from erupting volcanoes, *J. Volc. Geotherm. Res.*, *121*, 15–63, doi:10.1016/s0377-0273(02)00409-2.

Johnson, J. B., R. C. Aster, and P. R. Kyle (2004), Volcanic eruptions observed with infrasound, *Geophys. Res. Lett.*, *31*, L14,604, doi:10.1029/2004GL020020.

Jones, K., J. Johnson, R. Aster, P. Kyle, and W. McIntosh (2008), Infrasonic tracking of large bubble bursts and ash venting at Erebus Volcano, Antarctica, *J. Volc. Geotherm. Res.*, *177*(3), 661 – 672, doi:DOI:10.1016/j.jvolgeores.2008.02.001.

Junger, M. C. (1966), Energy exchange between incompressible near and acoustic far field for transient sources, *J. Acoust. Soc. Am.*, *40*, 1025–1030.

Kaminuma, K. (1994), The seismic activity of Mt. Erebus in 1980 – 1991, in *Volcanological and Environmental studies of Mount Erebus, Antarctica*, *Antarct. Res. Ser.*, vol. 66, edited by P. Kyle, pp. 35–50, Am. Geophys. Union, Washington, D.C., Washington.

Kanamori, H., and J. Given (1982), Analysis of long-period seismic waves excited by the May 18, 1980, eruption of Mount St. Helens- A terrestrial monopole?, *J. Geophys. Res.*, *87*(B7), 5422–5432.

Kanamori, H., and J. Mori (1992), Harmonic excitation of mantle Rayleigh waves by the 1991 eruption of Mount Pinatubo, Philippines, *Geophys. Res. Lett.*, *19*(7), 721–724.

Kanamori, H., J. Given, and T. Lay (1984), Analysis of seismic body waves excited by the Mount St. Helens eruption of May 18, 1980, *J. Geophys. Res.*, *89*(B3), 1856–1866.

Kelly, P. J., N. W. Dunbar, P. R. Kyle, and W. C. McIntosh (2008a), Refinement of the late Quaternary geologic history of Erebus volcano, Antarctica using 40Ar/39Ar and 36Cl age determinations, *J. Volc. Geotherm. Res.*, *177*(3), 569 – 577, doi:10.1016/j.jvolgeores.2008.07.018.

Kelly, P. J., P. R. Kyle, N. W. Dunbar, and K. W. Sims (2008b), Geochemistry and mineralogy of the phonolite lava lake, Erebus volcano, Antarctica: 1972-2004 and comparison with older lavas, *J. Volc. Geotherm. Res.*, *177*(3), 589 – 605, doi:10.1016/j.jvolgeores.2007.11.025.

Kienle, J., and G. E. Shaw (1979), Plume dynamics, thermal energy and long-distance transport of vulcanian eruption clouds from Augustine Volcano, Alaska, *J. Volc. Geotherm. Res.*, *6*, 139–164, doi:10.1016/0377-0273(79)90051-9.

Kienle, J., C. Rowe, P. Kyle, W. McIntosh, R. Dibble, K. Kaminuma, and K. Shibuya (1985), Eruption of Mount Erebus and Ross Island seismicity, 1984-1985, *Antarct. J. U.S.*, *20*(5), 25–28.

Kinney, G., and K. Graham (1985), *Explosive shocks in air*, 282 pp., Springer-Verlag, Berlin and New York.

Kirchdörfer, M. (1999), Analysis and quasistatic FE modeling of long period impulsive events associated with explosions at Stromboli volcano (Italy), *Ann. Geofisica*, *42*, 379–390.

Koopmann, A. (2004), Magma mingling: The hydrodynamic genesis of magmatic dispersions, Ph.D. thesis, Institut fr Geologie, Fakultät für Geowissenschaften, Universität Würzburg.

Krüssenberg, A., H. Prasser, and A. Schaffrath (2000), A new criterion for the identification of the bubble slug transition in vertical tubes, *Kerntechnik(1987)*, *65*(1), 7–13.

Kulkarny, V. (1978), Impulsive discharge noise: Balloon burst problem and engine exhaust pulses, *J. Acoust. Soc. Am.*, *64*, 298.

Kyle, P. (1977), Mineralogy and glass chemistry of recent volcanic ejecta from Mt. Erebus, Ross Island, Antarctica, *NZ J. Geol. Geophys.*, *20*, 1123–1146.

Kyle, P. (1994), Preface, in *Volcanological and Environmental studies of Mount Erebus, Antarctica*, *Antarct. Res. Ser.*, vol. 66, edited by P. Kyle, pp. xiii–xiv, Am. Geophys. Union, Washington, D.C., Washington.

Kyle, P., R. Dibble, W. Giggenbach, and W. Keys (1982), Volcanic activity associated with the anorthoclase phonolite lava lake, Mount Erebus, Antarctica., *Antarc. Geosci.*, *11*, 270271.

Kyle, P., K. Meeker, and D. Finnegan (1990), Emission rates of sulfur dioxide, trace gases and metals from Mount Erebus, Antarctica, *Geophys. Res. Lett.*, *17*(12), 2125–2128.

Kyle, P., J. Moore, and M. Thirlwall (1992), Petrologic Evolution of Anorthoclase Phonolite Lavas at Mount Erebus, Ross Island, Antarctica, *J. Petrol.*, *33*(4), 849–875.

Kyle, P. R. (1990), Erebus volcanic province, in *Volcanoes of the Antarctic Plate and Southern Oceans*, edited by W. LeMasurier et al., pp. 81–88, Ant. Res. Ser., Am. Geophys. Union.

Lane, S., M. James, and S. Corder (2005), Experimental investigation of volcano-seismic forces generated during gas-slug expansion in Strombolian eruptions, *Eos Trans. AGU, Fall Meet. Suppl.*, *85*, Abstr. V31D–0652.

Larsen, J., C. Neal, P. Webley, J. Freymueller, M. Haney, S. McNutt, D. Schneider, S. Prejean, J. Schaefer, and R. Wessels (2009), Eruption of Alaska volcano breaks historic pattern, *Eos Trans. AGU*, *90*(20), 173, doi:10.1029/2009EO200001.

Le Guern, F., J. Carbonnelle, and H. Tazieff (1979), Erta'ale lava lake: heat and gas transfer to the atmosphere, *J. Volc. Geotherm. Res.*, *6*(1-2), 27 – 48, doi:10.1016/0377-0273(79)90045-3.

Lejeune, A., and P. Richet (1995), Rheology of crystal-bearing silicate melts: An experimental study at high viscosities, *J. Geophys. Res.*, *100*(B3), 4215–4229.

Lighthill, J. (1978), *Waves in Fluids*, Cambridge University Press, New York.

Lu, N., H. Oguz, and A. Prosperetti (1989), The oscillations of a small floating bubble, *Phys. Fluids A*, *1*, 252, doi:10.1063/1.857495.

MacDonald, G. (1972), *Volcanoes*, Prentice-Hall, Englewood Cliffs, NJ.

Macfarlane, D., G. Wadge, D. Robertson, M. James, and H. Pinkerton (2006), Use of a portable topographic mapping millimetre wave radar at an active lava flow, *Geophys. Res. Lett.*, *33*(3), L03,301, doi:10.1029/2005GL025005.

Machado, F., W. Parsons, A. Richards, and J. Mulford (1962), Capelinhos eruption of Fayal volcano, Azores, 1957-1958, *J. Geophys. Res.*, *67*, 3519–3529, doi:10.1029/JZ067i009p03519.

Marchetti, E., and M. Ripepe (2005), Stability of the seismic source during effusive and explosive activity at Stromboli Volcano, *Geophys. Res. Lett.*, *32*(3), L03,307, doi:10.1029/2004GL021406.

Marzano, F., G. Vulpiani, and W. Rose (2006a), Microphysical characterization of microwave radar reflectivity due to volcanic ash clouds, *IEEE Trans. Geosci. Rem. Sens.*, *44*(2), 313–327, doi:10.1109/TGRS.2005.861010.

Marzano, F., S. Barbieri, G. Vulpiani, and W. Rose (2006b), Volcanic ash cloud retrieval by ground-based microwave weather radar, *IEEE Trans. Geosci. Rem. Sens.*, *44*(11 Part 2), 3235–3246, doi:10.1109/TGRS.2006.879116.

Massol, H., and C. Jaupart (1999), The generation of gas overpressure in volcanic eruptions, *Earth and Planetary Science Letters*, *166*, 57–70, doi:10.1016/S0012-821X(98)00277-5.

Matoza, R., M. Hedlin, and M. Garcés (2007), An infrasound array study of Mount St. Helens, *J. Volc. Geotherm. Res.*, *160*(3-4), 249–262, doi:10.1016/j.jvolgeores.2006.10.006.

Matoza, R., M. Garcés, B. Chouet, L. D'Auria, M. Hedlin, C. De Groot-Hedlin, and G. Waite (2009), The source of infrasound associated with long-period events at Mount St. Helens, *J. Geophys. Res.*, *114*(B4), B04,305, doi:10.1029/2008JB006128.

McCall, G. J. H., R. W. LeMaitre, A. Malahoff, G. P. Robinson, and P. J. Stephenson (1971), The geology and geophysics of the Ambrym Caldera, New Hebrides, *Bull. Volc.*, *34*, 681–696.

McGetchin, T., and B. Chouet (1979), Energy budget of the Volcano Stromboli, Italy, *Geophys. Res. Lett.*, *6*(4), 317–320.

McNutt, S. (2005), Volcanic Seismology, *Annu. Rev. Earth Planet. Sci.*, *32*, 461–491, doi:10.1146/annurev.earth.33.092203.122459.

Meier, K., E. Garaebiti, A. Gerst, M. Harrison, M. Hort, S. Kremers, J. Wassermann, and B. Weiss (2009), Preliminary insights into an integrated geophysical approach for a better understanding of Strombolian activity at Yasur volcano, Vanuatu, *Eos Trans. AGU, Fall Meet. Suppl.*, *90*(52), V23D–2098.

MEVO (2008), Mount Erebus Volcano Observatory webpage: http://erebus.nmt.edu/.

Mikumo, T., and B. Bolt (1985), Excitation mechanism of atmospheric pressure waves from the 1980 Mount St Helens eruption, *Geophys. J. R. astron. Soc.*, *81*(2), 445–461, doi:10.1111/j.1365-246X.1985.tb06412.x.

Minakami, T. (1942), On the distribution of volcanic ejecta (part i.): The distributions of volcanic bombs ejected by the recent explosions of Asama, *Bull. Earthquake Res. Inst. Tokyo Univ.*, *20*, 65 – 92.

Morrissey, M., and B. Chouet (1997), Burst conditions of explosive volcanic eruptions recorded on microbarographs, *Science*, *275*(28 February 1997), 1290–1293, doi:10.1126/science.275.5304.1290.

Nakamura, K. (1965), Energy dissipated with volcanic activities. Classification and evolution, *Bull. Vol. Soc. Japan*, *10*, 81–90.

Neuberg, J., R. Luckett, M. Ripepe, and T. Braun (1994), Highlights from a seismic broadband array on Stromboli volcano, *Geophys. Res. Lett.*, *21*(9), 749–752.

Newhall, C., and S. Self (1982), The Volcanic Explosivity Index (VEI): an estimate of explosive magnitude for historical volcanism, *J. Geophys. Res.*, *87*, 1231–1238.

Ohminato, T. (2008), Source mechanisms of vulcanian eruptions at Mt. Asama, Japan, inferred from volcano seismic signals, in *Fluid Motion in Volcanic Conduits: A Source of Seismic and Acoustic Signals*, vol. 307, edited by S. J. Lane and J. S. Gilbert, p. 189, Geol. Soc., London, Special Publications, doi:10.1144/SP307.0.

Ohminato, T., and B. Chouet (1997), A free-surface boundary condition for including 3D topography in the finite-difference method, *Bull. Seismol. Soc. Am.*, *87*, 494–515.

Ohminato, T., B. Chouet, P. Dawson, and S. Kedar (1998), Waveform inversion of very long period impulsive signals associated with magmatic injection beneath Kilauea Volcano, Hawaii, *J. Geophys. Res.*, *103*(B10), 23,839–23,862.

Oppenheimer, C., and P. Francis (1998), Implications of longeval lava lakes for geomorphological and plutonic processes at Erta'Ale volcano, Afar., *J. Volc. Geotherm. Res.*, *80*, 101–111.

Oppenheimer, C., and P. Kyle (2008a), Volcanology of Erebus volcano, Antarctica, *J. Volc. Geotherm. Res.*, *177*(3), v – vii, doi:DOI:10.1016/j.jvolgeores.2008.10.006.

Oppenheimer, C., and P. R. Kyle (2008b), Probing the magma plumbing of Erebus volcano, Antarctica, by open-path FTIR spectroscopy of gas emissions, *J. Volc. Geotherm. Res.*, *177*(3), 743 – 754, doi:10.1016/j.jvolgeores.2007.08.022.

Oppenheimer, C., A. S. Lomakina, P. R. Kyle, N. G. Kingsbury, and M. Boichu (2009), Pulsatory magma supply to a phonolite lava lake, *Earth and Planetary Sci. Lett.*, *284*(3-4), 392 – 398, doi:10.1016/j.epsl.2009.04.043.

Parfitt, E., and L. Wilson (1995), Explosive volcanic eruptions-IX. The transition between Hawaiian-style lava fountaining and Strombolian explosive activity, *Geophys. J. Int.*, *121*(1), 226–232.

Parfitt, E. A. (2004), A discussion of the mechanisms of explosive basaltic eruptions, *J. Volc. Geotherm. Res.*, *134*(1-2), 77–107.

Patrick, M., A. Harris, M. Ripepe, J. Dehn, D. Rothery, and S. Calvari (2007), Strombolian explosive styles and source conditions: insights from thermal (FLIR) video, *Bull. Volc.*, *69*(7), 769–784, doi:10.1007/s00445-006-0107-0.

Peters, G. (1995), *Entwicklung des Micro Rain Radars MRR-1*, METEK Meteorologische Messtechnik GmbH, Elmshorn.

Pierce, A. (1981), *Acoustics: An Introduction to Its Physical Principles and Applications*, 678 pp., McGraw-Hill, New York.

Polonsky, S., L. Shemer, and D. Barnea (1999a), The relation between the Taylor bubble motion and the velocity field ahead of it, *Int. J. Multiph. Flow*, *25*(6-7), 957–975.

Polonsky, S., D. Barnea, and L. Shemer (1999b), Averaged and time-dependent characteristics of the motion of an elongated bubble in a vertical pipe, *Int. J. Multiph. Flow*, *25*(5), 795–812.

Pyle, D. (1995), Mass and energy budgets of explosive volcanic eruptions, *Geophys. Res. Lett.*, *22*(5), 563–566.

Raue, H. (2004), A new model for the fracture energy budget of phreatomagmatic explosions, *J. Volc. Geotherm. Res.*, *129*(1-3), 99–108, doi:10.1016/S0377-0273(03)00234-8.

Richards, A. F. (1963), Volcanic sounds: Investigation and analysis, *J. Geophys. Res.*, *68(3)*, 919 – 928, doi:10.1029/JZ068i003p00919.

Ripepe, M., and E. Gordeev (1999), Gas bubble dynamics model for shallow volcanic tremor at Stromboli, *J. Geophys. Res.*, *104(B5)*, 10,639–10,654, doi:10.1029/98JB02734.

Ripepe, M., and E. Marchetti (2002), Array tracking of infrasonic sources at Stromboli volcano, *Geophys. Res. Lett.*, *29(22)*, 2076, doi:10.1029/2002GL015452.

Ripepe, M., M. Rossi, and G. Saccorotti (1993), Image processing of explosive activity at Stromboli, *J. Volc. Geotherm. Res.*, *54*, 335–351, doi:10.1016/0377-0273(93)90071-X.

Ripepe, M., P. Poggi, T. Braun, and E. Gordeev (1996), Infrasonic waves and volcanic tremor at Stromboli, *Geophys. Res. Lett.*, *23*(2), 181–184.

Ripepe, M., S. Ciliberto, and M. D. Schiava (2001), Time constraints for modelling source dynamics of volcanic explosions at Stromboli, *J. Geophys. Res.*, *106(B5)*, 8713–8727, doi: 10.1029/2000JB900374.

Ripepe, M., A. J. Harris, and R. Carniel (2002), Thermal, seismic and infrasonic evidences of variable degassing rates at Stromboli Volcano, *J. Volc. Geotherm. Res.*, *118*, 285–297, doi: 10.1016/s0377-0273(02)00298-6.

Ripepe, M., P. Poggi, and E. Marchetti (2004a), Small aperture infrasonic array monitors activity of Stromboli volcano, *Inframatics*, *7*, 1–14.

Ripepe, M., E. Marchetti, P. Poggi, A. Harris, A. Fiaschi, and G. Ulivieri (2004b), Seismic, acoustic, and thermal network monitors the 2003 eruption of Stromboli Volcano, *Eos Trans. AGU*, *85*(35), 329, doi:10.1029/2004EO350001.

Rowe, C., R. Aster, P. Kyle, J. Schlue, and R. Dibble (1998), Broadband recording of Strombolian explosions and associated very-long-period seismic signals on Mount Erebus Volcano, Ross Island, Antarctica, *Geophys. Res. Lett.*, *25*(13), 2297–2300.

Rowe, C., R. Aster, P. Kyle, R. Dibble, and J. Schlue (2000), Seismic and acoustic observations at Mt. Erebus volcano, Ross Island, Antarctica, 1994–1998, *J. Volc. Geotherm. Res.*, *101*, 105–128.

Scharff, L., A. Gerst, M. Hort, and J. B. Johnson (2007), The dynamics of explosions at Santiaguito volcano, Guatemala, in *Eos Trans. AGU Fall Meet. Suppl.*, vol. 88, pp. Abstract V31E–0718.

Scharff, L., M. Hort, A. Harris, M. Ripepe, J. Lees, and R. Seyfried (2008), Eruption dynamics of the SW crater of Stromboli volcano, Italy – An interdisciplinary approach, *J. Volc. Geotherm. Res.*, *176*(4), 565–570, doi:10.1016/j.jvolgeores.2008.05.008.

Scharff, L., M. Hort, and N. Varley (2009), Installation of a permanent Doppler radar monitoring system, in *XI Reunión Internacional Volcán de Colima*, p. 71.

Schmincke, H.-U. (2004), *Volcanism*, Springer-Verlag Berlin Heidelberg New York, ISBN 3-540-43650-2.

Schneider, D. J., W. I. Rose, and L. Kelley (1995), Tracking of 1992 eruption clouds from Crater Peak Vent of Mount Spurr Volcano, Alaska, using AVHRR, *USGS Bulletin*, *2139*, 27–36.

Seyfried, R. (1997), Magmatische Fragmentierung und vulkanische Fontänen: Theoretische Analyse und experimentelle Simulation der strömungsmechanischen Prozesse, Ph.d., Christian-Albrechts-Universität zu Kiel.

Seyfried, R., and A. Freundt (2000), Experiments on conduit flow and eruption behavior of basaltic volcanic eruptions, *J. Geophys. Res.*, *105*(B10), 23,727–23,740.

Seyfried, R., and M. Hort (1999), Continuous monitoring of volcanic eruption dynamics: a review of various techniques and new results from a frequency-modulated radar Doppler system, *Bull. Volc.*, *60*, 627–639, doi:10.1007/s004450050256.

Shaw, H. (1969), Rheology of basalts in the melting range, *J. Petrol.*, *10*, 510–535.

Shimozuru, D. (1968), Discussion on the energy partition of volcanic eruption, *Bull. Volc.*, *32*(2), 383–394.

Simkin, T., and K. Howard (1970), Caldera collapse in the Galapagos Islands, 1968, *Science*, *169*(3944), 429–437, doi:10.1126/science.169.3944.429.

Sims, K., J. Blichert-Toft, P. Kyle, S. Pichat, P. Gauthier, J. Blusztajn, P. Kelly, L. Ball, and G. Layne (2008), A Sr, Nd, Hf, and Pb isotope perspective on the genesis and long-term evolution of alkaline magmas from Erebus volcano, Antarctica, *J. Volc. Geotherm. Res.*, *177*(3), 606–618.

Slezin, Y. (2003), The mechanism of volcanic eruptions (a steady state approach), *J. Volc. Geotherm. Res.*, *122*(1-2), 7–50.

Small, C., and T. Naumann (2001), The global distribution of human population and recent volcanism, *Global Environmental Change B: Environmental Hazards*, *3*(3-4), 93–109.

SOM (2010), Supporting online material for this document, online publication, University of Hamburg, Germany, urn:nbn:de:gbv:18-42516, `http://nbn-resolving.de/urn:nbn:de:gbv:18-42516`.

Sparks, R. (1978), The dynamics of bubble formation and growth in magmas: A review and analysis, *J. Volc. Geotherm. Res.*, *3*, 1–37.

Sparks, R., M. Bursik, S. Carey, J. Gilbert, L. Glaze, H. Sigurdsson, and A. Woods (1997), *Volcanic Plumes*, John Wiley & Sons Ldt., New York.

Spiel, D. (1992), Acoustical measurements of air bubbles bursting at a water surface: Bursting bubbles as Helmholtz resonators, *J. Geophys. Res.*, *97*(C7), 11,443–11,452.

Stepanishen, P. (1998), Transient radiation, in *Handbook of Acoustics*, edited by M. Crocker, pp. 119–126, Wiley-Interscience.

Strauch, R. G. (1976), Theory and application of the FM-CW Doppler radar, Ph.D. thesis, Faculty of the graduate school, Boulder.

Sweeney, D., P. R. Kyle, and C. Oppenheimer (2008), Sulfur dioxide emissions and degassing behavior of Erebus volcano, Antarctica, *J. Volc. Geotherm. Res.*, *177*(3), 725 – 733, doi:10.1016/j.jvolgeores.2008.01.024.

Taha, T., and Z. F. Cui (2006), CFD modelling of slug flow in vertical tubes, *Chem. Eng. Sci.*, *61*(2), 676–687, doi:doi:10.1016/j.ces.2005.07.022.

Takei, Y., and M. Kumazawa (1994), Why have the single force and torque been excluded from seismic source models?, *Geophys. J. Int.*, *118*(1), 20–30.

Tazieff, H. (1984), Mt. Nyiragongo: Renewed activity of the lava lake, *J. Volc. Geotherm. Res.*, *20*(3-4), 267–280, doi:10.1016/0377-0273(84)90043-X.

Temkin, S. (1981), *Elements of Acoustics*, John Wiley & Sons, New York.

Thompson, A., and B. N. Taylor (2008), *The NIST Guide for the use of the International System of Units*, NIST Special Publication 811.

Urbanski, N., M. Vöge, R. Seyfried, L. Rüpke, T. Petersen, T. Hanebuth, and M. Hort (2002), Fifteen days of continuous activity survey at Stromboli volcano, Italy, in late September 2000: Doppler radar, seismicity, infrared, soil humidity, and mapping of the crater region, *Int. J. Earth Sci.*, *91*(4), 712–722, doi:10.1007/s00531-001-0242-y.

Vergniolle, S. (1998), Modelling two-phase flow in a volcano, *Proc. of 13th Australasian Fluid Mech. Conf., Aristoc offset Printers for Monash University, Melbourne*, pp. 647–650.

Vergniolle, S., and G. Brandeis (1994), Origin of the sound generated by Strombolian explosions, *Geophys. Res. Lett.*, *21(18)*, 1959–1962, doi:10.1029/94GL01286.

Vergniolle, S., and G. Brandeis (1996), Strombolian explosions 1. A large bubble breaking at the surface of a lava column as a source of sound, *J. Geophys. Res.*, *101 (B9)*, 20,433–20,447, doi:10.1029/96JB01178.

Vergniolle, S., and J. Caplan-Auerbach (2004), Acoustic measurements of the 1999 basaltic eruption of Shishaldin volcano, Alaska: 2. Precursor to the subplinian phase, *J. Volc. Geotherm. Res.*, *137*, 135 – 151, doi:10.1016/j.jvolgeores.2004.05.004.

Vergniolle, S., and C. Jaupart (1990), Dynamics of degassing at Kilauea Volcano, Hawaii, *J. Geophys. Res.*, *95 (B3)*, 2793–2809.

Vergniolle, S., G. Brandeis, and J.-C. Mareschal (1996), Strombolian explosions 2. eruption dynamics determined from acoustic measurements, *J. Geophys. Res.*, *101 (B9)*(96JB01925), 20,449 – 20,466, doi:10.1029/96JB01925.

Vergniolle, S., M. Boichu, and J. Caplan-Auerbach (2004), Acoustic measurements of the 1999 basaltic eruption of Shishaldin volcano, Alaska: 1. Origin of Stromolian activity, *J. Volc. Geotherm. Res.*, *137*, 109–134, doi:10.1016/j.jvolgeores.2004.05.003.

Vidal, V., J. Geminard, T. Divoux, and F. Melo (2006), Acoustic signal associated with the bursting of a soap film which initially closes an overpressurized cavity, *Eur. Phys. J. B*, *54*(3), 321–339, doi:10.1140/epjb/e2006-00450-0.

Vöge, M., and M. Hort (2008), Automatic classification of dome instabilities based on Doppler radar measurements at Merapi volcano, Indonesia: Part I, *Geophys. J. Int.*, *172*(3), 1188–1206, doi:10.1111/j.1365-246X.2007.03605.x.

Vöge, M., and M. Hort (2009), Installation of a Doppler radar monitoring system at Merapi volcano, Indonesia, *IEEE Trans. Geosci. Rem. Sens.*, *47*(1 Part 2), 251–271, doi: 10.1109/TGRS.2008.2002693.

Vöge, M., M. Hort, and R. Seyfried (2005), Monitoring volcano eruptions and lava domes with Doppler radar, *Eos Trans. AGU*, *86*(51), 537, 541, doi:10.1029/2005EO510001.

Vöge, M., M. Hort, R. Seyfried, and A. Ratdomopurbo (2008), Automatic classification of dome instabilities based on Doppler radar measurements at Merapi volcano, Indonesia: Part II, *Geophys. J. Int.*, *172*(11), 1207–1218, doi:10.1111/j.1365-246X.2007.03665.x.

Wadge, G., D. Macfarlane, D. Robertson, A. Hale, H. Pinkerton, R. Burrell, G. Norton, and M. James (2005), AVTIS: A novel millimetre-wave ground based instrument for volcano remote sensing, *J. Volc. Geotherm. Res.*, *146*(4), 307–318, doi:10.1016/j.jvolgeores.2005.03.003.

Wadge, G., D. Macfarlane, M. James, H. Odbert, L. Applegarth, H. Pinkerton, D. Robertson, S. Loughlin, M. Strutt, G. Ryan, et al. (2006), Imaging a growing lava dome with a portable radar, *Eos Trans. AGU*, *87*, 23, doi:10.1029/2006EO230003.

Walker, D., and O. Mullins Jr. (1981), Surface tension of natural silicate melts from 1200°-1500°C and implications for melt structure, *Contrib. Mineral. Petrol.*, *76*, 455–462.

Wallis, G. (1969), *One-Dimensional Two-Phase Flow*, McGraw-Hill.

Wardell, L., P. Kyle, and D. Counce (2008), Volcanic emissions of metals and halogens from White Island (New Zealand) and Erebus volcano (Antarctica) determined with chemical traps, *J. Volc. Geotherm. Res.*, *177*(3), 734 – 742, doi:DOI:10.1016/j.jvolgeores.2007.07.007, volcanology of Erebus volcano, Antarctica.

Wassermann, J. (1997), Locating the sources of volcanic explosions and volcanic tremor at Stromboli volcano (Italy) using beam-forming on diffraction hyperboloids, *Phys. Earth Planet. In.*, *104*, 271–281.

Watson, T., A. Nyblade, D. Wiens, S. Anandakrishnan, M. Benoit, P. Shore, D. Voigt, and J. VanDecar (2006), P and S velocity structure of the upper mantle beneath the Transantarctic Mountains, East Antarctic craton, and Ross Sea from travel time tomography, *Geochem. Geophys. Geosyst.*, *7*(7), Q07,005, doi:10.1029/2005GC001238.

Webb, S., and D. Dingwell (1990), Non-Newtonian rheology of igneous melts at high stresses and strain rates: experimental results for rhyolite, andesite, basalt, and nephelinite, *J. Geophys. Res.*, *95*(B10), 15,695–15,701.

Weill, A., G. Brandeis, S. Vergniolle, F. Baudin, J. Bilbille, J.-F. Fèvre, B. Piron, and X. Hill (1992), Acoustic sounder measurements of the vertical velocity of volcanic jets at Stromboli Volcano, *Geophys. Res. Lett.*, *19(23)*, 2357–2360, doi:10.1029/92GL02502.

White, E., and R. Beardmore (1962), The velocity of rise of single cylindrical air bubbles through liquids contained in vertical tubes, *Chem. Eng. Sci*, *17*(35), 1–6.

White, F. M. (1961), Fluid mechanics, in *Handbook of Chemistry*, edited by N. Lange, 10 ed., p. 1524, McGraw-Hill, New York.

Williams, H., and A. McBirney (1979), *Volcanology*, 397 pp., WH Freeman, New York.

Wilson, L. (1980), Relationship between pressure, volatile content and ejecta velocity in three types of volcanic eruptions, *J. Volc. Geotherm. Res.*, *8*, 297–314, doi:10.1016/0377-0273(80)90110-9.

Wilson, L., R. Sparks, T. Huang, and N. Watkins (1978), The control of volcanic column heights by eruption energetics and dynamics, *J. Geophys. Res.*, *83*(B4), 1829–1836.

Witham, F., and E. Llewellin (2006), Stability of lava lakes, *J. Volc. Geotherm. Res.*, *158*(3-4), 321–332, doi:10.1016/j.jvolgeores.2006.07.004.

Woods, A. (1995), The dynamics of explosive volcanic eruptions, *Rev. Geophys.*, *33*(4), 495–530.

Woulff, G., and T. McGetchin (1976), Acoustic noise from volcanoes: theory and experiment, *Geophys. J. R. astr. Soc.*, *45*, 601–616, doi:10.1111/j.1365-246X.1976.tb06913.x.

Wright, R., and E. Pilger (2008a), Satellite observations reveal little inter-annual variability in the radiant flux from the Mount Erebus lava lake, *J. Volc. Geotherm. Res.*, *177*(3), 687–694, doi:10.1016/j.jvolgeores.2008.03.005.

Wright, R., and E. Pilger (2008b), Radiant flux from Earth's subaerially erupting volcanoes, *Int. J. Rem. Sens.*, *29*(22), 6443–6466, doi:10.1080/01431160802168210.

Yamasato, H. (1997), Quantitative analysis of pyroclastic flows using infrasonic and seismic data at Unzen Volcano, *Jap. J. Phys. Earth*, *45*(6), 397–416.

Yamasato, H. (1998), Nature of infrasonic pulse accompanying low frequency earthquake at Unzen Volcano, Japan, *Bull. Vol. Soc. Japan*, *43*(1), 1–13.

Yokoo, A., M. Ichihara, A. Goto, and H. Taniguchi (2006), Atmospheric pressure waves in the field of volcanology, *Shock Waves*, *15*(5), 295–300, doi:10.1007/s00193-006-0009-2.

Yokoyama, I. (1956), Energetics in active volcanoes. 1st paper.: Activities of volcano Mihara, Ooshima Island during the period 1953 – 54, *Bull. Earthquake Res. Inst. Tokyo Univ.*, *34*, 185–195.

Yokoyama, I. (1957), Energetics in active volcanoes. 2nd paper, *Bull. Earthquake Res. Inst. Tokyo Univ.*, *35*, 75–97.

Yokoyama, I., S. De la Cruz-Reyna, and J. Espindola (1992), Energy partition in the 1982 eruption of El Chichón volcano, *J. Volc. Geotherm. Res.*, *51*, 1–21.

Ziemen, F. A. (2008), Theoretische Betrachtungen zu Dopplerradarmessungen an Vulkanen, Diplomarbeit, Institut für Geophysik, Universität Hamburg, http://www.mpimet.mpg.de/fileadmin/staff/ziemenflorian/diplomarbeit.pdf.

Zobin, V., G. Reyes, E. Guevara, and M. Bretón (2009), Scaling relationship for Vulcanian explosions derived from broadband seismic signals, *J. Geophys. Res.*, *114*(B3), B03,203, doi:10.1029/2008JB005983.

Index

List of Symbols

The following list summarises the the most frequently used symbols and constants. Page numbers refer to location of first use.

Symbol	Meaning
A	Surface area (general) (p. 45)
A_{cap}	Surface area of bubble cap (section of sphere) (p. 59)
c	Speed of sound (general) (p. 40)
c_{gas}	Speed of sound (hot magmatic gas) (p. 206)
c_a	Speed of sound (air) (p. 44)
C_p	Specific heat capacity at constant pressure (general) (p. 44)
C_V	Specific heat capacity at constant volume (general) (p. 44)
$c_{p,m}$	Specific heat capacity at constant pressure (magma) (p. 75)
E, W	Energy (general) (p. 65)
E_{atm}	Energy radiated into atmosphere (e.g. sound) (p. 65)
E_{diss}	Energy dissipated in magma cap (p. 65)
E_{kin}	Kinetic energy of magma cap (p. 65)
E_{pot}	Potential energy of magma cap in Earth's gravity (p. 65)
E_{seis}	Seismic energy radiated into ground (p. 65)
E_{therm}	Thermal energy of magma cap (p. 65)
$\dot{E}_{\text{sound,mono}}$	Power emitted by an acoustic monopole source (p. 72)
f	Function (general) (p. 40)
$F_{\text{ground,z}}$	Vertical ground force caused by an explosion (p. 73)
g	Gravitational acceleration on Earth's surface (p. 68)
H	Zenith height of magma cap (p. 57)
h	Thickness of bubble cap shell (p. 56)
h_0	Initial thickness of bubble cap shell (p. 57)
He	Helmholtz number, compactness of a sound source (p. 48)
$I, \vec{I}$	Acoustic intensity of a sound source (p. 41)
k	Wave number (general) (p. 48)
M_{gas}	Molar mass of magmatic gas (H_2O / CO_2) [≈ 0.028 kg/mol] (p. 206)
M_A	Molar mass (dry air) [≈ 0.0289645 kg/mol] (p. 43)
m_m	Total mass of the magma in bubble shell (p. 59)
$\hat{\vec{n}}$	Surface normal unit vector (p. 83)
p	Overpressure of gas (general) (p. 40)
$\hat{p}$	Absolute pressure of gas (general) (p. 41)
$P, \dot{E}$	Power (general) [J/s] (p. 65)
p_{gas}	Overpressure inside a gas bubble (p. 66)
$\hat{p}_{\text{gas}}$	Absolute pressure inside a gas bubble (p. 66)
q	Model parameter of magma cap (p. 59)
$R, \vec{R}$	Radius / radial vector of a spherical bubble (p. 58)
$\vec{r}$	Position vector (general) (p. 61)
r	Radius; distance from a point or coordinate origin (general) (p. 45)
$\dot{\vec{r}}$	Velocity (general) (p. 62)
$\ddot{r}, \dot{v}$	Acceleration (general) (p. 73)
R_L	Lava lake radius (p. 57)
R_m	molar / universal gas constant [8.314472(15) J/(mol K)] (p. 43)
T	Temperature (general) [K] (p. 43)
t	Time (general) (p. 40)
t'	Retarded time (for compact sound sources) (p. 46)
T_{gas}	Temperature [K] (magmatic gas) (p. 77)
$\vec{u}$	Acoustic particle velocity (p. 40)
U_{gas}	Internal energy (magmatic gas) (p. 66)
u_r	Acoustic particle velocity (radial) (p. 46)
V	Volume (general) (p. 43)
$\vec{v}$	Velocity (general) (p. 62)

continued on next page...

...continued.

Symbol	Meaning
$v, \dot{r}$	Speed (general) (p. 45)
V_{cap}	Volume of bubble cap (section of sphere) (p. 59)
V_{gas}	Volume of a gas bubble (consisting of cap & slug tail) (p. 66)
V_{source}	Volume of a sound source (general) (p. 49)
V_m	Volume of magma in cap shell (p. 57)
v_R	Velocity component along radar beam (= *radar velocity*) (p. 64)
$v_{\mathrm{R,cut}}$	Distinctive cutoff velocity near the maximum of a radar velocity spectrum (p. 63)
W_{gas}	Pressure-volume work (magmatic gas) (p. 65)
Z	Vertical coordinate of magma cap centre (p. 58)
η_m	Ratio of permanently ejected material to total shell mass (p. 75)
$\dot{\varepsilon}$	Largest local principal strain rate in magma shell (p. 69)
γ	Ratio of specific heats, or adiabatic index (general) (p. 44)
λ	Wave length (general) (p. 48)
μ_m	Viscosity of magma (p. 69)
ω	Oscillation frequency (general) (p. 48)
Φ	Azimuth (general) (p. 60)
Φ_A	Acoustic velocity potential (p. 39)
ϕ_R	Elevation angle between radar beam and the horizontal (p. 63)
ρ	Density (general) (p. 41)
ρ_a	Density (atmospheric air) (p. 41)
ρ_m	Density (magma) (p. 59)
σ	Standard error interval (general) (p. 126)
σ_m	Specific surface energy (magma) (p. 70)
θ	Angle between a vector and the vertical (general) (p. 52)

And in the end
it's not the years in our life that count.
It's the life in our years.

Abraham Lincoln